FOURIER OPTICS APPROACHES TO ENHANCED DEPTH-OF-FIELD APPLICATIONS IN MILLIMETRE-WAVE IMAGING AND MICROSCOPY

by

Bertrand M. Lucotte

HERIOT WATT UNIVERSITY

Submitted for the degree of Doctor of Philosophy
at Heriot Watt University
on Completion of Research in the
School of Engineering and Physical Sciences
March 26, 2010

Abstract

In the first part of this thesis millimetre-wave interferometric imagers are considered for short-range applications such as concealed weapons detection. Compared to real aperture systems, synthetic aperture imagers at these wavelengths can provide improvements in terms of size, cost, depth-of-field (DoF) and imaging flexibility via digital-refocusing. Mechanical scanning between the scene and the array is investigated to reduce the number of antennas and correlators which drive the cost of such imagers. The tradeoffs associated with this hardware reduction are assessed before to jointly optimise the array configuration and scanning motion. To that end, a novel metric is proposed to quantify the uniformity of the Fourier domain coverage of the array and is maximised with a genetic algorithm. The resulting array demonstrates clear improvements in imaging performances compared to a conventional power-law Y-shaped array. The DoF of antenna arrays, analysed via the Strehl ratio, is shown to be limited even for infinitely small antennas, with the exception of circular arrays.

In the second part of this thesis increased DoF in optical systems with Wavefront Coding (WC) is studied. Images obtained with WC are shown to exhibit artifacts that limit the benefits of this technique. An image restoration procedure employing a metric of defocus is proposed to remove these artifacts and therefore extend the DoF beyond the limit of conventional WC systems. A transmission optical microscope was designed and implemented to operate with WC. After suppression of partial coherence effects, the proposed image restoration method was successfully applied and extended DoF images are presented.

Анне.

Acknowledgements

Declaration statement

Throughout this thesis I have acknowledged the contributions made by collaborators. The rest of the research presented here is mine alone. Significant contributions were made in the following areas:

- Chapter 3: The simulated brightness temperature image of a human body with an embedded metallic target was provided by Dr. Beatriz Grafulla-González.

- Chapter 5: The MAD metric for estimating the defocus parameter in wavefront decoded images was proposed by Mads Demenikov.

- Chapter 6: Dr. Gonzalo Muyo assisted me for the aspects of optical design undertaken with the software Zemax. This concerns the design of the Köhler illumination system and the design of the beam expander for implementation of the square aperture cubic phase mask in the wavefront coded microscope. The petal phase mask used in the wavefront coded microscope was designed by Dr. Gonzalo Muyo for a different application and was fabricated by PowerPhotonic.

Contents

Publications

The results presented in this thesis have been published in the following journals and conferences.

Papers in journals:

- B. M. Lucotte, B. Grafulla-González, and A. R. Harvey. Array rotation aperture synthesis for short-range imaging at millimeter wavelengths. *Radio Sci.*, 44(RS1006), 2009.

Papers in conferences:

- B. M. Lucotte and A. R. Harvey. Antenna rotation aperture synthesis for short-range personnel scanning at mm wavelengths. In *PIERS Proc*, pages 400–410, 2007. Prague, Czech Republic.

- A.R. Harvey, T. Vettenburg, M. Demenikov, B. Lucotte, G. Muyo, A. Wood, N. Bustin, A. Singh, and E. Findlay. Digital image processing as an integral component of optical design. In *Novel optical systems design and optimization XI*, volume 7061 of *SPIE*, pages 6104–6104, 2008.

Patents:

- M. Demenikov, E. Findlay, A. Harvey, B. Lucotte, and G. Muyo. Artifact removal from phase encoded images. US patent number: 20100008597. Assignees: STMicroelectronics (Research & Development) Limited.

Chapter 1

Introduction

Fourier optics can be defined as the treatment of classical optics, and in particular imaging systems, with Fourier analysis tools. In signal processing these mathematical tools state that any signal can be decomposed into a finite, or infinite, number of sinusoids with different frequencies, amplitudes and phases. Similarly, in optics it is possible to decompose the radiation of a source into a set of plane waves with different amplitudes and propagating in different directions [1]. The performances of imaging systems can be characterised by analysing their ability to transmit and record these plane waves, also called spatial frequencies. When the source or object lies in the far-field of an incoherent optical system, simplifications can be made to reduce the image formation process to a spatial filtering of the object by the point-spread-function (PSF) of the optical system. In this thesis we apply Fourier-optics analysis to imaging systems as different as millimetre-wave synthetic aperture imagers, wavefront coding systems and optical microscopes. This choice of applications was originally motivated by the availability of research funding in these two separate fields, which were treated independently from each other to a large extent. We will show however that these imaging modalities share a wealth of common principles, tradeoffs and issues.

The spatial resolution is a critical parameter of every imaging systems. By spatial resolution one usually refers to the transverse resolution of an imaging system, although the term can also include the equally important axial resolution. The latter is proportional to the depth-of-field (DoF) of the system which is more commonly discussed

in the literature. The spatial resolution is well known to be intimately related to the radiometric sensitivity or signal-to-noise ratio (SNR) in the image. Indeed, if noise-free conditions were obtained, one could build a perfect model of the source and achieve an infinitely high resolution by interpolation. Thus it should be kept in mind that the DoF also fundamentally depends on the SNR in the image. The central question across this thesis is that of the limited DoF in the seemingly very different imaging systems mentioned above. Objects that lie outside the depth-of-focus region (the object space conjugate to the DoF) of an imaging system appear in the recorded image as strongly blurred or washed out compared to the image of an in-focus object. In conventional imaging systems such as photography the DoF must be traded with the transverse resolution and light throughput. In optical microscopy, high-numerical-aperture optics are employed to achieve high spatial resolution. This may be desirable to exclude object features that lie outside the region of interest. In conventional optical systems, light outside the focal plane is spread over a wider transverse region but the integrated intensity of light in each transverse plane remains constant. This is not true of confocal microscopes, which use a pinhole in front of a single detector to further attenuate light coming from out-of-focus features, and are therefore said to have an optical sectioning ability. In confocal fluorescence microscopy one seeks to minimise the size of the excitation spot in order to selectively excite molecules of interest to increase the SNR in the image, and to minimise tissue damage. Conversely it may be desirable to attain a large DoF, *i.e.* a low axial resolution, to record a two-dimensional projection of a three-dimensional stack in a snapshot. Such examples can be found in microscopy to understand the surface structure of a sample, or to monitor rapid dynamic biological processes.

The limited DoF of imaging systems is due to their redundant sampling of the Fourier domain. When the system is in-focus these redundant measurements add up in-phase. The amount of redundant measurements at each spatial frequency determines the modulation transfer function (MTF) of the system, *i.e.* the transmittance of the system for each spatial frequency. In the presence of defocus however, different points in the aperture contribute to the sampling of the Fourier domain with a phase term that is proportional to the square of the distance to the aperture origin. Thus, with in-

creasing amount of defocus, redundant measurements at each spatial frequency add up increasingly out of phase until the sum eventually reaches zero and then oscillates. This results in a degradation of the MTF of the system, which attenuates or even suppresses spatial frequencies from the object spectrum. The term DoF refers to the maximum amount of defocus for which the loss of transmitted information compared to the in-focus system is deemed acceptable. Wavefront coding (WC) systems offer reduced sensitivity to defocus by removing the destructive interferences between redundancies in the aperture plane with a specifically designed phase filter. The tradeoff for this reduced sensitivity to defocus is an attenuation of the in-focus MTF, which can be compensated for with a digital post-processing. Real-aperture millimetre-wave personnel scanners also suffer from a limited DoF and could theoretically benefit from the WC technique. Synthetic aperture imagers at these wavelengths on the other hand have greatly reduced redundancies in the aperture and generally provide an extended DoF.

Among the physical quantities central to this thesis is the complex degree of coherence of light. In millimetre-wave synthetic aperture imaging, recording this quantity allows the reconstruction of the brightness temperature distribution of an incoherent source via the Van-Cittert Zernike theorem [2]. In transmission optical microscopy, the complex degree of coherence in the object plane is a critical parameter since it determines the image formation mechanism, coherent, incoherent or partially coherent, and consequently determines the balance between contrast and resolution. Other similarities unite the wavefront coding (WC) and synthetic aperture imaging techniques. Similar to incoherent imaging systems considered for WC, synthetic aperture arrays have a cutoff frequency given by the aperture of the array normalised to the wavelength. The spatial filtering inherent to image formation in optical systems is performed digitally in millimetre-wave synthetic aperture imagers. Synthetic aperture arrays however have a PSF that can exhibit high sidelobe levels because of their sparse coverage of the Fourier domain. Even in the ideal case of a hypothetical array that sampled the Fourier domain perfectly uniformly, the sinc-type PSF would have a maximum sidelobe level a factor of 2 higher than that of a diffraction-limited real-aperture imager which has a $sinc^2$-type PSF. These sidelobes greatly degrade the image by inducing strong

oscillations and replicas. In most cases it is therefore necessary to deconvolve the image in order to attenuate these artifacts. This is similar to WC systems. Thus one faces the same tradeoff associated with digital deconvolution methods, namely that between noise amplification and image sharpness. One may further emphasise the strong links between the different imaging modalities discussed in this thesis by looking at their successful combination in recently developed imaging techniques. Such examples include optical coherence tomography (OCT) [3, 4], where low coherence interferometry is used to decouple the high transverse resolution achieved in microscopy from the axial resolution to record a three-dimensional image, interferometric synthetic aperture microscopy (ISAM) a computational imaging method built on OCT that achieves depth-invariant transverse resolution by solving the inverse scattering problem [5]. Recent breakthroughs in super-resolution optical microscopy have also been enabled by the joint exploitation of these techniques, *e.g.* as in stimulated emission depletion (STED) fluorescence microscopy where a doughnut-shaped depletion beam engineered with a binary phase masks is employed to attain subdiffraction resolution [6], or in structured illumination microscopy (SIM) where interferometric fringes are projected onto the sample to shift the spatial frequency coverage of the microscope objective [7, 8].

During recent years microwave radiometry has been widely studied in remote sensing [9], medical imaging and personnel scanning [10, 11, 12]. Imagers at these wavelengths provide an image of the brightness temperature of the target and are currently being deployed at public sites for personal screening and threat detection such as weapons or explosives. Imagers at these wavelengths provide a spatial resolution of the order of the wavelength, typically 10mm, that is sufficient for threat detection applications. There are privacy concerns associated with the screening of the brightness temperature of human bodies at this spatial resolution. However millimetre-wave scanners may provide a more acceptable compromise between resolution and privacy than higher resolution imaging modalities such as x-ray scanners. Moreover, in spite of the very small doses emitted by x-ray scanners operating in backscatter mode (doses per scan are typically 60 times smaller than the daily exposure to x-ray due to background radiation [13]), millimetre-waves present the significant advantage of being non ionising. Real-aperture

millimetre-wave personnel scanners are necessarily fairly large in transverse and depth dimensions, even when multiple reflections are used to reduce their depth. They also suffer from a limited depth-of-field (DoF), typically of the order of 50cm at a 2m distance, because of the fast optics required to achieve high spatial resolution. On the other hand synthetic aperture systems may be less thick, offer increased imaging flexibility due to their beam-steering ability and can be designed to offer an extended DoF. Synthetic aperture arrays require N small aperture antennas to form a high resolution image with $\approx N \times N$ pixels. The raw image data consists of the cross-correlation between pairs of antenna signals, and must be digitally processed to form the final image. When the scene lies in the far-field of the array, the image reconstruction is reduced to performing a Fourier transform. Synthetic aperture imaging has been successfully applied to radio-astronomy and the remote-sensing of the earth [14, 2], where a wealth of useful literature can be found and applied to short-range imaging [15]. The earth rotation synthesis (ERS) technique used in astronomy [2] is such an example. This imaging technique extends the aperture synthesis principle by taking advantage of the earth's rotation to reduce the array complexity at the cost of a very long observation time (typically several hours). In the first part of this thesis we seek to apply the ERS principle to short-range synthetic aperture millimetre-wave imagers in order to reduce their array complexity and therefore their cost. Indeed the cost of such systems is still driven by the cost of receivers, typically around £1000 per receiver. In Chapter 2 the fundamentals of millimetre-wave synthetic aperture imaging are described. We highlight the tradeoffs between antenna count, imaging frame rate and radiometric sensitivity when a motion is introduced between the source and the array. A significant difficulty in synthetic aperture imaging is the understanding of the accumulation of noisy signals, radiated by the source, into the correlator's output. Our analysis of the radiometric sensitivity in the reconstructed image follows the rigourous work by Ruf *et al.* in [9]. Chapter 3 deals with the system design and the combined optimisation of the array and its motion relative to the source. When the array is in translation relative to the scene, the technique is known as radiometric synthetic aperture radar (RADSAR) [16]. For personnel scanners however we show that rotational scanning provides a more efficient sampling of the Fourier space. We therefore propose to optimise

the Fourier domain coverage of antenna arrays after rotational scanning, a technique we term aperture rotation synthesis. To that end a metric of the uniformity of the Fourier domain coverage of the array was developed. Uniform coverage of the Fourier domain was previously proposed [17] but a quantitative metric of coverage uniformity is scarcely discussed. The metric we propose is similar to that described in [18] but is more computationally efficient and is more rigourously derived. It therefore contributes to improving array design and the understanding of its underlying principles. An array design is presented after optimisation of this metric with a genetic algorithm (GA) [19]. The imaging performances of this array are compared to more conventional arrays, e.g. Y-shaped arrays, using simulated millimetre-wave scenes. The sensitivity of the proposed technique to instrument errors is discussed in a final section. The results presented in this Chapter have been published in [20, 21]. In Chapter 4 we show that the depth-of-field of millimetre-wave synthetic aperture imagers can be derived in the same way as for real-aperture optical systems. This analysis shows that real-aperture millimetre-wave personnel scanners suffer from a limited depth-of-field and that synthetic aperture arrays enable an extended DoF. Based on this analysis a new antenna array is designed using the approach described in Chapter 3, with the additional constraint that the antennas be circularly distributed. This added constraint results in the convergence of the GA to an array that exhibits a slightly reduced uniformity in its coverage of the Fourier domain. This is however outweighed by the greatly increased DoF of this array, which suppresses the need for digital refocusing at different ranges.

In the second part of this thesis we study hybrid optical/digital systems that offer a larger depth-of-field than diffraction limited imaging systems, without sacrificing their light gathering ability or transverse resolution. In such imaging systems the optical design is optimised to account for image quality improvements that can be achieved with a post-processing digital image restoration. Such systems are sometimes referred to as *integrated computational imaging systems* (ICIS). An early ICIS system combined an apodised pupil function with a Wiener restoration to extend the DoF [22, 23]. The apodised amplitude pupil function however reduces the light throughput of the system. The benefits of this approach to designing imaging systems were accentuated after image restoration methods successfully corrected for the spherical aberrations

present in the early images measured by the Hubble Space Telescope [24, 25]. This new paradigm was further advanced by Dowski *et al.* [26] who devised a technique they termed "Wavefront Coding". It consists of locating a phase filter in the entrance pupil of the system so that its sensitivity to defocus is much decreased. The effect of the phase filter can be understood by looking at the optical transfer function (OTF), which characterises the transmittance of object spatial frequencies by the optical system. Contrary to the OTF of diffraction limited systems, the OTF is now relatively invariant with defocus and does not exhibit nulls at specific spatial frequencies and defocus values. In that way, the image recorded is blurred but is easily restored with a single filter for a large range of defocus values.

In Chapter 5 different techniques to extend the DoF of imaging systems are reviewed and the principles of wavefront coding are described. We detail two approaches to designing pupil phase masks. The first one is analytical and leads to cubic phase masks. It is based on the constraint that an approximation of the amplitude of the ambiguity function be constant with respect to defocus [26]. The second method, proposed by Prasad *et al.* [27] and termed pupil phase engineering, involves the numerical optimisation of two competing terms: the sensitivity to defocus and the image restorability. This approach is attractive in that it directly addresses the tradeoff between a reduction of the sensitivity of the system to defocus and an attenuation of the amplitude of spatial frequencies transmitted by the system. This attenuation degrades the spatial resolution of the recorded image which appears blurred and must be digitally restored. We also describe a novel metric of the defocus sensitivity of the system proposed in [28] which allows for an efficient optimisation of pupil phase functions. We discuss different metrics of image restorability and argue that the Strehl ratio metric employed in [27, 28] is inappropriate because it is biased by phase effects such as a transverse translation of the PSF. When using the Strehl ratio metric our results are in agreement with those obtained in [27]. However, changing the image restorability metric to exclude phase information drastically changes the phase mask design, which becomes very close to the cubic phase masks derived by Dowski *et al.* in [26].

Extended DoF images obtained with pupil phase encoded systems are well known to suffer from image artifacts. Surprisingly, very few publications can be found on this subject, although they are mentioned and explained in [29]. The origin of these artifacts mostly resides in the variations with defocus of the phase of the OTF. This argument is illustrated with practical examples and a method is devised to remove these artifacts, which are used as a signature of the defocus effect to estimate the defocus parameter W_{20}. The recorded image is then restored with the appropriate filter. This image restoration procedure has been registered as a US patent [30]. The robustness of several metrics of defocus are assessed. We demonstrate that small errors of the order of $\lambda/4$ in the defocus estimate still allow for a significant reduction of the amplitude of these artifacts. In Chapter 6 the potential benefits and challenges of implementing WC in transmission microscopy are described. A transilluminated optical microscope is designed and implemented to accommodate pupil phase filters. This allows us to test experimentally the algorithms and metrics described in Chapter 5.

Chapter 2

Theory of millimetre-wave aperture synthesis imaging

2.1   Introduction

Passive and semi-passive mm-wave imaging techniques are currently receiving considerable attention for short-range imaging, such as personnel scanners, due to their ability to detect concealed weapons through obscurants such as clothing [10, 11, 12]. In contrast to conventional real-aperture imaging systems, synthetic aperture systems allow for digital refocusing using an antenna array that is sparse and essentially planar. For space-borne remote sensing applications, synthetic aperture imagers have traditionally been considered for the recording of high-spatial-resolution images in a single snapshot. Snapshot operation necessarily requires a large number of antennas, which contributes to the high cost of these systems. It is therefore highly desirable to reduce the antenna count without adversely affecting the spatial resolution of the imager. To that end it is possible to take advantage of a relative motion between the array and the source. In Earth rotation synthesis [2], a technique used in radio-astronomy, the motion is naturally provided by the rotation of the earth relative to the source. For near-field imaging the motion can be provided by an airborne or spaceborne platform in translation relative to the source. Examples of such scanning techniques are found in synthetic aperture radar (SAR), and the currently developed radiometric synthetic aperture radar (RADSAR) [16]. Since the visibility samples are recorded in time-

sequence, the reduction in antenna-count is achieved at the cost of either a reduced imaging frame-rate or a reduced radiometric sensitivity.

In section 2.2 and 2.3 we recall the fundamental imaging equations and image reconstruction algorithms for near-field imaging [15], before considering in Section 2.4 the requirements of the array to adequately sample the near-field image spatial frequencies. Section 2.5 presents an analysis of the spectrum of the interference pattern for different antenna-pair configurations. The tradeoffs associated with the reduction in array complexity are discussed in Section 2.6. In comparison with a snapshot aperture synthesis radiometer, the time-sequential recording of n_t visibility data sets will be shown to enable the number of antennas to be reduced by a factor of approximately $\sqrt{n_t}$ without reduction in spatial resolution or sampling density.

2.2 The Visibility Function

In aperture synthesis one aims to construct an image of the brightness temperature distribution of a radiating source with an array of antennas. The image formed is based on the mm-wave signals recorded by each antenna, which are then correlated by pair. These measurements constitute samples of the so-called visibility function. Conventional synthetic aperture imagers record $N(N-1)$ samples of the complex visibility function in a snapshot using N antennas. Figure 2.1 shows a simple antenna configuration with $N = 2$, recording a source with a brightness temperature distribution $T_B(\vec{r})$, where $\vec{r}$ is the vector from the origin of the antenna array to a point on the source.

In the far-field, the spatial frequency recorded by a pair of antennas equals the length of this baseline measured in wavelengths and projected onto a plane normal to the direction of the source [2]. Since the projected baseline varies with the direction of the source, it is possible to record several spatial frequencies with a single baseline in a time-sequence. The *modus-operandus* of the Earth-rotation-synthesis technique [2], used in radio astronomy, takes advantage of this principle. The visibility function for a pair of antennas denoted by indices n and m is described in [15]:
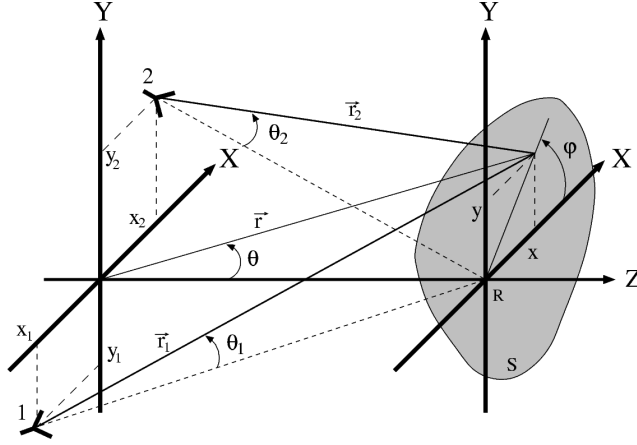
Figure 2.1: *Antenna configuration. The source S is in the far-field of the antennas but in the near-field of the baseline formed by antennas 1 and 2.*

$$\mathcal{V}_{nm} = \frac{k_B \Delta \nu}{\sqrt{\Omega_n \Omega_m}} \iint_S T_B(\vec{r}) K_{nm}(\vec{r}) F_W(\Delta r_{nm}, \Delta \nu) e^{-\frac{j 2\pi}{\lambda_0} \Delta r_{nm}} \, \mathrm{d}S, \qquad (2.1)$$

where:

$$K_{nm}(\vec{r}) = \frac{1}{\|\vec{r}_n\| \|\vec{r}_m\|} \sqrt{P_n(\vec{r}) P_m(\vec{r}) \cos \theta_n \cos \theta_m}, \qquad (2.2)$$

$$\Delta r_{nm} = \|\vec{r}_n\| - \|\vec{r}_m\|, \qquad (2.3)$$

$$\|\vec{r}_n\| = \sqrt{(x_n - x)^2 + (y_n - y)^2 + R^2}, \qquad (2.4)$$

$$= r \sqrt{1 - 2\left(\frac{x_n}{r}\sin\theta\cos\varphi + \frac{y_n}{r}\sin\theta\sin\varphi\right) + \left(\frac{x_n}{r}\right)^2 + \left(\frac{y_n}{r}\right)^2}, \quad (2.5)$$

and k_B is the Boltzmann constant, $\Delta\nu$ is the bandwidth of the antenna channels, Ω_n and Ω_m are the beam solid-angles of antenna n and m respectively, $T_B(\vec{r})$ is the brightness temperature distribution of the source, $K_{nm}(\vec{r})$ is an amplitude term due to the power patterns of antenna n and m, $P_n(\vec{r})$ and $P_m(\vec{r})$ denote the antenna power pattern of antenna n and m respectively. The antennas may be oriented so that they point at a specific point source, as shown in Figure 2.1. The angles between a point source at location $\vec{r}$ and the beam centre of antennas n and m is denoted by θ_n and θ_m respectively. It is assumed that the scene is in the far-field of the array elements, but in the near-field of the array. F_W is the fringe-wash function and depends on the frequency response of the antenna channels and the path difference Δr_{nm} between the point source at $\vec{r}$ and antennas n and m. Note the dependance of Δr_{nm} on $\vec{r}$ has been omitted to simplify the notations. The expression for the fringe wash function for

antenna channels with constant gain over the bandwidth $\Delta\nu$ is:

$$F_W(\Delta r_{nm}, \Delta\nu) = \frac{\sin \pi \Delta\nu \Delta r_{nm}/c}{\pi \Delta\nu \Delta r_{nm}/c} . \qquad (2.6)$$

For wide-band signals, of the order of 10GHz at a centre frequency $\nu_0 = 94GHz$ for example, the first nulls of the fringe wash function can be located within the field-of-view (FoV), *e.g.* $\approx 30°$. This results in a degradation in the signal-to-noise ratio (SNR) of the visibility samples measured, and also of the reconstructed image. One possible solution to reduce this degradation is to introduce artificial delay lines into one antenna channel of each baseline so as to translate the fringe-wash function in azimuth. Maximum signal power can then be recorded over the entire FoV by appropriately choosing these time delays. For a single baseline, the lost signal is recovered by summing all these translated, fringe-washed interference patterns. Another approach consists in splitting the wide-band signal into a set of narrow-band signals such that their fringe washing can be neglected over the FoV. The narrow band signals must be correlated separately and an image is formed at each subband. These subband images have higher noise levels than the full bandwidth image but can be averaged together to reduce the noise back to the same level. These two approaches are reminiscent of the XF and FX correlators [2], which use the WienerKhinchin theorem [2] to implement the signal correlation in the time and spectral domains respectively.

Eq. (2.1) represents a projection of the brightness distribution onto a set of weighted interference patterns. When the source is in the far-field of the array, these interference patterns are complex exponentials and are invariant in the direction orthogonal to the baseline. However, when the source is in the near-field of the array, the frequencies of these interference patterns are chirped and the orientation of the fringes is spatially variant over the source extent.

2.3   Image Reconstruction Algorithm

When the source is located in the far-field of the array, the Van Cittert-Zernike theorem states that the visibility function is equal to the Fourier Transform of the brightness temperature distribution of the source [2]. Hence the image reconstruction is reduced to an inverse Fourier Transform. In the near-field of the array however, this relationship

is no longer valid and the image reconstruction must account for the amplitude and frequency modulations of the interference patterns. This can be achieved by cross-correlating the visibility function with the function $\Phi_{nm}(\vec{r})$, defined as the interference pattern weighted by the inverse of the amplitude modulation [15]:

$$\widehat{T}_B(\vec{r}) = \frac{1}{N(N-1)} \sum_{\substack{n=1 \\ n \neq m}}^{N} \sum_{m=1}^{N} \mathcal{V}_{nm} \Phi_{nm}^*(\vec{r}) \,, \tag{2.7}$$

with:

$$\Phi_{nm}(\vec{r}) = \frac{e^{-\frac{j2\pi}{\lambda_0}\Delta r_{nm}}}{K_{nm}(\vec{r})} \,. \tag{2.8}$$

For simplicity the fringe-wash function was neglected since this term can be removed with one of the two methods described in the previous section. Eq. (2.7) can be rewritten as the linear combination of the scene $T_B(\vec{r})$ and a spatially variant PSF noted $h(\vec{r'}, \vec{r})$:

$$\widehat{T}_B(\vec{r}) \propto \iint_{S'} T_B(\vec{r'}) h(\vec{r'}, \vec{r}) \, dS' \,, \tag{2.9}$$

with $h(\vec{r'}, \vec{r})$ defined as:

$$h(\vec{r'}, \vec{r}) = \frac{1}{N(N-1)} \sum_{\substack{n=1 \\ n \neq m}}^{N} \sum_{m=1}^{N} \frac{K_{nm}(\vec{r'})}{K_{nm}(\vec{r})} e^{\frac{j2\pi}{\lambda_0}(\Delta r'_{nm} - \Delta r_{nm})} \,. \tag{2.10}$$

For simplification the system is approximated as linear and translation invariant and Eq. (2.9) is reduced to:

$$\widehat{T}_B(\vec{r}) \propto \iint_{S'} T_B(\vec{r'}) h_0(\vec{r} - \vec{r'}) \, dS' \,, \tag{2.11}$$

where $h_0(\vec{r}) = h(\vec{r}_0, \vec{r})$ is the PSF at the origin of the synthesised map. For small antennas, of the order of a wavelength, and for short-range personnel scanning applications one can approximate the term $K_{nm}(\vec{r}_0)/K_{nm}(\vec{r})$ to unity over the FoV, typically 30°. Hence Eq. (2.10) becomes:

$$
\begin{aligned}
h_0(\vec{r}) &= \frac{1}{N(N-1)} \sum_{\substack{n=1 \\ n \neq m}}^{N} \sum_{m=1}^{N} e^{\frac{j2\pi}{\lambda_0}(\Delta r_{0nm} - \Delta r_{nm})} \,, \\
&= \frac{2}{N(N-1)} \sum_{n=1}^{N} \sum_{m=n+1}^{N} \cos\left[\frac{2\pi}{\lambda_0}(\Delta r_{0nm} - \Delta r_{nm})\right] \,.
\end{aligned} \tag{2.12}
$$

Eq. (2.12) shows that the PSF of the array is real and is given by the sum of all the interference patterns obtained with each antenna pair. It is important to note that in

contrast with conventional real aperture imaging systems, the PSF $h(\vec{r'}, \vec{r})$ can have negative values because the autocorrelation terms (*i.e.* $m = n$) are excluded from the correlation in Eq. (2.7).

2.4 Spatial Resolution and Sampling Requirements

Each antenna pair in the array forms an interferometer which records different interference patterns with spatial frequencies denoted as u and v. The longest baseline in the array is denoted as D. When imaging a source at a range R that is in the near-field of the array, *i.e.* when the far-field approximation $D^2/\lambda_0 << R$ does not hold, the stationary phase principle can be used to provide a first-order approximation of the spatial frequencies (u, v) recorded at a position $\vec{r}$:

$$u(\vec{r}) = \left. \frac{1}{\lambda_0} \frac{\partial \Delta r_{nm}}{\partial \theta} \right|_{\varphi=0} , \qquad v(\vec{r}) = \left. \frac{1}{\lambda_0} \frac{\partial \Delta r_{nm}}{\partial \theta} \right|_{\varphi=\pi/2} . \tag{2.13}$$

The highest spatial frequency $u_{\max}$ recorded by the array at the origin of the source ($\theta = 0$), assuming a horizontal baseline such that $x_n = -x_m$ ($y_m = y_n = 0$) and $x_m - x_n = D$, is obtained by combining Eq. (2.13) with Eq. (2.3) and (2.5):

$$u_{\max} = \frac{D}{\lambda_0} \frac{1}{\sqrt{1 + \frac{D^2}{4R^2}}} . \tag{2.14}$$

To restrict the aliased responses to regions outside the synthesised map, the sampling period Δu and Δv in the Fourier domain must obey the Nyquist sampling requirements:

$$\Delta u \leq \frac{1}{2\sin\theta_{\max}} , \quad \Delta v \leq \frac{1}{2\sin\theta_{\max}} . \tag{2.15}$$

where $\theta_{\max}$ is the maximum zenith angle within the FoV. In the case of a one-dimensional imager, the minimum number of samples M required in the Fourier interval $[0, u_{\max}]$ is:

$$M = \frac{u_{\max}}{\Delta u} = \frac{D}{\lambda_0} \frac{2\sin\theta_{\max}}{\sqrt{1 + \frac{D^2}{4R^2}}} . \tag{2.16}$$

For a representative system used in personnel scanning, a diffraction-limited system with an aperture diameter of $D = 0.7m$ and a centre frequency ν_0=94GHz is used as a reference. In the Fraunhoffer region, the angular resolution of this system is $1.22\lambda_0/D$. For a source at close range, *e.g.* $R = 2$m, the radius of the Airy disk

is approximately 11mm. Considering a $28°$ FoV, *i.e.* $\theta_{\max} = 14°$, the number of measurements M required to Nyquist sample the Fourier plane with a cutoff frequency $u_{\max}$ is approximately 36,500. A conventional interferometric array would require 192 elements to record the visibility samples in a snapshot. We aim to reduce this antenna-count, typically by an order of magnitude, to reduce the system complexity and cost.

2.5 Frequency content of the interference pattern

In this section the frequency content of the interference pattern recorded by a baseline in motion with respect to a point-source is analysed. An important configuration is considered here and consists of a translation motion along the X-axis between the baseline and the point source. The output of the correlator is expressed as:

$$\mathcal{V}(\theta) = A(\theta)e^{j\phi(\theta)}, \tag{2.17}$$

with:

$$A(\theta) = \frac{\sqrt{P_1(r_1)P_2(r_2)\cos\theta_1\cos\theta_2}}{r_1 r_2} F_W(\Delta r, \Delta\nu), \tag{2.18}$$

and $\phi(\theta) = 2\pi\Delta r/\lambda$. Eq. (2.17) represents an amplitude and frequency-modulated complex signal, sometimes referred to as chirp and illustrated in Figure 2.2. One way to analyse the frequency content of this signal is by looking at its Fourier transform, denoted by $\chi(u)$ and written as:

$$\chi(u) = \int_{-\infty}^{+\infty} A(\theta)e^{j\phi(\theta)}e^{-j2\pi u\theta}\, \mathrm{d}\theta. \tag{2.19}$$

We recall that the Fourier Transform in Eq. (2.19) is equivalent to a projection of $\mathcal{V}(\theta)$ onto the set of complex exponentials $e^{-j2\pi u\theta}$. Moreover, in Eq. (2.19) there may exist frequencies u for which the rate of change in $\phi(\theta)$ is very different from the rate of change in the term $2\pi u\theta$. This results in a neglectable projection in Eq. (2.19) and no net contribution to the integral value. Contribution to the integral will occur when the two phases have similar rate of change, see [31], *i.e.* for frequencies u that satisfy the following relation:

$$2\pi u = \frac{\partial\phi(\theta)}{\partial\theta}. \tag{2.20}$$

This approximation is known as the stationary-phase principle. $\partial\phi(\theta)/\partial\theta$ has the dimension of spatial frequency expressed in $[cycles/rad]$ and decreases with $|\theta|$ as

shown on Figure 2.2. The maximum of $\partial \phi(\theta) / \partial \theta$ is reached for $\theta = 0$ and increases with the ratio of the baseline length to the wavelength as in far-field interferometry. The stationary-phase principle provides an approximation of the bandwidth Δu of the chirp's spectrum. We denote by $u_{\min} = u_0 - \Delta u / 2$ and $u_{\max} = u_0 + \Delta u / 2$ the minimum and maximum spatial frequencies respectively that satisfy Eq. (2.20). In order to further characterise $\chi(u)$ two different cases may be distinguished. 1) the source is scanned from both sides and 2) the source is scanned from one side only.

(a) (b)
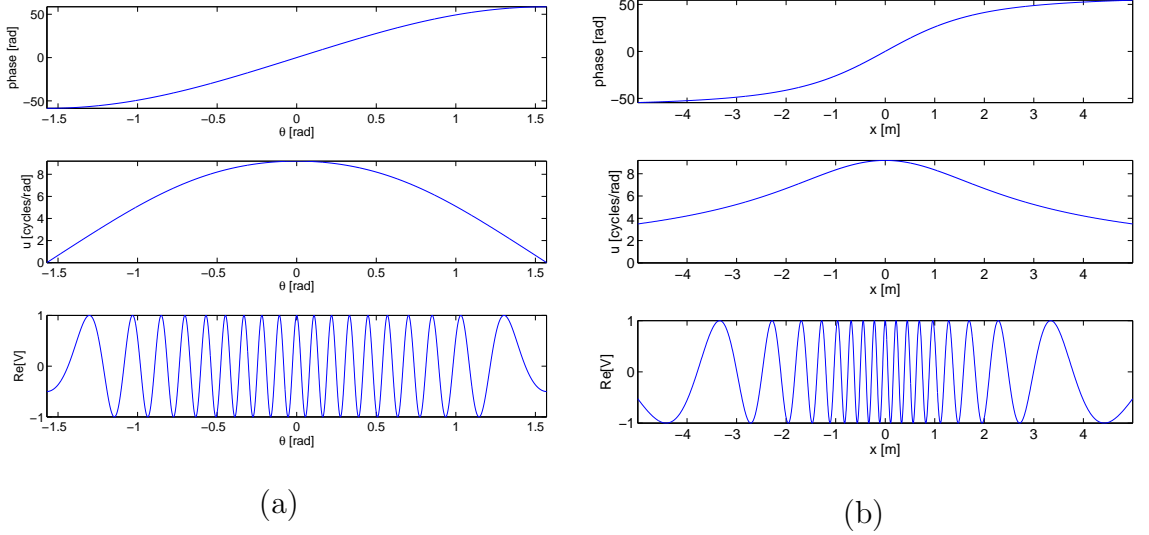
Figure 2.2: *From top to bottom respectively: phase, instantaneous spatial frequency and real part of the interference pattern for a baseline length of $D/\lambda \approx 9.3$. a) angular plot, b) linear plot.*

2.5.1 Bilateral scanning

Since in a bilateral scan $A(\theta)$ and $\phi(\theta)$ are respectively even and odd relative to θ, as is shown in Figure 2.2, $\mathcal{V}(\theta)$ is Hermitian and its Fourier transform $\chi(u)$ is real. Thus Eq. (2.19) becomes:

$$
\begin{aligned}
\chi(u) &= \int_{-\infty}^{+\infty} A(\theta) \cos(\phi(\theta) - 2\pi u \theta) \, \mathrm{d}\theta \,, \\
&= 2 \int_{0}^{+\infty} A(\theta) \cos(\phi(\theta) - 2\pi u \theta) \, \mathrm{d}\theta \,, \\
&= A(u) \cos(\Phi(u)) \,.
\end{aligned}
$$

(2.21)

(2.22)

Eq. (2.22) readily shows that for bilateral scanning the frequency response of the baseline is a real chirped signal with an amplitude modulation. Because of the cosine term in Eq. (2.22) the frequency response contains non-desirable oscillations and zeros, which are illustrated in Figure 2.3. Spatial frequencies where zeros occur will be suppressed in the reconstructed image. It is therefore highly desirable to remove these zeros to improve the quality of the reconstructed images.

2.5.2   Unilateral scanning

One way to reduce these oscillations and remove the zeros present in $\chi(u)$ is to scan the source from one side only, $e.g.$ for $\theta \geq 0$. The spectrum $\widetilde{\chi}(u)$ for an unilateral scan of the point source is expressed as:

$$
\begin{aligned}
\widetilde{\chi}(u) &= \int_0^{+\infty} \widetilde{\mathcal{V}}(\theta) e^{-j2\pi u\theta}\, \mathrm{d}\theta\,, \\
&= \int_0^{+\infty} A(\theta)\cos\left[\phi(\theta) - 2\pi u\theta\right]\, \mathrm{d}\theta + j \int_0^{+\infty} A(\theta)\sin\left[\phi(\theta) - 2\pi u\theta\right]\, \mathrm{d}\theta \quad (2.23)
\end{aligned}
$$

From Eq. (2.21) one recognises that the first term in Eq. (2.23) equals $\chi(u)/2$. We recall that the real and imaginary parts of the spectrum of a causal signal are Hilbert pairs. Hence the second term on the right side of Eq. (2.23) is the Hilbert pair of the first term and is denoted as $\chi_I(u)/2$. Using Eq. (2.22), $\widetilde{\chi}(u)$ may be rewritten as:

$$
\begin{aligned}
\widetilde{\chi}(u) &= \frac{1}{2}\left[\chi(u) + j\chi_I(u)\right]\,, \qquad\qquad (2.24) \\
&= \frac{1}{2} A(u)\exp\left[j\Phi(u)\right]\,.
\end{aligned}
$$

Hence, it is shown that the amplitude of the spectrum of the interference pattern for unilateral scanning equals half the amplitude of the oscillations of the spectrum with bilateral scanning. Most importantly, the cosine term in Eq. (2.22) has been replaced by a complex exponential in Eq. (2.23). Thus the zeros present in $\chi(u)$ are removed in $\widetilde{\chi}(u)$. Figure 2.3 shows the spectrum $\chi(u)$ and $2\widetilde{\chi}(u)$. Finally we conclude that the source must be scanned only for positive (or negative) values of θ since it results in a more constant frequency response of the correlator than if the scan extends on both sides of the source.
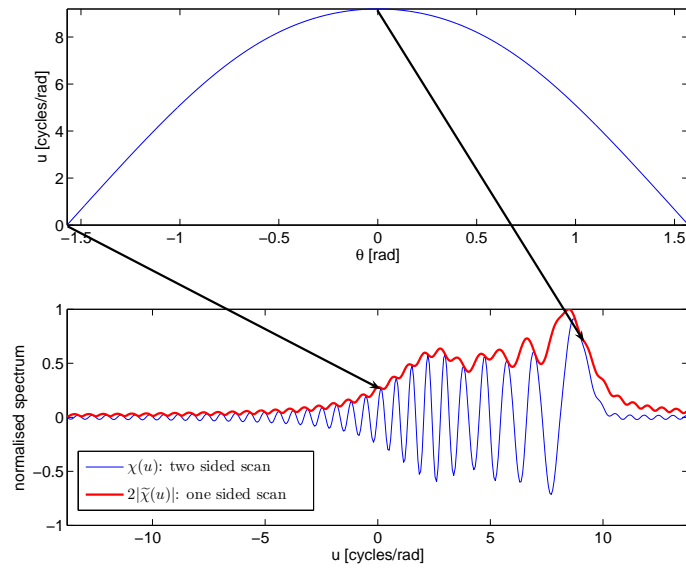
Figure 2.3: *From top to bottom respectively, instantaneous spatial frequency and Fourier transform of the interference pattern shown on Figure 2.2.*

2.5.3 Effect of rotating the baseline around the Y axis

We have seen that a single baseline can record all the spatial frequencies from $\approx D/\lambda$ down to the DC component when the source is scanned at azimuth angles $-\pi/2 \leq \theta \leq \pi/2$, see Figure 2.2 a). For a translated baseline that is colinear to the plane of the scene this requires an infinite scan extent, see Figure 2.2 b), and therefore can not be implemented in reality. To reduce the scan extent one can artificially increase the azimuth angle by rotating the baseline about the Y axis. Figure 2.4 shows the phase, the spatial frequency and the real part of the interference pattern recorded by the same baseline as in Figure 2.2 but when rotated by 30° around the Y axis. Such a baseline enables the recording of lower frequencies with shorter scan extents, see Figure 2.4 b). As expected the angular frequency response of a baseline being rotated by an angle β around the Y axis is translated by the same angle, and is illustrated in Figure 2.5.

In this section the frequency content of the interference pattern recorded by a baseline in motion relative to the source was analysed. It was shown that for a translation motion along the X-axis each antenna pair performs a band-pass filtering of the spatial frequencies present in the scene. A bilateral scan exhibits strong oscillations and zeros within this pass-band, whereas no zeros degrade the baseline frequency response if an
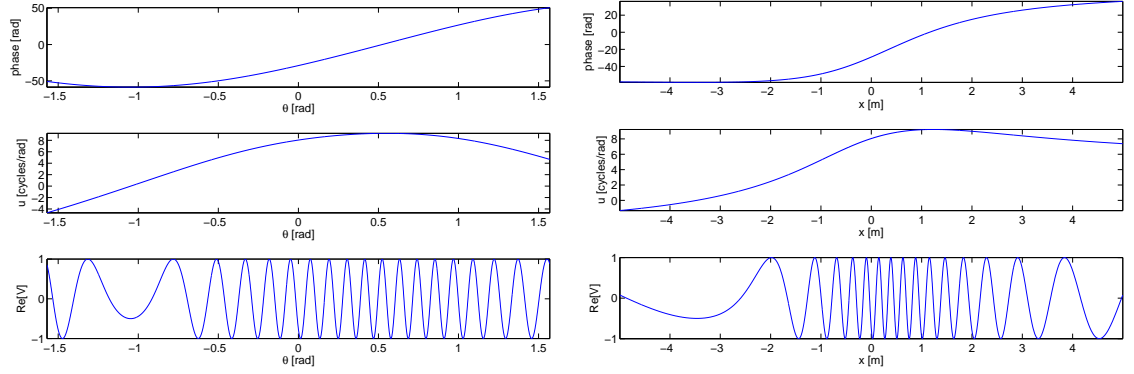
Figure 2.4: *Phase (top row), instantaneous spatial frequency (centre row) and real part of the interference pattern (bottom row) for a baseline length of $D/\lambda \approx 9.3$ that is rotated by 30° around the Y axis. Angular plot (left column) and linear plot (right column) are presented.*
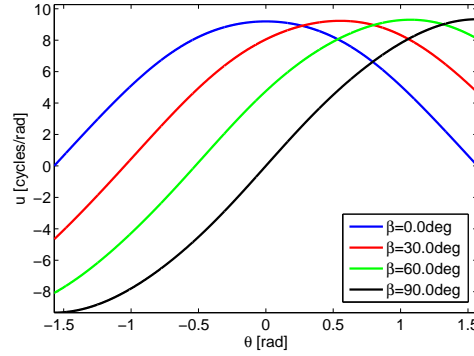
Figure 2.5: *Spatial frequencies recorded by a baseline of length $D/\lambda \approx 9.3$ that is rotated by an angle β around the Y axis. The angular frequency response is translated by the same angle β.*

unilateral scan is performed. Furthermore, the extent of the scan to record low spatial frequencies may be reduced by rotating the baseline with respect to the Y-axis. Apart from the spatial frequency response, the radiometric sensitivity is another critical characteristic determining the imaging performances of synthetic aperture arrays. In the next section this property will be described and the tradeoffs inherent to the reduction in array complexity will be assessed.

19

2.6 Radiometric Sensitivity and Trade-offs

In order to understand the radiometric sensitivity achieved in synthetic aperture arrays it is necessary to study how the noisy signals emitted by each point-source are recorded by each antenna with different delays, accumulated in the correlators, transmitted to the visibility data and later to the reconstructed image. For the earth rotation synthesis technique used in radio astronomy this analysis can be simplified because the angular extent of the source is generally small compared with the angular extent of individual antenna patterns [2]. In this case the radiometric sensitivity mainly depends on the redundancies in the spatial frequency measurements of the array. In remote-sensing of the earth or near-field imaging however, the radiometric sensitivity also depends on the brightness temperature distribution of the source and is detailed in [9]. For a uniform source and a zero-redundancy array, the radiometric sensitivity ΔT at the bore-sight pixel of the image is given by:

$$\Delta T = (T_O + T_R) \left(\frac{M}{2 \Delta \nu \tau} \right)^{1/2} .$$
(2.25)

where $M = N.(N-1)$, N is the number of antennas, T_O and T_R are the received brightness temperature and the noise temperature of the receivers respectively, τ is the integration time of the receivers. A mechanical scan of an array performs a time-sequential multiplexing of the baselines and therefore enables a reduction in antenna-count. An N-elements antenna-array, scanning a source at n_t successive positions, records $N(N-1)n_t$ visibility samples in the time $n_t \tau$. This represents a reduction in antenna-count by a factor of $\sqrt{n_t}$. Assuming continuous integration, the integration time τ is related to the frame rate F of the imager as follows:

$$\tau = \frac{1}{n_t F} = \frac{N(N-1)}{M.F} .$$
(2.26)

Combining Eq. (2.25) and (2.26) the radiometric sensitivity is expressed as a function of N and F:

$$\Delta T = (T_O + T_R) \left(\frac{F}{2 \Delta \nu N(N-1)} \right)^{1/2} M .$$
(2.27)

Eq. (2.27) shows that reducing the number of antennas by a factor of $\sqrt{n_t}$ degrades the radiometric sensitivity by the same factor, or alternatively degrades the imaging frame-rate by a factor of n_t. Therefore there is a trade-off between the reduction in

antenna-count, the radiometric sensitivity and the frame rate of the imager. Figure 2.6 and Table 2.1 show the radiometric sensitivity achieved with various degrees of scanning between the source and the array. These results are obtained using $T_O = 300K$, $T_R = 500K$, $\Delta\nu = 15GHz$, $M = N(N-1)n_t \approx$36,500 and show *e.g.* that an image with ΔT=0.9K can be recorded at a frame rate of 1Hz with a 192 antenna-array. Alternatively an image with the same ΔT can be recorded in a time-sequence with a 61 antenna-array at a frame-rate of 0.1Hz.
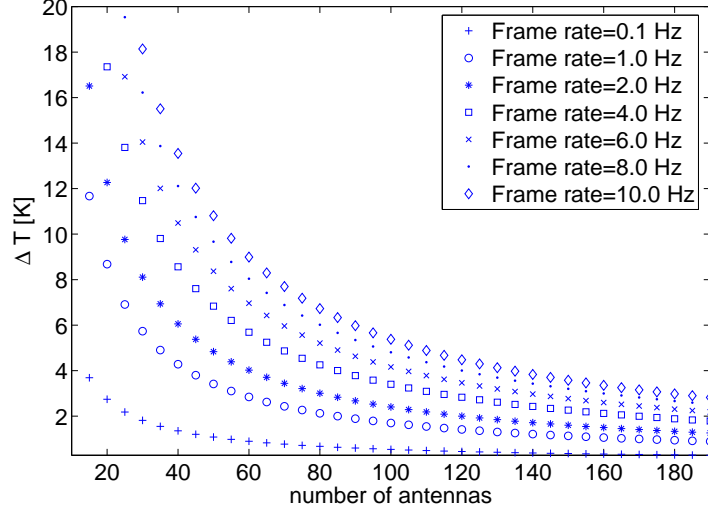
Figure 2.6: *Radiometric sensitivity achieved by a synthetic aperture radiometer for different antenna counts. T_O=300K, T_R=500K, $\Delta\nu$=15GHz, $M = N(N-1)n_t \approx$36,500*

2.7 Conclusions

The fundamentals of millimetre-wave synthetic aperture imaging were described. In particular near-field effects associated with short-range imaging were accounted for in the image reconstruction algorithm and sampling requirements. The frequency content of the interference pattern measured by a two-antennas interferometer was analysed when a displacement is introduced between the baseline and a point-source. When the displacement is a translation along the direction of the baseline, it was shown that each baseline performs band-pass filtering of the spatial frequencies present in the scene. This band-pass frequency response is degraded by strong oscillations and zeros for a bilateral scan, whereas this is not the case with unilateral scans. Moreover,

F [Hz]	0.1		1		2		4		6		8		10	
ΔT [K]	N	n_t	N	n_t	N	n_t	N	n_t	N	n_t	N	n_t	N	n_t
0.9	61	10	192	1										
1	54	13												
2	27	52	86	5										
4	14	201	43	20	61	10	86	5					136	2
6			29	45	40	23	56	12	68	8	79	6	86	5
8	7	872	22	79	30	42	43	20	52	14	61	10	68	8
10	6	1221	17	135	24	66	34	33	42	21	48	16	54	13

Table 2.1: *Radiometric sensitivity ΔT in the image for different values of the imaging frame rate F, antenna-count N and number of time-sequential data acquisitions n_t. Parameters are the same as in Figure 2.6.*

the extent of the scan to record low spatial frequencies may be reduced by rotating the baseline with respect to the Y-axis. It was also shown that in synthetic aperture near-field mm-wave imaging, time-sequential recording of the visibility function offers a route to reduced antenna count and hence the potential for reduced complexity. If the visibility function is recorded with n_t time-sequential samples during which the array is moved relative to the target, point-spread-function quality can be maintained for a factor $\sqrt{n_t}$ reduction in the number of antennas and a factor n_t reduction in the number of correlators. This simplification is obtained at the cost of a deterioration in radiometric sensitivity, which can be recovered only by a factor n_t increase in the total integration time. In principle, for certain applications where long integration times are feasible, acceptable sensitivity of 2K could be obtained for systems in which the number of antennas is an order of magnitude lower than for snapshot systems.

In Chapter 3 the design of scanning synthetic aperture mm-wave imagers will be treated in more detail. In particular, the optimisation of the array configuration will be considered and the improved spatial frequency coverage provided by scene scanning will be accounted for.

Chapter 3

System Design and performances

3.1 Introduction

We now consider the system design, and in particular the simultaneous optimisation of the array design and the relative motion between the array and the scene. We propose a technique that we call 'Array rotation aperture synthesis' that provides the low antenna-count of Earth-rotation synthesis whilst enabling the near-field operation required in short-range applications such as personnel scanning. In Section 3.2 we show that rotational scanning presents advantages over linear scanning in terms of spatial frequency coverage efficiency and imaging rates. In Section 3.3 antenna arrays are optimised by means of a genetic algorithm (GA) [19, 32] for maximally uniform (u, v) coverage after rotational scanning. The imaging performances of the array are assessed using simulated millimetre-wave scenes and are compared with those achieved with a conventional power-law Y-shaped array. Section 3.4 is concerned with the hardware required to reduce bandwidth decorrelation. Section 3.5 presents a discussion on phenomena that may degrade the imaging performance of a time-sequential system relative to a snapshot system. These phenomena are 1) variations in the instrument response during the acquisition time, 2) variations in the incident radiation from the background during the acquisition time, 3) non uniform illumination of the scene. Conclusions are presented in Section 3.6.

3.2 Array Motion

Optimising arrays with large antenna numbers, N, is a complex task because the search space has $2N$ dimensions for an array operating in a snapshot and $2Nn_t$ when a scan is included. Although the optimal system ideally requires optimisation of the array and its motion relative to the scene simultaneously, the search space has been restricted to linear and rotational motions only in order to simplify the optimisation and reduce the computation time. In this section we consider the properties of linear and rotational scans in order to determine which is more efficient for short-range imaging applications such as personnel scanning.

3.2.1 Translation

When antenna signals are correlated by pairs while the array is in translation relative to the source, *e.g.* along the x-axis, as in RADSAR [16], the spatial frequency recorded by each baseline decreases as the array is translated away from a source. In the far-field, one can show that $\Delta r_{12} \approx D \sin\theta$, with D the baseline length, and $u(\theta) \approx D\cos\theta/\lambda_0$. Hence the spatial frequency recorded by this baseline is maximum at zenith. In the near-field case however, the exact expression of Δr_{12} must be taken into account. For a point source that lies along the x-axis ($\varphi = 0$) at a range R from antennas 1 and 2 at locations (x_1, y_1, z_1) and (x_2, y_2, z_2) respectively, $u(\theta)$ and $v(\theta)$ are obtained using Eq. (2.13):

$$u(\theta) = \frac{1}{\lambda_0 \cos\theta} \left(\frac{x_2 a_u - x_1 b_u + R \tan\theta (b_u - a_u)}{a_u b_u} \right), \tag{3.1a}$$

$$v(\theta) = \frac{1}{\lambda_0 \cos\theta} \left(\frac{x_2 a_v - x_1 b_v + R \tan\theta (b_v - a_v)}{a_v b_v} \right), \tag{3.1b}$$

with:

$$a_u = \sqrt{1 + \frac{(x_1^2 + y_1^2 - 2Rz_1 + z_1^2)\cos^2\theta - Rx_1 \sin\theta}{R^2}}, \tag{3.2a}$$

$$b_u = \sqrt{1 + \frac{(x_2^2 + y_2^2 - 2Rz_2 + z_2^2)\cos^2\theta - Rx_2 \sin\theta}{R^2}}, \tag{3.2b}$$

$$a_v = \sqrt{1 + \frac{(x_1^2 + y_1^2 - 2Rz_1 + z_1^2)\cos^2\theta - Ry_1 \sin\theta}{R^2}}, \tag{3.2c}$$

$$b_v = \sqrt{1 + \frac{(x_2^2 + y_2^2 - 2Rz_2 + z_2^2)\cos^2\theta - Ry_2 \sin\theta}{R^2}}. \tag{3.2d}$$

In this case one can show that if $R \geq D$, then $u(\theta)$ reaches maximum at zenith and decreases with increasing θ. This means that translating the array relative to the source does not provide dense coverage at high spatial frequencies. Figure 3.1 (a) shows an array of 14 antennas evenly distributed on a Reuleux triangle [17]. This array is translated along the x-axis as shown in Figure 3.1 (b). Figure 3.1 (c) and (d) present the snapshot Fourier domain coverage of this array at boresight and at the scan position $x = 2$m respectively. Figure 3.1 (e) shows the (u, v) coverage achieved after 10 translations between $x = 0$m and $x = 3$m. Note the higher density of measurements recorded at low spatial frequencies.

3.2.2 Rotation

When the array is rotated about the Z-axis, the spatial frequencies recorded are also rotated. Figure 3.2 presents the (u, v) coverage of the array shown in Figure 3.1 (a) after 10 rotations by 6°. Comparing the (u, v) coverage on Figure 3.1 (e) and Figure 3.2 shows that a rotational scan clearly achieves a higher density of measurements at high spatial frequencies compared with a linear scan and a more even coverage overall. A major issue when linear scans are employed for personnel scanning applications, is the relatively long scan path required to fill the (u, v) plane. On the other hand, this example illustrates that a rotational scan about the Z-axis efficiently yields uniform (u, v) coverage without significantly increasing the size of the system. Furthermore the logistics of rotational scanning are in practice generally simpler and more amenable to high frame-rates than is the reciprocating motion required for linear scans. As a consequence, the array design will be optimised for operating with a rotational scan.

3.3 Array Design

Two approaches for optimising the antenna array have been considered. The first consists of minimising the sidelobe levels of the PSF of the array [19, 33, 34], while the second aims to achieve a uniform coverage of the Fourier domain [17, 35, 36] in order to minimise the effective measurement redundancies. In addition, since redundant measurements of spatial frequencies by an imaging system limit its DoF, uniform
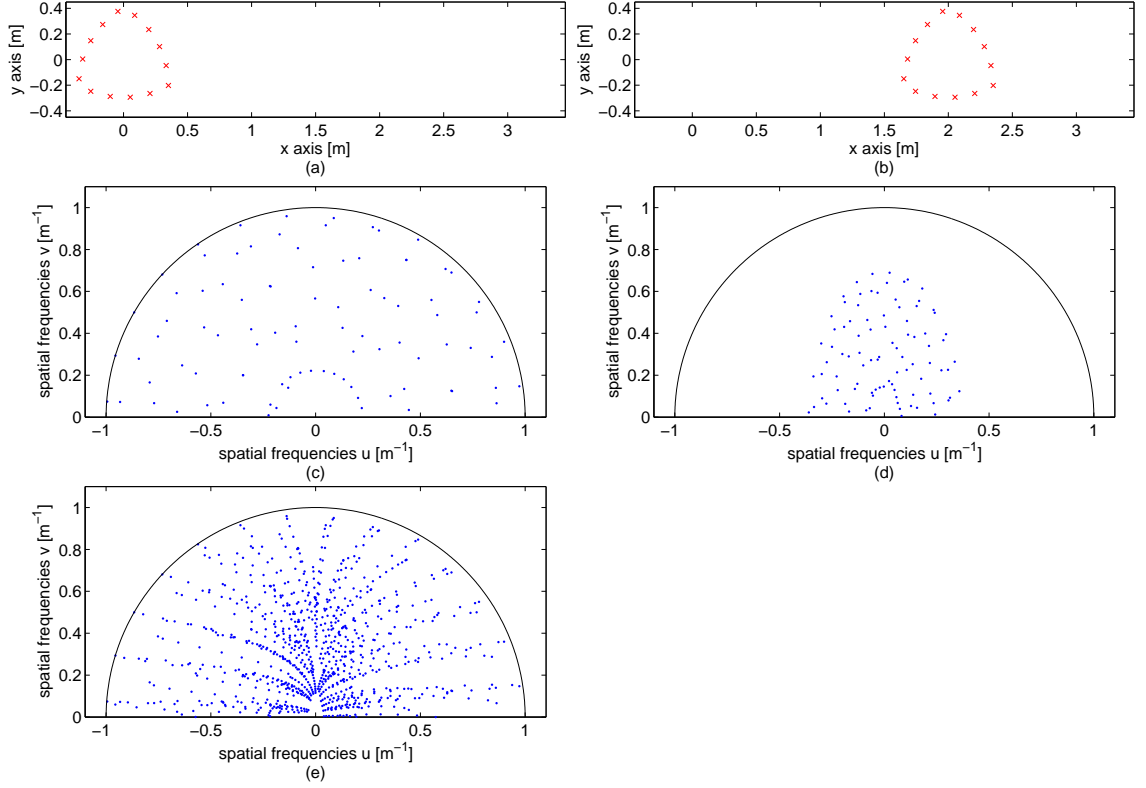
Figure 3.1: *(a) Evenly distributed Reuleux triangle array with 14 antennas centered at the source origin $(x, y) = (0, 0)$. (b) Same array translated by 2m along the x-axis. (c) (d) Snapshot spatial frequency coverage of the array shown in (a) and (b) respectively. (e) Spatial frequency coverage achieved when the array is translated by increments of 0.3m up to 3m.*
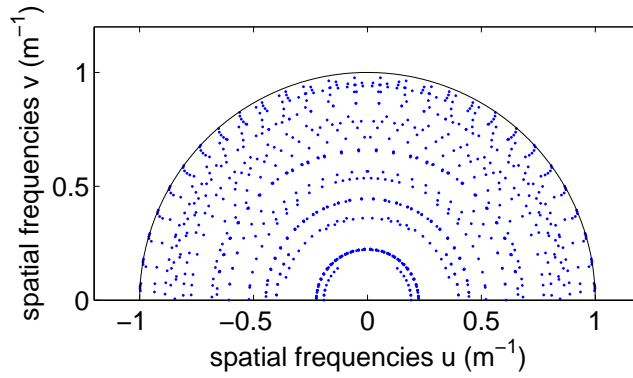
Figure 3.2: *(u, v) coverage of the array shown in Figure 3.1 (a) when rotated around the z-axis by increments of 6° up to 60°.*

coverage of the (u, v) plane is desirable to achieve a large DoF. The DoF of antenna arrays will be further discussed in Chapter 4. For these reasons it was decided to maximise the uniformity of the scanned (u, v) coverage of the array. This leaves the possibility to apply a tapering window to reduce the sidelobe levels near the central peak if required. Note that in the literature for both approaches, optimisation of the snapshot characteristics of the array is widely reported even when the array operates in a scanning mode. To our knowledge, the scanned characteristics of the array have only been considered in [37]. Optimum configurations for uniform (u, v) coverage are believed to have been found for up to 30 elements in 1D [35] and 2D [36]. Because of the $2Nn_t$ dimension of the search space and because of the theoretical convergence of GA to global optimum after an infinite number of iterations only, the solution obtained in practice is likely to be different from the global optimum. Thus, the solution depends on the initial antenna positions and therefore a 'good' initial configuration is required. Isotropic sampling of the (u, v) plane, or at least an isotropic cutoff frequency, is a highly desirable characteristic and may be used to restrict the space of possible initial configurations. Hence, arrays in the shape of curves of constant width are natural candidates [17]. When antennas are evenly distributed along curves of constant width with a rotational degree of symmetry n (invariance to a $2\pi/n$ rotation), the Fourier domain coverage exhibits a degree of rotational symmetry $2n$. Therefore antenna arrays distributed along Reuleux triangles ($n = 3$) provide (u, v) coverage with the smallest degree of rotational symmetry among the shapes of constant width. This configuration is used as the starting configuration of the GA. The motion considered is a rotation of $\pi/3$ rad about the z-axis.

3.3.1 Metric of (u, v) coverage uniformity

Rationale

In this section we seek a metric that is maximised, or minimised, when the (u, v) samples are distributed uniformly over the unit circle. Let us drop the constraint of the support of the (u, v) samples and assume that the (u, v) samples are observations of a random process with a probability density $p(u, v)$ that is continuous over $\Re^2$. Then a natural metric of the uniformity of $p(u, v)$ is the differential entropy H_{diff}, since it

will be maximised when $p(u, v)$ is uniform. H_{diff} is given by:

$$H_{\text{diff}} = - \int_S p(u, v) \log_2 p(u, v) \, dS . \tag{3.3}$$

The differential entropy characterises the behaviour of the entropy of discrete versions of $p(u, v)$ in the limit of small bin widths [38]. This quantity is of interest since it is independent of the bin width parameter and because it captures the greatest amount of detail. Kozachenko *et al.* have derived an unbiased estimator $\widehat{H}_{\text{diff}}$ of the differential entropy based on the nearest neighbour distances d_j between samples [39]. $\widehat{H}_{\text{diff}}$ is described in [38] by:

$$\widehat{H}_{\text{diff}} = \log_2 \left[\pi(M-1) \right] + \frac{\gamma}{\ln 2} + \frac{2}{M} \sum_{j=1}^{j=M} \log_2 d_j . \tag{3.4}$$

Where $\gamma = 0.5772156649$ is the Euler-Mascheroni constant. Eq. (3.4) shows that the maximum of $\widehat{H}_{\text{diff}}$ occurs when the geometrical mean of the nearest neighbour distances d_j is maximised. Note that $\widehat{H}_{\text{diff}}$ can be greater than the value of H_{diff} obtained for a uniform distribution. This is easily shown by considering a probability density $p(u, v) = 1/a^2$ over a square domain of area a^2 centered at the origin, and $p(u, v) = 0$ outside this domain. In this case $H_{\text{diff}} = \log_2(a^2)$. When the M samples are distributed on a rectangular grid and if $M >> 1$, we have $\widehat{H}_{\text{diff}} \approx H_{\text{diff}} + \frac{\gamma}{\ln 2} + \log_2(\pi)$. This difference is perfectly normal since $\widehat{H}_{\text{diff}}$ is an unbiased estimator and is only on average equal to H_{diff} for random samples. This example also suggests that a reference other than the value of H_{diff} for a uniform distribution should be used to assess $\widehat{H}_{\text{diff}}$. The value of $\widehat{H}_{\text{diff,hex}}$ obtained for samples distributed on a hexagonal grid filling the unit circle can be employed to estimate the maximum value of $\widehat{H}_{\text{diff}}$. This is useful to assess how close an array is to sampling the Fourier domain uniformly. For $M \approx 36500$, as in the representative system discussed in Chapter 2, $\widehat{H}_{\text{diff,hex}} = 4.342$.

It was found *a posteriori* that a similar metric had previously been proposed by Cornwell [18] to optimise the spatial frequency coverage of correlation arrays. Eq. 3.4 is however computationally more efficient than the metric proposed in [18] because it only necessitate to compute the M nearest neighbour distances between samples, as opposed to all of the $M(M-1)/2$ distances between samples in Cornwell's metric. Furthermore, the use of the logarithm is rationalised in [18] to concentrate on closely

spaced samples. The maximisation of the differential entropy and its estimation with Eq. (3.4) provides different understanding and a rigorous justification for the use of the logarithm of the nearest neighbour distances.

Maximisation of $\widehat{H}_{\text{diff}}$ guarantees that the uniformity of the distribution of the (u, v) samples is also maximised but without constraints on the cutoff frequency. A constraint on the extent of the (u, v) coverage is introduced with the term $\mathcal{P}$ that penalises antenna arrays with (u, v) samples that lie outside the circle with the desired cutoff frequency:

$$\mathcal{P} = \sum_{j} \text{pos}\left(e^{l_j - 1} - 1\right) , \tag{3.5}$$

where l_j is the L2 norm of the sample (u_j, v_j) and $\text{pos}(x)$ is such that:

$$\text{pos}(x) = \begin{cases} x, & x \geq 0 \\ 0, & x < 0 \end{cases} \tag{3.6}$$

Finally the cost function to minimise is expressed as follows:

$$\mathcal{C} = -\widehat{H}_{\text{diff}} + \mathcal{P} \tag{3.7}$$

Efficient computation of $\widehat{H}_{\text{diff}}$

Calculating $\widehat{H}_{\text{diff}}$ with Eq. 3.4 necessitates that one computes the nearest neighbour for each of the M (u, v) samples. Using a brute force method, this would require computation of $M(M-1)/2$ distances. This can be computationally expensive when M is large, typically of the order of 10^4 here. In the next section we describe genetic algorithms as a means to maximise $\widehat{H}_{\text{diff}}$. It is important to note that the implementation and evaluation of the merit function is an important factor in the speed and efficiency of these algorithms. Consequently an efficient method for computing Eq. (3.4) is highly desirable. Delaunay triangulation can be used to obtain a small set of natural neighbours for each point, thereby reducing considerably the number of Euclidian distances d_j to compute. Delaunay triangulation can be obtained very efficiently using the Quickhull Algorithm [40] as follows:

- The input sites are lifted to a paraboloid by adding the sum of the squares of the coordinates.

- The height of the paraboloid is scaled to improve numerical precision.

- The convex hull of the lifted sites is computed and the lower convex hull is projected back to the input.

3.3.2 Genetic algorithm

When optimising the Fourier domain coverage of antenna arrays, one has to cope with multiple local minima. This prevents the use of local optimisation methods like the gradient descent. For a two-dimensional antenna array with N elements, the number of parameters to optimise is $2N$. In the present case $N = 27$ and the number of parameters is 54. Even if the antenna positions are constrained to lie on a rectangular grid with a period of $\lambda/2$ the number of combinations is so large that an exhaustive search is not practical. Simulated annealing and genetic algorithms (GA) are "global" numerical optimisation methods that can handle a large set of discrete parameters. Simulated annealing mirrors in principle the slow cooling process of a metal in a liquid state to a metal in a solid state. GA on the other hand are inspired by the natural selection processes of genetic evolution. We have chosen to implement a GA because of previous experience working with these algorithms. Although these two algorithms provide no guarantee of convergence to the global optimal in a finite amount of time, but only after an infinite number of iterations, it has been shown that they can still achieve useful results for array design problems, see *e.g.* [19, 32]. The structure of the GA implemented is based on the algorithm described in [19] and is as follows:

Parameter encoding: Each parameter, namely the horizontal and vertical positions of each antenna, is encoded into a N_{bit} bit sequence called a gene. To minimise the number of bits required, the displacement relative to a reference position is encoded rather than the absolute position. All the genes together form an array of $2NN_{\mathrm{bit}}$ bits called a chromosome, which has an associated cost $\mathcal{C}$, calculated with Eq. (3.7). The total number of possible antenna arrays is therefore $2^{2NN_{\mathrm{bit}}}$.

Initialisation: The algorithm starts with a large set of N_{chro} randomly generated chromosomes which form the initial population. This means each bit of each gene is equiprobable. The cost $\mathcal{C}$ of each chromosome is computed.

Selection: Chromosomes are ranked and discarded according to a selection threshold. In our implementation a 50% selection threshold was applied but randomly varying selection thresholds are also possible.

Reproduction: Pairs of remaining chromosomes are randomly mated and generate two offsprings as follows: a cross-over point is randomly selected. For every genes all the bits strictly less significant than the cross-over bit are swapped between the pair of chromosomes. Thus the size of the population is constant at each iteration.

Mutations: A small percentage p_{mut} of bits in the list of chromosomes are changed.

Iteration: Repeat selection and successive steps until stopping criterion is satisfied.

3.3.3 Results

The initial array provided to the GA has 27 antennas evenly distributed along a Reuleux triangle. This is shown on Figure 3.4 (a) with its snapshot (u, v) coverage (b). This array can operate at a frame-rate of 0.1Hz with a radiometric sensitivity of 2K. The number of antennas was chosen to enable straightforward comparison with a Y-shaped array, where the same number of antennas are distributed on three arms separated from each other by an angle of $2\pi/3$rad. The GA optimised the (u, v) coverage of this array for a rotational scan of 60° in 52 steps. Thus, the number of (u, v) samples is $M = 27 \times 26 \times 52 = 36504$ and satisfies the sampling requirements, expressed in Eq. (2.14) and (2.15), for an array with a resolution of 11mm at a 2m range and a 28° FoV. The parameters of the genetic algorithm are reported in Table 3.1. Figure 3.3 shows the evolution of the minimum cost of the population every 10 iterations. Note that the initial value of $\widehat{H}_{\mathrm{diff}}$ equals $-\infty$ because of redundancies in the scanned (u, v) coverage of the initial array. A minimum cost $\mathcal{C}_{\mathrm{min}} = -2.1247$ was reached after 1260 iterations and the algorithm was stopped after 1480 iterations because no further improvements of this result had been obtained. The resulting antenna array and its snapshot (u, v) coverage are shown on Figure 3.4 (c) and (d) respectively. The spatial coordinates of the optimised array are given in Appendix B. Figure 3.4 and 3.5 enable a comparison of the snapshot and scanned (u, v) coverage before and after

optimisation. The optimisation clearly yields more even coverage, especially at low spatial frequencies. Figure 3.6 shows the PSF obtained after scanning for the non-optimised and optimised arrays. The full width at half maximum (FWHM) of these two PSFs are both equal to 0.2°. The level of the first sidelobes are very similar; -9.4dB and -8.9dB for the non-optimised and optimised arrays respectively. This sidelobe can only be improved by tapering the (u, v) cover, and is equal to -8.9dB in the case of a perfectly uniform coverage. However the level of higher-order sidelobes is typically reduced by 5dB to 10dB by the optimisation as can be seen in Figure 3.6 (c). This improvement can be measured by the ratio of the energy in the main beam to the energy in the sidelobes, which is increased by a factor of 3.4 by the optimisation procedure.

p_{mut}	N_{chro}	N_{bit}	ΔX & ΔY	$\mathcal{C}_{\mathrm{min}}$	iterations	Number of combinations
0.01	500	5	1mm	-2.1247	1480	2^{270}

Table 3.1: *Values of the parameters used in the genetic algorithm optimisation of a 27 antenna Reuleux triangle array.*
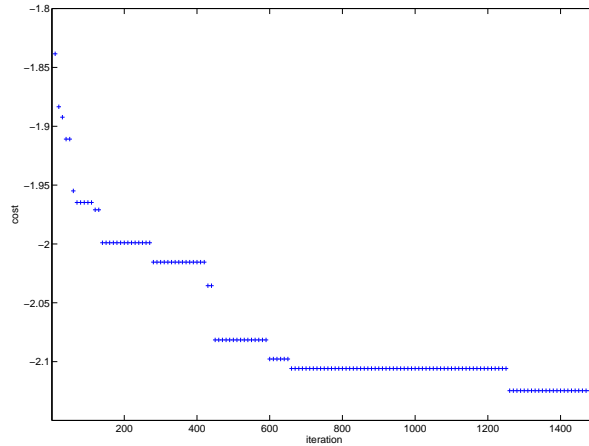
Figure 3.3: *Evolution of the minimum cost $\mathcal{C}$ associated with the 27 antennas array optimised with a genetic algorithm.*

The improved imaging performances provided by the optimised Reuleux triangle array are illustrated here with simulated images. To that end, the mm-wave brightness temperature image of a human body with an embedded rectangular metallic object
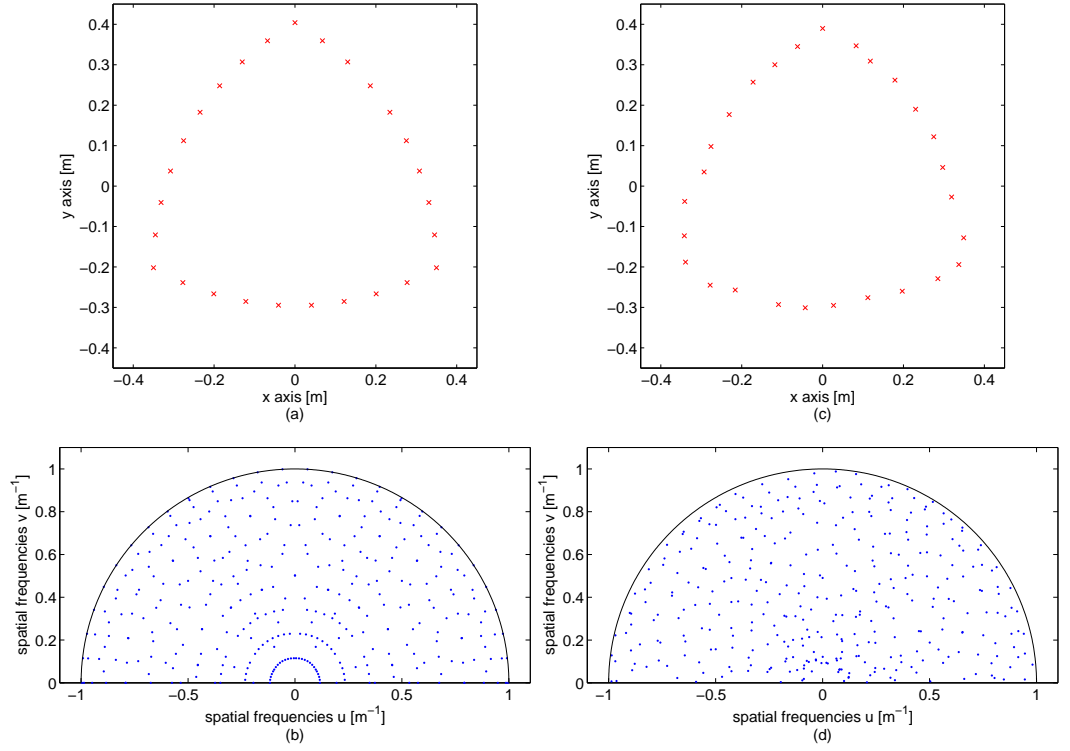
Figure 3.4: *(a) and (b) Evenly distributed Reuleux triangle array with 27 antennas and its snapshot (u, v) coverage. (c) and (d) 27 antennas Reuleux triangle array, optimised for maximum uniform (u, v) coverage after a rotational scan of $60°$ in 52 steps, and its Snapshot (u, v) coverage. FoV=$28°$, ν_0=$94GHz$, $D = 0.7m$, $R = 2m$.*
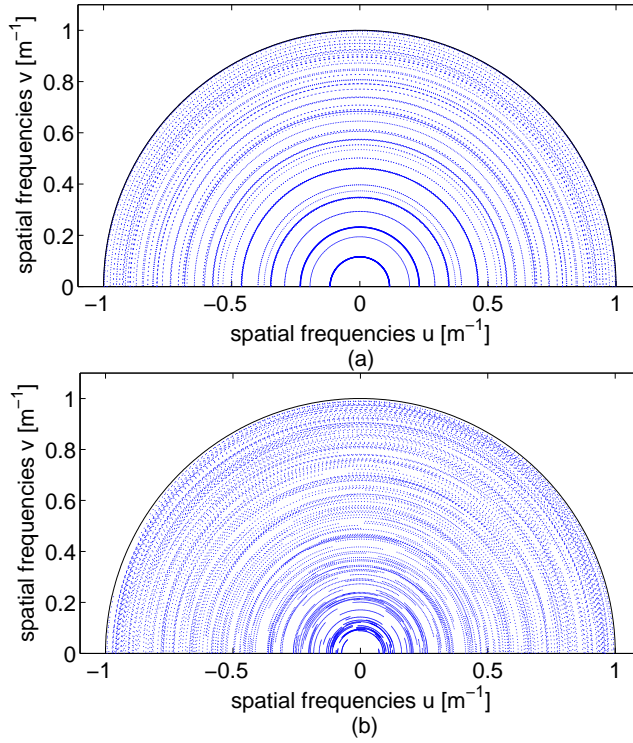
Figure 3.5: *(a) and (b) (u, v) coverage at boresight after rotational scanning of the arrays shown in Figure 3.4 (a) and (c) respectively.*

is modelled [41], see Figure 3.7 a). The body and metallic object have a uniform temperature of 290K and the imaging system is passive. The changes observed in the measured brightness temperature are related to variations in emissivity across the scene due to the angular dependence of the Fresnel relations at a dielectric interface. We assume the angular distribution of the brightness temperature incident from the background is constant and stable over the acquisition time. The image recorded by the array is simulated by the convolution of this raw image with the PSF of the antenna array, and the addition of a white gaussian noise with a standard deviation of $2K$. This corresponds to a 43dB SNR (using the $20 \log_{10}$ definition) in the recorded image. A Wiener filter is then used to restore the image. This process is performed with three arrays that each have 27 antennas and include a rotational scan of 60° in 52 steps. The first array is a power-law Y-shaped array with $\alpha = 1.7$ [42, 2], the other two arrays are the pre-optimised and post-optimised arrays shown in Figure 3.4 a) and b). Figure 3.7 b), c) and d) show the restored images obtained with the Y-shaped array, the Reuleux triangle array and the optimised Reuleux triangle array respectively. Figure 3.8 shows
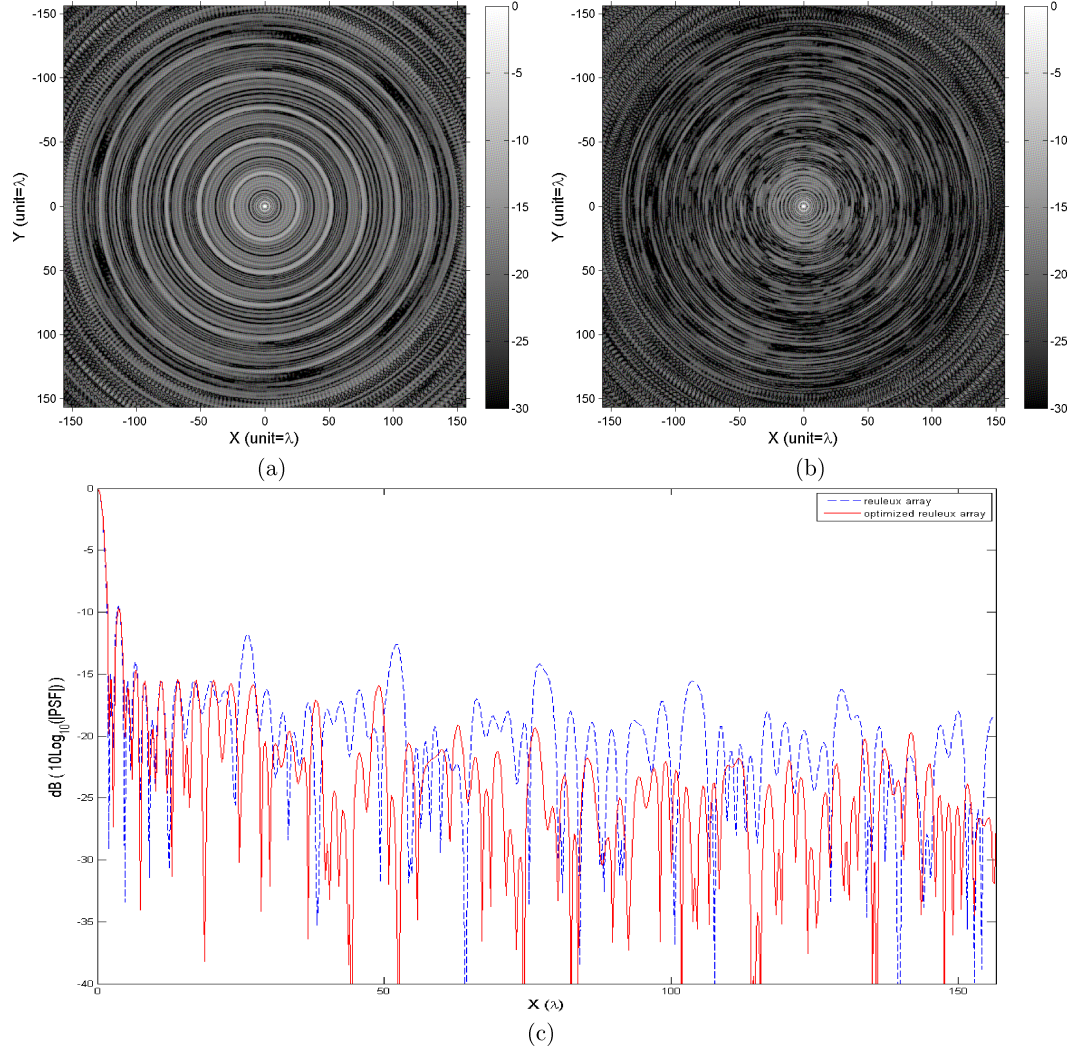
Figure 3.6: *(a) and (b) Density plots in dB (*$10Log_{10}\left(\left|PSF\right|\right)$*) of the PSF at boresight of the array shown in Figure 3.4 (a) and (c) respectively, after rotational scanning. (c) 1-dimensional plot of the PSF shown in (a) and (b):*$PSF(x, y = 0)$

the profiles of the raw and restored images along the white line drawn in Figure 3.7 top left. Note this plot incorporates the metallic object. The image obtained with the evenly distributed Reuleux triangle array (3.7 c) appears sharper than the image obtained with the Y-shaped array (3.7 b) due to its higher density of measurements at high spatial frequencies. The sharpness of the image is further improved with the optimised array, where noticeably lower levels of artifacts are present. The RMS error between the restored images and the raw image are 5.6%, 4.7% and 3.3% for the images shown in Figure 3.7 b), c) and d) respectively. These values are averages over 10 observations. This endorses the better imaging performances provided by the Reuleux triangle arrays compared with the Y-shaped array and illustrates the improvements provided by the optimisation of the array.

The design of antenna arrays for short-range imaging that include a rotational scan was described. The design is aimed at optimising the uniformity of the sampling of the Fourier domain by antenna arrays. We proposed to measure this quantity with an estimator of the differential entropy of the density of measurements. This metric was optimised with a GA and it was demonstrated that the resulting array achieves significantly higher imaging performances than the non-optimised array or a conventional Y-shaped array. In the next section, the fringe wash function effect due to wideband receivers is addressed.

3.4   Reduction of Bandwidth Decorrelation

It was stated in section 2.2 that the unwanted amplitude modulation of the visibility function due to the fringe-wash function can be greatly reduced by introducing delay lines in the antenna channels. Since the delay lines must be introduced before the correlator, an additional correlator is included for each delay line. We seek now to estimate the number of delay-lines required. To that end we estimate the period $X_{IP_{nm}}$ of the interference pattern and the position $X_{FW_{nm}}$ of the first null of the fringe-wash function. To simplify the analysis we consider a horizontal baseline with coordinates $(-D_{nm}/2, 0, 0)$ and $(D_{nm}/2, 0, 0)$. Using Eq. (2.4) and (2.6) we obtain $X_{IP_{nm}}$ and
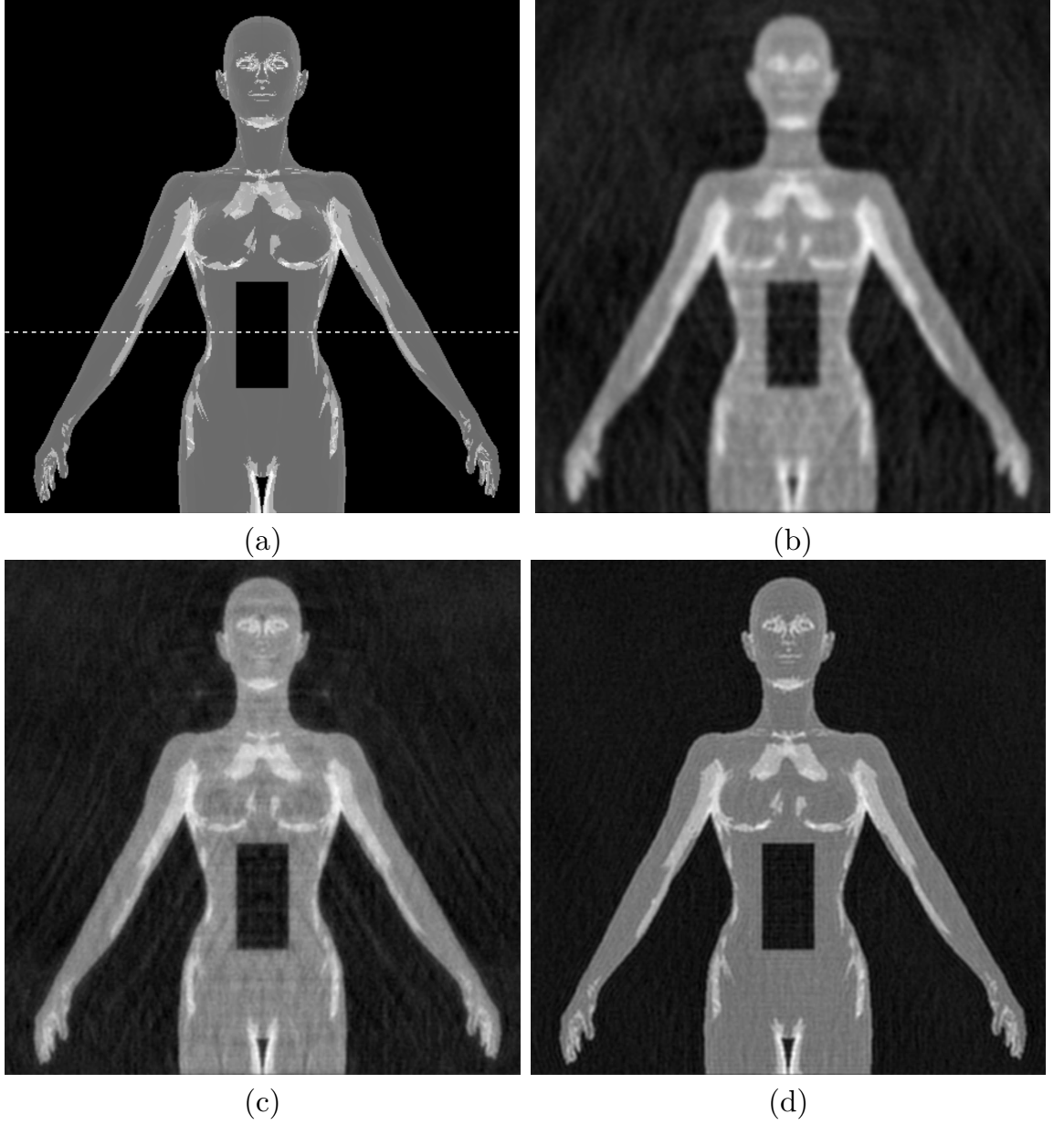
Figure 3.7: *Imaging performances of various antenna arrays. a) Simulated mm-wave image of a human body including a rectangular metallic object. Noise level in the recorded images is $\Delta T = 2K$ and corresponds to a 43 dB SNR. b) c) and d) Images restored with the Wiener filter and recorded with the Y-shaped array, the Reuleux triangle array and the optimised Reuleux triangle array respectively.*
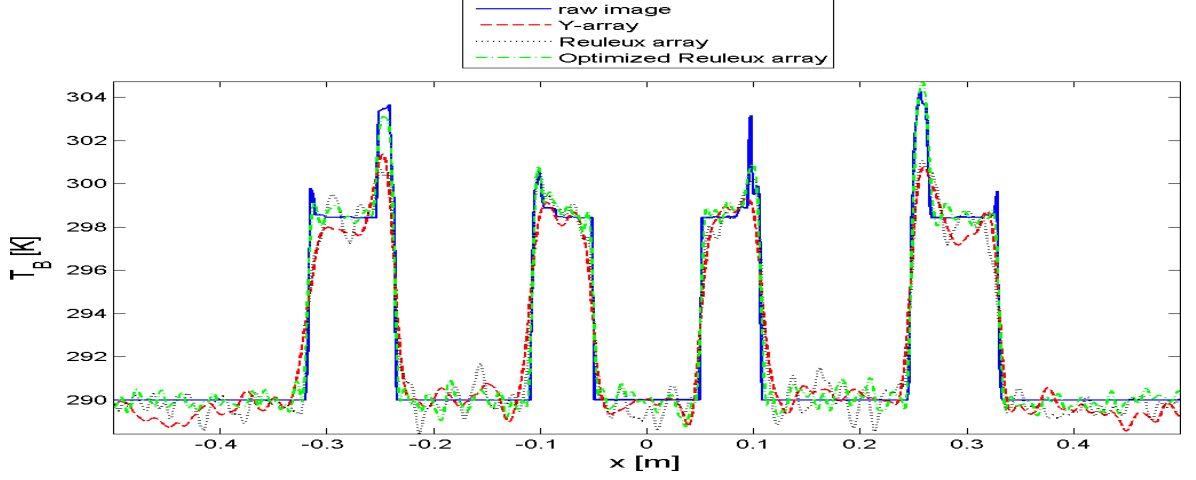
Figure 3.8: *Imaging performances of various antenna arrays. 1-dimensional plot of the restored images including the metallic object.*

$X_{FW_{nm}}$:

$$X_{IP_{nm}} = \frac{\lambda_0}{2}\sqrt{1 + \frac{4R^2}{D_{nm}^2 - \lambda_0^2}}\,, \tag{3.8}$$

$$X_{FW_{nm}} = \frac{c}{2\Delta\nu}\sqrt{1 - \frac{4R^2}{\left(\frac{c}{\Delta\nu}\right)^2 - D_{nm}^2}}\,. \tag{3.9}$$

The interference patterns must be translated by ΔX_{nm} so that they sum in-phase. The translation $\Delta X_{nm} = \text{Round}\left(\frac{X_{FW_{nm}}}{X_{IP_{nm}}}\right)X_{IP_{nm}}$ provides a reasonable amplitude modulation after addition of all the translated interference patterns. Typically the amplitude modulation is less than 4%. Thus the number of delay lines for the baseline nm is $\text{Round}\left(\frac{2x_{max}}{\Delta X_{nm}}\right)$. Finally, the number ,$\mathcal{N}$, of delay lines and correlators to be introduced to compensate for the fringe-wash function can be estimated as:

$$\mathcal{N} = \sum_{n=1}^{N}\sum_{m=n+1}^{N} round\left(\frac{2x_{max}}{\Delta X_{nm}}\right)\,. \tag{3.10}$$

For the array shown in Figure 3.4 (c), we estimate $\mathcal{N} \approx 4000$.

The subband, or spectral, implementation described in section 2.2 requires a complex correlator per baseline and per subband. For the system considered here, the 15GHz bandwidth would have to be divided into approximately 30 subbands in order to record 90% of the signal at the edges of the 28° FoV. This leads to a total number of correlators of 10500, a factor of more than 2.5 times the number of correlators required with the

delay-lag implementation also described in section 2.2. However, the spectral technique has the significant advantage of requiring narrow-band correlators that operate at a frequency a factor of 30 lower than that of the wideband correlators needed in the delay line technique. Thus, the lower cost associated with the reduction in the frequency of the correlators clearly outweighs the extra cost due to the increased number of narrow-band correlators required with the spectral technique. Compared to the delay line technique, the spectral method therefore seems more cost efficient to implement. Note that since both implementations require a number of correlators that increases with the number of baselines, sequential acquisition of the visibility data in n_t iterations enables a reduction in the number of correlators by the same factor compared with a snapshot array.

3.5 System sensitivity to errors

3.5.1 Instrument errors

Instrument errors in correlation antenna arrays degrade the retrieved brightness temperature map. Extensive modelling of these errors has been reported in the literature, see *e.g.* [43, 44]. A non-exhaustive list of instrument errors comprise 1) antenna position errors, 2) radiation voltage mismatch (in phase and amplitude) between antennas, 3) mutual coupling between antennas, *i.e.* the alteration in individual antenna patterns due to interactions with other antennas, 4) frequency response mismatch between receiver channels, 5) correlator errors such as phase errors in the quadrature arm of the complex correlator. Several calibration procedures have been proposed to correct for different errors [45, 46, 47]. In this section, the aim is to assess the degradation in imaging performances due to the increased acquisition time demanded by the proposed technique. Time-sequential acquisition of the visibility data will normally reduce the number of short antenna baselines and hence the effects of mutual coupling between receivers should be reduced, simplifying calibration of this effect. Conversely the increased time necessary to sample the visibility function increases sensitivity to drift in electronic gain and offset of the receivers and correlators compared to snapshot acquisition. In many short-range imaging applications for which the proposed technique is

of interest, real-time calibration may be implemented by recording the visibilities for calibration images which incorporate point-source beacons. It is of interest however to consider the impact of drift in the absence of such on-line calibration. We address this by supposing a linear drift with time in the gain and offset of the recorded correlations and compare the image quality of a snapshot imager with that of a sequential imager. For each baseline (m, n), we assume errors introduced in the original calibration to be negligible. Thus the time varying gain of the correlator can be expressed as:

$$G_{mn}(t) = 1 + (\rho_{r_{mn}} + j\rho_{i_{mn}})t \,, \tag{3.11}$$

where $\rho_{r_{mn}}$ and $\rho_{i_{mn}}$ are the drift rates in the real and imaginary part of the gain respectively, and are simulated as zero mean Gaussian distributed random variables with standard deviation σ, noted $\mathrm{Gaussian}(0, \sigma)$. Similarly, the offset of the correlator is written as:

$$O_{mn}(t) = (\rho_{r_{mn}} + j\rho_{i_{mn}})t \,, \tag{3.12}$$

Hence, the measured visibility $\widetilde{\mathcal{V}}_{mn}$ is related to the true visibility $\mathcal{V}_{mn}$ as:

$$\widetilde{\mathcal{V}}_{mn} = \mathcal{V}_{mn}G_{mn}(t) + O_{mn}(t) \,. \tag{3.13}$$

We seek to formulate how these errors affect the synthesised image. Using Eq. (2.7) and (3.13) the synthesised image with instrument errors can be written as:

$$\widetilde{T}_B(\vec{r}) \propto \sum_i T_B(\vec{r}_i)\widetilde{h}(\vec{r}_i, \vec{r}) + \mathcal{O}(\vec{r}) \,, \tag{3.14}$$

with:

$$\widetilde{h}(\vec{r}_i, \vec{r}) = \sum_{m \neq n} G_{mn}\Phi_{mn}(\vec{r}_i)\Phi_{mn}^*(\vec{r}) \,, \tag{3.15}$$

$$\mathcal{O}(\vec{r}) = \sum_{m \neq n} O_{mn}\Phi_{mn}^*(\vec{r}) \,. \tag{3.16}$$

Eq. (3.14) may be simplified if we assume that $\vec{r}$ is restricted to an isoplanatic region of the system so that $\widetilde{h}(\vec{r}_i, \vec{r})$ only depends on the vector displacement $\vec{r} - \vec{r}_i$. Thus, the system is linear translation invariant and Eq. (3.14) is approximated by:

$$\widetilde{T}_B(\vec{r}) \propto T_B(\vec{r}) * \widetilde{h}_0(\vec{r}) + \mathcal{O}(\vec{r}) \,, \tag{3.17}$$

where $*$ denotes the convolution product and $\widetilde{h}_0(\vec{r}) = \widetilde{h}(\vec{r}_0, \vec{r})$ is the distorted kernel at the centre of the synthesised map. Eq. (3.17) shows that instrument gain errors are convolutive whereas instrument offset errors are additive in the synthesised map. We seek to quantify the degradation of the performances of the array shown in Figure 3.4 (c), $n_t = 52$, due to the instrument drift. To that end, the RMS error ε in the synthesised image was calculated for 10 observations so as to account for the random nature of the instrument drift. In addition, we also record the standard deviation σ_G of the phase errors in the gain, the RMS value of the offset term $\mathcal{O}_{\mathrm{rms}}$ in the synthesised image, see Eq. (3.16), and the RMS errors in the visibility function ϵ_V and in the restored images ϵ_I. All these parameters vary linearly with the RMS drift rate ρ_{rms} as is shown on Figures 3.9, 3.10 and 3.11.
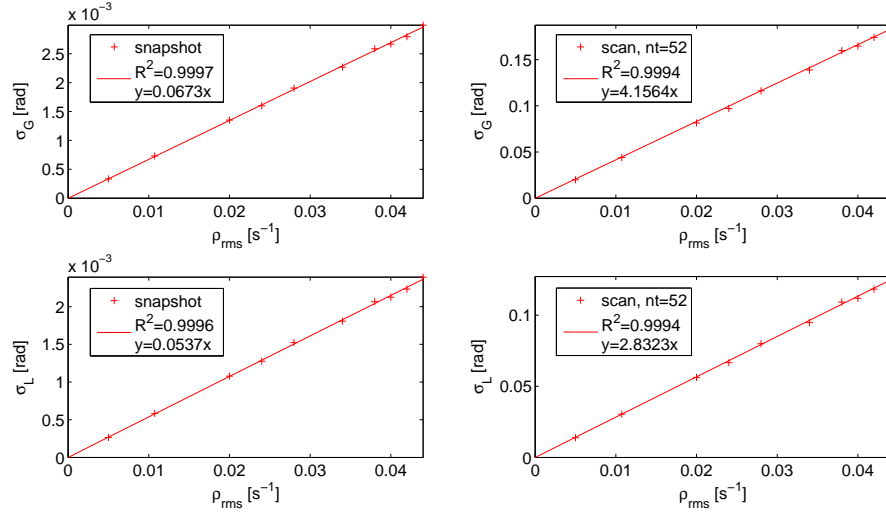
Figure 3.9: *Parameters of the distribution of the phase in the gain of the correlator as a function of the drift rate ρ_{rms}. Left: snapshot system, right: scanning system with n_t=52. σ_G is the standard deviation, σ_L is the scale parameter of the Laplace distribution.*

We use a metric similar to the Strehl ratio to measure the distortion of the PSF due to instrument errors. The Strehl ratio measures the reduction of the peak power of the distorted PSF compared with the peak power of the non distorted PSF, usually the
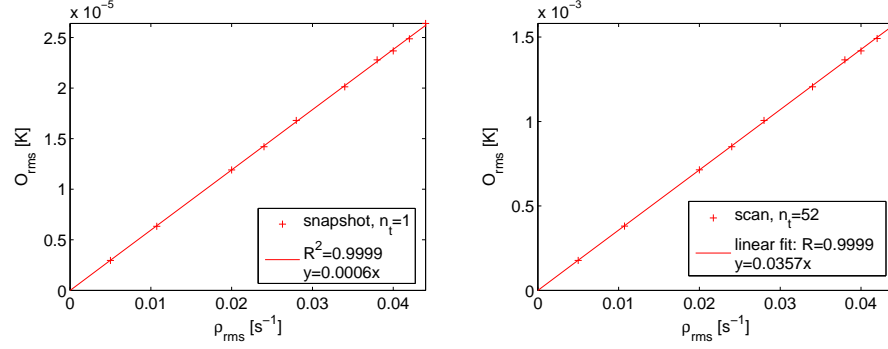
Figure 3.10: *RMS value $\mathcal{O}_{rms}$ of the offset image as a function of ρ_{rms}. Left: snapshot system, right: scanning system with $n_t=52$.*
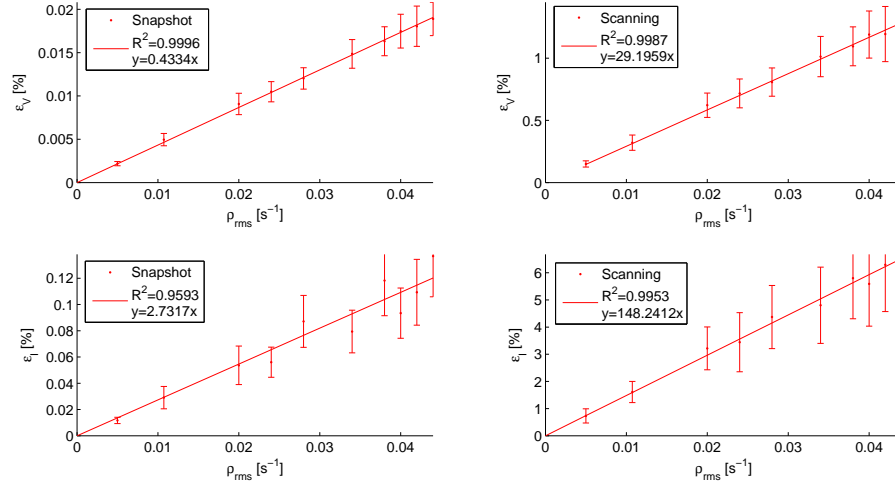
Figure 3.11: *RMS errors in the visibility function (top row) and in the restored image (bottom row) as a function of ρ_{rms}. A snapshot system (left column) and a scanning system with $n_t=52$ (right column) are compared.*

diffraction limited PSF. For a synthesised imager one can define the Strehl ratio S as:

$$S = \frac{\left| \sum_{m \neq n} G_{mn} \right|^2}{\left(\sum_{m \neq n} |G_{mn}| \right)^2} . \tag{3.18}$$

When only phase aberrations occur and have a Gaussian distribution with a standard deviation σ_G, S can be expressed as [48]:

$$S = e^{-\sigma_G^2} \left(1 + \frac{e^{\sigma_G^2} - 1}{M} \right) , \tag{3.19}$$

where M is the number of terms in the sums of Eq. (3.18). When $M >> e^{\sigma_G^2} - 1$, S is dominated by the term $e^{-\sigma_G^2}$. For drift rates that follow a Laplace distribution however, S is different from Eq. (3.19). We will show later that this assumption leads to a more accurate modelling of S in the presence of a linear instrument drift with gaussian distributed drift rates. The distribution of phase errors in the gain after $n_t = 13$ time-sequential measurements are shown in Figure 3.12. Clearly the Laplace distribution provides a better fit to data than the Gaussian distribution. The Laplace distribution is characterised by two parameters: the location μ and the scale parameter σ_L. For a Laplace distribution, with $\mu = 0$, S may be expressed as:

$$S = \frac{1}{(1 + \sigma_L^2)^2} \left(1 + \frac{\sigma_L^2}{M} (2 + \sigma_L^2) \right) . \tag{3.20}$$

When $M >> \sigma_L^2 (2 + \sigma_L^2)$, the Strehl ratio is dominated by the term $1/(1 + \sigma_L^2)^2$. The derivation of Eq. (3.19) and (3.20) is detailed in Appendix C. Figure 3.13 shows that Eq. (3.19) accurately models S for small values of σ_G only, typically below 0.2rad. Eq. (3.20) on the other hand accurately predicts S even for large phase errors such that $\sigma_L = 0.6$rad. Note σ_G and σ_L have been estimated with maximum likelihood estimators.

We also seek to assess the degradation in the performance of the system for increasing acquisition times. In order to maintain the geometry of the array constant, we artificially split the sequentially recorded baselines in different sequences. For instance, the 18252 baselines were recorded in 52 time-sequential steps, 351 at a time. We now
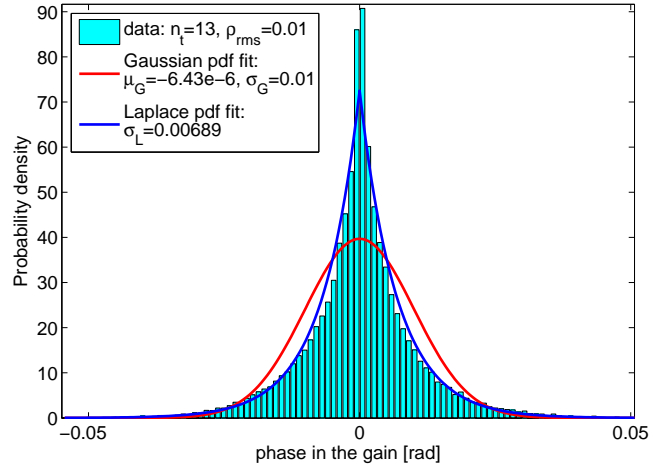
Figure 3.12: *Probability density function of the phase errors in the gain of the instrument due to a linear drift. The Laplace distribution provides a better fit to the data than a gaussian distribution.*
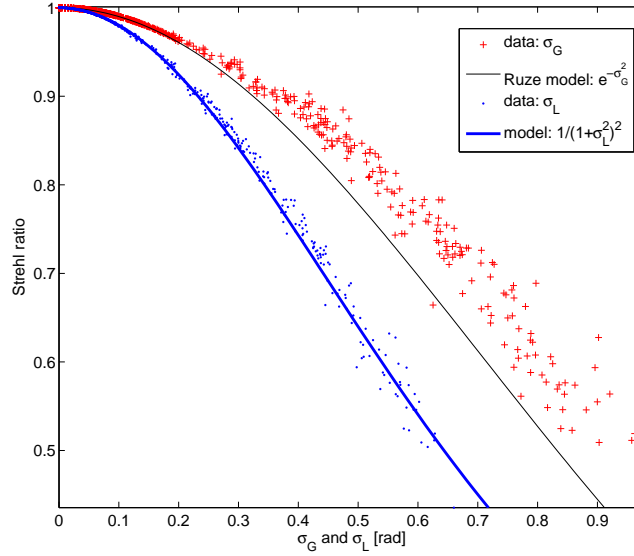
Figure 3.13: *Strehl ratio variation as a function of 1) (red cross) the standard deviation σ_G of the phase errors (obtained from the best fit with a Gaussian distribution), 2) (blue dot) the scale factor σ_L of the phase errors (obtained from a best fit with a Laplace distribution).*

simulate the effect of recording 1404 baselines in $n_t = 13$ sequential steps. We repeat this simulation for other values of n_t and perform a linear regression between ρ_{rms} and the parameters σ_G, $\mathcal{O}_{\text{rms}}$, ϵ_V and ϵ_I. The regression parameters C_ϕ, C_{offset}, C_V and C_I are such that:

$$\sigma_L = C_\phi \rho_{\text{rms}} \tag{3.21a}$$

$$\mathcal{O}_{\text{rms}} = C_{\text{offset}} \rho_{\text{rms}} \tag{3.21b}$$

$$\epsilon_V = C_V \rho_{\text{rms}} \tag{3.21c}$$

$$\epsilon_I = C_I \rho_{\text{rms}} \tag{3.21d}$$

Figure 3.14 shows that C_ϕ, C_{offset}, C_V and C_I increase linearly with n_t. This is evidence that the error in the restored image increases linearly with the acquisition time in the presence of a linear instrument drift. This corresponds to a challenging calibration problem. Figure 3.15 further illustrates this issue and displays the linear increase in ϵ_I with n_t for three different values of ρ_{rms}. Combining Eq. (3.21a) and (3.21d) results in the linear relationship $\epsilon_I = 8.377\sigma_L$ which may only be valid for small values of σ_L ($\sigma_L < 38°$ in this simulation). We estimate that for the brightness temperature image shown in Figure 3.7 a) a value of $6.8°$ in σ_L of the phase of the gain and offset of the correlator causes a RMS error of 1K in the restored image.
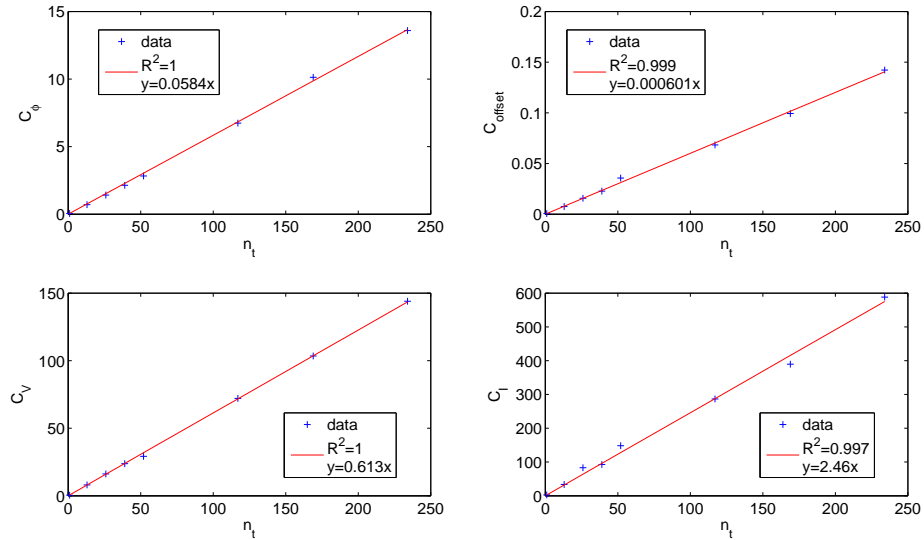
Figure 3.14: *Variation with n_t of the parameters C_ϕ, C_{offset}, C_V and C_I.*
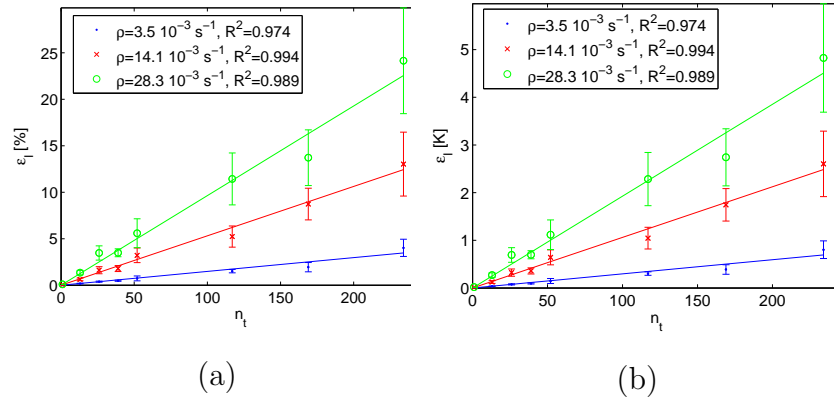
Figure 3.15: *RMS error in the synthesised image as a function of n_t. Conversion to absolute error assumes a signal amplitude (difference between maximum and minimum values) of 20K.*

3.5.2 Background Illumination

In the simulations illustrated in Figure 3.7, the scene illumination is from ambient surroundings and is considered to be constant with time and uniform in angular distribution [41]. For applications such as personnel scanning it will be possible for the background and illumination to be kept relatively constant during the acquisition times considered here, however, the longer acquisition times of the proposed technique will increase sensitivity to temporal changes in average illumination compared to a snapshot technique. For completeness we briefly describe the impact of the illumination on the synthesised map.

- The angular distribution of the incident radiation is not uniform but stable in time. Because of specular reflections, the background brightness temperature measured $T_C(\vec{r_i}, mn)$ will also depend upon the antenna positions m and n. Hence the measured visibility is:

$$\widetilde{\mathcal{V}}_{mn} = \sum_i \left(T_B(\vec{r_i}) + T_C(\vec{r_i}, mn) \right) \Phi_{mn}(\vec{r_i}), \qquad (3.22)$$

and the synthesised image follows:

$$\widetilde{T}_B(\vec{r}) \propto \sum_i T_B(\vec{r_i}) \widetilde{h}(\vec{r_i}, \vec{r}), \qquad (3.23)$$

with:

$$\widetilde{h}(\vec{r_i}, \vec{r}) = \sum_{m \neq n} \Phi_{mn}(\vec{r_i}) \Phi_{mn}^*(\vec{r}) \left(1 + \frac{T_C(\vec{r_i}, mn)}{T_B(\vec{r_i})} \right). \qquad (3.24)$$

46

This situation also corresponds to a convolutive error in the synthesised image.

- The angular distribution of the incident radiation is uniform but not stable with time. One can show that this is equivalent to having an offset term in the visibility measurements:

$$O_{mn} = T_C(mn) \sum_i \Phi_{mn}(\vec{r_i}) \,, \tag{3.25}$$

$$\widetilde{T}_B(\vec{r}) = \widehat{T}_B(\vec{r}) + \sum_{m \neq n} O_{mn} \Phi_{mn}^*(\vec{r}) \,. \tag{3.26}$$

3.6 Conclusions

Recording n_t images in a time-sequence with an interferometric synthetic aperture array in motion relative to the scene enables a reduction in the antenna-count by a factor of $\sqrt{n_t}$, but at the cost of a degradation in the radiometric sensitivity by a factor of $\sqrt{n_t}$, or a degradation in the imaging frame rate of the imager by a factor of n_t. Introducing a relative motion between the array and the source can be seen as an additional degree of freedom in the optimisation process. We have presented the advantages of rotational scanning over linear scanning of the array in terms of spatial frequency coverage efficiency and imaging frame rates.

We developed a new and more rigourous understanding of the metric of the (u, v) coverage uniformity. In addition, the proposed metric is computationally more efficient than the one discussed in [18]. Using this metric, antenna arrays were optimised with a genetic algorithm for time-sequential scanning acquisition. A 27-antenna array was presented and clearly demonstrates increased imaging performances over the non optimised array and conventional Y-shaped array.

The potential for reducing the antenna-count with the concept of antenna rotation aperture synthesis was assessed. Reduction factors can be extended to 10 or more for mm-wave imaging applications where low frame rates of the order of 0.1Hz are acceptable. The longer acquisition times of the proposed technique however increases sensitivity to instrument drift and temporal changes in average illumination, compared to a snapshot technique. This represents a serious calibration problem and increases the necessity for a real-time calibration procedure.

Chapter 4

Depth of field of antenna arrays

4.1   General description

The depth-of-field (DoF) of an optical system can be defined as the range extent in the object that remains acceptably sharp in the image [49]. The concept of DoF is illustrated in Figure 4.1 where a point outside the plane of best focus results in a wavefront error relative to the ideal spherical wavefront originating from an in-focus point. This wavefront error is generally characterised by the defocus parameter W_{20}. W_{20} is defined as the optical path length intercept, at the edge of the exit pupil, between the wavefront of an axially defocused point and the spherical wavefront of the axially focused point. The optical path difference $W(x, y)$ between a defocused wavefront and
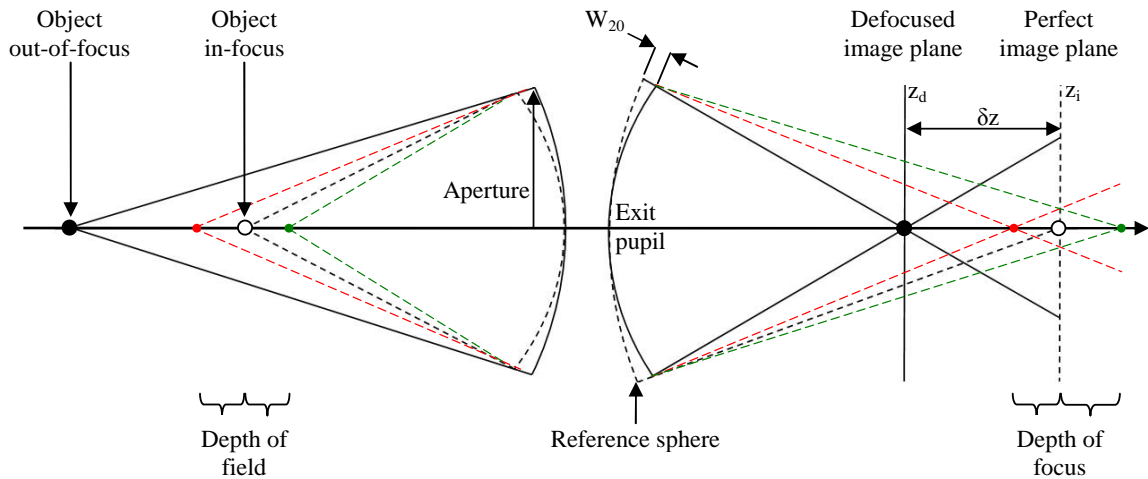
Figure 4.1: *Depth of field, depth of focus and the defocus coefficient W_{20}.*

the ideal wavefront at any point (x, y) within the exit pupil of an optical system is [1]:

$$W(x, y) = \frac{1}{2} \left(\frac{1}{z_d} - \frac{1}{z_i} \right) (x^2 + y^2), \qquad (4.1)$$

where z_d and z_i are the distances from the exit pupil to the defocused plane and image plane respectively. At the edge of a circular exit pupil of radius a, W defines the magnitude of the defocus coefficient W_{20} which measures the severity of the defocus effect:

$$W_{20} = \frac{a^2}{2} \left(\frac{1}{z_d} - \frac{1}{z_i} \right). \qquad (4.2)$$

Note that W_{20} is usually compared with the wavelength and may therefore be expressed in units of wavelengths. Some authors tend to use the defocus parameter ψ such that:

$$\psi = \frac{2\pi}{\lambda} W_{20}. \qquad (4.3)$$

Various criteria have been proposed to define the acceptable reduction in image sharpness associated with defocus: the Strehl ratio [50], the Rayleigh quarter-wave criterion [51] and the generally accepted Hopkins criterion [52, 53]. Hopkins criterion states that the system can be considered in-focus if the MTF does not fall below 80% of that of an in-focus diffraction limited system at any spatial frequency. For a clear circular aperture this criterion determines that ψ must be approximately less than 1, which corresponds to $W_{20} \approx 0.215\lambda$.

For a rotationally symmetric optical system, the pupil function associated with a defocused wavefront is defined as the 1-dimensional function $P(r)$, with $r = x/a$ the normalised pupil function variable. $P(r)$ may be written as:

$$P(r) = p(r)e^{j\frac{2\pi}{\lambda}W_{20}r^2}, \qquad (4.4)$$

with $p(r) = 1$ for $|r| \leq 1$ and $p(r) = 0$ otherwise.

4.2 Array refocusing

Real aperture imagers perform a redundant sampling of the spatial frequencies. When the system is focused these redundant frequencies add up in-phase. In a defocused system, however, there is a phase mismatch between redundant frequencies which therefore interfere with each other. This leads to an amplitude reduction of the modulation

transfer function (MTF) of the system compared with a focused system. For specific values of defocus and spatial frequencies these interferences create nulls in the MTF. This corresponds to a loss of information that will result in an increased blur in the recorded image, or alternatively in an increased noise level if one attempts to correct for this effect. Synthetic aperture imagers on the other hand record spatial frequencies separately and require the image to be formed in computer hardware, which enables refocus of the system for any distance. This is the reason these imagers are sometimes inaccurately considered to have an infinite depth of field. The only variations with range that occur in the (u, v) coverage of the array or its refocused PSF are due to near-field effects. Figure 4.2 shows that only very small variations in the (u, v) cover occur when the range of the array shown in Figure 3.4 (c) changes from 1.8m to 4.2m corresponding to a defocus parameter W_{20} of -1λ and +5λ respectively. Figure 4.3 confirms that the corresponding PSF of the array is almost invariant with range.
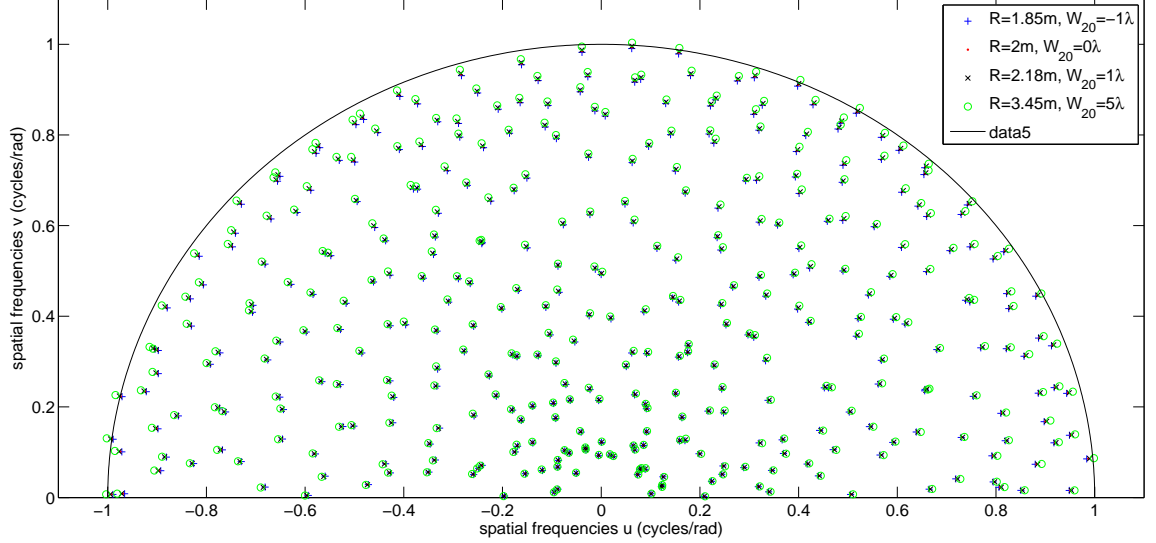
Figure 4.2: *Variation with range of the (u, v) coverage of the optimised Reuleux array.*

4.3 Impact of refocusing errors - Depth of field

When the refocusing of the array is performed without error we have shown that negligible variations with range occur in the PSF of the array. However one can wonder what impact refocusing errors have on the performance of the array. In other words, we seek to analyze the depth of field of synthetic aperture arrays. To that end we
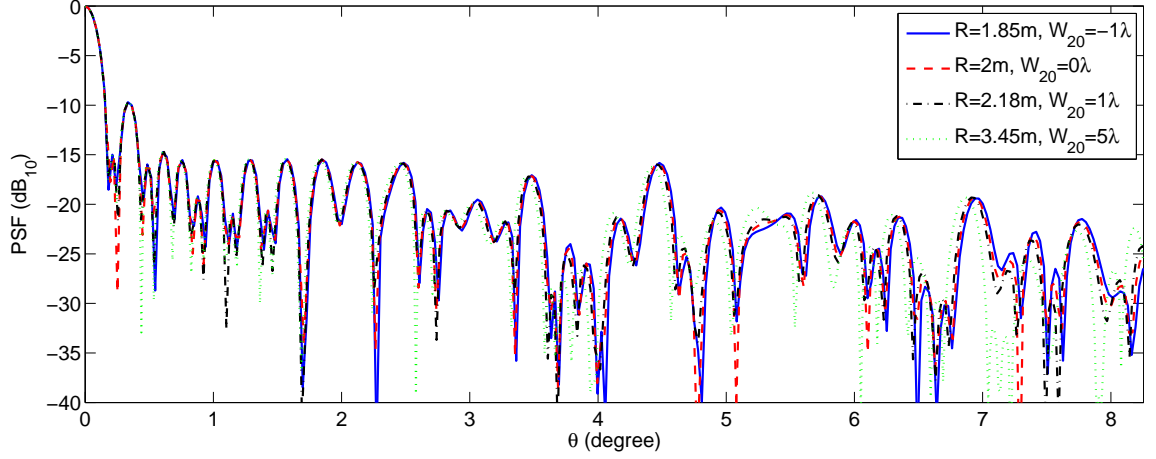
Figure 4.3: *PSF of the optimised Reuleux array refocused at different range distances.*

measure the Strehl ratio of different arrays and compare them with that of a real, circular aperture imager with a focal distance f. For a circular real-aperture optical system one can show that except for an irrelevant phase factor, the axial amplitude impulse response $Q(W_{20})$, within the paraxial approximation, is [54]:

$$
\begin{aligned}
Q(W_{20}) &= \frac{\pi(N_F - 2W_{20})}{f} \int_{-0.5}^{0.5} e^{-j2\pi W_{20}\xi} \, d\xi \,, \\
&= \frac{\pi(N_F - 2W_{20})}{f} \text{sinc}(W_{20}) \,,
\end{aligned}
\tag{4.5}
$$

where ξ is the normalised radial pupil coordinate, W_{20} is in units of wavelengths and N_F is the Fresnel number of the aperture such that:

$$
N_F = \frac{a^2}{\lambda f} \,,
\tag{4.6}
$$

with a the radius of the pupil. Hence the Strehl ratio of a real, circular aperture optical system with a defocus parameter W_{20} is described as:

$$
S(W_{20}) = \frac{|Q(W_{20})|^2}{|Q(0)|^2} = \frac{(N_F - 2W_{20})^2}{N_F^2} \text{sinc}^2(W_{20}) \,.
\tag{4.7}
$$

Note that Eq. (4.7) shows that the axial value of the PSF for such optical systems is null when W_{20} expressed in wavelengths is an integer. The factor $(N_F - 2W_{20})^2/N_F^2$ in Eq. (4.7) is equal to unity for large Fresnel apertures, typically $N_F \geq 100$, and can therefore be neglected in most optical systems operating at visible frequencies. However this factor becomes significant for low-Fresnel-number apertures, as is the case in mm-wave imaging (here $N_F \simeq 19$), and is responsible for an axial shift of the maximum axial intensity away from the focal plane and towards the exit pupil [54].

51

We seek to establish the expression for $S(W_{20})$ for synthetic-aperture imagers in order to compare their DoF with that of real circular aperture systems. For simplicity we derive this expression for a source that lies in the far-field of the array. We also consider finite size antenna dishes. Using Eq. (4.4) the pupil function of the array, in the presence of defocus, is given by:

$$P(\vec{r}, W_{20}) = \sum_k [\delta(\vec{r} - \vec{r_k}) * p(rr_a)] e^{j2\pi \frac{W_{20}}{\lambda} r^2}, \tag{4.8}$$

where $*$ denotes the convolution product, r is the normalised radial pupil coordinate, r_a the radius of each antenna dish normalised to the semi array aperture size. The impulse response $\widehat{P}(\vec{\rho}, W_{20})$ of the array is equal to the Fourier-transform of the pupil function $P(\vec{r}, W_{20})$:

$$\widehat{P}(\vec{\rho}, W_{20}) = 2\pi r_a^2 \sum_k \left[e^{j2\pi \vec{r_k} \cdot \vec{\rho}} \cdot \frac{J_1(2\pi \rho r_a)}{2\pi \rho r_a} \right] * \widehat{L}(\rho, W_{20}), \tag{4.9}$$

with:

$$\widehat{L}(\rho, W_{20}) = \frac{e^{j\pi/4}}{\sqrt{\frac{4\pi|W_{20}|}{\lambda}}} e^{-j\frac{\lambda \rho^2}{8\pi W_{20}}}. \tag{4.10}$$

We denote the pupil vector $\vec{r}$ and the image plane vector $\vec{\rho}$ as $\vec{r} = (\xi, \eta)$ and $\vec{\rho} = (x, y)$. Hence Eq. (4.9) can be rewritten as:

$$\widehat{P}(\vec{\rho}, W_{20}) = \frac{2\pi r_a^2 e^{j\pi/4}}{\sqrt{\frac{4\pi|W_{20}|}{\lambda}}} \sum_k \iint e^{j2\pi(\xi_k x' + \eta_k y')} \cdot \frac{J_1(2\pi \rho r_a)}{2\pi \rho r_a} e^{-j\frac{\lambda}{8\pi W_{20}}[(x-x')^2 + (y-y')^2]} \, \mathrm{d}x' \, \mathrm{d}y', \tag{4.11}$$

where one recognises the Fourier transform with frequency parameters (ξ_k, η_k). Thus Eq. (4.11) reduces to:

$$\begin{aligned}
\widehat{P}(\vec{\rho}, W_{20}) &= \sum_k p(r_k r_a) * e^{j2\pi\left[\frac{W_{20}}{\lambda}(\xi_k^2 + \eta_k^2) + x\xi_k + y\eta_k\right]}, \tag{4.12} \\
&= \sum_k e^{j2\pi\left[\frac{W_{20}}{\lambda} r_k^2 + x\xi_k + y\eta_k\right]} \\
&\quad \times \iint p(r' r_a) e^{j2\pi \frac{W_{20}}{\lambda} r'^2} e^{-j2\pi[\xi' u + \eta' v]} \, \mathrm{d}\xi' \, \mathrm{d}\eta', \tag{4.13}
\end{aligned}$$

where we make use of the radial coordinate $r_k = \sqrt{\xi_k^2 + \eta_k^2}$, $r' = \sqrt{\xi'^2 + \eta'^2}$ and the following change of coordinates:

$$u = x + 2\frac{W_{20}}{\lambda}\xi_k, \tag{4.14a}$$

$$v = y + 2\frac{W_{20}}{\lambda}\eta_k. \tag{4.14b}$$

52

The double integral in Eq. (4.13) is a rotationally symmetric function since it is the Fourier transform of a rotationally symmetric function. Thus it is necessary to define the radial coordinate ζ associated with the cartesian coordinates u and v:

$$\zeta = \sqrt{\left(x + 2\frac{W_{20}}{\lambda}\xi_k\right)^2 + \left(y + 2\frac{W_{20}}{\lambda}\eta_k\right)^2}. \tag{4.15}$$

Hence Eq. (4.13) can be reduced to:

$$\widehat{P}(\vec{\rho}, W_{20}) = \sum_k e^{j2\pi\left[\frac{W_{20}}{\lambda}r_k^2 + x\xi_k + y\eta_k\right]} F(\vec{\rho}, W_{20}, r_k, r_a), \tag{4.16}$$

where $F(\vec{\rho}, W_{20}, r_k, r_a)$ is in general a complex scalar that depends on the location of the antenna, its size and the location of the source. $F(\vec{\rho}, W_{20}, r_k, r_a)$ is expressed as:

$$F(\vec{\rho}, W_{20}, r_k, r_a) = 2\pi \int_0^{r_a} e^{j2\pi\frac{W_{20}}{\lambda}r'^2} J_0(2\pi\zeta r')r' \, \mathrm{d}r', \tag{4.17}$$

with $J_0(x)$ the Bessel function of the first kind of order zero. In order to compute $S(W_{20})$ we are interested in $\widehat{P}(0, W_{20})$, which is derived from Eq. (4.16) and (4.17):

$$\widehat{P}(0, W_{20}) = \sum_k e^{j2\pi\frac{W_{20}}{\lambda}r_k^2} F(0, W_{20}, r_k, r_a). \tag{4.18}$$

At this point it is useful to decompose the scalar $F(0, W_{20}, r_k, r_a)$ in Eq. (4.18) into its amplitude and phase components such that:

$$F(0, W_{20}, r_k, r_a) = A_k^{W_{20}} e^{j\theta_k^{W_{20}}}. \tag{4.19}$$

Note that $F(0, 0, r_k, r_a)$ equals the area of the antenna dish. The PSF is defined as the square modulus of the impulse response, i.e. $PSF(\vec{\rho}, W_{20}) = \widehat{P}(\vec{\rho}, W_{20})\widehat{P}^*(\vec{\rho}, W_{20})$. For synthetic aperture arrays, the cross terms only are included in the PSF. Combining Eq. (4.18) and (4.19) one obtains the expression of the PSF at the origin:

$$
\begin{aligned}
PSF(0, W_{20}) &= \sum_{m \neq n}^{N(N-1)} e^{j2\pi\frac{W_{20}}{\lambda}(r_m^2 - r_n^2)} A_m^{W_{20}} A_n^{W_{20}} e^{j(\theta_m^{W_{20}} - \theta_n^{W_{20}})}, \\
&= 2 \sum_{m \neq n}^{N(N-1)/2} A_m^{W_{20}} A_n^{W_{20}} \cos\left[2\pi\frac{W_{20}}{\lambda}(r_m^2 - r_n^2) + \theta_m^{W_{20}} - \theta_n^{W_{20}}\right] \quad (4.20)
\end{aligned}
$$

Hence the Strehl ratio $S(W_{20}) = PSF(0, W_{20})/PSF(0, 0)$ of an antenna array can be written as:

$$S(W_{20}) = \frac{2}{N(N-1)(\pi r_a^2)^2} \sum_{m \neq n}^{N(N-1)/2} A_m^{W_{20}} A_n^{W_{20}} \cos\left[2\pi\frac{W_{20}}{\lambda}(r_m^2 - r_n^2) + \theta_m^{W_{20}} - \theta_n^{W_{20}}\right]. \tag{4.21}$$

If we consider the limit case of point-like antennas, Eq. (4.12) becomes:

$$\widehat{P}(\vec{\rho}, W_{20}) = \sum_k e^{j2\pi\left[\frac{W_{20}}{\lambda}r_k^2 + \vec{r_k}\cdot\vec{\rho}\right]} \ . \tag{4.22}$$

In this case $f(r_k, W_{20}, r_a)$ equals unity and Eq. (4.21) reduces to:

$$S(W_{20}) = \frac{2}{N(N-1)} \sum_{m\neq n}^{N(N-1)/2} \cos\left[2\pi\frac{W_{20}}{\lambda}(r_m^2 - r_n^2)\right] \ . \tag{4.23}$$

It is clear from Eq. (4.23) that for an array of infinitely small antennas distributed along a circle, $S(W_{20})$ equals unity independently of the amount of defocus. This is equivalent to an infinite DoF. If one accounts for the finite size of the antennas, then for this type of arrays $S(W_{20})$ is such that:

$$S(W_{20}) = \frac{2}{N(N-1)(\pi r_a^2)^2} \sum_{m\neq n}^{N(N-1)/2} A_m^{W_{20}} A_n^{W_{20}} \cos\left[\theta_m^{W_{20}} - \theta_n^{W_{20}}\right] \ . \tag{4.24}$$

Note that for arrays with any degrees of rotational symmetry, a rotational scan around the centre of symmetry of the array will not change the value of $S(W_{20})$, and the number N of added terms in Eq. (4.23) can be reduced to the number of antennas in the array. Figures 4.4, 4.5, 4.6 and 4.7 show the horizontal slice at $y = 0$ of the PSF after a rotational scan for the power law Y array, the Reuleux triangle array and the optimised Reuleux triangle array respectively. The different curves on each figure have been obtained for the defocus values $W_{20} = 0\lambda, 0.25\lambda, 0.5\lambda, 1\lambda$. It is worth mentioning that the optimised Reuleux array and the circular array have different aperture size than the Y array and the regular Reuleux array despite having the same maximum baseline. This means W_{20} has to be recalculated for each array. Comparing Figures 4.4, 4.5 and 4.6 it can be observed that the PSF of the Y array is significantly more degraded with increasing defocus than for Reuleux arrays. This is because the Y array differs more from a circular array than the Reuleux arrays. As expected the PSF of the circular array, see Figure 4.7, is invariant with defocus. The measured Strehl ratio of these arrays are plotted on Figure 4.8 as a function of W_{20} and are in good agreement with the models described in Eq. (4.23). The measured Strehl ratio are shown on Figure 4.9 together with the Strehl ratio of a real, circular aperture imager obtained from Eq. (4.7). Figure 4.9 clearly shows the smaller depth of field provided by the Y array compared with that achieved by the Reuleux arrays. It also illustrates the

invariance with defocus of the PSF of a circular array. Note that the two Reuleux arrays achieve a very similar depth of field, which is extended compared with that of the real aperture imager. On the other hand the Y array reduces the depth of field compared with the real aperture imager, or alternatively provides axial super-resolution. In order to quantify the depth of field of these imagers we use the Hopkins criterion ($W_{20} \approx 0.215\lambda$) and measure $S(\pm 0.215\lambda)$ for the real circular aperture system. We consider the more restrictive value $S_{DOF} = S(-0.215\lambda) \approx 0.896$ and quantify the depth of field of the antenna arrays as the defocus W_{20} for which $S(W_{20}) \approx S_{DOF}$. Using this procedure one estimates a DoF of $\approx 0.37\lambda$ and 0.16λ for the Reuleux arrays and Y array respectively. Figure 4.9 (b) is magnified around $W_{20} = 0\lambda$ and highlights the asymmetric profile of $S(W_{20})$ for a real aperture imager due to the focal shift effect discussed above. The impact on $S(W_{20})$ of the factor $f(r_k, W_{20}, r_a)$ due to the finite size of antenna dishes is shown on Figure 4.10 for antennas that are λ in diameter ($r_a \approx 0.004$). The reduction in DoF due to this antenna size is of the order of $\lambda/100$ for the Y-shaped and Reuleux arrays and can be neglected. The DoF of the circular array with antenna diameter λ is of the order of 33λ. This corresponds to a hyperfocal distance of 58cm, with all objects beyond 45cm acceptably sharp. It is important to remember that the $F/\#$ of the array increases with the focused range and therefore that the depth-of-focus increase with the square of the focused range. We find that even when focusing at a distance of 4m the Y-array, the circular real aperture system and the Reuleux arrays have a depth-of-focus of 27cm, 36cm and 62cm respectively. This highlights the very limited depth-of-focus of real aperture mm-wave imaging systems and shows that this characteristic can be extended with the use of synthetic aperture Reuleux arrays.

4.4 Design of antenna arrays with an infinite depth-of-field

We have seen in Section 4.3 that correlation arrays with circularly distributed antennas have an on-axis PSF that is invariant with defocus, in the limit of infinitely small antennas. This is because the wavefront emitted by an on-axis point-source is recorded
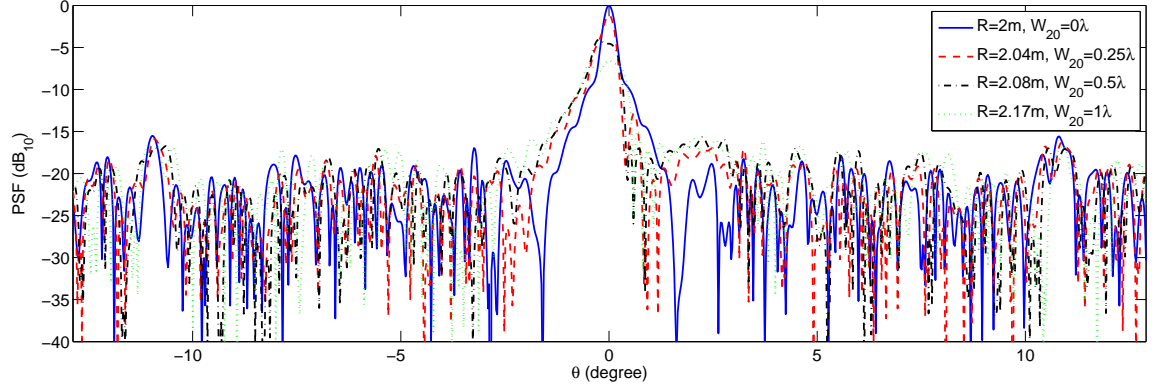
Figure 4.4: *Variation with defocus of the PSF of the power law Y array.*
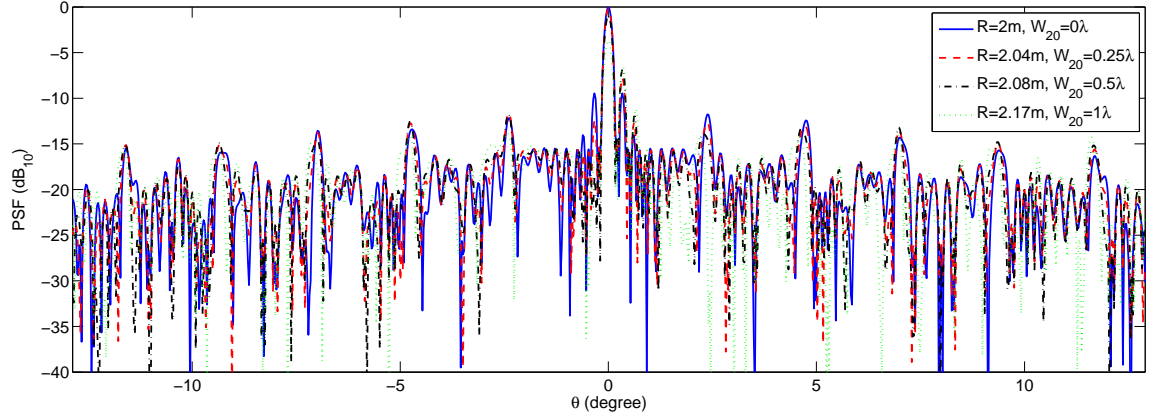
Figure 4.5: *Variation with defocus of the PSF of the non optimised Reuleux array.*
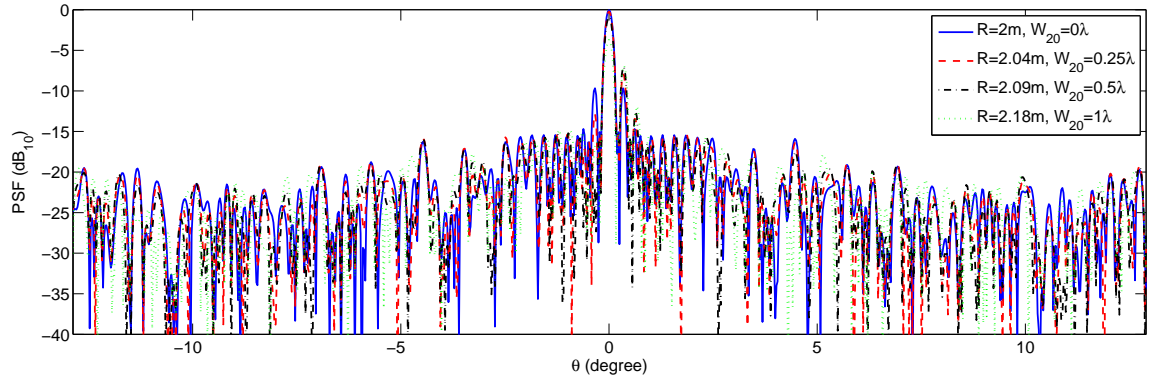
Figure 4.6: *Variation with defocus of the PSF of the optimised Reuleux array.*
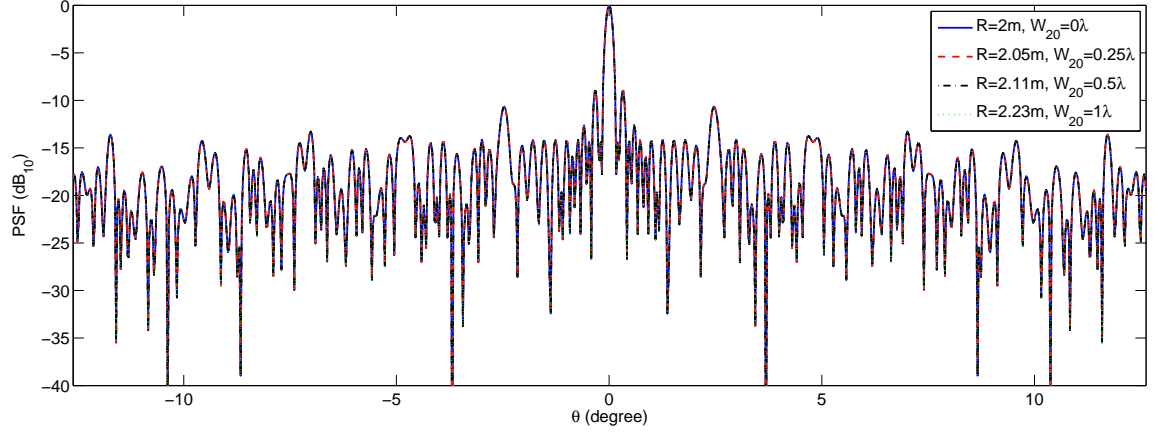
Figure 4.7: *PSF of a circular array after a rotational scan for different values of W_{20}.*

(a)

(b)

(c)
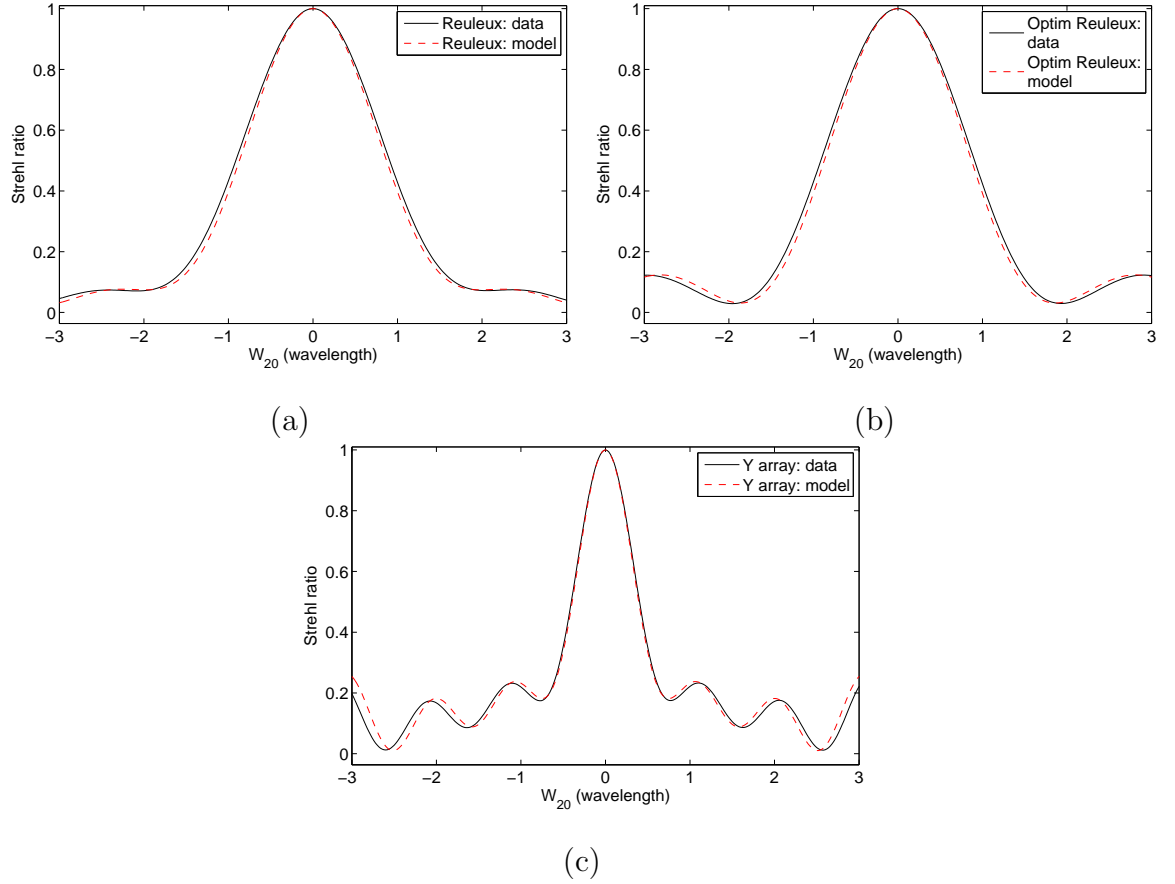
Figure 4.8: *Measured and modelled Strehl ratio VS defocus for a) the non optimised Reuleux triangle array, b) the optimised Reuleux triangle array and c) the power law Y array.*
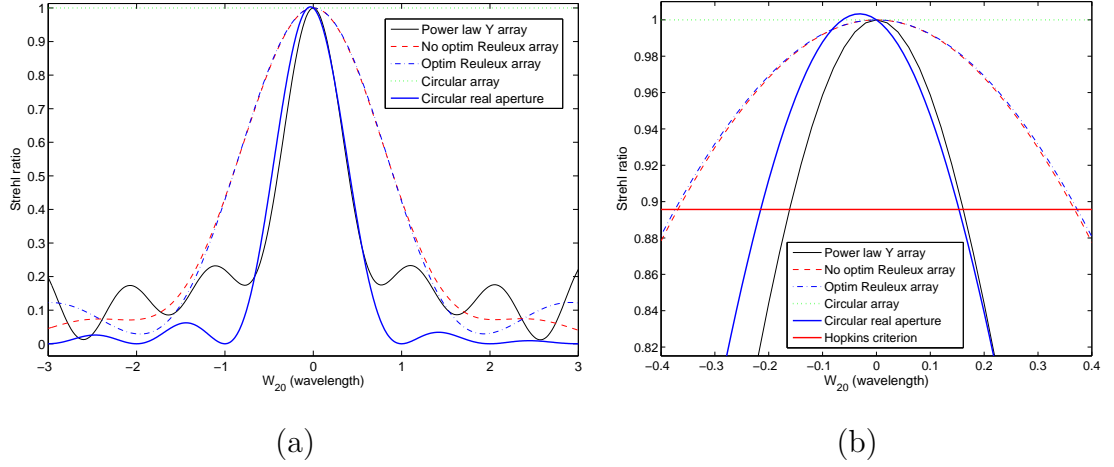
Figure 4.9: *(a) Strehl ratio vs defocus for different arrays and a real, circular aperture system. (b) magnification around $W_{20} = 0\lambda$ showing the focal shift effect of the real aperture imager and Hopkins' criterion.*
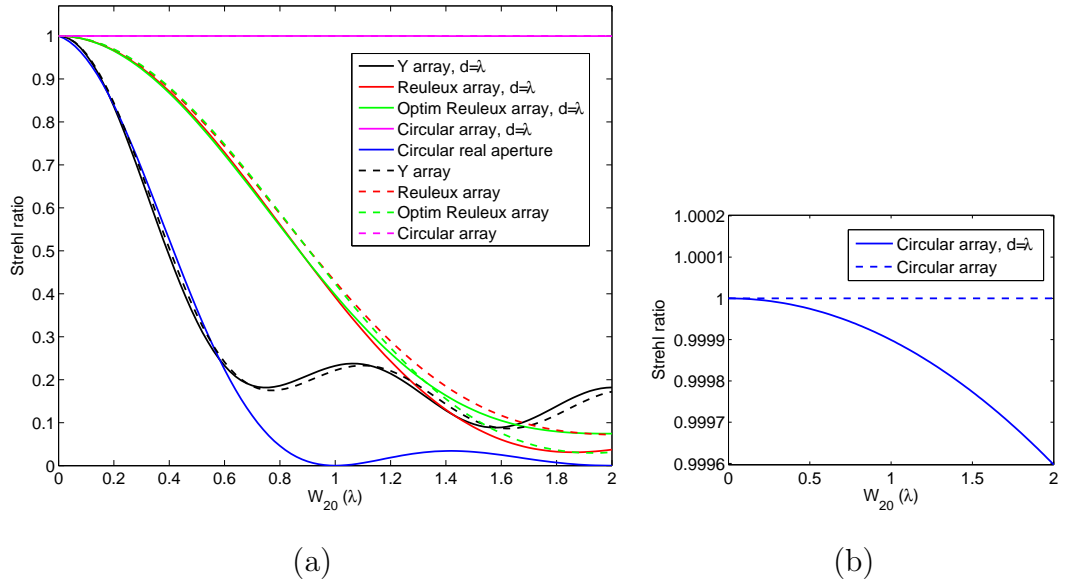
Figure 4.10: *(a) Strehl ratio vs defocus for different antenna arrays. Results show the influence of real size antenna dishes that are λ in diameter. (b) magnification around $S(W_{20}) = 1$ showing the almost infinite DoF achieved with circular array of antennas that are λ in diameter.*

by all antennas of a circular array with the same phase. This constant phase term for all antennas cancels out when correlations between pairs of antenna signals are performed, independently of the source range. In this section we seek to take advantage of this property to design antenna arrays with an infinite DoF. Evenly distributed circular arrays however have a poor coverage of the Fourier domain because of their rotational symmetry [17] and their PSF therefore suffer from high sidelobe levels. We apply here the array optimisation method and algorithms described in section 3.3 to the subset of circular arrays. This approach presents the advantage of reducing the dimension of the search space from $2N$ to N, with N the number of antennas in the array.

In order to fit the bit-encoded-parameter implementation of the GA described in section 3.3, the angular position of circularly distributed antennas is discretised. The angular sampling period $\delta\theta$ is based on a minimum spacing between antennas $\delta\rho$ equal to the wavelength, and is defined as $\cos\delta\theta = 1 - 2\delta\rho^2/D^2$. We recall that the displacement of each antenna relative to a reference position is encoded in order to minimise the number of bits required. The reference array is taken to be the evenly distributed circular array which defines an angular separation $\theta_0 = 2\pi/N$ between antennas. If the maximum angular displacement allowed is $\pm 2\theta_0$, the number of bits N_{bit} required for the parameter encoding can be estimated with $\log_2(2\theta_0/\delta\theta)$. For a 27-antenna circular array, as considered in section 4.3, we have $2\theta_0/\delta\theta \approx 51$. This corresponds to 6 bits per parameter plus one bit for the sign of the displacement, thus $N_{\text{bit}} = 7$. The parameters of the genetic algorithm used to optimise the 27-antenna circular array are summarised in Table 4.1. For comparison with the array design obtained in section 3.3, rotational scanning of the array is maintained at $\pi/3\text{rad}$. The angular coordinates of the optimised array are given in Appendix B. Note that the algorithm was run here for an extra 40% in computational time compared to the optimisation of the Reuleux array presented in section 3.3, see Table 3.1. In spite of this additional computation, the algorithm converged to a solution with a cost function $\mathcal{C}_{\text{min}} = -2.007$, that is higher than the value $\mathcal{C}_{\text{min}} = -2.1247$ obtained for the optimised Reuleux array. This indicates that the optimised circular array performs a less uniform sampling of the Fourier domain than that achieved with the optimised Reuleux array. This may be due to the increased constraint on the search space and possibly a less favorable starting position.

The optimised circular array is presented in Figure 4.11 with its snapshot and scanned MTF. An evenly distributed circular array is also shown for comparison. Note again the much increased uniformity of the scanned (u, v) coverage achieved by the optimised circular array.

						Number of	
p_{mut}	N_{chro}	N_{bit}	$\delta\rho$	$\delta\theta$	$\mathcal{C}_{\mathrm{min}}$	iterations	combinations
0.01	500	7	λ	9.1 mrad	-2.007	2060	2^{189}

Table 4.1: *Values of the parameters used in the genetic algorithm optimisation of a 27 antenna circular array.*
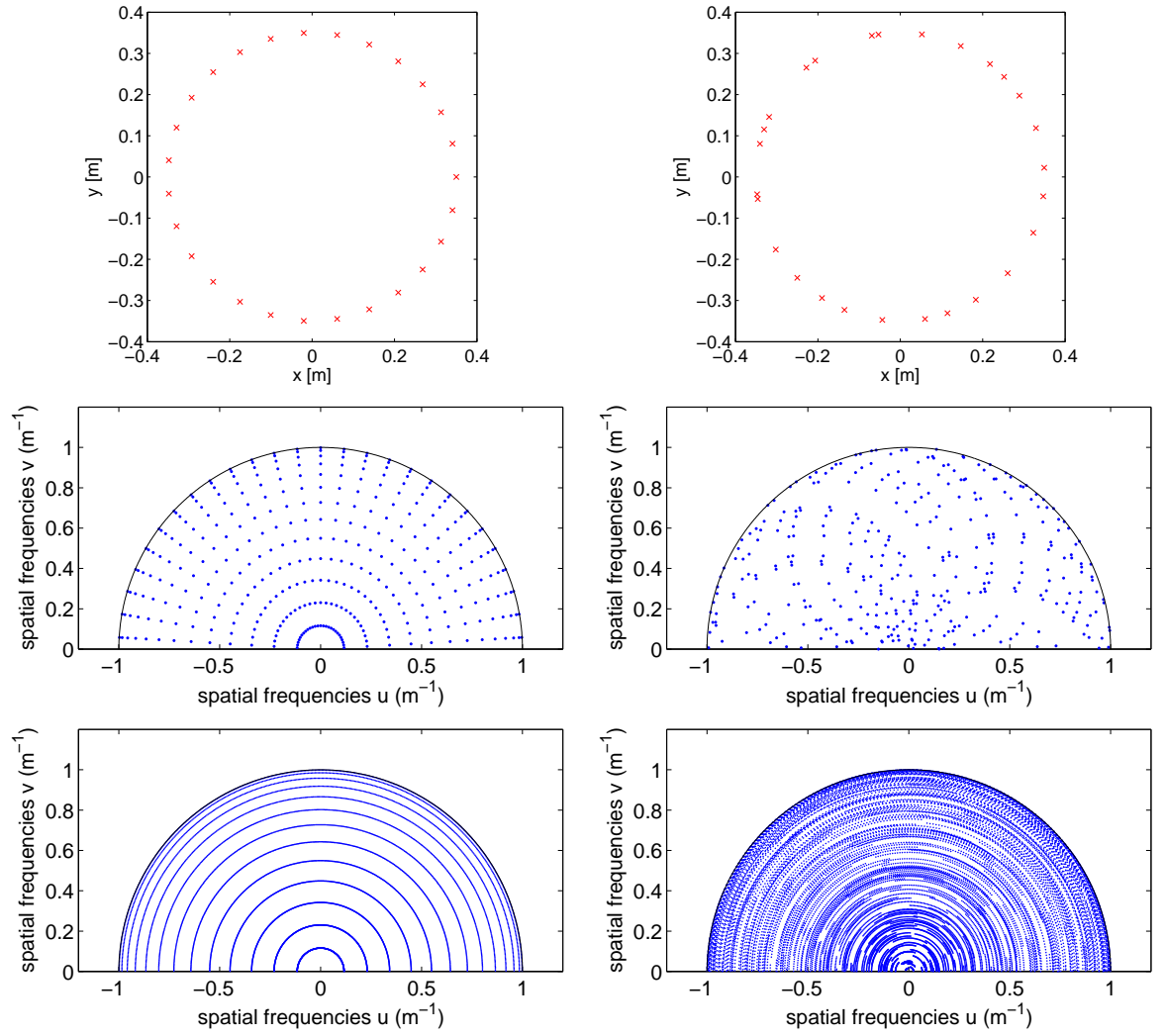
Figure 4.11: *Circular array optimised for maximum uniform* (u, v) *coverage (right column) and infinite depth-of-field. Snapshot and scanned* (u, v) *coverage are shown below. An evenly distributed circular antenna array is presented for comparison.*

4.5 Conclusions

In this chapter we introduced the defocus parameter W_{20} used to characterise the severity of the defocus effect in imaging systems. We showed that without refocusing errors the axial PSF of synthetic aperture arrays is invariant with range, with the exception of negligible near-field effects. We show that digital refocusing errors in synthetic aperture imagers are mathematically equivalent to the defocus effect applied to the amplitude pupil function of the array. Using the Strehl ratio as a metric of the system sensitivity to defocus, we show that the depth-of-field (DoF) of antenna arrays depends solely on the radial positions of the antennas, and that Reuleux arrays have a larger DoF than both the Y-array and real circular-aperture systems with equal $F_{/\#}$. It also follows that arrays with antennas distributed on a circle exhibit an infinite DoF at the array boresight. Following the optimisation method described in section 3.3, we take advantage of this property to maximise the uniformity of the Fourier domain coverage of an infinite DoF antenna array. The effect of finite size antennas on the DoF of the array is also modelled. For the 27-element circular array considered here and a single antenna diameter equal to the wavelength, corresponding to a fill factor of ~ 0.004, the DoF is of the order of $W_{20} = 33\lambda$. This is equivalent to a hyperfocal distance of 58cm. Further investigation will be necessary to obtain a general relationship between the fill factor of the array and its DoF.

Chapter 5

Wavefront coding theory

In this chapter we are concerned with the depth-of-field (DoF) of optical systems. We study a method called "wavefront coding" that enables to extend the DoF without reducing the transverse resolution and sensitivity of the system. This method relies on the combination of an additional optical element designed to reduce the sensitivity of the system to defocus, with a post-processing digital restoration. In section 5.1 we review the various approaches proposed to increase the DoF and show how wavefront coding emerged as the state-of-the-art method in this field. In section 5.2 we describe the principles of this method and present two approaches to designing pupil phase filters for enhanced DoF: 1) an analytical method that leads to phase filters with a cubic profile. This derivation however is restricted to rectangular, linearly separable filters. 2) A numerical optimisation of phase filters with higher order polynomials. This method can be applied to circular aperture optical systems and results in two types of phase filters, namely cubic and petal, depending on the type of constraint applied in the optimisation algorithm. Section 5.3 describes the Wiener filter employed to restore the recorded images. The tradeoffs associated with wavefront coding are discussed in section 5.4. We present in section 5.5 a restoration method that improves the quality of the extended DoF images.

5.1 Depth of field - a review

We have introduced the DoF of an optical system in section 4.1 and described its relationship to the defocus parameter W_{20}. The most common way to increase the depth-of-field of an optical system consists of closing down the aperture stop. This is universally used in conventional photography. However, reducing the diameter of the aperture stop by a factor n effectively increases the $F_{/\#} = f/D$ (where f is the focal length and D is the diameter of the aperture stop of the system) by the same factor and increases the depth-of-field by a factor n^2. This method suffers from a reduction in the optical power throughput by a factor n^2 and a reduced transverse resolution by a factor n. While this may be acceptable in many situations such as conventional photography, it can be highly desirable to extend the DoF without reducing the light gathering ability and transverse resolution of the optical system. Such applications include imaging in dim light illumination and optical microscopy where spatial resolution and photon sensitivity cannot be traded for an extended DoF. One of the first methods proposed that avoids this tradeoff was in fact developed in microscopy [55]. It consists in moving the focus of the microscope along the optical axis as the image is being recorded. Thus, the effective MTF of the microscope is the average of the MTF at the different focuses. The recorded image is blurred but is easily restored with a digital filter because the effective MTF does not contain nulls anymore.

One of the early descriptions of annular apertures as a means to increase the DoF is given in [56]. Interestingly, the reduction in speed, i.e. optical power throughput, associated with an increased DoF is the same for both annular and stopped down circular apertures. However the former offers improved resolution over the latter. The ambiguity function (AF) was employed to demonstrate the increased DoF of centrally obscured rectangularly separable pupils [57]. Similarly it was used to design rotationally symmetric amplitude pupil filters for reducing the sensitivity to spherical aberrations [58]. Rotationally symmetric amplitude and phase filters were also described in [59] to increase the transverse resolution of confocal microscopes. Castañeda *et al.* [22] have been arguably the first to combine (amplitude only) pupil filters, for reducing the sensitivity to defocus, with digital post-processing for improving the quality of the

extended depth-of-field (EDF) images. This new paradigm, where the pupil filter is designed to facilitate the digital restoration, was applied to phase-only pupil functions and termed wavefront coding in [26]. Arguing that these filters do not degrade the system speed, such filters were designed to minimise the variation of the amplitude of the AF with defocus [26], see also [60]. Rectangularly separable cubic phase masks (CPM) were shown to be optimal in this sense. Note that the appearance of nulls in the MTF of such systems is restricted to large amounts of defocus. This facilitates the image restoration, similarly to the technique proposed in [55]. A very similar phase pupil function, coined the logarithmic phase mask because its phase follows $\alpha \text{sign}[x]x^2 \log |x|$, is obtained when minimising the variation of the PSF with defocus [61]. Phase-only pupil functions have been discussed for various other purposes: two-zone annular phase masks for increasing the axial resolution in confocal microscopes [62], rotationally symmetric phase masks the mitigation of spherical aberrations [63], coma and astigmatism [64]. In [54] the Strehl ratio is used instead to characterise the extended DoF of non-centrally obscured pupil functions. Building on the work in [26], Prasad *et al.* proposed to optimise higher order phase polynomials numerically [27]. This scheme minimises the system sensitivity to defocus and is regularised by a competing term, the image restorability. A computationally efficient metric of the system sensitivity to defocus is detailed in [28, 65]. Radially symmetric quartic and logarithmic phase masks do not require digital post-processing and have been shown to allow the mitigation of modest amounts of aberrations.

The DoF can also be decoupled from the aperture size by digitally refocusing an image recorded with an integral imaging system [66, 67]. Digital refocusing denotes the process of reconstructing an image focused on a specific plane based on the information recorded at a different focus. It is strictly speaking not a method for extending the depth-of-field since this feature remains unchanged in the synthesized image. Digital refocusing requires to measure the four-dimensional (4D) light field with an integral imaging system such as a plenoptic camera [68]. The 4D light field is composed of the two spatial dimensions, plus two additional dimensions that define the orientation of each light ray arriving on the detector. A plenoptic camera focuses the light from the object plane onto a microlens array, positioned so that each microlens forms an image

of the aperture of the main lens onto N pixels of the detector. This design is similar to the Shack-Hartmann sensor used to measure optical aberrations [69]. The plenoptic camera yields N sub-images of the object formed through N different sub-apertures of the main lens, each sub-aperture being N times smaller than the aperture of the main lens. Hence the DoF in the sub-images should be a factor N^2 larger than that in an image recorded with the main lens. This larger DoF puts a physical limit to the amount of defocus that can be exactly compensated for with a plenoptic camera. Post processing of the 4D light field also enables range estimations, see e.g. [69, 70] for more details.

5.2 Wavefront coding principles

5.2.1 Optical transfer function and ambiguity function

We assume the system is incoherently illuminated, that is to say linear in intensity, and translation invariant, i.e. the PSF is considered to be constant across the field of view. For simplicity we consider a one-dimensional system but the following calculations can be easily extended to two-dimensional systems. The optical transfer function $H(u)$ characterises the system response to the spatial frequencies u and is defined as the autocorrelation of the generalised pupil function $P(\xi)$:

$$H(u) = \frac{\displaystyle\int_{-\infty}^{+\infty} P(\xi + u/2)P^*(\xi - u/2)\,\mathrm{d}\xi}{\displaystyle\int_{-\infty}^{+\infty} |P(\xi)|^2\,\mathrm{d}\xi}\,, \tag{5.1}$$

where ξ is the normalised pupil coordinate and u is the normalised spatial frequency. The generalised pupil function is described by:

$$P(\xi) = p(\xi)e^{jkW(\xi)}\,, \tag{5.2}$$

where $W(\xi)$ is the one-dimensional aberration function and $p(\xi)$ is such that:

$$p(\xi) = \begin{cases} 1 & \text{If } |\xi| \leq 1 \\ 0 & \text{otherwise} \end{cases} \tag{5.3}$$

When the system suffers from defocus aberration only, $P(\xi)$ is described by Eq. (4.4) and can be substituted into Eq. (5.1) to yield:

$$H(u, W_{20}) = \frac{1}{2} \int_{-\infty}^{+\infty} p(\xi + u/2) p(\xi - u/2) e^{j\frac{2\pi}{\lambda} 2W_{20} u \xi} \, \mathrm{d}\xi \, . \tag{5.4}$$

The ambiguity function is a very useful tool in signal processing and optics. It is well known to be related to the OTF and has been previously used to characterise it in the presence of aberrations [71, 57, 58]. We denote the ambiguity function operator as A. The ambiguity function $AP(u,t)$ of the pupil function $P(u)$ is defined as [72]:

$$AP(u,t) = \int_{-\infty}^{+\infty} P(\xi + u/2) P^*(\xi - u/2) e^{j2\pi t \xi} \, \mathrm{d}\xi \, . \tag{5.5}$$

Comparing Eq. (5.5) with Eq. (5.4) we observe that the ambiguity function and the OTF are related as follow:

$$H(u, W_{20}) = \frac{1}{2} AP\left(u, \frac{2W_{20} u}{\lambda}\right) \, . \tag{5.6}$$

Thus, except for the factor $1/2$, a slice of the ambiguity function along the line $t = 2W_{20}u/\lambda$ provides the OTF for the defocus value W_{20}. Hence the ambiguity function of the generalised pupil function is a polar representation of the OTF with defocus as variable [71]. The ambiguity function can be seen as a generalisation of the OTF since it characterises completely the behaviour of the OTF with respect to defocus. Note the ambiguity function is closely related to the Wigner distribution function [73, 74] and both have been used to simplify greatly the image formation formalism under partially coherent light [75, 76]. It is important to note that the analysis of two-dimensional optical systems with the ambiguity function is limited to rectangularly separable, or circularly symmetric pupil functions [60, 63].

5.2.2 Phase mask design for extending the depth of field

In this section we seek to establish the optimum phase filter for extending the DoF. The choice of phase-only filters is guided by the objective of maximising the light gathering and resolution.

Reducing the sensitivity of the ambiguity function to defocus

One approach to designing phase-only filters for enhanced depth of field is to minimise the variation of the amplitude of the ambiguity function with respect to defocus. For the sake of completeness we summarise here the main steps of the derivation leading to the phase mask design and described in [26].

The generalised pupil function $P(\xi)$ of phase-only filters is described as:

$$P(\xi) = \begin{cases} \exp[j\theta(\xi)] & \text{If } |\xi| \leq 1 \\ 0 & \text{otherwise} \end{cases} \tag{5.7}$$

where $\theta(\xi)$ is the phase delay profile to be determined. The ambiguity function of this pupil function is obtained by substituting Eq. (5.7) into Eq. (5.5):

$$\mathrm{A}P(u,t) = \int_{-1+|u|/2}^{1-|u|/2} \exp[j\theta(\xi + u/2)] \exp[-j\theta(\xi - u/2)] \exp[j2\pi t\xi] \, \mathrm{d}\xi \,. \tag{5.8}$$

Developing the phase profile $\theta(\xi + u/2)$ and $\theta(\xi - u/2)$ into their Taylor series, Eq. (5.8) becomes:

$$\mathrm{A}P(u,t) = \int_{-1+|u|/2}^{1-|u|/2} \exp[jp(\xi)] \exp[j2\pi t\xi] \, \mathrm{d}\xi \qquad \text{for} \quad |u| \leq 2 \,, \tag{5.9}$$

with $p(\xi)$ given by:

$$p(\xi) = 2\left[\theta'(\xi)\left(\frac{u}{2}\right) + \frac{1}{3!}\theta^{(3)}(\xi)\left(\frac{u}{2}\right)^3 + ... + \frac{1}{(2n+1)!}\theta^{(2n+1)}(\xi)\left(\frac{u}{2}\right)^{2n+1}\right], \tag{5.10}$$

and where $\theta'(\xi)$ and $\theta^{(n)}(\xi)$ denote the first and n^{th} derivative of $\theta(\xi)$ relative to ξ respectively. The integral in Eq. (5.9) can be approximated by mean of the stationary phase principle [31]. This principle states that for each value of t the rate of change in $p(\xi)$ is very different from the rate of change in the term $2\pi t\xi$ for most values of ξ, thus giving no net contribution to the integral value. Contribution to the integral will occur when the two phases have similar rate of change, which occurs at the stationary point denoted ξ_s, such that:

$$\left.\frac{\partial p(\xi)}{\partial \xi}\right|_{\xi_s} + 2\pi t = 0 \,. \tag{5.11}$$

We assume that the stationary point is unique and that $p(\xi)$ has some degree of smoothness. Thus Eq. (5.9) can be rewritten as:

$$\mathrm{A}P(u,t) \approx \exp[j\left(p(\xi_s) + 2\pi t\xi_s\right)] \int_{-\infty}^{\infty} \exp\left[j\frac{1}{2}p''(\xi_s)(\xi - \xi_s)^2\right] \, \mathrm{d}\xi \,, \tag{5.12}$$

where $p''(\xi_s)$ denotes the second derivative of $p(\xi)$ with respect to ξ evaluated at ξ_s. The Gaussian integral in Eq. (5.12) can be determined analytically and one can show that $\mathrm{A}P(u,t)$ is approximated as:

$$\mathrm{A}P(u,t) \approx \frac{1}{2}\sqrt{\frac{2\pi}{|p''(\xi_s)|}} \exp[j\,(p(\xi_s) + 2\pi t\xi_s)]\,. \tag{5.13}$$

Differentiating Eq. (5.11) with respect to t we obtain:

$$\left.\frac{\partial^2 p(\xi)}{\partial \xi^2}\frac{\partial \xi}{\partial t}\right|_{\xi_s} + 2\pi = 0\,, \tag{5.14}$$

$$\left.\frac{\partial \xi}{\partial t}\right|_{\xi_s} = -\frac{2\pi}{p''(\xi_s)}\,. \tag{5.15}$$

Eq. (5.13) shows that the amplitude of $\mathrm{A}P(u,t)$ is independent of the parameter t if $p''(\xi_s)$ is itself independent of t. This is the constraint applied in [26] to increase the DoF of the system. Eq. (5.15) shows that this condition is satisfied if there is a linear relationship between ξ_s and t. Consequently, there must also be a linear relationship between $p'(\xi_s)$ and ξ_s. Implementing this relationship into Eq. (5.10) we obtain:

$$\begin{aligned} p'(\xi) &= 2\left[\theta''(\xi)\left(\frac{u}{2}\right) + \frac{1}{3!}\theta^{(4)}(\xi)\left(\frac{u}{2}\right)^3 + ... + \frac{1}{(2n+1)!}\theta^{(2n+2)}(\xi)\left(\frac{u}{2}\right)^{2n+1}\right]\,, \\ &= a_1\xi + a_0\,. \end{aligned} \tag{5.16}$$

$\theta(\xi)$ represents the solution to this differential equation. By differentiating Eq. (5.16) twice with respect to ξ we obtain a polynomial in u that must be equal to zero for all u. This is only possible if all the coefficients $\theta^{(4)}(\xi)$, $\theta^{(6)}(\xi)$, ...,$\theta^{(2n+4)}(\xi)$ are null. Hence Eq. (5.16) reduces to a second order differential equation:

$$\theta''(\xi) = a_1\xi + a_0\,, \tag{5.17}$$

where the dependance on u was implicitly included in the coefficients a_1 and a_0. Eq. (5.17) is straightforward to solve, and $\theta(\xi)$ is therefore given by a third order polynomial:

$$\theta(\xi) = a_3\xi^3 + a_2\xi^2 + a_1\xi + a_0\,, \tag{5.18}$$

with $a_3 \neq 0$. As mentioned in [29], the coefficient a_2 can be neglected since it represents a defocus term to which the ambiguity function was designed to be independent. The coefficients a_1 and a_0 represent the tilt, and thickness of the phase filter respectively

and can be set to zero as they have no physical interest. Consequently it is shown that the optimal phase mask that minimises the sensitivity to defocus of the modulation transfer function (MTF) of the system is simply described as:

$$\theta(\xi) = a_3\xi^3\,, \tag{5.19}$$

where a_3 controls the amplitude of the phase delay function and is usually expressed in terms of λ:

$$a_3 = \frac{2\pi\alpha}{\lambda}\,, \tag{5.20}$$

with the parameter α controlling the optical path difference introduced by the phase mask expressed in spatial units. Combining the expression of the phase mask in Eq. (5.19) with Eq. (5.10) to solve Eq. (5.11) one easily obtains an approximation of the ambiguity function of the cubic phase mask:

$$\mathrm{AP}(u,t) \approx \frac{1}{2}\sqrt{\frac{\pi}{3|a_3 u|}}\exp\left[-j\frac{\pi^2 t^2}{3a_3 u}\right]\exp\left[j\frac{a_3 u^3}{4}\right]\,, \tag{5.21}$$

with $u \neq 0$. Note that the expression of the phase mask in Eq. (5.19) can be readily extended to rectangularly separable two-dimensional systems:

$$\theta(\xi,\eta) = a_3(\xi^3 + \eta^3)\,. \tag{5.22}$$

Although not valid for circular apertures, this result has been used to justify cubic phase masks with such apertures since they are almost universally found in optical systems. Such phase masks actually exhibit greater imaging performances, perhaps due to an apodising effect of the circular aperture.

The limits of this approach reside in the fact that although the amplitude term in Eq. (5.21) is independent of t, and therefore of W_{20}, the exact expression of $\mathrm{AP}(u,t)$ actually shows significant variations in amplitude with respect to t beyond a certain value, thereby limiting the depth of field. Another limitation is the variation of the phase term in Eq. (5.21) with t^2. Note that these phase variations decrease with the amplitude of the phase delay function a_3. These variations imply that the phase of the defocused OTF can not be perfectly compensated with a single restoration filter based on the OTF at $W_{20} = 0\lambda$, and that the residual phase error will create artifacts in the restored images.

Pupil phase engineering

Building on the work of Dowski and Cathey [26] proposing the purely cubic phase mask, higher order polynomials pupil functions have been considered. Prasad *et al.* [27] coined the term pupil phase engineering for the numerical optimisation of these polynomial coefficients with regard to two competing terms: the system sensitivity to defocus and its image restorability. The image restorability term penalises solutions with excessively low OTF. Thus convergence to an infinitely strong phase mask is prevented and the tradeoff between defocus invariance and restorability is addressed. This last point will be further discussed in section 5.4.1.

In [27] the sensitivity of the system to defocus is analysed in the spatial domain via the PSF rather than in the spatial frequency domain with the OTF. Desirable properties of the phase filters have been proposed to limit the search space of $\theta(\xi, \eta)$. Assuming that the filter be optimised equally relative to ξ and η, then it must be invariant under an $\xi \leftrightarrow \eta$ exchange operation. The phase filter can also be required to be odd, i.e. $\theta(-\xi, -\eta) = -\theta(\xi, \eta)$, so that the Taylor expansion of the PSF, and OTF, with respect to W_{20} has only even power terms. Hence the generalised cubic phase profile to be optimised is now of the form [27]:

$$\theta(\xi, \eta) = a_0(\xi^3 + \eta^3) + a_1(\xi^2\eta + \xi\eta^2). \qquad (5.23)$$

Higher order cubic-pentic polynomials have also been considered in [27, 28, 65]. Similarly to Eq. (5.20), a_0 and a_1 are expressed in terms of the wavelength λ:

$$a_0 = \frac{2\pi\alpha}{\lambda}, \quad a_1 = \frac{2\pi\beta}{\lambda}. \qquad (5.24)$$

The generalised cubic phase mask is often referred to as the petal phase mask because of its profile, shown in Figure 5.1 with a square aperture. The even parity of the PSF and OTF with respect to defocus for odd parity pupil phase functions can be proven by looking at the expression of their PSF. For clarity we describe below the expression of a one-dimensional PSF, but the expression readily extends to two-dimensional systems. The PSF $h(x; W_{20})$ of an incoherent system can be expressed as the square modulus of the coherent impulse response $\hat{P}(x; W_{20})$:

$$h(x; W_{20}) = \left| \hat{P}(x; W_{20}) \right|^2, \qquad (5.25)$$
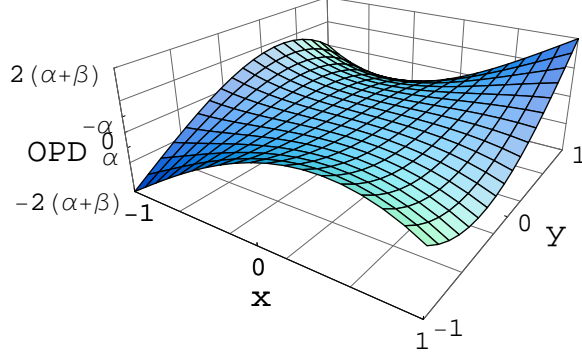
Figure 5.1: *OPD of the rectangularly separable generalised cubic phase mask with parameters α and β.*

with $\hat{P}(x; W_{20})$ equal to the Fourier transform of the generalised pupil function:

$$\hat{P}(x; W_{20}) = \frac{1}{\lambda f \sqrt{A}} \int_{-\infty}^{+\infty} p(\xi) \exp\left[j \left\{ \frac{2\pi}{\lambda} \left(-\frac{a}{f} \xi x + W_{20} \xi^2 \right) + \theta(\xi) \right\} \right] \, d\xi, \quad (5.26)$$

where f is the focal length of the system, a and A are the half width and length of the aperture respectively. Thus if $\theta(\xi)$ is odd, combining Eq. (5.25) and (5.26) one obtains:

$$h(x; W_{20}) = \frac{1}{A^2} \int_{-\infty}^{+\infty} \int_{-\infty}^{+\infty} p(\xi) p(\eta) \cos\left[\frac{2\pi}{\lambda} W_{20}(\xi^2 - \eta^2) \right]$$
$$\cos\left[-\frac{2\pi}{\lambda} \frac{a}{f} x(\xi - \eta) + \theta(\xi) - \theta(\eta) \right] \, d\xi \, d\eta. \quad (5.27)$$

Eq. (5.27) shows that the PSF depends on the cosine of the defocus parameter, and therefore exhibits only even power terms in its Taylor expansion at $W_{20} = 0\lambda$. This is also valid for the OTF of such pupil functions. Hence the OTF around $W_{20} = 0$ can be approximated as:

$$H(u; W_{20}) \approx H(u; 0) + \left. \frac{\partial^2 H(u; W_{20})}{\partial W_{20}^2} \right|_{W_{20}=0} \frac{W_{20}^2}{2}. \quad (5.28)$$

We remind that the phase mask design require us to define a metric of the sensitivity of the system to defocus. Metrics such as the Strehl ratio S_R have been proposed to quantify the sensitivity of the system to defocus. This metric is however fundamentally limited by the wealth of information disregarded. Indeed, as is the case for the purely cubic phase mask which ignores the variation with defocus of the phase transfer function, the Strehl ratio only accounts for the on-axis value of the PSF. A metric based on

the Fisher-information answers that shortcoming [27] but involves heavy computations. Suitable metrics for an implementation in numerical optimisation algorithms must be computationally efficient. One can think of a simple approach where the OTF is computed at different values of W_{20} over a given range. A meaningful metric of the sensitivity to defocus could be defined as the average of the L^2 norm of $H(u; W_{20}) - H(u; 0)$ over this range of defocus values. Unfortunately, such a metric is computationally heavy, since many two-dimensional OTF have to be computed, and can not realistically be implemented in an optimisation algorithm. Recently however an efficient computation method that approximates the L^2 norm of $H(u; W_{20}) - H(u; 0)$ has been described in [28, 65]. From Eq. (5.28) the L^2 norm of the error $H(u; W_{20}) - H(u; 0)$ can be approximated as:

$$||H(u; W_{20}) - H(u; 0)|| \approx M \frac{W_{20}^2}{2}, \tag{5.29}$$

with:

$$M = \left\| \frac{\partial^2 H(u; W_{20})}{\partial W_{20}^2} \bigg|_{W_{20}=0} \right\|. \tag{5.30}$$

We recall that the L^p norm of a vector $x = [x_1, x_2, ..., x_n]$ is defined as:

$$||x||_p = \left(\sum_{i=1}^{n} |x_i|^p \right)^{1/p}. \tag{5.31}$$

It was shown in [28] that the metric M in Eq. (5.30) accurately describes the sensitivity of the OTF for values of W_{20} up to 1.5λ. Beyond this value of W_{20} the quartic term in the Taylor expansion can be included in the metric to increase its accuracy. Most importantly, this metric accounts for both amplitude and phase variations of the OTF with defocus. This represents a fundamental improvement over the analytical approach previously described, where variations with defocus in the phase of the ambiguity function were neglected. In addition, M can be computed very efficiently. The derivation of the efficient computation of M is given in [28] and is reported here for the slightly simplified case of odd pupil phase functions that concerns us. This metric derives from applying Parceval's relation to Eq. (5.5). Thus it is shown in [77] that $AP(u, t)$ can equally be written as:

$$AP(u, t) = \int_{-\infty}^{+\infty} \hat{P}(x + t/2)\hat{P}^*(x - t/2)e^{-j2\pi ux} \, dx, \tag{5.32}$$

$$AP(u, t) = A\hat{P}(t, -u), \tag{5.33}$$

where the role of the variables t and u has been exchanged compared with Eq. (5.5). Combining Eq. (5.6) and Eq. (5.32) we obtain a new form of the OTF:

$$H(u; W_{20}) = \frac{1}{2} A \hat{P}\left(\frac{2W_{20}u}{\lambda}, -u\right), \qquad (5.34)$$

which can be expanded to:

$$H(u; W_{20}) = \frac{1}{2} \int_{-\infty}^{+\infty} \hat{P}\left(x + \frac{2W_{20}u}{\lambda}\right) \hat{P}^*\left(x - \frac{2W_{20}u}{\lambda}\right) \exp[-j2\pi ux]\, dx. \qquad (5.35)$$

The relationships between the quantities $P(\xi, \eta)$, $\hat{P}(x, y; W_{20})$, $h(x, y; W_{20})$ and $H(u, v; W_{20})$ are summarised in Figure 5.2. Differentiating Eq. (5.35) twice with respect to W_{20},
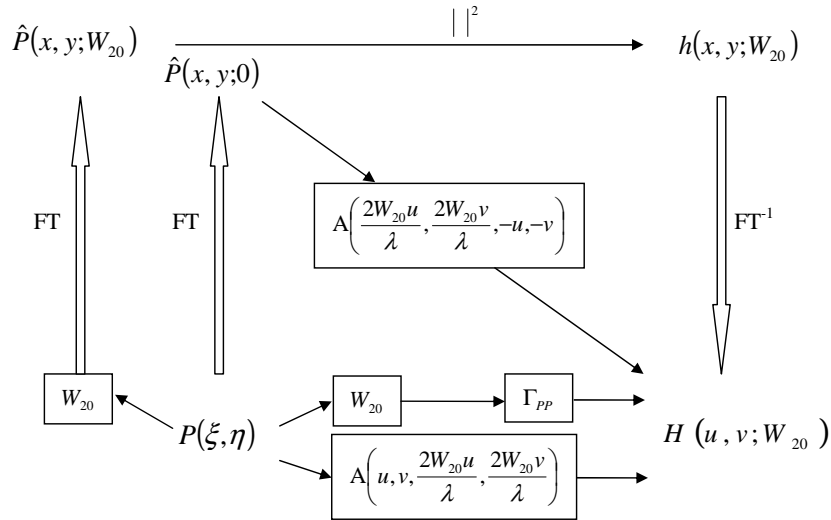
Figure 5.2: *Relationships between $P(\xi, \eta)$, $\hat{P}(x, y; W_{20})$, $h(x, y; W_{20})$ and $H(u, v; W_{20})$. Γ_{PP} denotes the autocorrelation operator, FT and FT^{-1} denote the two-dimensional Fourier and inverse Fourier transforms respectively, the block labelled W_{20} denotes a multiplication by the term $\exp[j2\pi W_{20}(\xi^2 + \eta^2)/\lambda]$. $||^2$ denotes the square modulus operator.*

and evaluating the resulting function at zero defocus yields:

$$\frac{\partial^2 H(u; 0)}{\partial W_{20}^2} = \left(\frac{u}{2\pi}\right)^2 \int_{-\infty}^{+\infty} \mathcal{P}(x) \exp[-j2\pi ux]\, dx, \qquad (5.36)$$

where $\partial^2 H(u; 0)/\partial W_{20}^2$ denotes the second derivative of $H(u; W_{20})$ with respect to W_{20} and evaluated at $W_{20} = 0$, and with:

$$\mathcal{P}(x) = \hat{P}^*(x)\frac{\partial^2 \hat{P}(x)}{\partial x^2} - 2\frac{\partial \hat{P}(x)}{\partial x}\frac{\partial \hat{P}^*(x)}{\partial x} + \hat{P}(x)\frac{\partial^2 \hat{P}^*(x)}{\partial x^2}. \qquad (5.37)$$

One recognises in Eq. (5.36) the Fourier transform of $\mathcal{P}(x)$, denoted as $\hat{\mathcal{P}}(u)$. Eq. (5.36) readily extends to two-dimensional systems [65]:

$$\frac{\partial^2 H(u,v;0)}{\partial W_{20}^2} = \left(\frac{u}{2\pi}\right)^2 \hat{\mathcal{P}}_{x,x}(u,v) + \left(\frac{v}{2\pi}\right)^2 \hat{\mathcal{P}}_{y,y}(u,v) + \frac{uv}{2\pi^2}\hat{\mathcal{P}}_{x,y}(u,v), \qquad (5.38)$$

where the circumflex denotes a two-dimensional Fourier transform. For the special case of hermitian pupil functions $P(\xi,\eta)$ (i.e. odd phase function), $\hat{P}(x,y)$ is real. Thus $\mathcal{P}_{d,d}(x,y)$ for $d=x$ or $d=y$, and $\mathcal{P}_{x,y}(x,y)$ reduce to:

$$\mathcal{P}_{d,d}(x,y) \;=\; 2\left[\hat{P}(x,y)\frac{\partial^2 \hat{P}(x,y)}{\partial d^2} - \left(\frac{\partial \hat{P}(x,y)}{\partial d}\right)^2\right], \qquad (5.39\text{a})$$

$$\mathcal{P}_{x,y}(x,y) \;=\; 2\left[\hat{P}(x,y)\frac{\partial \hat{P}(x,y)}{\partial x \partial y} - \frac{\partial \hat{P}(x,y)}{\partial x}\frac{\partial \hat{P}(x,y)}{\partial y}\right]. \qquad (5.39\text{b})$$

Eq. (5.38) enables one to visualise instantly the sensitivity to defocus of the OTF for any odd pupil phase function. Thus it can be considered to serve the same purpose as the ambiguity function, but extended to two-dimensional systems. Furthermore Eq. (5.38) can be computed very efficiently with only four fast Fourier transforms (FFT).

In our implementation of Eq. (5.38), the derivatives are calculated via convolution with a 3x1 derivative of gaussian filter, normalised for unit energy, instead of the finite difference approximation advised in [28], in order to maintain symmetry. Figure 5.3 shows the MTF of a DL system, and the pupil functions $(\alpha,\beta)=(2.5,0)$ and $(\alpha,\beta)=(3.39,-10.17)$ at $W_{20}=0\lambda$ and $W_{20}=1\lambda$. These two pupil functions have been selected here because they model phase masks that we have implemented in an optical microscope, and will be further discussed in Chapter 6. Note that the MTF varies significantly less between $W_{20}=0\lambda$ and $W_{20}=1\lambda$ with the two phase masks than in the DL system. In Figure 5.4 we present the second derivative of the OTF with respect to defocus for the same pupil functions, calculated with Eq. (5.38). These graphs are a good approximation of $|H(u,v;W_{20})-H(u,v;0)|$ for $W_{20}\leq 1.5\lambda$. Attention should be paid to the difference in intensity scale which illustrates again the reduced sensitivity to defocus of these pupil functions relative to that of the DL system.

As mentioned previously, Prasad proposed to add a regularisation term to the defocus sensitivity metric to minimise in order to avoid convergence to infinitely strong
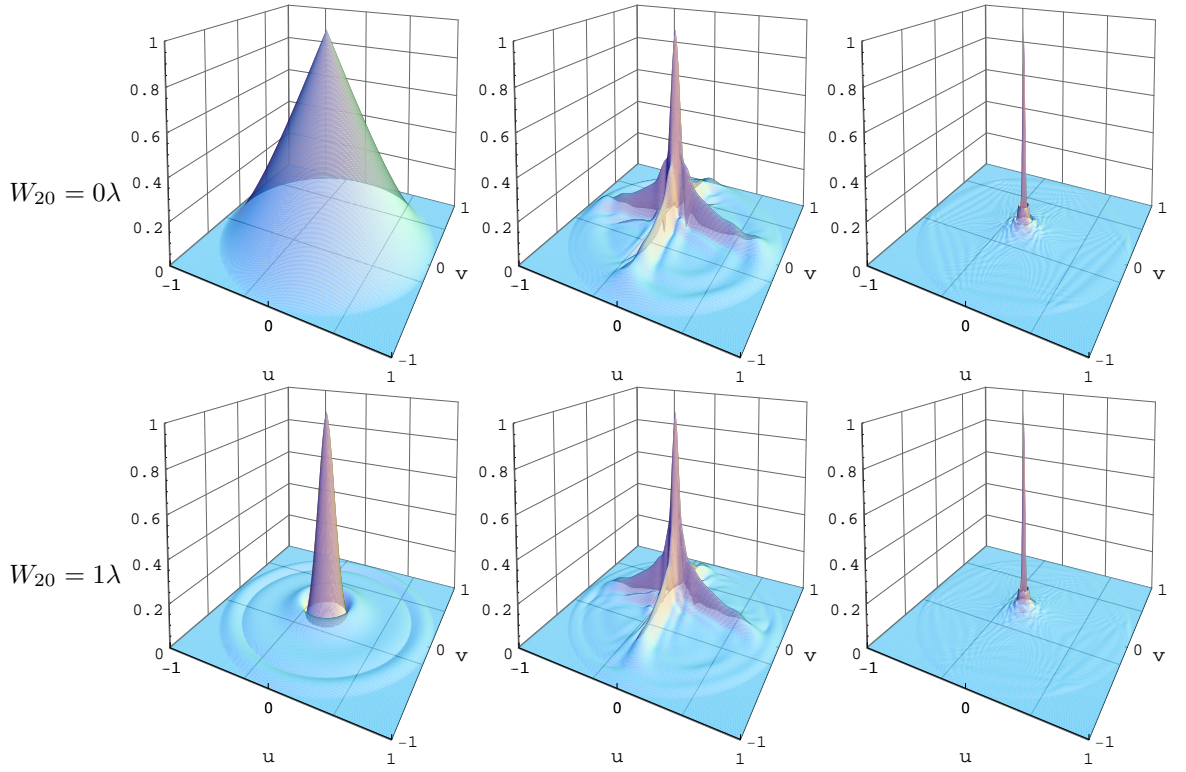
Figure 5.3: *MTF of different pupil functions. From left to right: diffraction limited system, $(\alpha, \beta) = (2.5, 0)$ and $(\alpha, \beta) = (3.39, -10.17)$. Top row: $W_{20} = 0\lambda$, bottom row: $W_{20} = 1\lambda$.*
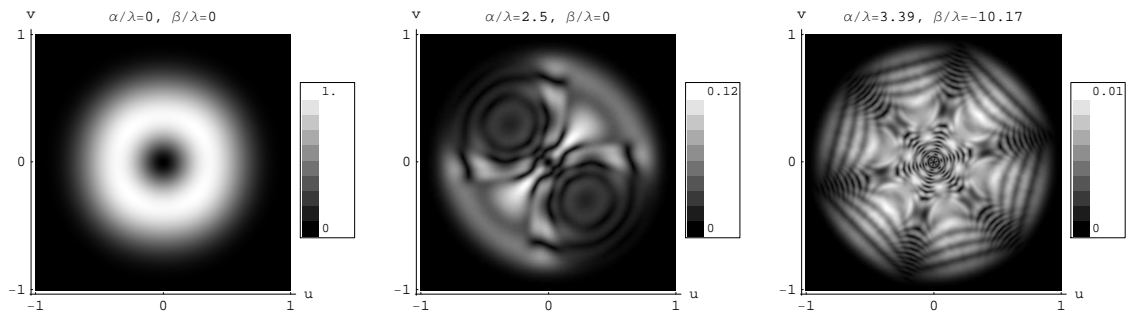
Figure 5.4: *Normalised absolute value of the second derivative of the OTF with respect to defocus for different pupil functions.*

phase masks [27]. Such phase masks are not desirable because the higher the parameters α and β, the greater the attenuation of the OTF. This attenuation determines the amplification of spatial frequencies that must be performed during the image restoration. Since noisy signals at amplified frequencies can not be separated from the object spectrum, these spurious signals will also be amplified and will degrade the quality of restored images. We therefore use a Wiener filter to restore the images and will further describe this filter later on. Nevertheless, the tradeoff between defocus invariance and image restorability must be accounted for. This can be accomplished by including a term that penalises phase masks with unacceptably attenuated OTF. Hence the cost function $C_\Psi(a_0, a_1)$ to minimise is expressed as:

$$C_\Psi(a_0, a_1) = M(a_0, a_1) + P_\Psi(a_0, a_1),\tag{5.40}$$

where $M(a_0, a_1)$ is the metric of the sensitivity of the system to defocus and $P_\Psi(a_0, a_1)$ is the regularisation term, sometimes referred to as the penalty term. We use the Fermi-Dirac regularisation function as proposed in [27]:

$$P_\Psi(a_0, a_1) = K(1 - \Psi(a_0, a_1))\frac{1}{\exp(\eta(\Psi(a_0, a_1) - \Psi_0)) + 1},\tag{5.41}$$

where $\Psi(a_0, a_1)$ is the metric of restorability, Ψ_0 is the minimum acceptable value of this metric, K and η define the amplitude and slope of the penalty function respectively.

A commonly employed metric of restorability is the in-focus Strehl ratio S_R [27, 28, 65], defined as the axial value of the PSF of the in-focus optical system to that of a diffraction limited system with similar aperture size and $F_{/\#}$. Note this definition differs from that of $S(W_{20})$ in Eq. (4.7). This is justified because we now seek to measure the image restorability whereas $S(W_{20})$ measures the sensitivity of the system to defocus. We will discuss other metrics of restorability in the next section and show that it has a significant impact on the design of the phase mask.

5.2.3 Phase mask optimisation results

In this section we 1) detail the optimisation procedure, 2) discuss various image restorability metrics and 3) present the results of the optimisation. In particular we will show that purely cubic phase masks and petal phase masks with $\beta = -3\alpha$ provide a good

tradeoff between defocus invariance and image restorability depending on the metric of restorability.

Because the (α, β) search space exhibits multiple local minimum we randomly generate the starting points of a local minimisation algorithm (Quasi-Newton). We use the FindMinimum function in Mathematica to perform the Quasi-Newton minimisation at each of these starting points. Each local minimisation therefore converges to a local optimum in the (α, β) plane. The global optimum is calculated as the one point among these local optimum that minimises C_Ψ. Note that the algorithm is restricted to values of α and β within the $[-19\lambda, 19\lambda]$ range. Figure 5.5 displays the metric M at the random starting positions of the local optimisation, where defocus sensitivity is color coded and increases from blue to red. Figure 5.6 shows the values of Ψ, P_Ψ and C_Ψ at these starting points ($K = 0.1$, $\eta = 500$, $\Psi_0 = 10^{-3}$). For $\Psi = S_R$, left column of Figure 5.6, the penalty term P_Ψ strongly penalises purely cubic phase masks, yielding comparatively better phase masks around the line $\beta = -3\alpha$. Indeed the graph of C_Ψ, shown on the bottom left of Figure 5.6, exhibits a valley along the line $\beta = -3\alpha$ and the global optimum is found to be close to this line:

$$\alpha = 3.423\lambda, \qquad \beta = -13.754\lambda. \tag{5.42}$$

This result is in good agreement with the results presented in [27], where the solution $(\alpha, \beta) = (5.2, -16.2)$ is also close to the $\beta = -3\alpha$ line. The difference in the solutions found is due to different settings for the minimum acceptable Strehl ratio. These results strongly indicate that phase masks with $\beta = -3\alpha$ provide a good compromise between defocus invariance and image restorability. In Chapter 6 we will implement the phase mask $(\alpha/\lambda, \beta/\lambda) = (3.39, -10.17)$ in an optical microscope to extend its DoF. This phase mask is designed so that $\beta = -3\alpha$ and was readily available at the time the microscope was being developed. Note however that it is close in performances and design to the phase mask $(\alpha/\lambda, \beta/\lambda) = (3.423, -13.754)$, as is shown in Figures 5.4 and 5.8 and Table 5.1.

We now discuss desirable properties of the metric of image restorability. In particular, we argue that the metric of image restorability should solely depend on the amplitude
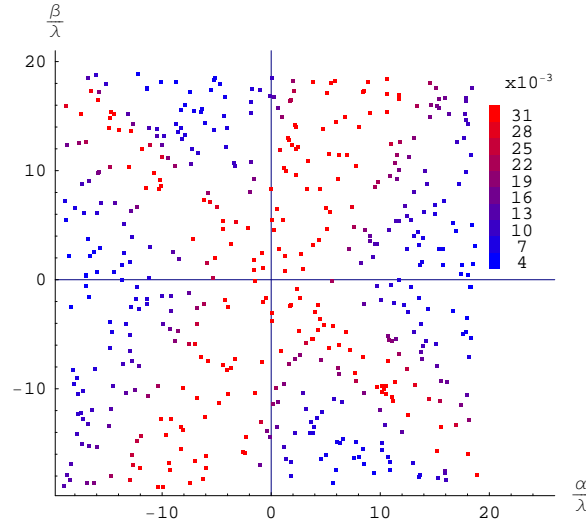
Figure 5.5: *Value of the metric M at the random starting points of the local optimisation.*

of the OTF and exclude the phase of the OTF. Indeed, the phase information can theoretically always be recovered provided that the SNR is sufficiently high. Therefore S_R may be biased by phase effects since we have $S_R \propto \int H(u)\,\mathrm{d}u$. For instance, S_R will underestimate the restorability of purely cubic phase masks because of the lateral shift of the peak PSF value they introduce. Consequently we argue that the design of phase masks whose penalty term includes S_R are suboptimal. It may be preferable instead to use the normalised L^2 norm of the PSF or OTF:

$$
E = \frac{\displaystyle\int_{-\infty}^{+\infty} |H(u;0)|^2\,\mathrm{d}u}{\displaystyle\int_{-\infty}^{+\infty} |H_{\mathrm{dl}}(u;0)|^2\,\mathrm{d}u} = \frac{\displaystyle\int_{-\infty}^{+\infty} |h(x;0)|^2\,\mathrm{d}x}{\displaystyle\int_{-\infty}^{+\infty} |h_{\mathrm{dl}}(x;0)|^2\,\mathrm{d}x}, \tag{5.43}
$$

where $h_{\mathrm{dl}}(x;0)$ and $H_{\mathrm{dl}}(u;0)$ denote the in-focus diffraction limited PSF and OTF respectively. In place of E one may employ $\sqrt{E}$ to be more consistent with the definition of the metric M. Another metric, denoted E_2, similar to $\sqrt{E}$ is based on the L^2 norm of the ratio of the in-focus MTF to the DL MTF:

$$
E_2 = \sqrt{\int_{-\infty}^{+\infty} \frac{|H(u;0)|^2}{|H_{\mathrm{dl}}(u;0)|^2}\,\mathrm{d}u}\,. \tag{5.44}
$$

These metrics have closely related definitions and the optimisation results they yield are unlikely to significantly differ from one another, provided the parameters of the penalty function Ψ are adjusted correspondingly. The right column in Figure 5.6 displays E, its
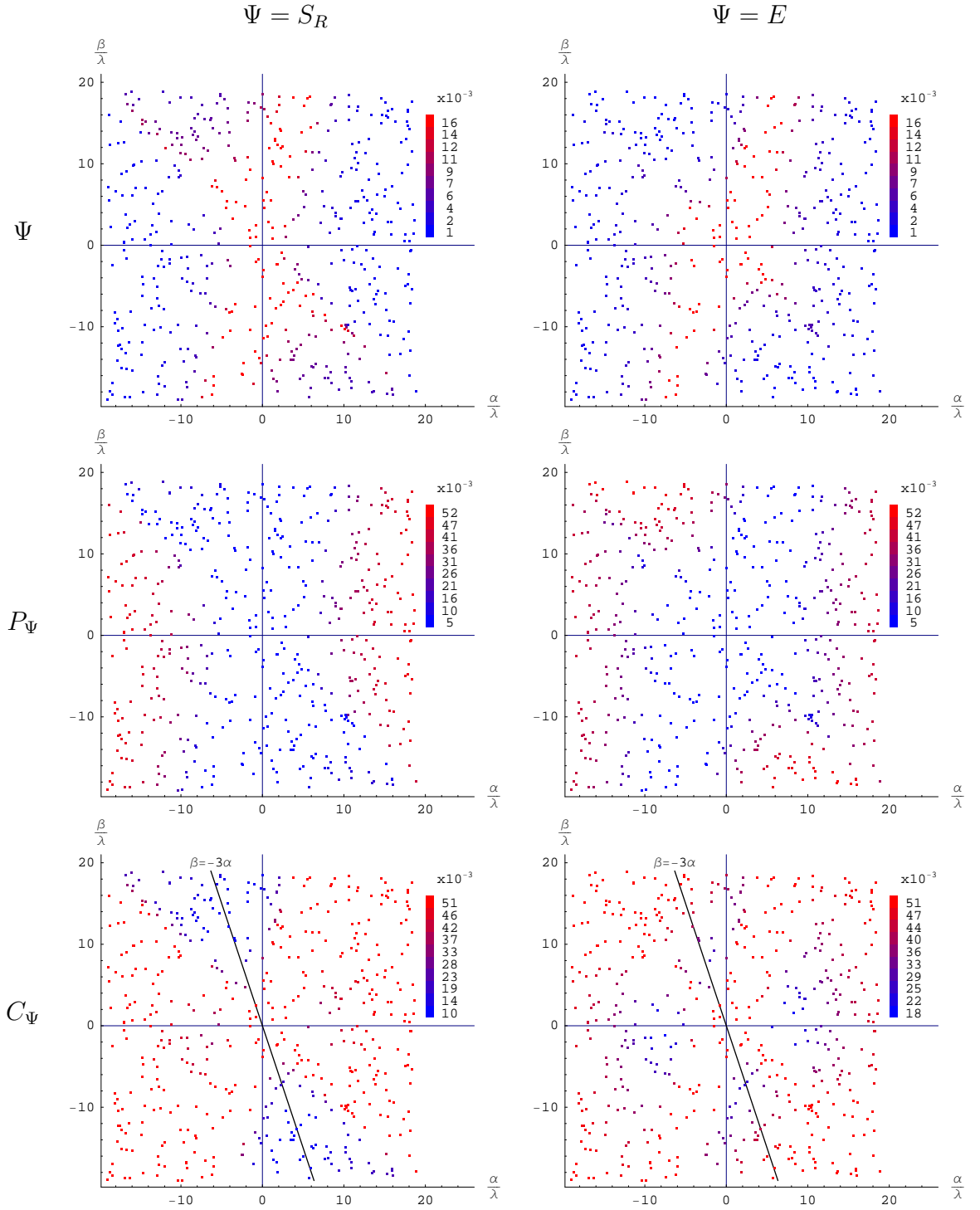
Figure 5.6: *Random starting points of the local optimisation. From top to bottom: metric of restorability Ψ, penalty term P_Ψ and cost function C_Ψ. Ψ is from left to right the Strehl ratio S_R and the normalised L^2 norm of the PSF E.*

associated penalty and cost functions P_Ψ and C_Ψ respectively. Note that the penalty P_Ψ applied to cubic phase masks is now similar to that of the petal phase masks. The optimal phase mask using $\Psi = E$ was found to be almost purely cubic:

$$\alpha = 7.247\lambda, \qquad \beta = 0.463\lambda. \tag{5.45}$$

The MTF of these two pupil functions are shown in Figure 5.7 at $W_{20} = 0\lambda$ and $W_{20} = 1\lambda$. Again, the variation of their OTF with defocus is well approximated by the second derivative of their OTF with respect to defocus, which are displayed in Figure 5.8. The parameters of these pupil functions are summarised in Table 5.1.
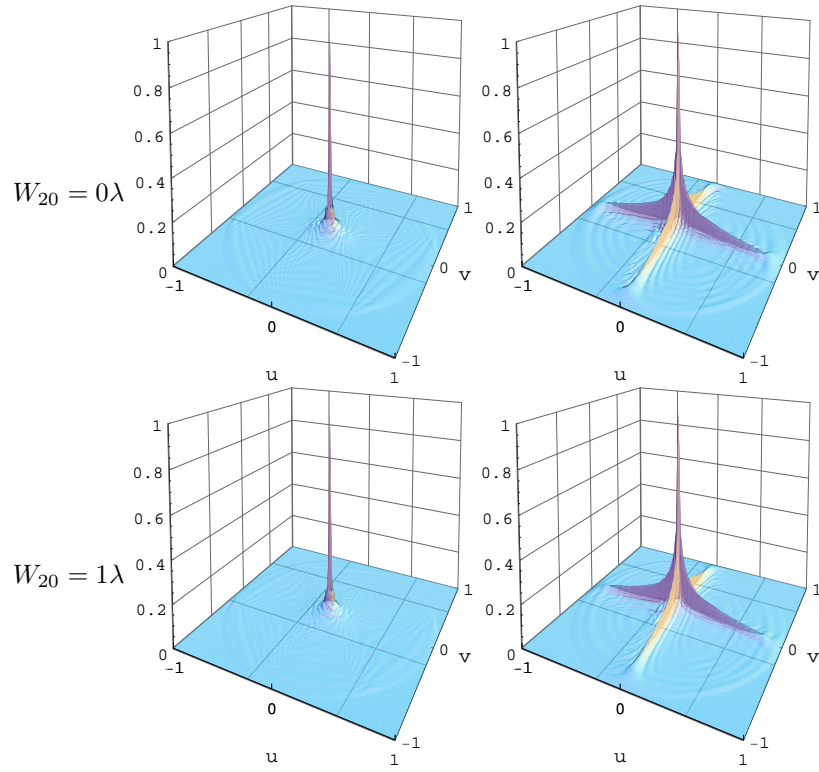
Figure 5.7: *MTF of different pupil functions. From left to right:* $(\alpha, \beta) = (3.423, -13.754)$ *and* $(\alpha, \beta) = (7.247, 0.463)$. *Top row:* $W_{20} = 0\lambda$, *bottom row:* $W_{20} = 1\lambda$.

5.3   Image restoration

We previously assumed the system to be linear in intensity because of incoherent illumination. We also assume the angular extent of the object is small enough to fall
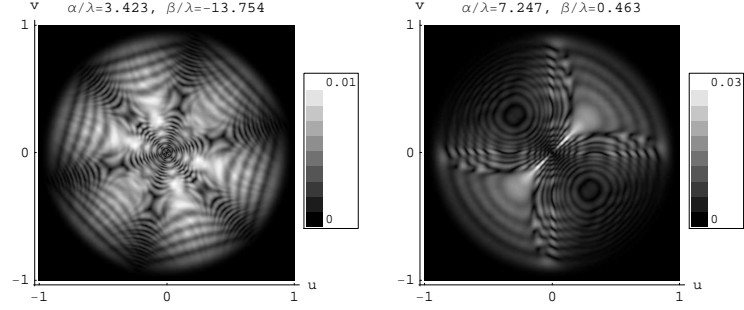
Figure 5.8: *Normalised absolute value of the second derivative of the OTF with respect to defocus for different pupil functions.*

$(\alpha/\lambda, \beta/\lambda)$	M	S_R	E	C
$(2.5, 0)$	0.07541	0.01542	0.04759	0.07541
$(3.39, -10.17)$	0.01062	0.01114	0.00347	0.03308
$(3.423, -13.754)$	0.00766	0.00898	0.00226	0.04236
$(7.247, 0.463)$	0.01460	0.00365	0.00798	0.01754

Table 5.1: *Parameters of different pupil functions defined by their coefficients $(\alpha/\lambda, \beta/\lambda)$. The metric of restorability used in C is $\Psi = E$. For a diffraction limited system $(\alpha, \beta) = (0, 0)$ all the parameters are equal to unity.*

in an isoplanatic region of the system (region over which aberrations are constant), i.e. that the PSF of the system is translation invariant [78]. Thus the image of the object formed by the system is equal, to a good approximation, to the convolution product between the object and the system PSF:

$$\mathcal{I}(x,y) = \int_{-\infty}^{+\infty} \int_{-\infty}^{+\infty} \mathcal{O}(x',y')h(x-x',y-y')\,\mathrm{d}x'\,\mathrm{d}y'\,, \tag{5.46}$$

where $\mathcal{O}(x,y)$, $\mathcal{I}(x,y)$ and $h(x,y)$ are the object, image and PSF of the system respectively. We seek to recover $\mathcal{O}(x,y)$ from the measurement of $\mathcal{I}(x,y)$ and the knowledge of $h(x,y)$. Linear estimators are commonly used in deconvolution procedures and estimate the object spectrum as the product of the image spectrum and the spectrum of a linear filter. The restored image is then obtained by taking the inverse Fourier-transform of this product:

$$\hat{\mathcal{O}}(x,y) = \frac{1}{2\pi} \int_{-\infty}^{+\infty} \int_{-\infty}^{+\infty} I(u,v)G(u,v)\exp[j2\pi(ux+vy)]\,\mathrm{d}u\,\mathrm{d}v\,, \tag{5.47}$$

where $\hat{\mathcal{O}}(x,y)$, $I(u,v)$, $G(u,v)$ are the restored image, the image spectrum and filter spectrum respectively. The Wiener filter is the optimal linear filter in the sense that it minimises the mean-square-error between the restored image spectrum $\hat{O}(u,v) = \mathrm{FT}[\hat{\mathcal{O}}(x,y)]$ and the true object spectrum $O(u,v) = \mathrm{FT}[\mathcal{O}(x,y)]$, in the presence of noise with a known power-spectral-density $|P(u,v)|^2$. Obviously $G(u,v)$ must be a function of the in-focus OTF $H(u,v;0)$, since phase masks were designed to reduce defocus sensitivity at $W_{20} = 0\lambda$. One can show that the Wiener filter is written as:

$$G(u,v) = \frac{H(u,v;0)^*}{|H(u,v;0)|^2 + \frac{|P(u,v)|^2}{|O(u,v)|^2}}\,. \tag{5.48}$$

In order to compare the quality of the deconvolved images with that of a diffraction limited (DL) system, we apodise $G(u,v)$ with a window equal to the in-focus OTF of a DL system of similar aperture size and $F_{/\#}$. This OTF, denoted as $H_{\mathrm{dl}}(\nu;0)$ where ν is the normalised radial spatial frequency coordinate such that $\nu = \sqrt{u^2 + v^2}$, is equal to the Fourier transform of the Airy disk and can be expressed as [79]:

$$H_{\mathrm{dl}}(\nu;0) = \frac{2}{\pi}\left[\arccos\left[\nu\right] - |\nu|\sqrt{1-\nu^2}\right]\,. \tag{5.49}$$

Hence the restoration filter becomes:

$$G(u,v) = \frac{H(u,v;0)^*}{|H(u,v;0)|^2 + \frac{|P(u,v)|^2}{|O(u,v)|^2}}H_{\mathrm{dl}}(\nu;0)\,. \tag{5.50}$$

Since we seek to recover the object $O(u, v)$, a good estimate of its power spectral density $|O(u, v)|^2$ is crucial in determining the quality of the restoration. A possible estimate is the power spectral density of the detected image $|I(u, v)|^2$ [80]. We found this estimate to excessively amplify certain spatial frequencies, thus leading to artificial oscillations in the restored image. Better image quality was obtained by use of a Wiener filter employing a user-defined constant noise-to-signal power ratio, i.e. $|P(u, v)|^2/|O(u, v)|^2 = K$. Thus Eq. (5.50) reduces to:

$$G(u, v) = \frac{H(u, v; 0)^*}{|H(u, v; 0)|^2 + K} H_{\mathrm{dl}}(\nu; 0) \,. \tag{5.51}$$

As it will be shown, it is convenient for Eq. (5.51) to be generalised to account for an estimate $\hat{W}_{20}$ of the defocus parameter W_{20}. Eq. (5.51) is therefore rewritten as:

$$G(u, v) = \frac{H(u, v; \hat{W}_{20})^*}{|H(u, v; \hat{W}_{20})|^2 + K} H_{\mathrm{dl}}(\nu; 0) \,. \tag{5.52}$$

It is also useful to define the absolute radial spatial frequency coordinate ν' expressed in units of cycles/mm. ν' is such that $\nu = \nu'/\nu_0$, where $\nu_0 = 1/\lambda F_{/\#}$ is the optical cutoff frequency.

5.4 Wavefront coding tradeoffs

5.4.1 Extended depth-of-field vs restorability

When designing a phase mask to extend the depth-of-field, there is a compromise between defocus invariance and image restorability. The optimisation of this tradeoff is key to the pupil-phase-engineering approach presented in section 5.2.2. Figures 5.5 and 5.6 present the defocus sensitivity metric M and the restorability metric E at uniformly distributed random locations in the (α, β) plane. These scatter-plots were chosen for computational efficiency but the sampling density enables us to highlight the conflict between these two metrics. To underline this tradeoff we pose the problem of choosing the strength of a particular type of phase mask. For cubic phase masks and petal phase masks with $\beta = -3\alpha$, this comes down to choosing the value of α. Figure 5.9 displays M and $\sqrt{E}$ versus α for these two phase masks. Observe that both metrics decrease monotonically with the phase mask strength α for both types of phase mask.

This graph therefore clearly indicates that extended depth-of-field (EDF) is achieved at the expense of a reduced SNR in the restored image. Note that for $\alpha > 1\lambda$ there is approximately a 6.4dB and 4.5dB difference in M and $\sqrt{E}$ respectively between the two types of phase masks. This means that purely cubic phase masks must have a larger α value than that of petal phase masks with an identical defocus sensitivity.
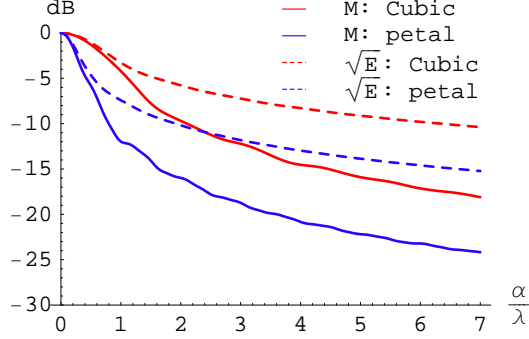
Figure 5.9: *Metrics of defocus sensitivity M and restorability $\sqrt{E}$ vs phase mask strength. dB=10log.*

5.4.2 Restored images artifacts

We have seen in Section 5.2.2 that phase masks can be designed to minimise the sensitivity of the system to defocus for a given noise level. Nevertheless, the system can only be assumed invariant to defocus in a specific range. Indeed, the defocus sensitivity metric M only tends asymptotically towards zero as the phase mask strength increases, see Figure 5.9. Outside this region, variations in the OTF become significant and have an impact on the final image quality. Variations in the MTF have little impact on the restored image quality as long as the MTF remains significantly higher than the noise level. Variations in the phase of the OTF however, create artifacts which may significantly degrade the quality of the restored images. The nature and amplitude of these artifacts naturally depend on the phase mask, the amplitude of the phase disparity and the object spectrum.

We seek here to show that, for modest values of W_{20}, the origin of the artifacts lies in variations of the phase of the OTF. To that end we consider the situation where

we successively capture the images of an object located at different distances from the focal plane of the system. We denote by $I_1(u,v)$ and $I_2(u,v)$ the spectrum of the images recorded in noise-free conditions at these two positions and denote by w_1 and w_2 the values of the defocus parameter associated with these two positions. We restore $I_1(u,v)$ with the filter given in Eq. (5.52) (with K=0) for the defocus w_2 and denote the resulting image by $\hat{O}_{12}(u,v)$. We proceed reciprocally for $I_2(u,v)$ and denote the image restored with w_1 by $\hat{O}_{21}(u,v)$. Thus the restored images can be expressed as:

$$\hat{O}_{12}(u,v) = O(u,v)\frac{|H(u,v;w_1)|}{|H(u,v;w_2)|}\exp[j\phi_{12}(u,v)], \qquad (5.53a)$$

$$\hat{O}_{21}(u,v) = O(u,v)\frac{|H(u,v;w_2)|}{|H(u,v;w_1)|}\exp[j\phi_{21}(u,v)], \qquad (5.53b)$$

with $\phi_{ij}(u,v) = \phi(u,v;w_i) - \phi(u,v;w_j)$ and $\phi(u,v;w_i)$ is the phase of the OTF at defocus w_i. Assuming that $|H(u,v;w_1)| \approx |H(u,v;w_2)|$, Eq. (5.53a) and (5.53b) reduce to $\hat{O}_{12}(u,v) \approx O(u,v)\exp[j\phi_{12}(u,v)]$ and $\hat{O}_{12}(u,v) \approx O(u,v)\exp[-j\phi_{12}(u,v)]$ respectively. Since the terms $\phi_{ij}(u,v)$ have an odd parity, the restored images $\hat{\mathcal{O}}_{12}(x,y)$ and $\hat{\mathcal{O}}_{21}(x,y)$ are the result of the convolution of the object $\mathcal{O}(x,y)$ with a real function $h_{12}(x,y)$ and $h_{21}(x,y)$ respectively:

$$h_{12}(x,y) = \mathrm{FT}^{-1}[\exp[j\phi_{12}(u,v)]], \qquad (5.54a)$$

$$h_{21}(x,y) = h_{12}(-x,-y). \qquad (5.54b)$$

Thus it is shown that if the MTF is approximately invariant between w_1 and w_2, the image artifacts in $\hat{\mathcal{O}}_{12}(x,y)$ are different from those in $\hat{\mathcal{O}}_{21}(x,y)$ but will exhibit a high degree of symmetry. We simulate the one-dimensional artifacts in the restored images of a vertical edge. Since the optical system is two-dimensional the simulation can be efficiently implemented using a one-dimensional edge and the Fourier Slice Theorem [81]. The images $\hat{\mathcal{O}}_{12}(x,y)$ and $\hat{\mathcal{O}}_{21}(x,y)$ obtained for $w_1 = \lambda$ and $w_2 = 0\lambda$ with the phase mask $(\alpha/\lambda, \beta/\lambda) = (3.39, -10.17)$ are shown in Figure 5.10. The artifacts in $\hat{\mathcal{O}}_{12}(x,y)$ and $\hat{\mathcal{O}}_{21}(x,y)$ clearly exhibit some symmetry, and show their origin to lie in the phase mismatch between the convolving OTF and the restoration filter. The images of an edge with increasing amount of defocus and restored with a filter at $W_{20} = 0$ are shown on left column of Figure 5.11, for different phase masks. The right column in Figure 5.11 shows the image of an in-focus edge restored with filters with

W_{20} varying from 0λ to 3λ. The artifacts shown in the left and right columns clearly exhibit the degree of symmetry discussed above. However when the MTF significantly varies between w_1 and w_2, the approximations in Eq. (5.54a) and (5.54b) are not valid anymore and the artifacts in $\hat{\mathcal{O}}_{12}(x,y)$ and $\hat{\mathcal{O}}_{21}(x,y)$ do not exhibit this high degree of symmetry. This is illustrated on the top row of Figure 5.11 (for the cubic phase mask $(\alpha/\lambda, \beta/\lambda) = (2.5, 0)$) where oscillations in the left and right column are clearly not symmetric anymore.
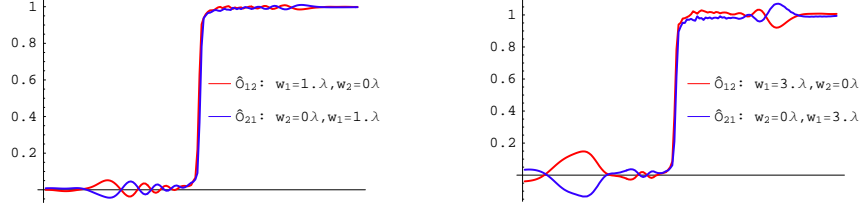
Figure 5.10: *Artifacts in restored images of an horizontal edge for the phase mask* $(\alpha/\lambda, \beta/\lambda) = (3.39, -10.17)$.

There exists a defocus effect that is specific to cubic phase masks (CPM). Using a phasor decomposition of the OTF, Muyo and Harvey obtained an approximation of the phase of the OTF $\phi(u)$ of rectangular, linearly separable cubic phase masks at low spatial frequencies [82, 29]:

$$\phi(u) = -4\pi \frac{W_{20}u}{3\alpha}, \quad \text{for } |u| < \sqrt{\frac{|W_{20}|}{3\alpha^2}}. \tag{5.55}$$

From the Fourier shift theorem one deduces that one effect of defocus for CPM is the translation of image features by a distance proportional to $W_{20}/3\alpha$. For the circular-aperture CPM an analytical expression of the phase is not readily available but the translation effect remains and can be clearly observed on Figure 5.12.

We now assess the image artifacts in two-dimensional images. The image of Lena, which has been widely employed by the image processing community, serves as a reasonable scene due to it complexity. Figure 5.13 shows the restored image of Lena obtained with different phase masks for a defocus $W_{20} = 1\lambda$, an estimated defocus $\hat{W}_{20} = 0\lambda$ and a 60dB SNR. We define the SNR in the coded images as:

$$\text{SNR} = 20\log\left(\frac{\text{Max} - \text{Min}}{\sigma}\right), \tag{5.56}$$
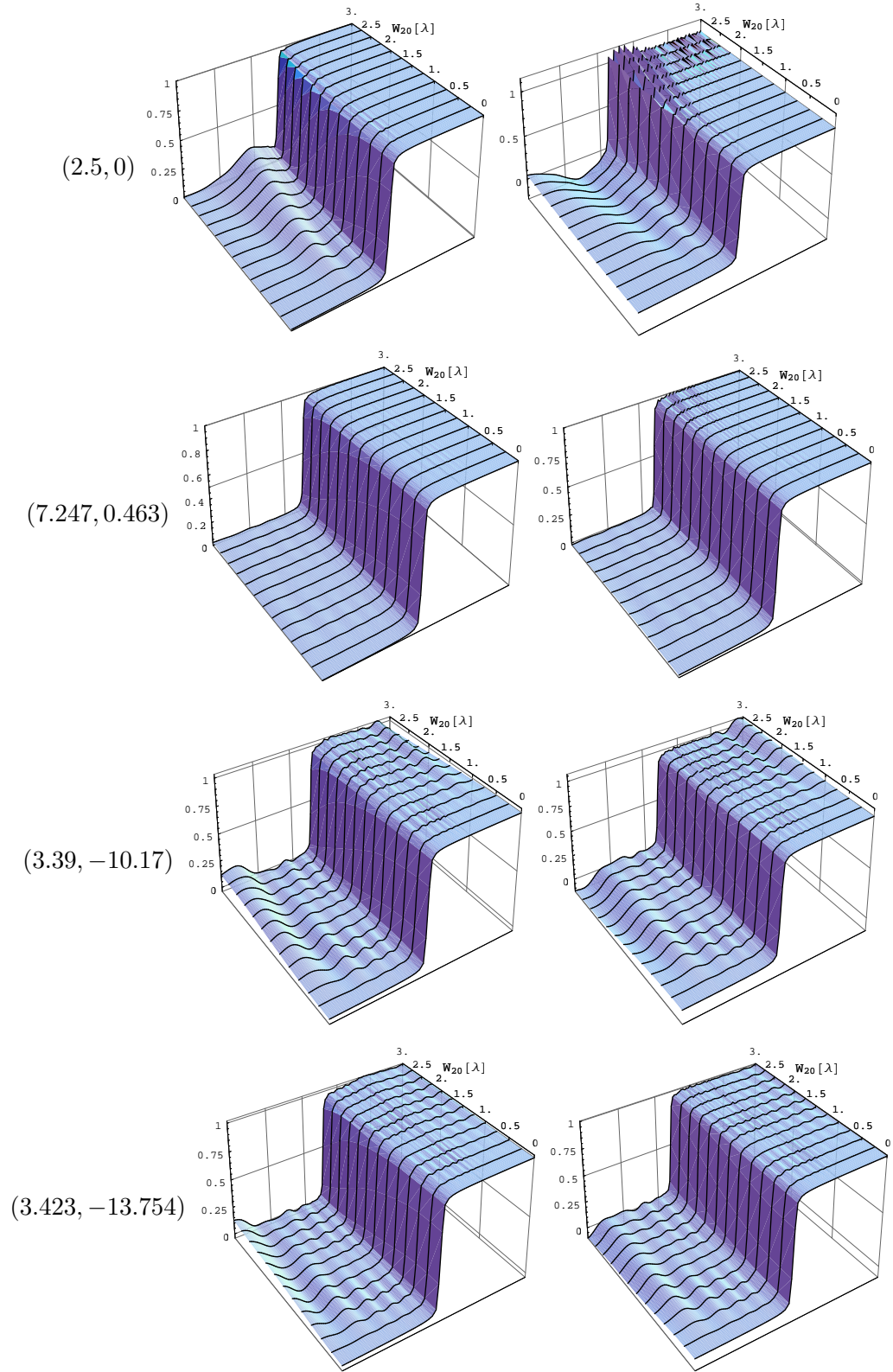
Figure 5.11: *Artifacts in restored images of a horizontal edge for different phase masks.*
Left: edge with increasing defocus restored with a single filter at $W_{20} = 0\lambda$. Right: in-
focus edge restored with various filters with increasing W_{20} values.
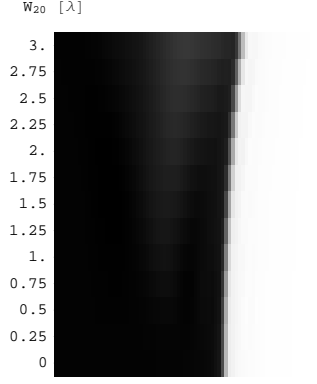
Figure 5.12: *Restored images of a vertical edge for increasing amounts of defocus and for the phase mask $(\alpha, \beta) = (2.5, 0)$. Note the translation of the position of the edge with increasing defocus.*

where σ denotes the standard deviation of the gaussian noise added to the coded image, Max and Min refer to the maximum and minimum values respectively of the coded image before noise addition. Other definitions of the SNR can be found in the literature but they yield very similar values. For instance, one could use the maximum value of the image in place of the dynamic range in Eq. (5.56). For the image of Lena, the difference between the two definitions is smaller than 0.2dB at 60dB and can be neglected. The 60dB SNR corresponds approximately to a dynamic range of 2250:1 achieved with the Hamamatsu C4742-95-12G04 camera implemented in the wavefront coded microscope described in Chapter 6. The reference image, shown in top left on Figure 5.13, is exactly recovered with any phase mask in ideal noise-free conditions when $W_{20} = \hat{W}_{20}$. The image obtained with a DL system, labelled as $(\alpha/\lambda, \beta/\lambda) = (0, 0)$, is also displayed for comparison. In this particular case the restored image is simply the convolution of the object with the defocused PSF because of the form of the Wiener filter in Eq. (5.50). For all the phase masks presented the restored images exhibit increased sharpness compared with that of a DL system with an equal amount of defocus. For the two cubic phase masks $(2.5, 0)$ and $(7.247, 0.463)$ artifacts consist of unidirectional oscillations and visible replicas near strong edge features (e.g. near the hat of Lena). The latter artifacts are dominant in images with the two petal phase masks $(3.39, -10.17)$ and $(3.423, -13.754)$. All these artifacts become more apparent as the mismatch between W_{20} and $\hat{W}_{20}$ increases. This illustrated in Figure

5.14 where the defocus effect is stronger, $W_{20} = 3\lambda$ and the estimated defocus is maintained at $\hat{W}_{20} = 0$. Despite strong image artifacts being now clearly visible for all phase masks, the image sharpness is still greatly improved relative to the DL system. Artifacts can be greatly reduced if the parameter K in Eq. (5.52) is increased. This means that the restoration filter amplifies less the spectrum of the detected image, which results in images with a reduced sharpness. Increasing K in the Wiener filter is usually associated with increasing levels of noise. We described in the previous section the tradeoff between the sensitivity to defocus and the noise level in the image. Similarly we can also see the artifacts in the restored images as another tradeoff to the depth-of-field extension.

To summarise, we have described the tradeoff between defocus sensitivity and image restorability. This tradeoff was accounted for in the phase mask design described in Section 5.2.2. Simulated images of vertical edges and two-dimensional images have demonstrated the extended DoF provided by different phase mask designs and also highlighted the presence of artifacts in the restored images. We have shown the origin of these artifacts to lie in the phase mismatch between the restoration OTF $H(u, v; 0)$ and the actual OTF $H(u, v; W_{20})$. The image quality degradation brought by these artifacts can be seen as a tradeoff to the EDF achieved in wavefront coded systems.

5.5 Estimation of defocus for artifacts removal

We seek to improve the imaging performance of wavefront- coded systems by removing the artifacts from the restored images. This can be treated as a general deconvolution problem where we assume the system is characterised, i.e. we know the OTF of the system $H(u, v; W_{20})$. There exists a plethora of general deconvolution approaches and algorithms in the literature and a comparison of their performances for wavefront coded systems is beyond the scope of this thesis. We choose to focus on removing the artifacts simply by estimating W_{20} from the artifacts in the restored image. Once an estimation $\hat{W}_{20}$ of W_{20} is available, we then deconvolve the coded image with the Wiener filter detailed in Eq. (5.52) and with the parameter $\hat{W}_{20}$.

$W_{20} = \hat{W}_{20}$	$(0,0)$	$(2.5,0)$
$(7.247, 0.463)$	$(3.39, -10.17)$	$(3.423, -13.754)$
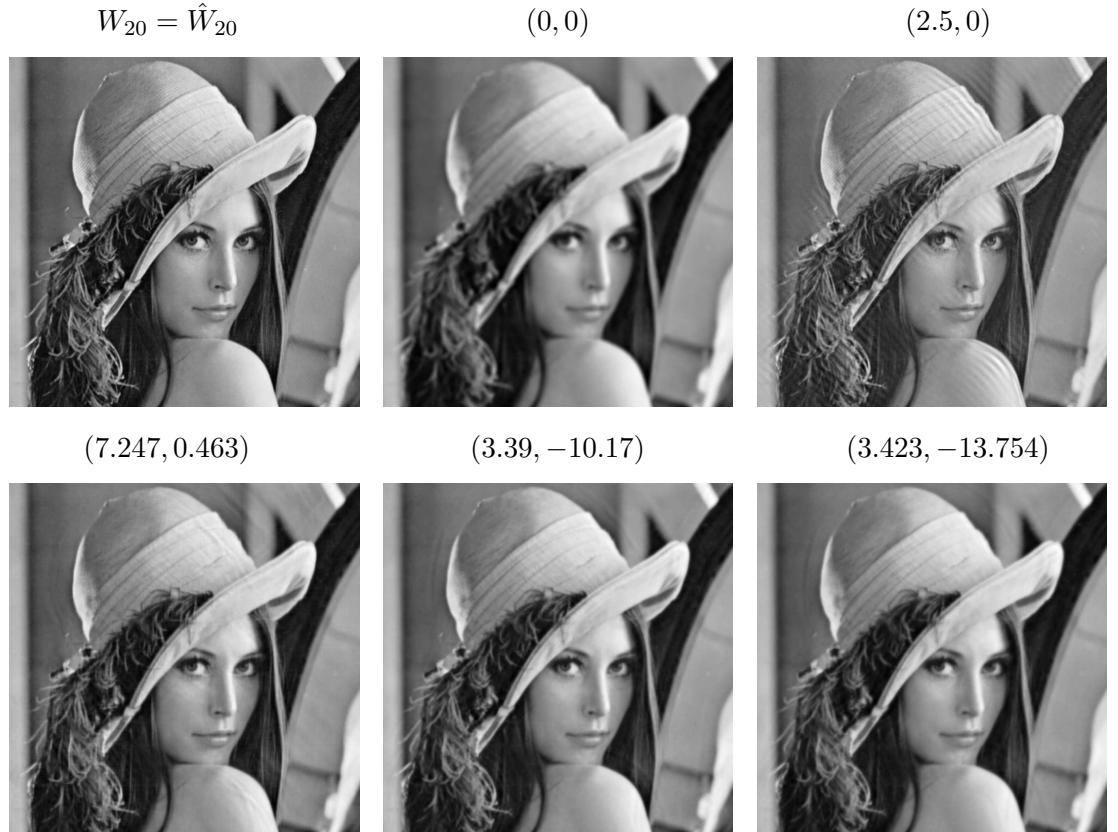
Figure 5.13: *Top left: reference image. Restored Images obtained with different phase masks, with parameters $(\alpha/\lambda, \beta/\lambda)$, are shown for a 60dB SNR, $W_{20} = 1\lambda$ and $\hat{W}_{20} = 0\lambda$.*

$W_{20} = \hat{W}_{20}$ $(0,0)$ $(2.5, 0)$

$(7.247, 0.463)$ $(3.39, -10.17)$ $(3.423, -13.754)$

Figure 5.14: *Restored images obtained with different phase masks $(\alpha/\lambda, \beta/\lambda)$ and for a 60dB SNR, $W_{20} = 3\lambda$ and $\hat{W}_{20} = 0\lambda$. Top left: reference image.*

5.5.1 Metrics of defocus

The oscillation artifacts near strong edges apparent in, for example Figures 5.11 and 5.14, not only introduce artificial features in the image but are also perceived as reducing image contrast. Therefore a contrast metric should be maximised when the artifacts are minimised, i.e. when $\hat{W}_{20} = W_{20}$. Different contrast metrics have been proposed for various applications. Michelson defined the visibility of interferometric fringes with the quantity $V = (I_{\mathrm{MAX}} - I_{\mathrm{MIN}})/(I_{\mathrm{MAX}} + I_{\mathrm{MIN}})$ [83], and is widely used to measure physical contrast in interferometry, see for example [84]. Other contrast metrics such as the L^p norm and the entropy have also been proposed for contrast-based phase calibration of beam-forming arrays [85]. We originally chose to maximise the variance of the normalised image, which is similar to the L^2 norm, for its simplicity and computational efficiency. Some authors (see e.g. [86]) argue that for complex signals or images only local measurements of contrast that fit the human perception of local contrast are meaningful. Peli shows in [86] that standard definitions of contrast, including V as described above, do not fit with experimental data for the human perception of contrast in Gabor signals (sinusoid with gaussian envelope). He proposed instead a metric based on multi-scale bandpass Gabor filtering which accurately models the human contrast perception of Gabor signals. However, to the best of our knowledge this model was not tested with other, more complex signals.

Recently Demenikov proposed a wavelet-based metric for estimating W_{20} in wavefront coded systems. The Haar wavelet is utilised with a median absolute deviation metric (MAD); i.e. the median of the $|x_i - \mathrm{median}[x]|$ values, of the coefficients in each high-frequency sub-bands is computed. The metric is defined as the sum of these values across all sub-bands. The multi-scale processing inherent to the wavelet framework is justified by psychophysical notions of the human visual system. Furthermore it concords with Peli's multi-scale contrast definition, but benefits from the orthogonal properties of the Wavelet decomposition. The flexibility of this metric, both an advantage and an inconvenience, stems from the required tuning in the number of decomposition levels which must be adapted to the target size. Demenikov argues that oscillating artifacts appear as high amplitude ripples in high-frequency sub-bands. Therefore a

minimisation of this metric should converge to an estimator $\hat{W}_{20}$ that minimises oscillating artifacts. How the metric discriminates between high amplitude coefficients due to edges and those due to artifacts remains unclear.

Following Peli's multi-scale contrast definition we investigate a third metric of defocus. Using the Haar Wavelet decomposition suggested by Demenikov, we measure the contrast as the L^2 norm of the wavelet coefficients across scales, after normalisation by their L^1 norm. We refer to this metric as the wavelet energy (WE) metric. It is also similar to the variance metric but is applied in the wavelet domain instead of the spatial domain.

The development of a general purpose, robust metric for estimating the defocus parameter from image artifacts is a difficult image-processing task and an on-going process. An easier approach consists in calibrating a metric for a given data set to ensure that the metric provides reasonably accurate estimates of W_{20}. In the next section we analyse the accuracy of the various metrics described above for different types of images and phase masks.

5.5.2 Defocus estimation results

In noise-free signals

We report here the defocus estimations of the metrics described above in noise-free conditions for a) a unit vertical step, b) the image of Lena which represents general image features. We include in these results two implementations of the MAD metric, denoted MAD and MAD$_3$, corresponding to a single level and three levels wavelet decomposition respectively. In order to quantify the accuracy of the metrics estimates we proceed as follow. For a set of actual defocus values W_{20} we compute the defocus estimates $\hat{W}_{20}$. We utilise the relative error between the vectors $\hat{W}_{20}$ and W_{20} to summarise the performance of each metric. The relative error $\delta[X, X_0]$ of a vector X with respect to a vector X_0, is defined for n-dimensional vectors as:

$$\delta[X, X_0] = \frac{||X - X_0||_n}{||X_0||_n} .$$

(5.57)

We therefore use the L^1 norm in Eq. (5.57) to compute $\delta[\hat{W}_{20}, W_{20}]$ and express it in %. Note that the step size in $\hat{W}_{20}$ and W_{20} is equal to $\lambda/4$. Further decreasing this step size is unlikely to have any significant impact on the outcome of this analysis but will increase significantly the computational time. Defocus estimations for the vertical step target are presented in Figure 5.15 and the values of $\delta[\hat{W}_{20}, W_{20}]$ are reported in Table 5.2. Since Figure 5.15 shows plots of $\hat{W}_{20}$ versus W_{20} an ideal metric would yield estimates that lie on the $\hat{W}_{20} = W_{20}$ line.These results show that for this target, the variance metric yields an unbiased estimator of defocus for the petal phase masks, and has a $\lambda/4$ bias at $W_{20} = 0$ for the two cubic phase masks, see top row on Figure 5.15. The WE metric is unbiased for all phase masks except for the cubic mask $(2.5, 0)$. The MAD metrics clearly do not provide meaningful estimates for the cubic mask $(2.5, 0)$ and only achieves reasonable accuracy with the petal phase mask $(3.423, -13.754)$. Defocus estimations for the target Lena are displayed in Figure 5.16 and the values of $\delta[\hat{W}_{20}, W_{20}]$ are reported in Table 5.3. It shows the MAD_3 and WE metrics are unbiased for all phase masks except for a $\lambda/4$ and $\lambda/2$ error respectively at $W_{20} = 3\lambda$ with the cubic phase mask $(2.5, 0)$.

We observe that the variance metric performs significantly better for the single edge than for the target Lena. This seems to indicate that the variance metric is a reasonable local measure of contrast but may be ill-suited to large, complex two dimensional images. These results indicate that the WE metric appears to be the most accurate estimator of defocus among those tested here in noise-free conditions.

$(\alpha/\lambda, \beta/\lambda)$	$(2.5, 0)$	$(7.247, 0.463)$	$(3.39, -10.17)$	$(3.423, -13.754)$
variance	1.3	1.3	0	0
MAD	46.2	14.1	11.5	3.8
MAD_3	64.1	6.4	14.1	2.6
WE	2.6	0	0	0

Table 5.2: *Relative error $\delta[\hat{W}_{20}, W_{20}]$ in percent of the defocus estimates for the vertical unit edge in noise-free conditions.*
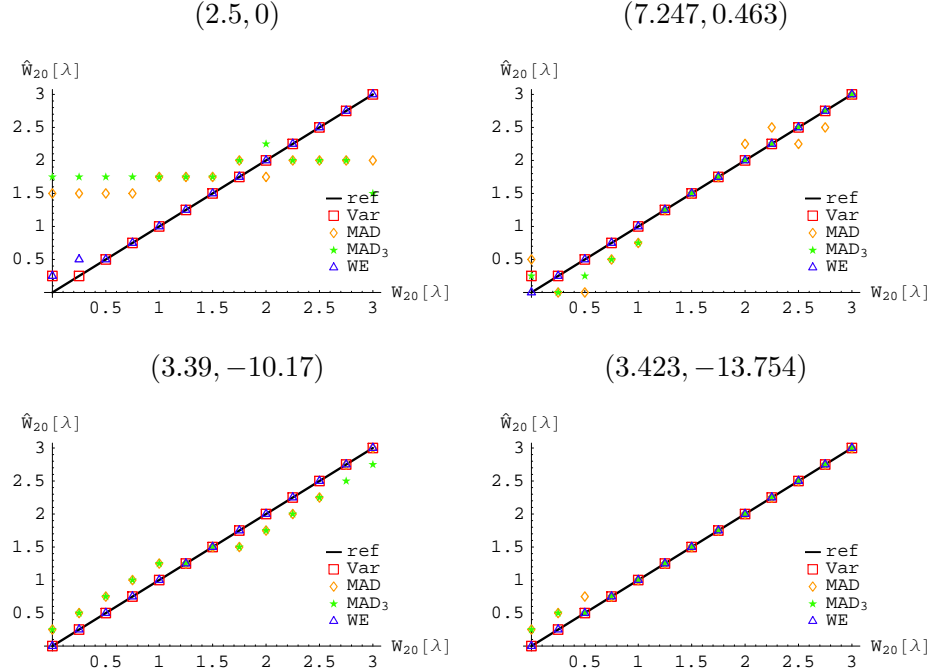
Figure 5.15: *Defocus estimation in restored images of a unit vertical edge, in noise-free conditions, with different metrics and phase masks $(\alpha/\lambda, \beta/\lambda)$.*
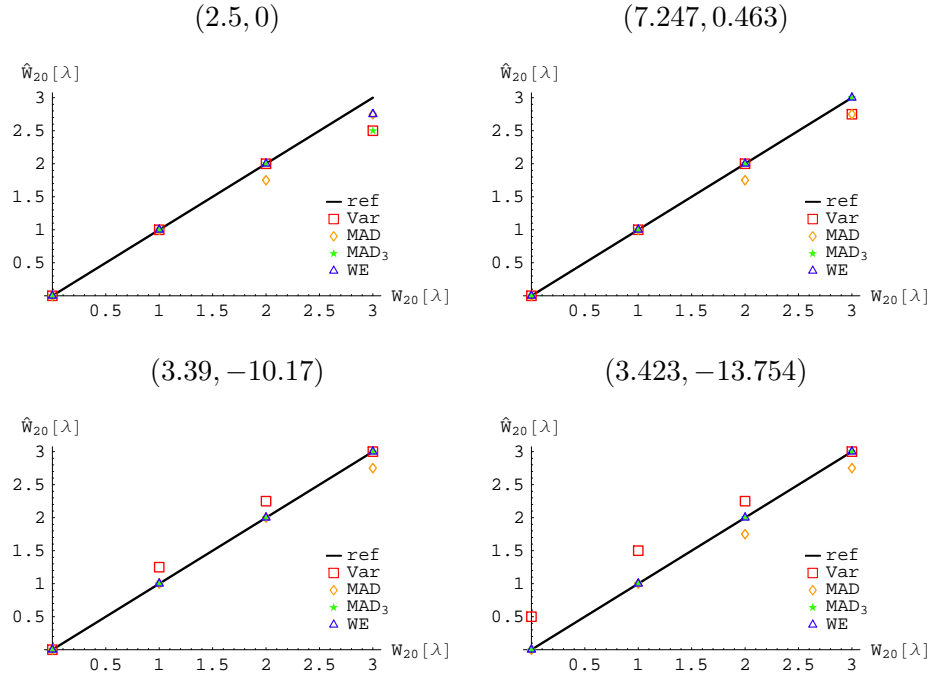

Figure 5.16: *Defocus estimation in the restored images of Lena, in noise-free conditions, with different metrics and phase masks $(\alpha/\lambda, \beta/\lambda)$.*

$(\alpha/\lambda, \beta/\lambda)$	$(2.5, 0)$	$(7.247, 0.463)$	$(3.39, -10.17)$	$(3.423, -13.754)$
variance	8.3	4.2	8.3	20.8
MAD	8.3	8.3	4.2	8.3
MAD_3	8.3	0	0	0
WE	4.2	0	0	0

Table 5.3: *Relative error $\delta[\hat{W}_{20}, W_{20}]$ in percent of the defocus estimates for the image of Lena in noise-free conditions.*

In noisy signals

The presence of noise in the coded image influences artifacts in the restored image and will in general degrade the accuracy of the defocus estimates. Indeed, the K value in the Wiener filter, given in Eq. 5.52, must be increased with the noise level in the coded image. Thus higher noise levels are associated with increased smoothing by the Wiener filter, which results in a decreased sharpness in restored images and an attenuation of the image artifacts. In other words, as the noise level increases it progressively degrades the image quality and takes over the image artifacts. It is therefore crucial to assess the performance of the metrics in the presence of noise. To that end we include an additive white gaussian noise to the coded image (SNR=60dB). We present the average and standard deviation values of the defocus estimates over 10 iterations. Figure 5.17 and 5.18 show the defocus estimations in a vertical edge for the cubic and petal phase masks respectively. The relative errors $\delta[\hat{W}_{20}, W_{20}]$ are reported in Table 5.4 and show that the WE metric yields the best estimate of defocus with a relative error as low as 2.6% achieved with petal mask $(3.423, -13.754)$. In agreement with the noise-free simulations the MAD metrics do not provide meaningful defocus estimations in the present of noise for the edge target. The defocus estimations with the Lena target are presented in Figure 5.19 and 5.20 for the cubic and petal phase masks respectively. The relative errors $\delta[\hat{W}_{20}, W_{20}]$ are reported in Table 5.5 show that the MAD metrics provide better accuracy than the WE and variance metrics for all phase masks (average relative error reduced by factors of 5 and 20 respectively) except the cubic mask $(2.5, 0)$ where WE has the smallest error. Furthermore the relative error $\delta[\hat{W}_{20}, W_{20}]$ achieved with MAD_3 is consistently below 1.3% for the two petal phase masks and even reaches

0% for the cubic phase mask $(7.247, 0.463)$ that was previously optimised.
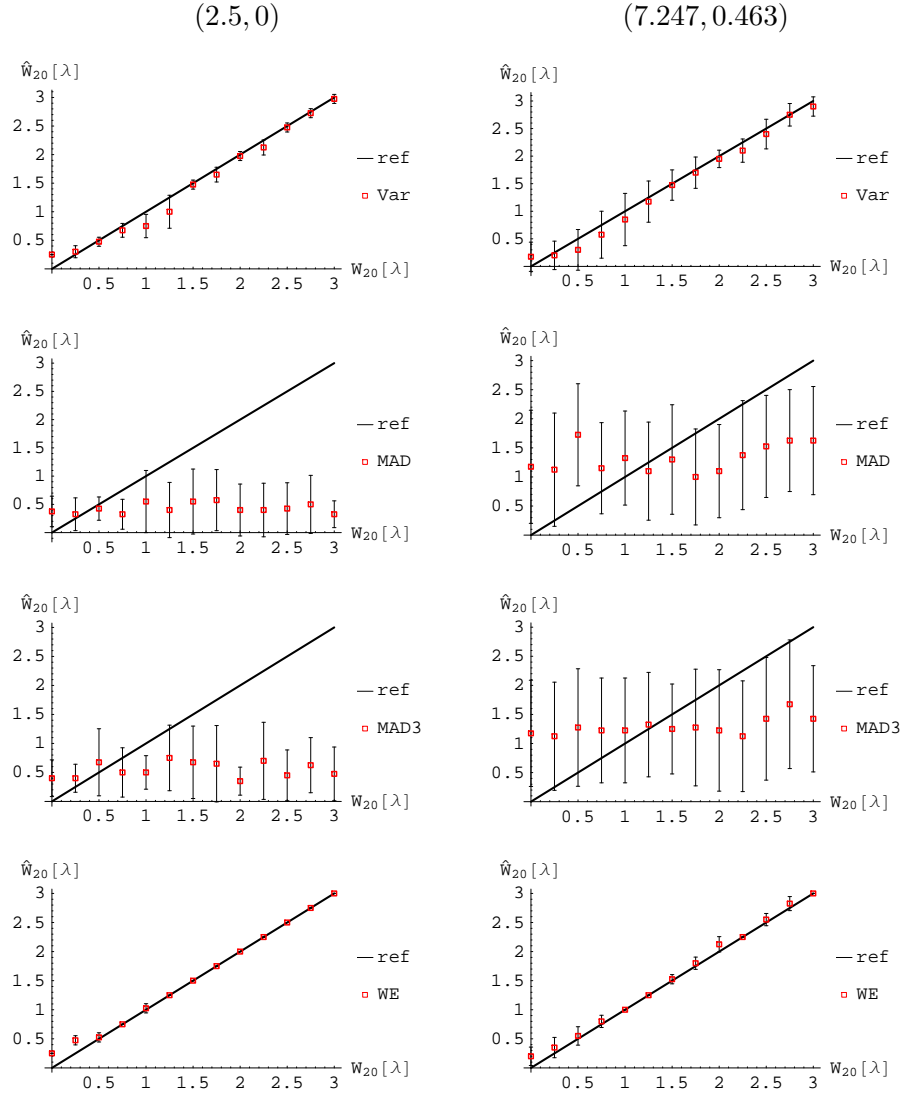
Figure 5.17: *Defocus estimation in restored images of a unit vertical edge with two CPM. The metrics employed are shown in the legend. SNR in coded image is 60dB.*
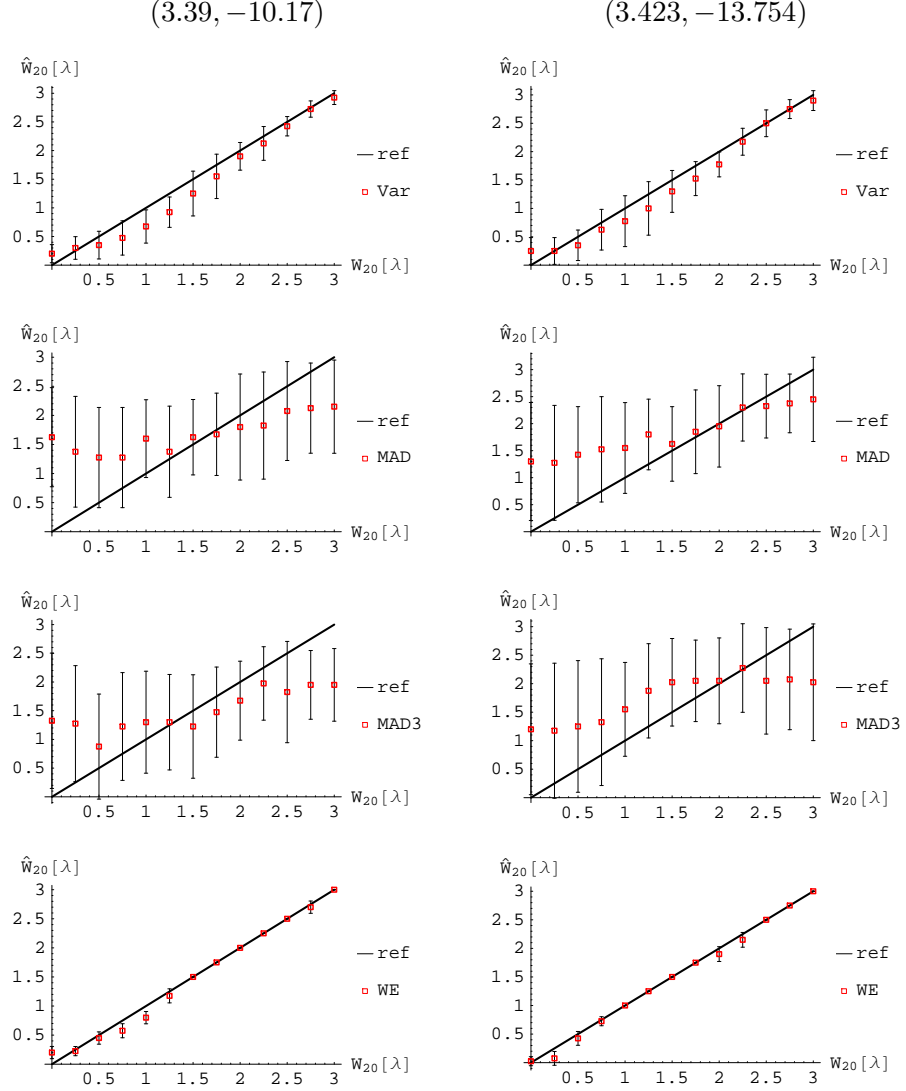
$(3.39, -10.17)$ $(3.423, -13.754)$

Figure 5.18: *Defocus estimation in restored images of a unit vertical edge with different metrics and petal phase masks $(\alpha/\lambda, \beta/\lambda)$. SNR in coded image is 60dB.*

$(\alpha/\lambda, \beta/\lambda)$	$(2.5, 0)$	$(7.247, 0.463)$	$(3.39, -10.17)$	$(3.423, -13.754)$
variance	6.4	13.6	13.2	15
MAD	78.3	65.6	53.8	47.7
MAD$_3$	74.3	68.5	53.2	55.3
WE	2.7	4.2	4	2.6

Table 5.4: *Average relative error in percent of the defocus estimates for the vertical unit edge. SNR in coded images is 60dB.*
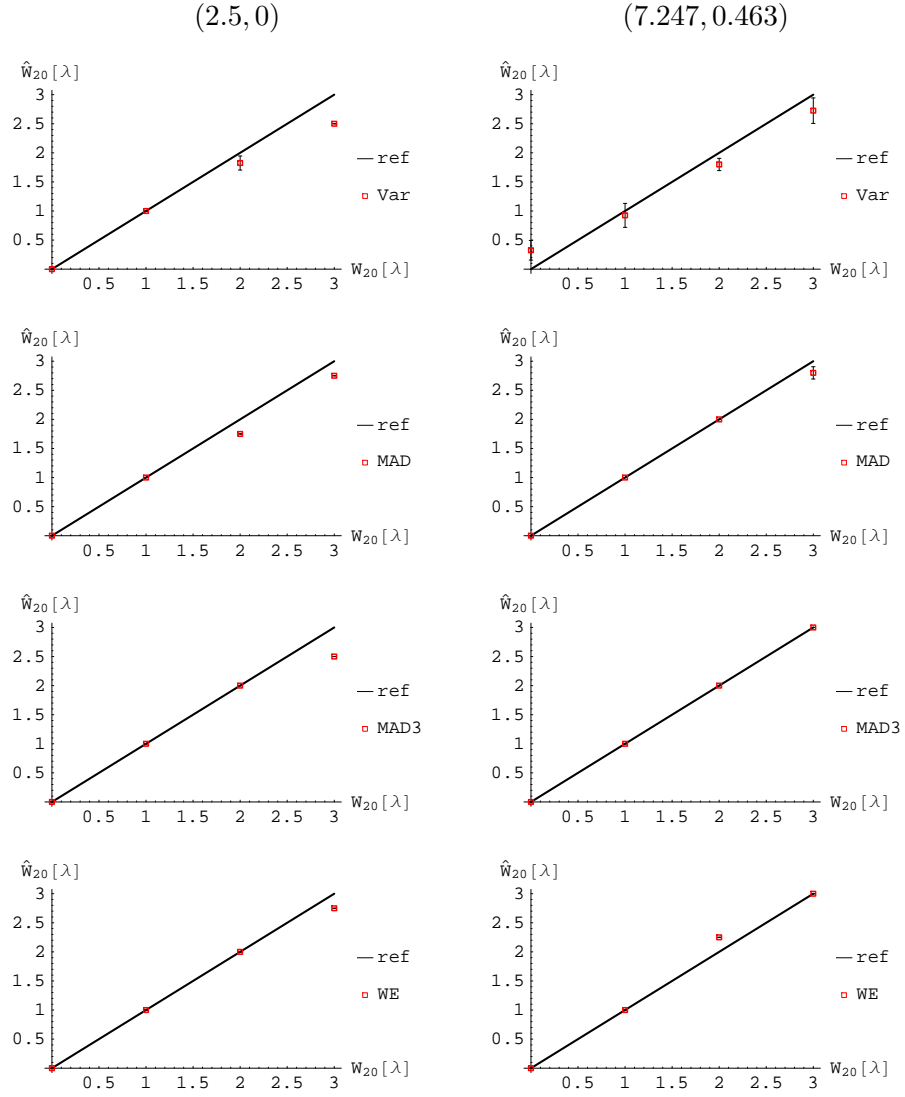
Figure 5.19: *Defocus estimation in restored images of Lena with different metrics and cubic phase masks $(\alpha/\lambda, \beta/\lambda)$. SNR in coded image is 60dB.*

$(\alpha/\lambda, \beta/\lambda)$	$(2.5, 0)$	$(7.247, 0.463)$	$(3.39, -10.17)$	$(3.423, -13.754)$
variance	11.3	16.3	22.5	12.1
MAD	8.3	3.3	3.8	0.4
MAD$_3$	8.3	0	1.3	1.3
WE	4.2	4.2	5.8	4.2

Table 5.5: *Average relative error in percent of the defocus estimates for the image Lena. SNR in coded images is 60dB.*
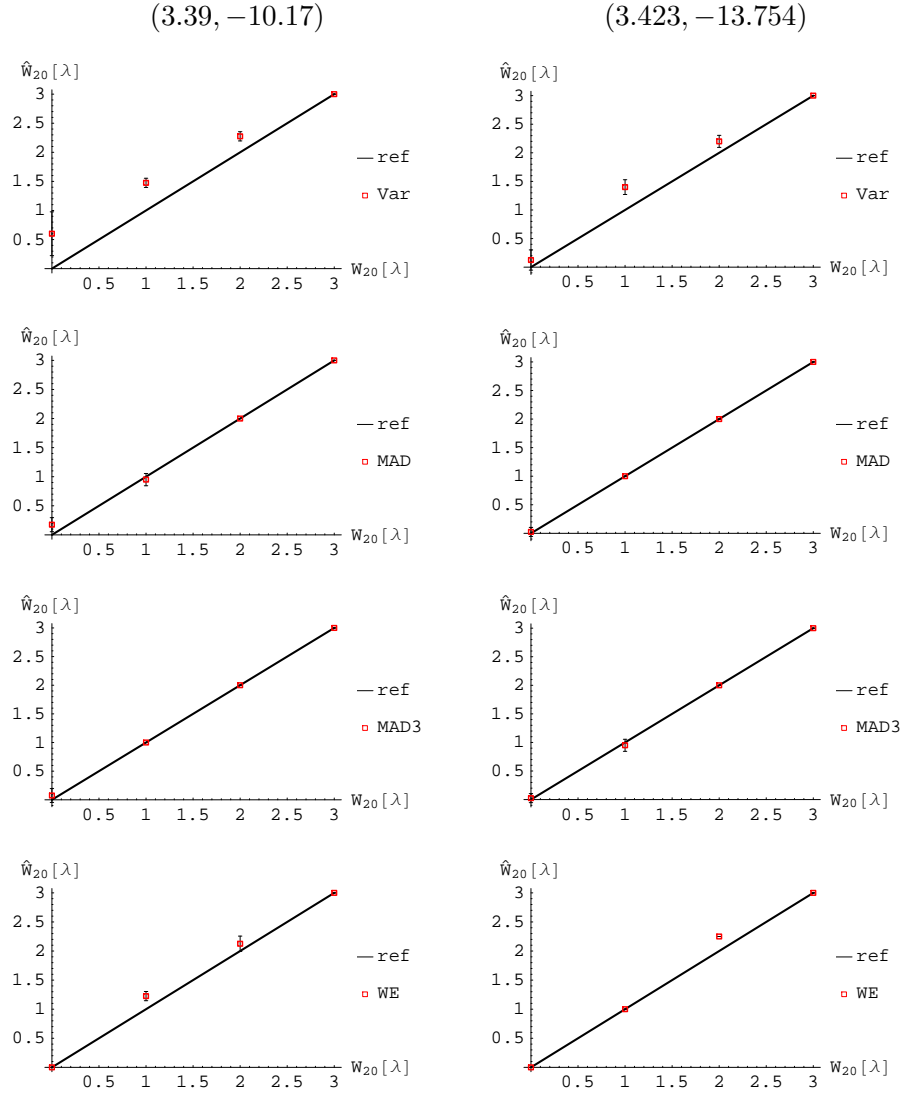
Figure 5.20: *Defocus estimation in restored images of Lena with different metrics and petal phase masks* $(\alpha/\lambda, \beta/\lambda)$. *SNR in coded image is 60dB.*

Further work on defocus metrics

We recently investigated a different approach to the problem of estimating the amount of defocus in wavefront coded images. The method takes advantage of the *a priori* knowledge of edge profiles in the restored images. Indeed, the profiles shown in Figure 5.11 constitute noise-free calibrated data of the artifacts in a step. Therefore the maximum of a set of correlations between the noisy and calibrated data should yield a robust estimate of the defocus parameter. Moreover this method is by definition unbiased in noise-free conditions. We employ Pearson's correlation coefficient between two discrete signals X_i and Y_i and record the maximum value of the spatial correlation function ρ_j defined as:

$$\rho_j = \frac{1}{n-1} \sum_{i=1}^{n} \frac{X_{i+j} - \bar{X}_j}{\sigma_{X_j}} \frac{Y_i - \bar{Y}}{\sigma_Y} , \qquad (5.58)$$

where $\bar{Y}$ and σ_Y denote the average and standard deviation of Y respectively, $\bar{X}_j$ and σ_{X_j} denote the moving average and standard deviation respectively of the sub-samples $\{X_{j+1}, X_{j+2}, ..., X_{j+n}\}$. The estimation method was implemented for a vertical edge. Interim simulations (with SNR=60dB) determined unbiased estimates for the CPM $(2.5, 0)$ and a relative errors of 0.4% for the CPM $(7.247, 0.463)$. These represent an increased robustness compared with the 2.7% and 4.2% errors respectively, previously attained with the WE metric. No improvement was detected with the petal phase masks. For two-dimensional images further improvements are expected since the calibrated data can include several directions.

5.5.3   Image quality improvements

It is important to note that the magnitude of the artifacts is greatly reduced by a restoration with $\hat{W}_{20}$ compared to the conventional restoration with $W_{20} = 0$. This remains valid for $\lambda/2$ or smaller biases in $\hat{W}_{20}$. Figure 5.21 illustrates the artifact reduction achieved, without noise, with a $\lambda/4$ bias in the defocus estimation for the petal phase mask $(3.39, -10.17)$. The relative error of the restored image is decreased by a factor of 8 in this case and the artifacts are hardly noticeable. Similar artifacts suppression is achieved when the proposed restoration procedure is applied to the other phase masks presented in this Chapter. Figure 5.22 presents the restored images in the

presence of a 60dB SNR. Again the artifacts are greatly reduced by a defocus estimation prior to the restoration. The degradation due to a $\lambda/4$ bias in $\hat{W}_{20}$, corresponding approximately to Hopkins' criterion, is hardly noticeable compared with the optimal restoration $\hat{W}_{20} = W_{20}$. Hence we showed that wavefront coding image artifacts can be removed to a large extent by estimating W_{20} in the restored images. This can be seen as a further extension of the DoF in wavefront coded images.

$$\hat{W}_{20} = W_{20} = 3\lambda \qquad \hat{W}_{20} = 0\lambda \qquad \hat{W}_{20} = 2.75\lambda$$
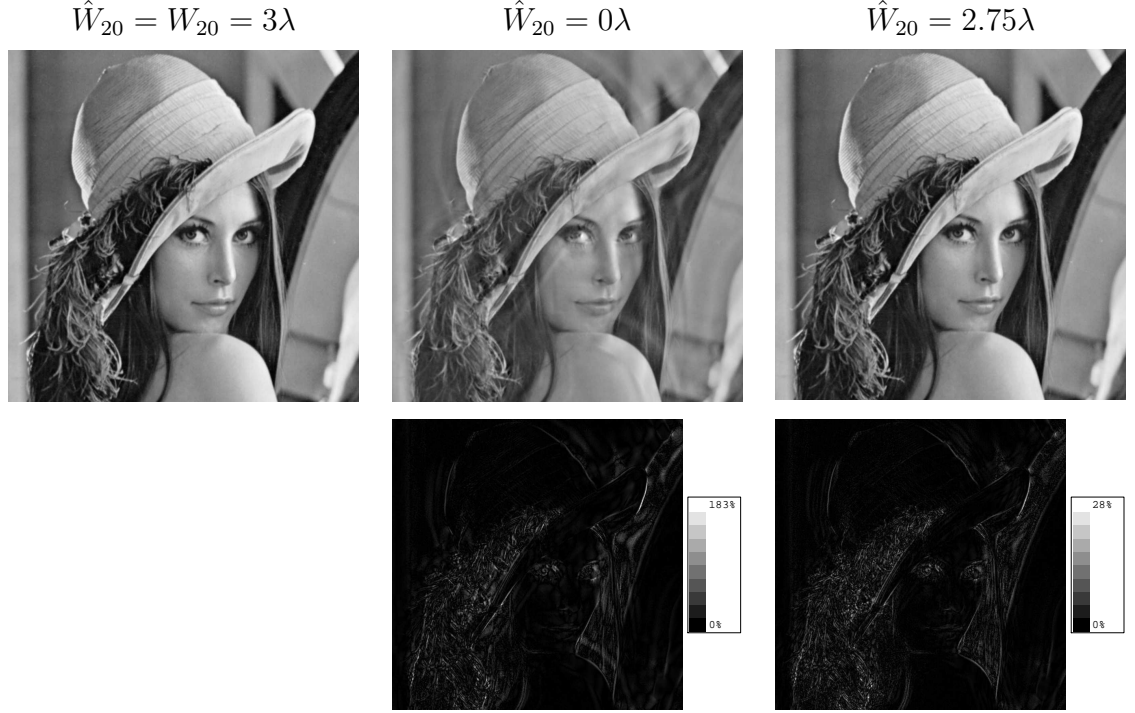
Figure 5.21: *Artifacts comparison in conventional restoration and with a defocus estimation (SNR=∞). True defocus is $W_{20} = 3\lambda$. Top row, from left to right: perfectly restored image, conventional wavefront coding restoration (relative error 2.5%), restoration with a defocus estimation (relative error 0.31%). Bottom row: relative error images. Phase mask is $(3.39, -10.17)$.*

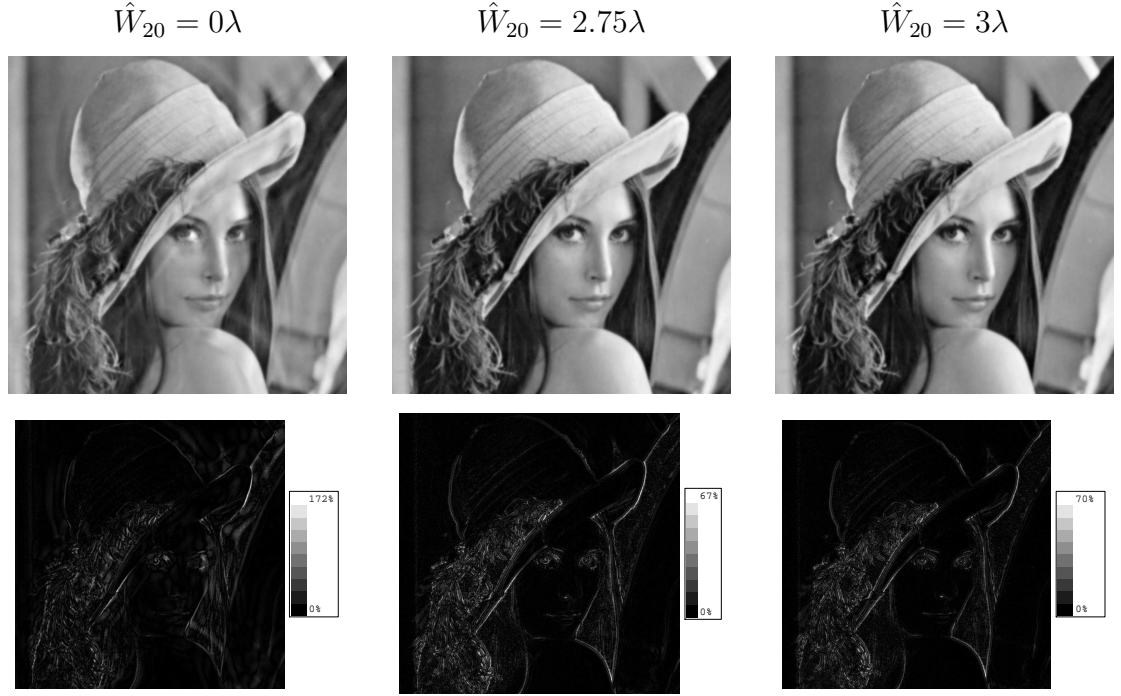Figure 5.22: *Artifacts comparison in conventional restoration and with a defocus estimation (SNR=60dB). True defocus is $W_{20} = 3\lambda$. From left to right: image obtained with a conventional wavefront coding restoration (relative error 2.2%), image obtained with a $\lambda/4$ bias in the defocus estimation (relative error 0.71%), image restored with the true defocus (relative error 0.68%). Phase mask is $(3.39, -10.17)$.*

5.6 Conclusions

In this chapter we seek to design and analyse optical systems that extend the depth of field (DoF) beyond that of diffraction-limited systems. We first describe the fundamental tools required to characterise optical systems, and in particular their response to defocus. We recall that for one-dimensional optical systems, the ambiguity function is a polar representation of the optical-transfer-function with the defocus parameter as the variable. This property can be extended to two-dimensional rectangularly separable systems. For such systems, pupil functions with a cubic-phase profile arise from the restriction that the amplitude of the ambiguity function be invariant to defocus [26]. The pupil-phase-engineering approach [27] optimises higher order polynomial pupil functions with two competing merit functions: the system sensitivity to defocus and its restorability. This approach directly addresses the tradeoff between extending the DoF and reducing the MTF of the system. We limit our optimisation to generalised cubic phase masks with parameters within $[-19\lambda, 19\lambda]$ and use the computationally efficient metric of the system sensitivity to defocus detailed in [28, 65]. When the restorability merit function is the in-focus Strehl ratio as proposed in [28], the algorithm converges to the phase mask $(\alpha/\lambda, \beta/\lambda) = (3.423, -13.754)$. However we argue that the Strehl ratio as employed in [27, 28, 65] underestimates the restorability of CPM because of the transversal shift they introduce in the image. We propose to use instead the L^2 norm of the OTF of the system normalised to that of a diffraction-limited system. Using this restorability metric the algorithm converges to the nearly cubic mask $(7.247, 0.463)$. The imaging performances of these phase masks is then assessed. Improved accuracy of the metric of sensitivity could be achieved by including the fourth order derivative of the OTF with respect to defocus.

The reduced sensitivity to defocus of wavefront coded systems allows for a restoration procedure that is independent of the defocus parameter W_{20}. Deconvolution is performed here with the Wiener filter. We show that this standard restoration filter leads to image artifacts which vary with the amount of defocus and the phase mask utilised. We determine the origin of these artifacts as the variations with defocus in the phase of the OTF. These artifacts can largely be removed if the correct value of W_{20} is

implemented in the Wiener filter. We therefore present several metrics of defocus and quantitatively assess their performances. The MAD metric offers the best robustness of the metrics tested. It also achieves best performance when combined with the optimised mask $(7.247, 0.463)$. In addition its flexibility allows for an adaptative estimation for any given image data set. Promising interim results were also obtained with a new approach based on the correlation of edge or step profiles with calibrated data. The images restored with the estimated defocus parameter exhibit greatly reduced artifacts. This remains valid even with small biases in $\hat{W}_{20}$, i.e. smaller than $\lambda/4$, and represent a significant improvement in the imaging performances of wavefront coding systems.

In the next Chapter we will apply the wavefront coding principles and the enhanced image restoration detailed here to extend the depth-of-field of an optical microscope. Indeed these optical systems exhibit a very small depth-of-field, of the order of 1μm. Enhanced depth-of-field may be required for specific applications such as to understand the surface structure of a sample or to monitor rapid dynamic behaviours of a biological specimen.

Chapter 6

Wavefront coded microscopy

6.1   Introduction

In this chapter we discuss implementation of wavefront coding (WC) within a transillu-
minated microscope to increase its depth-of-field (DoF). We also assess the validity of
the image restoration scheme detailed in Chapter 5 to remove wavefront coded image
artifacts. The main motivation for the development of a microscope was to investigate
the potential of WC for an imaging application other than conventional photography.
It turns out that the specificity of the transmission microscope, most notably the de-
pendance of the microscope imaging performances on the specimen structure and the
degree of coherence of light due to transillumination represent challenges to fully exploit
the potential of the WC technique.

In section 6.2 the fundamental principles of transmission microscopy are briefly de-
tailed. A review of the techniques used in microscopy to increase the DoF or, on the
contrary, achieve axial superresolution is given in Section 6.3. The WC microscope
design is described in Section 6.4. The modelled and measured OTF of the micro-
scope are presented in Section 6.5 for the aliasing-free configuration. Interim results
are presented in Section 6.6 for matched illumination and introduce the effect of the
transillumination on image formation that is discussed in Section 6.7. In Section 6.8,
restoration of images recorded with the WC microscope is shown to be greatly im-
proved when partial coherence effects have been removed. The "super" extended DoF

provided by multiple-kernel restoration is demonstrated. Spatially variant restoration is performed in Section 6.9 and "super" extended DoF images are presented. The accuracy of the range detection method is assessed in Section 6.10. The difficulties of restoring WC images of weak objects are discussed in Section 6.11. Conclusions are presented in section 6.12.

6.2 Fundamentals of microscopy

We briefly discuss here a few fundamental aspects of microscopy that have to be considered when designing a microscope and for its use with wavefront coding. Some aspects regarding image quality and image restoration are particularly important to WC.

6.2.1 Köhler illumination

Köhler illumination is a method of illumination used to achieve bright and even illumination across the whole specimen. Figure 6.1 shows the actual optical set up implemented in the microscope to achieve Köhler illumination. This design was performed with the optical design software ZEMAX. In Köhler illumination, the collector lens L1 creates an image of the source S in the front focal plane of the condenser lens L2. The condenser therefore collimates the ray bundle from each point source onto the specimen, see also Figure 6.2, and its front focal plane contains the aperture stop (AS) of the illumination system. Setting the diameter of this diaphragm properly is crucial to Köhler illumination since it determines the cone of light incident on the sample, i.e. it defines the numerical aperture NA_c of the illumination system. To achieve maximal transverse resolution, NA_c must be greater or equal to the numerical aperture of the microscope objective NA_o. We detail in a later section which value of NA_c provides optimal resolution. The object plane O and the field stop are conjugate planes and therefore every point in the specimen receive identical contributions from all points across the source. This ensures even illumination is achieved across the specimen. Parameter values of the implemented Köhler illumination are detailed in Figure 6.3.
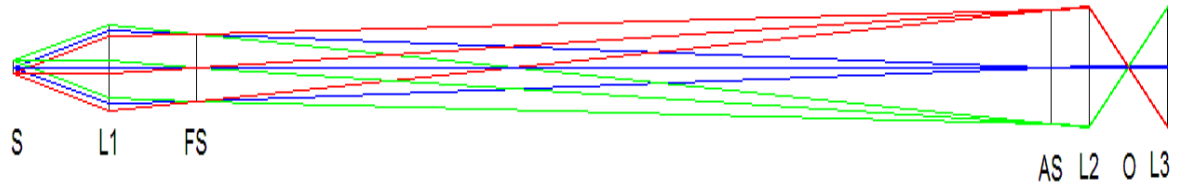
Figure 6.1: *Köhler illumination configuration designed (aspect ratio divided by two).*
S: source, L1: collector lens, FS: field stop, AS: aperture stop, L2: condenser lens, O:
object plane, L3: microscope objective.
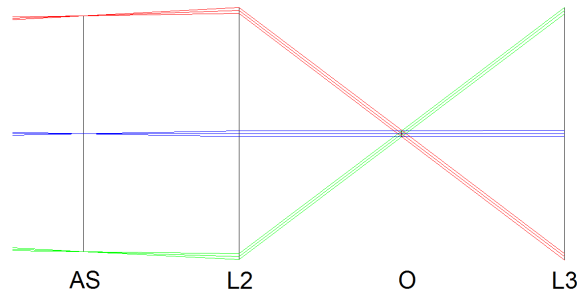
Figure 6.2: *Köhler illumination configuration. Enlargement of the object plane.*

Surf:Type		Radius	Thickness	Semi-Diameter	Conic	Par 1(unused)
OBJ	Standard	Infinity	33.060000	1.000000	0.000000	
1	Paraxial		30.000000	7.336500		30.000000
STO	Standard	Infinity	293.880000	5.750000 U	0.000000	
3	Standard	Infinity	13.000000	9.800646	0.000000	
4	Paraxial		13.570000	10.478837		13.000000
5	Standard	Infinity	13.570000	0.258170	0.000000	
IMA	Standard	Infinity	–	10.480904	0.000000	

Figure 6.3: *Köhler illumination parameters.*

6.2.2 Spatial resolution

Using the Rayleigh criterion, the spatial resolution r of a transmission microscope with an incoherent source is given by:

$$r = 1.22 \frac{\lambda_0}{\mathrm{NA}_c + \mathrm{NA}_o} \,.$$

(6.1)

When $\mathrm{NA}_c \geq \mathrm{NA}_o$ this expression reduces to:

$$r = 0.61 \frac{\lambda_0}{\mathrm{NA}_o} \,.$$

(6.2)

In a later section we will see that it is possible to improve slightly this resolution by carefully choosing NA_c.

6.2.3 Abbe's theory of image formation in the microscope

There are several types of mechanisms of contrast formation generally used in light microscopy. For bright field microscopy they are mainly absorption and diffraction. Abbe's theory of image formation in a microscope considers the simplifying case of a diffraction grating being illuminated by a plane wave. This theory states that an image of the grating is formed if the MO at least captures the first-order diffracted rays produced by the grating. All the rays of identical diffraction orders will interfere constructively in the back focal plane (BFP) of the MO, where the Fraunhofer diffraction pattern of the object wave can be observed. The object wave is defined as the product of the incident wave and the transmission function of the specimen. Abbe showed that the image is formed by the interferences between the spherical waves emitted by the secondary point sources in the BFP of the MO. The image formation in this case is coherent and is illustrated in Figure 6.4.
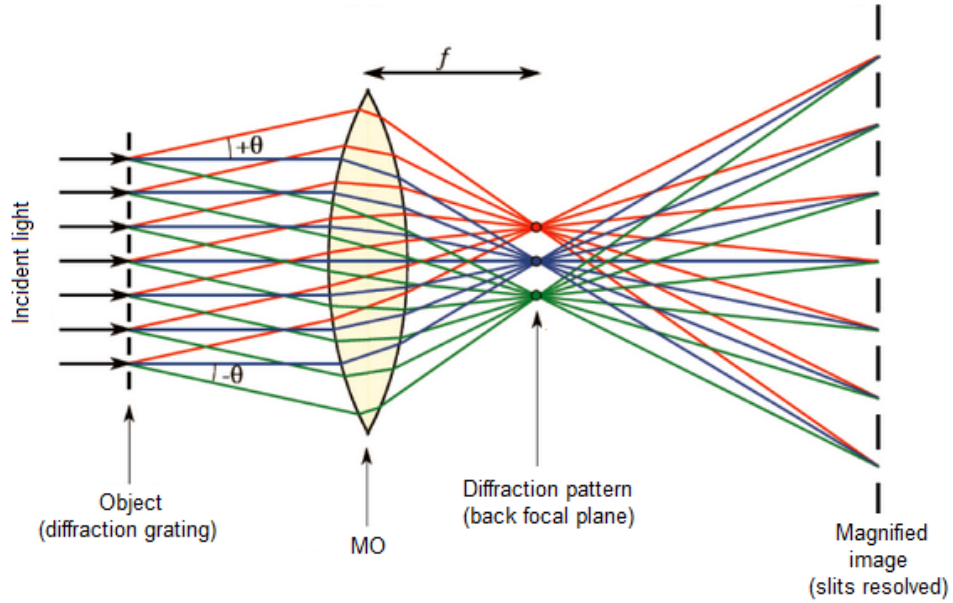
Figure 6.4: *Diagram depicting Abbe's description of the image formation by a lens. (Image courtesy of Cambridge University, DoITPoMS.)*

6.3 Review of depth-field alteration techniques in microscopy

In this section we shall focus on the various techniques employed in microscopy to modify the DoF. In microscopy it can be desirable to reject bright out-of-focus features that are superimposed upon faint in-focus regions of the specimen. Confocal microscopes include a pinhole placed in front of a photomultiplier tube (PMT) to reject most of the light coming from out-of-focus regions of the specimen, effectively reducing the DoF, or increasing the axial resolution. Thus the integrated intensity in each transverse plane decreases rapidly with the distance from the focal plane. This property called optical sectioning, is specific to confocal microscopes. A scanning unit can rapidly form a 2D image of the specimen. Recording a set of images at various depths enables 3D visualisation. Confocal microscopy is now widely used with fluorescence microscopy because of its ability to select and record a component of interest, labelled with a fluorescent molecule, in the specimen [87]. Because laser sources are usually employed due to the high intensity required to illuminate the specimen, such systems are called confocal laser scanning microscopes (CLSM). The image formation theory in

conventional and confocal microscopes is reviewed in [79]. Sheppard and Choudhury show that 1) contrary to the condenser lens in a conventional microscope, the aberrations in the collector lens of a confocal microscope affect its imaging performances, 2) confocal microscopes achieve slightly higher transverse resolution than conventional microscopes because the PSF of the former is equal to the square of the PSF of the latter, 3) annular pupils in confocal microscopes achieve transverse superresolution and extended depth-of-field (EDF), see also [79, 88].

The terms axial resolution and DoF are employed in the literature to characterise the axial discrimination capability of a microscope. We recall that the DoF of an optical system corresponds to $W_{20} = 0.25\lambda$, i.e. $z = 2\lambda F_{/\#}^2$, whereas the axial resolution can be defined with the Rayleigh criterion as the position of the first null of the point source diffraction pattern in the axial direction. This occurs when $W_{20} = 1\lambda$, i.e. when $z = 8\lambda F_{/\#}^2$ and can be compared with the transverse resolution given in Eq. (6.2) $1.22\lambda F_{/\#}$.

Axial superresolution with two-zone phase-only filters in CLSM has been investigated in [59, 62]. In [59] transverse resolution improvements by a factor of 2 are demonstrated but without presenting the associated changes in axial resolution. In [62], three properties of the PSF obtained with these filters are analyzed: the axial spot size, the axial maximum sidelobe level and the Strehl ratio. Other binary phase-only filters are reported in [89] and are designed to fit any desired PSF in three points only. The proposed filters reduce the axial and lateral half-widths to 80% (filters with eight phase levels in 45deg steps). Another filter proposed is worth mentioning and improves the lateral resolution to 85% at the cost of a decreased axial resolution, i.e. increased depth of field, by a factor of 2. This filter has an annulus and a centre with transmittivity +1 and -1 respectively. The annular structure of this filter can be related to the pupils discussed in [79] and to the circular array discussed in Chapter 4, and its EDF should come as no surprise. Note however that these filters do not require any digital post-processing, as is usually the case in WC systems, because of the mask symmetry.

A very large DoF may sometimes be desirable in microscopy to understand the surface structure of a sample or when counting the number of particles present within a thick specimen. Attempts to apply WC to microscopy have, to the best of our knowledge, so far been limited to low NA objectives and magnification (5x objective with NA=0.078) [90]. Access to the AS is obtained here with a relay system which increases aberrations in the optical system. These aberrations are then mitigated by the WC. WC could potentially correct field related aberrations (field curvature, spherical aberration, and chromatic aberrations) [64] which are expensive to correct, and thus could reduce the cost of lower end microscopes. Other potential applications include diagnostic microscopes in cytology, inspection of integrated circuit boards and applications that require the acquisition of a sequence of EDF images in quick succession to monitor the dynamic behaviour of a specimen.

In confocal microscopes the acquisition speed is limited by the speed at which the system can be refocused to acquire the image stacks. An innovative method of refocusing a confocal microscope is proposed in [91, 92] to achieve real-time EDF. This method is based on the use of a second MO and a mirror placed in its focal plane. The pupil planes of the two MO are mapped onto one another with a 4f imaging system. Provided that the second MO is carefully chosen [91], this system does not introduce any extra aberrations for different focal settings.

6.4 The wavefront coded microscope

In this section we describe the implementation of pupil phase masks in a wide-field microscope to extend its DoF using WC. The wavefront coded microscope developed will then be used to assess the quality of the multiple-kernel image restoration method described in Chapter 5.

6.4.1 System description

Optical set up

An objective lens with $NA_o = 0.6$ (Edmund optics) and a tube lens are used to form a compound microscope that is infinity-corrected. This set up, illustrated in Figure 6.5, enables the phase mask to be placed between the objective lens and the tube lens since the MO forms an image of the sample at infinity. For the system to be translation-invariant, the phase mask should be placed in the AS of the MO, which is a conjugate plane of the aperture of the condenser lens L_2, so that each point source in the object plane is similarly encoded by the phase mask. The set up shown on Figure 6.5 is said to be object-space telecentric since the entrance pupil is located at infinity. This is also a desirable property because such a system will have a constant magnification for all object distances. Note that the illumination of the sample is distributed over the entire FoV of the CCD sensor. The transversal magnification of the image is determined by the ratio f_2/f_1 which equals 20 here. Pictures of the experimental set up are shown on Figure 6.6.

We started this project with a microscope that had been assembled by a MSc student. The MO and the tube lens are still in use in the current system but the original system had to be entirely redesigned and reassembled to meet our requirements. A new and more powerful xenon arc light source (Perkin Elmer XL3000) was chosen for its high power (300W), broadband signal covering the entire visible spectrum and fiber optic cable providing enhanced flexibility. A new illumination system was designed in Zemax and then implemented to provide Köhler illumination. An additional diaphragm was placed as close as possible to the BFP of the MO to reduce its NA and remove aliasing. The 8-bit Infinity camera was replaced by a highly sensitive 12-bit camera (Hamamatsu C4742-95).

Illumination spectrum

In addition to the optical elements discussed above, the illumination system includes an IR filter to prevent heat transfer from the xenon arc lamp to the specimen and to the CCD sensor, which are very sensitive to IR. A UV filter is also included for safety
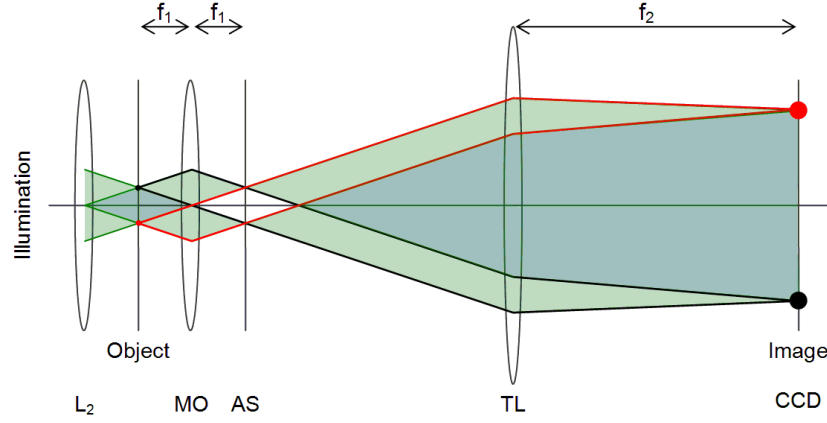
Figure 6.5: *Infinity-corrected microscope. L2: condenser lens, MO: microscope objective $f_1 = 10mm$, AS: aperture stop of the imaging part and conjugate to the aperture of the condenser, TL: tube lens with $f_2 = 200mm$.*
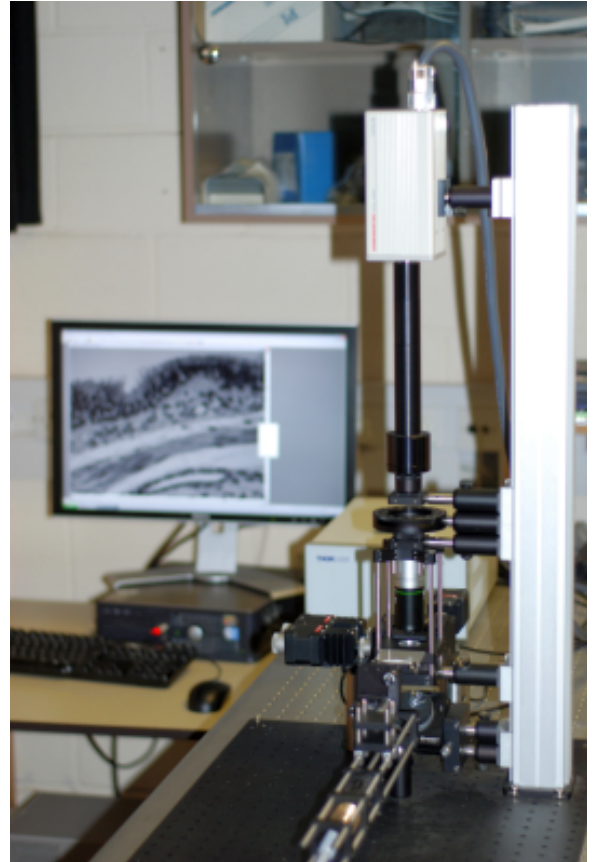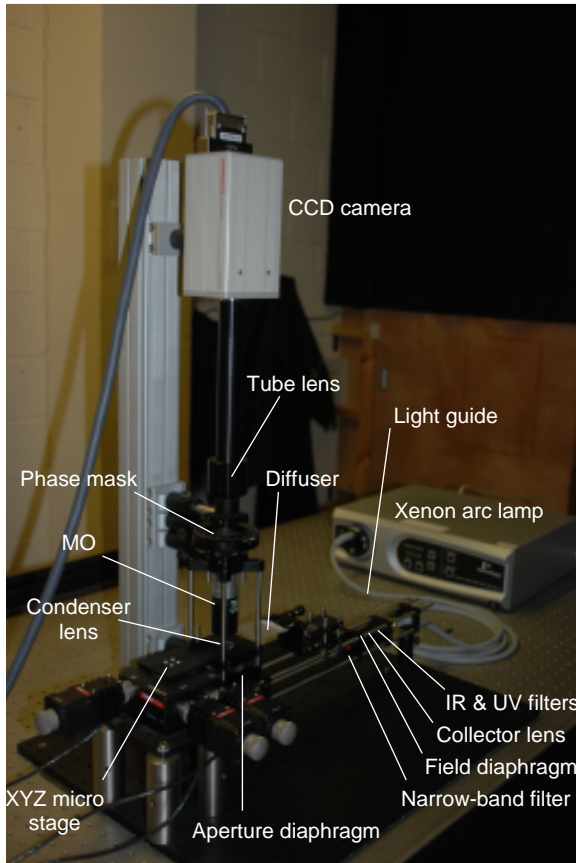
Figure 6.6: *Photographs of the wavefront coded microscope.*

reasons. This results in white light illumination with spectrum shown on Figure 6.7. This safe illumination is filtered with a $\Delta\lambda = 10$nm narrow band bandpass interference filter, to prevent spectral blurring by the phase mask. Thus the coherence length of the illumination source is $L = \lambda^2/\Delta\lambda \simeq 43.6\mu$m for a narrow band centered at $\lambda = 660$nm. Note that the temporal coherence of the illumination does not impact the equal time complex degree of spatial coherence in the object plane, see Eq. (6.4).
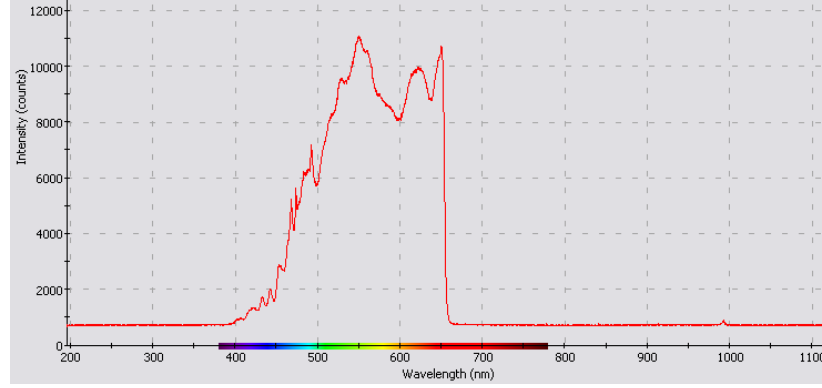
Figure 6.7: *Spectrum of the white light illumination after IR and UV filtering.*

Camera sensitivity and resolution

It was noted in the previous chapter that the SNR in the recorded images is the parameter limiting the extension of the DoF in WC systems. In addition to the light gathering ability of the illumination system, the sensitivity of the sensor is crucial. For this reason we use a highly sensitive CCD camera (Hamamatsu C4742-95) that uses Peltier cooling and which records 12 bit images. The effective dynamic range is smaller than the expected 4096 and is defined as the ratio of the full well capacity to the read out noise. It is equal to 2250 (manufacturer specification) and corresponds to an electronic SNR of $20\log_{10}(V_s/V_n) = 67$dB. Note that this value will be used in the Wiener filter restoration. The pixel size of this camera is 6.45μm in both directions and the number of pixels in the image is 1344(H)x1024(V).

6.4.2 Pre-processing of raw images

The acquisition time and illumination intensity are always adjusted so that the full dynamic range of the camera is exploited while ensuring that the sensor is not saturated.

200 images are then acquired and averaged together thereby providing an increase in SNR by a factor of 14. We systematically correct for the dark current bias introduced in the image by the camera sensor. This is achieved by recording a dark image and then subtracting it from the image of the specimen. When possible we also record a white image, without any specimen, to correct for slightly uneven illumination. Together, these corrections form the flat field correction which is standardly used in microscopy. It is illustrated on Figure 6.8 with images of spinal cord cells and lung cells with bronchus. Note that it is critically important to denoise the measured PSF prior to use in image restorations. To that end we subtract the dark current image and apply an hysteresis threshold. The rationale for such a threshold is to preserve low intensity levels that are connected to higher intensity levels.

6.4.3 Implementation issues

We detail in this section practical and fundamental issues encountered during the design and implementation of the WC microscope and discuss the solutions that were employed to address them. Such issues range from illumination matching, aliasing and the choice of phase mask.

Measuring the PSF: pinhole size requirement

Before measuring the PSF of the optical system we want to establish the diameter d_p of the largest pinhole that is unresolved by the MO. Highest resolution is achieved when $NA_c \geq \mathrm{NA}_o$ and is given by Eq. (6.2). Thus a pinhole with diameter $d_p < 0.67\mu$m will be unresolved by a MO with $\mathrm{NA}_o = 0.6$. The smallest pinhole that was commercially available is 0.5μm$\pm0.3\mu$m and therefore meets our requirements. When measuring the PSF of the microscope, the imaging system is decoupled from the illumination system because of the diffraction by the pinhole. This means the measured PSF equals that of an incoherent imaging system, independently of the degree of coherence in the illumination.
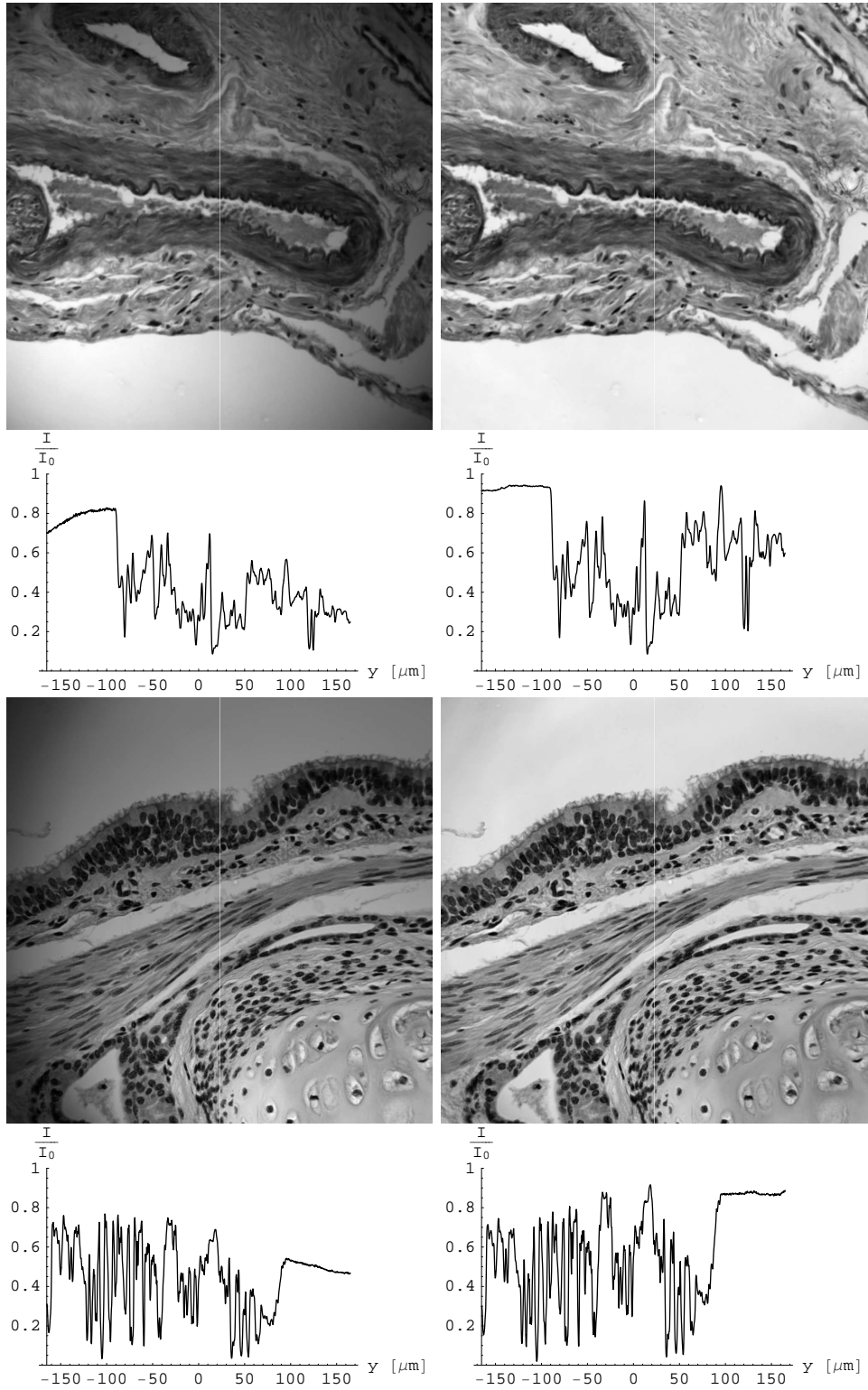
Figure 6.8: *From left right: raw and flat field corrected images. The first two rows are images and 1-dimensional slices of spinal cord cells. The last two rows are images and 1-dimensional slices of lung cells with bronchus. Specimen stained with Haematoxylin and Eosin.*

Aliasing

The sampling period x_s of the camera sensor determines the Nyquist frequency ν_{nyq}, which is given by $\nu_{\mathrm{nyq}} = 1/2x_s$. For the Hamamatsu camera C4742-95, $x_s = 6.45\mu$m and $\nu_{\mathrm{nyq}} = 77.5$cycles/mm. The cutoff frequency ν_0 of the MO is in the image space $\nu_0 = 2\mathrm{NA}/\lambda_0 M_T$, with M_T the transverse magnification of the MO-eyepiece combination. $\nu_0 = 109$cycles/mm for NA=0.6 at $\lambda_0 = 550$nm. Under these conditions the recorded images are degraded by aliasing since $\nu_0 > \nu_{\mathrm{nyq}}$. In order to preserve image quality, it was decided that aliasing should be removed, although the degradation associated with aliasing was demonstrated to be relatively benign in wavefront coded systems [93]. Aliasing can be removed by reducing the NA of the objective or by increasing λ_0 so that $\nu_0 \leq \nu_{\mathrm{nyq}}$. In order to maximise the benefits from wavefront coding in the microscope, it is preferable to increase λ_0 rather than reduce the NA. Indeed the transverse resolution, axial resolution, and the wavefront coding power decrease linearly with λ_0 whereas they decrease linearly, quadratically and cubically respectively for decreasing NA. Thus we choose $\lambda_0 = 660$nm since it is approximately the longest wavelength in the visible range. In order to satisfy the Nyquist condition, $\nu_0 \leq \nu_{\mathrm{nyq}}$, ν_0 was reduced to 74 cycles/mm by decreasing the active aperture of the MO from 11mm to $\simeq 9.75$mm. This represents a 11% reduction in aperture.

Matching NA$_o$ and NA$_c$

The illumination shown on Figure 6.1 is designed so that the NA of the condenser matches the NA of the MO. In practice however we could not match the effective NA of the condenser to NA$_o$ because of mechanical design issues: the condenser could not be placed close enough to the sample because of the thickness of the sample stage and condenser holder. A new mechanical design was required to solve this issue but could not be implemented due to time constraints. The implications of this issue will be further discussed in Section 6.6 and 6.7.

6.4.4 Choice of phase mask

The design of the MO used in the experimental set up does not permit access to its aperture plane. We therefore place the phase mask as close as practically possible to

the back surface of the MO. This means wavefronts from various off-axis field positions in the object plane will be encoded differently by the phase mask. This results in off-axis artifacts in restored images.

At the time the microscope was being implemented, two phase masks were available. The first one is a cubic phase mask designed to have a peak-to-valley OPD of 10λ at $\lambda = 550$nm, i.e $\alpha = 2.5$ at this wavelength, and has a square aperture of side 20mm. The objective on the other hand has an aperture of 11mm. To maximise the wavefront encoding, the beam exiting the MO would have to be expanded by a factor of ~ 2. A beam expander was therefore designed based on the Galilean telescope to minimise the added length between the MO and the tube lens. Its magnification $M = 1.8$ is given by the ratio of the focal length of the convex lens to that of the concave lens. It was optimised for spherical and chromatic aberrations and is shown on Figure 6.9. Its calculated MTF is shown on Figure 6.9 with a small amount of tilt in the two convex lenses. The OPD profile of the phase mask is shown in Figure 6.10 with its active pupil when implemented with the microscope and the beam expanders. The beam expander reduces the divergence of the output beam compared to that of the incident rays and therefore reduces the magnification of the microscope by a factor M. For the microscope magnification to be maintained another beam expander must be included head to tail after the phase mask. The added complexity of this design, which significantly increases the optical path length of the microscope, increases optical aberrations and therefore reduces the image contrast. Combined with a small DoF extension because of the weak phase encoding, 2.8λ peak-to-valley OPD, this overall design will be shown to be less favourable than the phase mask discussed below.

The second phase mask used is a circular aperture petal phase mask with a 11.8mm diameter. It was designed to have a peak-to-valley OPD of 11.52λ at $\lambda = 550$nm, i.e. $\alpha = 4.07$ at $\lambda = 550$nm, and $\beta = -3\alpha = -12.22$. At the 660nm wavelength that concerns us here, the parameters become $(\alpha, \beta) = (3.39\lambda, -10.18\lambda)$ and were included in the simulations described in Chapter 5. The active aperture of the phase mask is here reduced by a factor of $\simeq 0.83$ compared with the full aperture $\phi = 11.8$mm of this phase mask which corresponds to a peak-to-valley OPD of 5.4λ. This reduction in wavefront

encoding is illustrated on Figure 6.11. Figure 6.12 shows that variations with defocus in the MTF are greatly reduced with the CPM compared with a diffraction limited system, and are further reduced with the PPM. Compared to the CPM discussed above, the stronger coding power of this phase mask combined with the close match between its aperture and that of the MO removes the necessity for a beam expansion. This makes it a much preferred candidate for implementation within the microscope. Although some experiments were conducted with the CPM, we present here only experimental results obtained with the PPM because they were the most conclusive. Parameters of the two phase masks are summarised in Table 6.1.

Lens Data Editor

Edit Solves Options Help

Surf:Type		Comment	Radius	Thickness	Glass	Semi-Diameter	Conic	Par 0(unused)	Par 1(unused)
OBJ	Standard		Infinity	Infinity		Infinity	0.000000		
STO	Standard		Infinity	40.000000		5.727693	0.000000		
2*	Standard	325223	-46.305000	2.000000	N-BK7	11.200000 U	0.000000		
3*	Standard		35.227000	3.800000	SF5	11.200000 U	0.000000		
4*	Standard		104.410000	53.520567 V		11.200000 U	0.000000		
5*	Standard		179.468772	2.400000	SF5	15.500000 U	0.000000		
6*	Standard		60.975610	6.000000	BK7	15.500000 U	0.000000		
7*	Standard	22.0272	-82.481029	5.000000		15.500000 U	0.000000		
8*	Standard		Infinity	5.000000		10.000000 U	0.000000		
9*	Standard	22.0272	82.481029	6.000000	BK7	15.500000 U	0.000000		
10*	Standard		-60.975610	2.400000	SF5	15.500000 U	0.000000		
11*	Standard		-179.468772	53.520567 P		15.500000 U	0.000000		
12*	Standard		-104.410000	3.800000	SF5	11.200000 U	0.000000		
13*	Standard		-35.227000	2.000000	N-BK7	11.200000 U	0.000000		
14*	Standard	325223	46.305000	5.000000		11.200000 U	0.000000		
15	Paraxial			50.000000		6.824829			50.000000
IMA	Standard		Infinity	-		1.238723	0.000000		

Figure 6.9: *Beam expander design. From top to bottom: 3D layout, MTF, and design parameters. The magnification M is equals $-f_2/f_1 = 135/75 = 1.8$.*
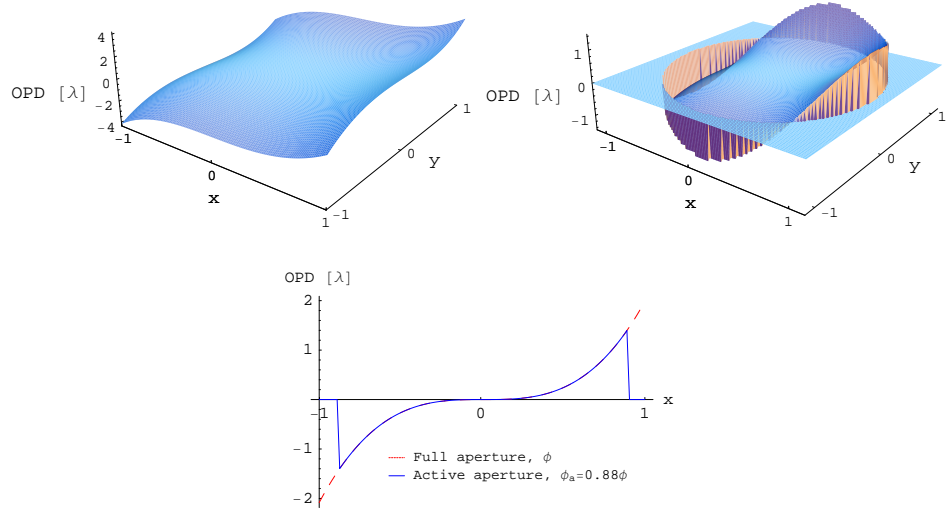
Figure 6.10: *OPD of the cubic phase mask with $\alpha = 2.08$ at $\lambda = 660nm$. Top left: full aperture, top right: active aperture. Bottom: 1D profile along the direction of maximum peak-to-valley OPD difference (x).*

Figure 6.11: *OPD of the petal phase mask with $\alpha = 3.39$ and $\beta = -10.18$ at $\lambda = 660nm$. Top left: full aperture, top right: active aperture. Bottom: 1D profile along the direction of maximum peak-to-valley OPD difference (y=x).*
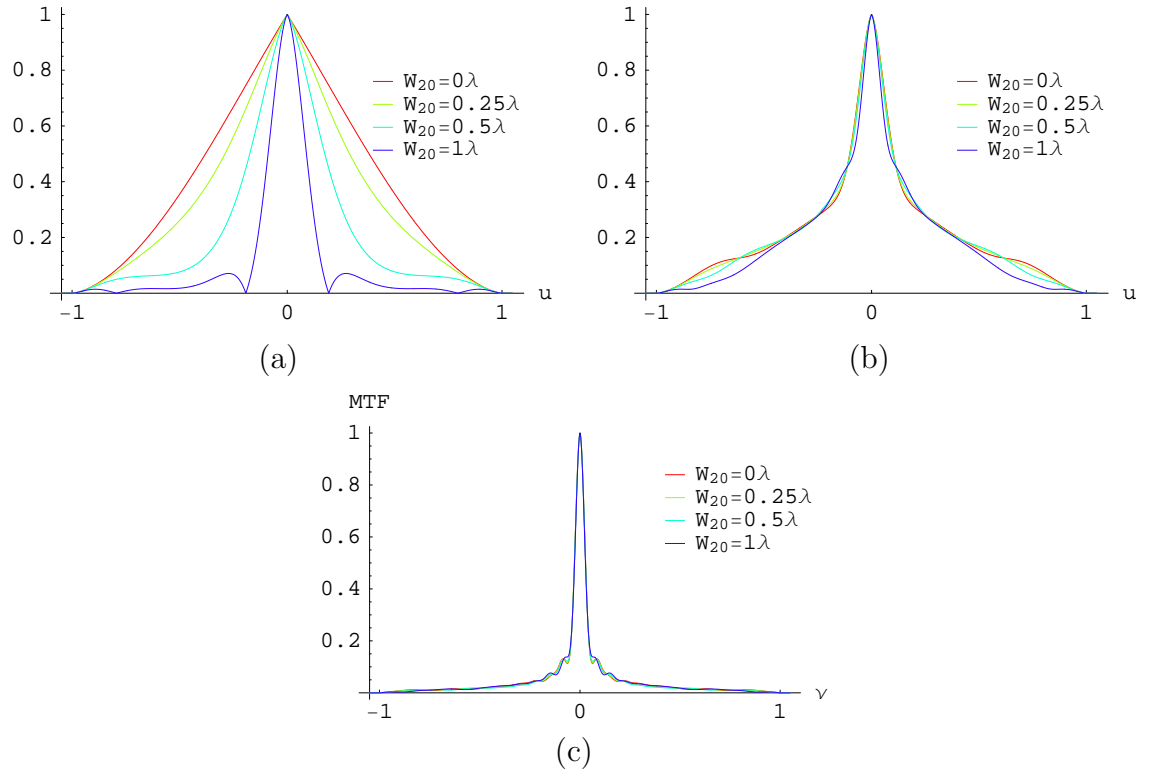
Figure 6.12: *MTF variation with defocus for various pupil functions. (a) diffraction limited system, (b) cubic phase mask ($\alpha = 2.08$ at $\lambda = 660nm$), (c) petal phase mask ($\alpha = 3.39$ and $\beta = -10.18$ at $\lambda = 660nm$).*

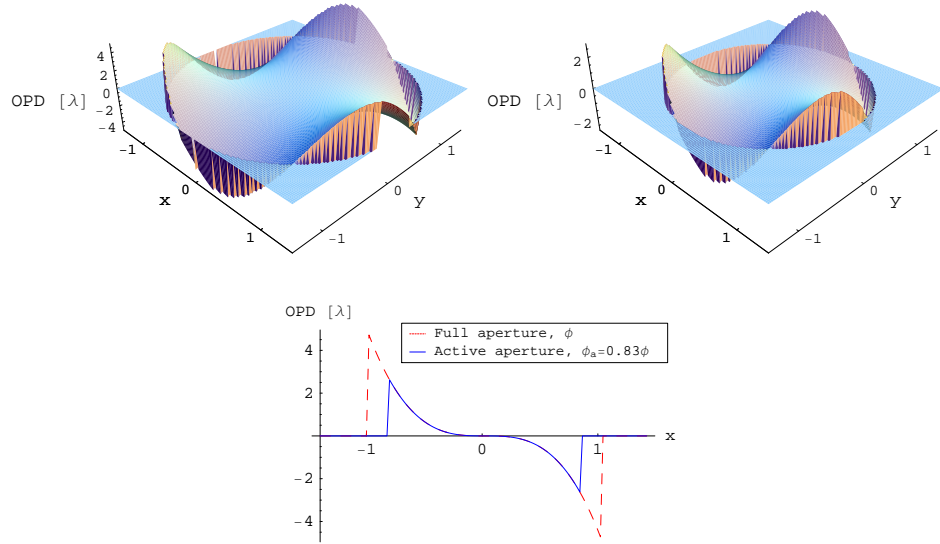|		
	Centre wavelength	$\lambda = 660$nm
	Bandwidth	$\Delta\lambda = 10$nm
Illumination	Source coherence length	$L \simeq 43.6\mu$m
	NA of condenser	$\text{NA}_c = 0.6$
	NA of objective	$\text{NA}_o = 0.6$
Imaging	Transverse magnification	$M_T = -20$
	peak to valley distance	13.8μm
	circular aperture diameter	ϕ=11.8mm
Petal phase mask	refractive index	$n_q = 1.459$
	parameters at $\lambda = 660nm$	$\alpha = 3.39$
		$\beta = -3\alpha = -10.18$
	peak to valley distance	11.98μm
	rectangular aperture side	20mm
Cubic phase mask	refractive index	$n_q = 1.459$
	parameters at $\lambda = 660nm$	$\alpha = 2.08$
	pixel size, sampling period	$x_s = 6.45\mu$m
Sensor	dynamic range	1:2250

Table 6.1: *Key parameters of the WC microscope*

6.5 PSF and OTF of the microscope

In order to restore wavefront coded images knowledge of the OTF of the system is required. The OTF can be estimated either by modelling or by indirect measurement via its PSF. Performing both estimations is important because it enables a cross-validation of the modelled and measured data. It also allows to calibrate future measurements.

6.5.1 OTF model

To achieve reasonable accuracy the model must include 1) the frequency response of the objective which is ultimately limited by diffraction, 2) the pixel response, 3) the sampling pattern. For incoherently illuminated optical systems the OTF is calculated as the autocorrelation of the generalised pupil function and was given in Eq. (5.1). To guarantee accurate simulations the cutoff frequency of the optical system is estimated in the measured PSF. The pixel response is due to the intensity integration over the area of each pixel performed at the detector. Its effect on the frequency response of the optical system is a multiplicative term $\sin ux_s \sin vx_s$. The sampling pattern results from the spatial variation of the detector response to a point source. Indeed the image of this source will depend on its position on the sensor. e.g. the image will be different if it falls between two pixels or if it is imaged on a single pixel. This only affects imaging systems that suffer from aliasing. In addition one can show that for such systems, the average contribution of this effect on the frequency response is another multiplicative term identical to the pixel frequency response [94]. Since the microscope described here is designed to exclude any aliasing, the sampling pattern is not included in the OTF model.

6.5.2 Validation of modelled and measured PSF

Figure 6.13 shows the simulated PSF and OTF of the microscope including the pixel frequency response for various amounts of defocus between $W_{20} = 0\lambda$ and $W_{20} = 0\lambda = 3\lambda$. Figure 6.14 shows the simulated PSF and OTF of the same system including the petal phase mask with $\alpha = 3.39$ and $\beta = -10.18$. It can be observed that the variation of the OTF with defocus is greatly reduced with the petal phase mask. This was

previously illustrated on Figure 6.12 where neglectable variations in the OTF can be observed between $W_{20} = 0\lambda$ and $W_{20} = 1\lambda$. Figure 6.15 and 6.16 enable comparison of the modelled and measured PSF and OTF of the system. A relative error of 19% between the measured and modelled OTF is calculated from Eq. (5.57). This error may be due to minor misalignments in the microscope, small errors in the estimates of the cutoff frequency and the transverse angular orientation of the phase mask. In addition, the accuracy of the model may be improved by including the discrete phase steps, of the order of λ, of the experimental petal phase mask employed. Nevertheless, Figure 6.16 highlights the good agreement between the model and the experimental data, especially with regard to the most important information, the phase of the OTF.

6.5.3 Defocus calibration of measured PSF

The defocus parameter of the measured PSF was calibrated by restoring these PSF with modelled PSF, whose defocus parameter is known. The defocus parameter W_{20} providing the restored PSF that was closest to the DL PSF was recorded. Figure 6.17 shows the measured PSF and OTF of the microscope for calibrated values of the defocus parameter $W_{20} = 0\lambda, 0.5\lambda, 1\lambda, 2\lambda$. Again, these measurements are in good agreement with the model shown in Figure 6.14.
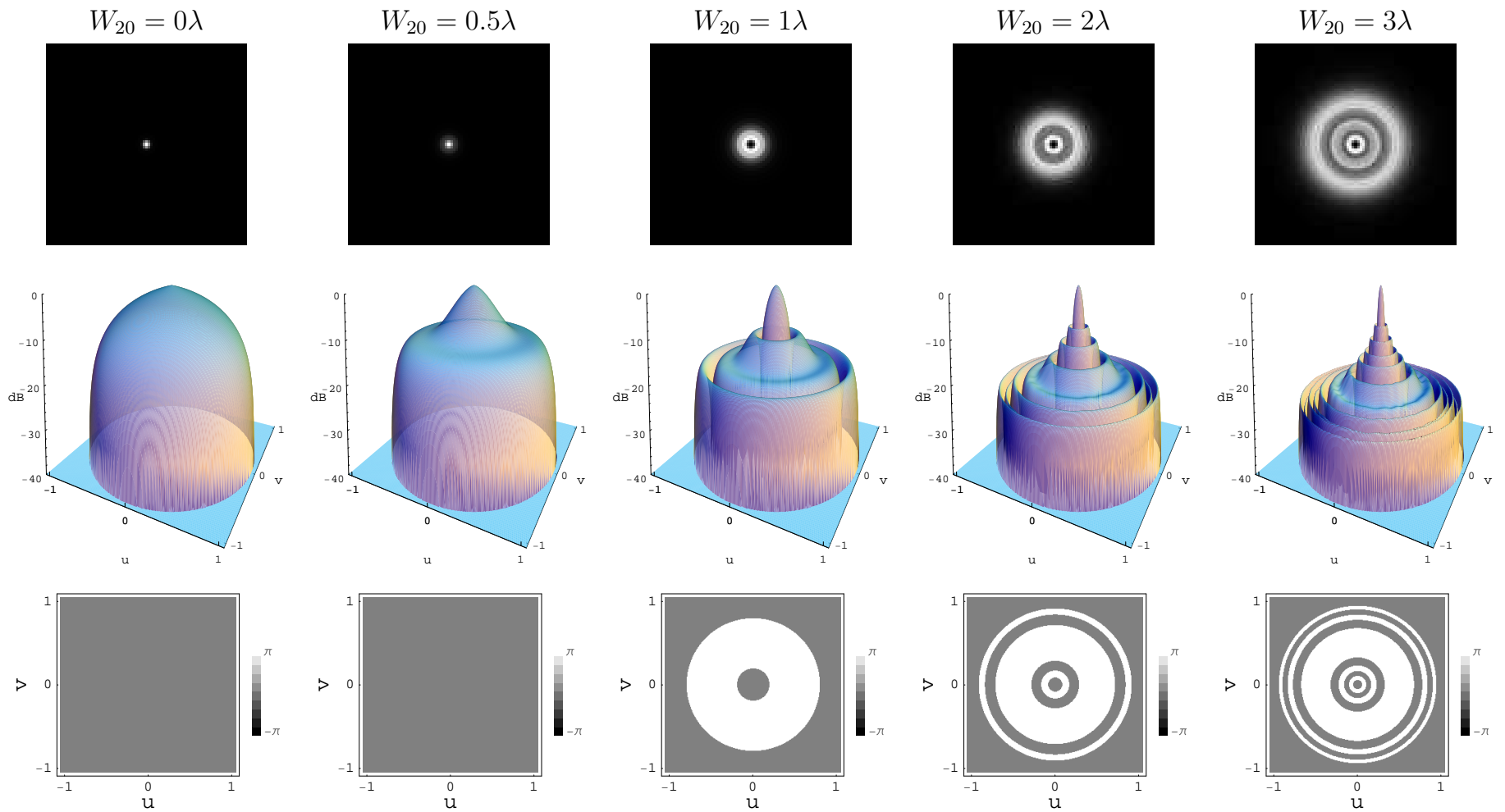
Figure 6.13: *From top to bottom: modelled PSF, MTF and phase of the OTF of the MO with varying defocus W_{20}. The pixel size of the PSF is $0.32\mu m$ in object space.*
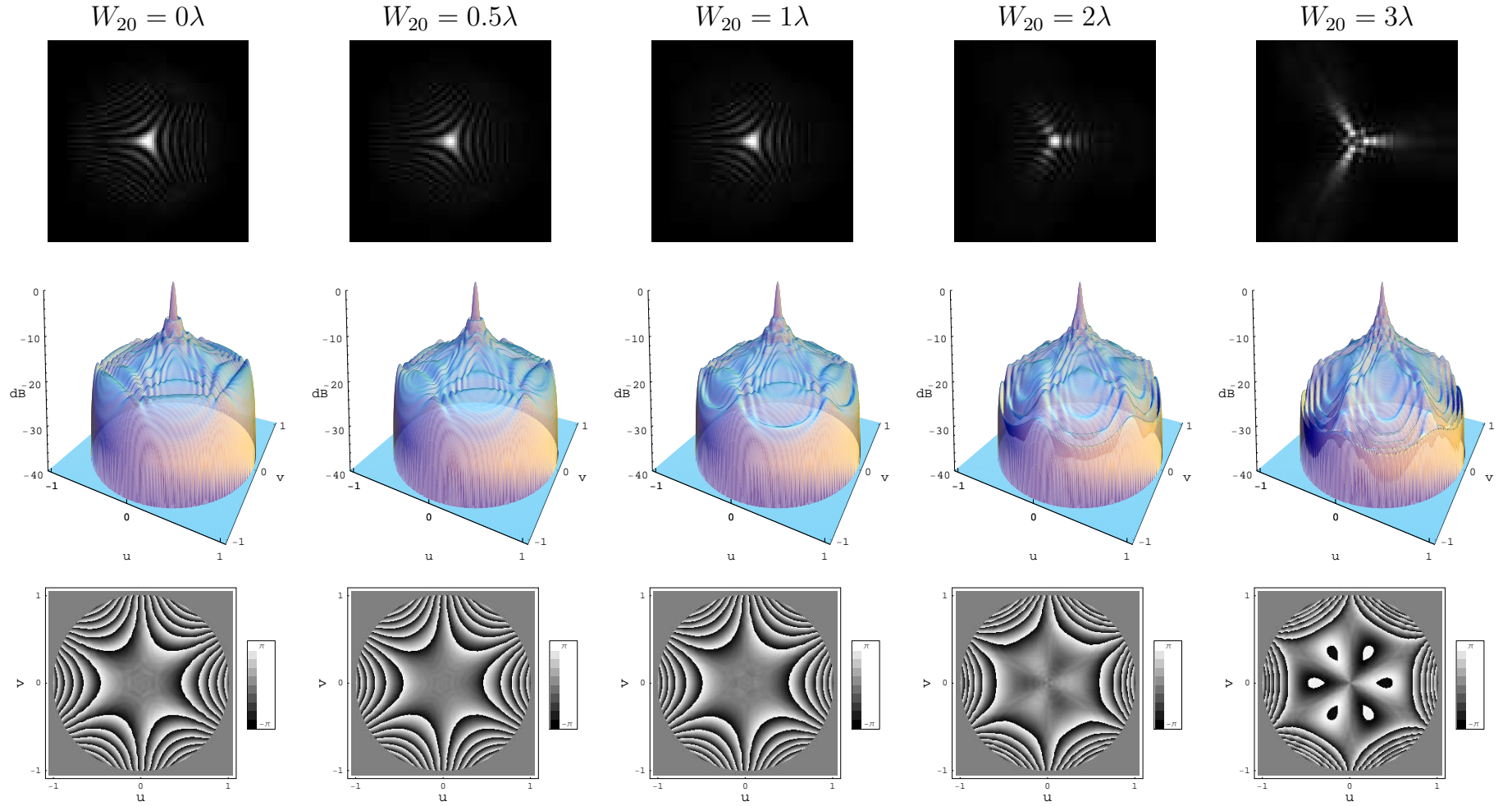
Figure 6.14: *From top to bottom: modelled PSF, MTF and phase of the OTF of the microscope including a petal phase mask with parameters $\alpha = 3.39$ and $\beta = -10.18$ for varying defocus W_{20}. The pixel size of the PSF is $0.32\mu m$ in object space.*
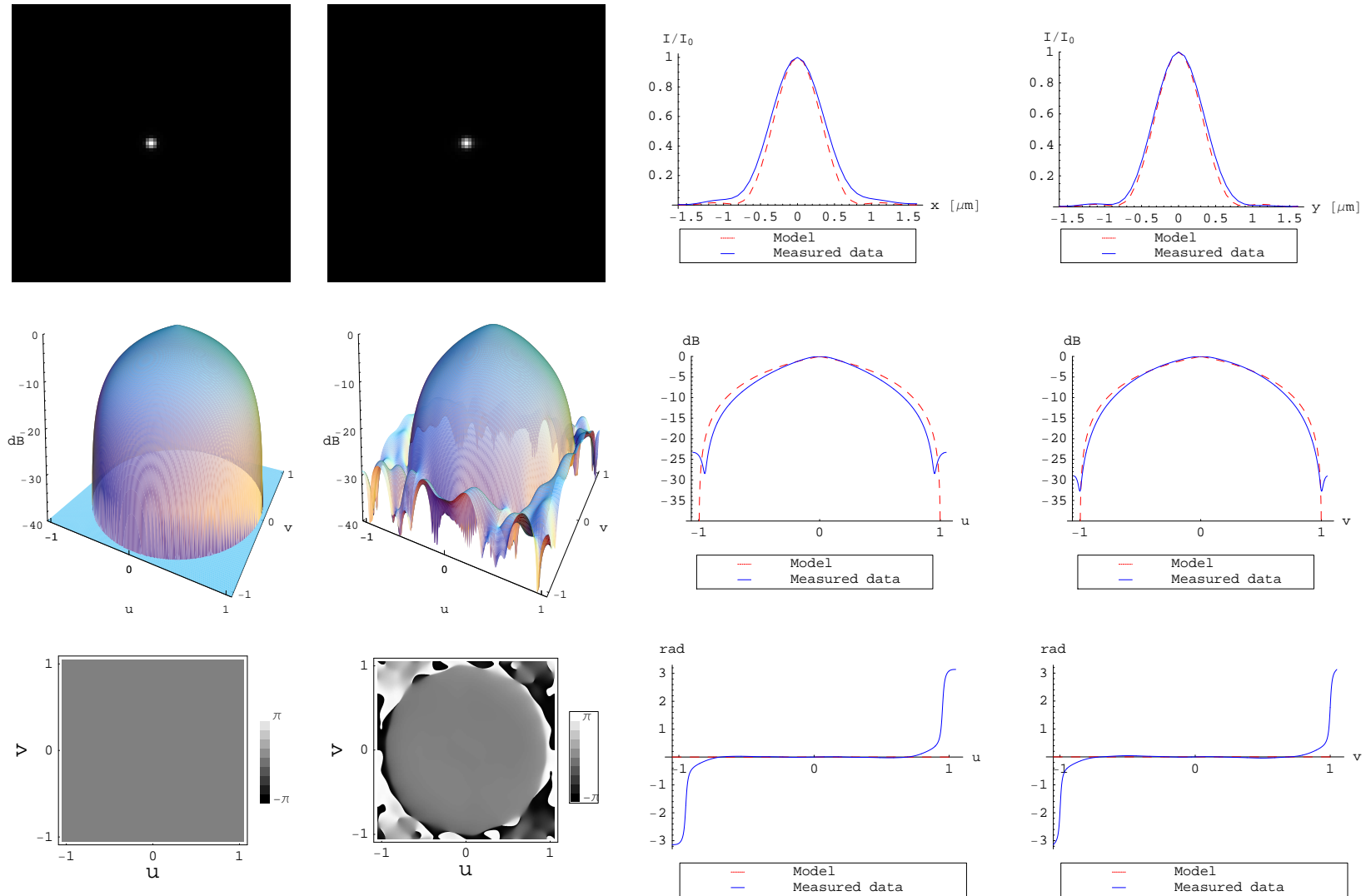
Figure 6.15: *From top to bottom: PSF, MTF and phase of the OTF of the microscope for $W_{20} = 0\lambda$. From left to right: modelled data, measured data, 1-dimensional horizontal and vertical plots. The pixel size of the PSF is $0.32\mu m$ in object space.*
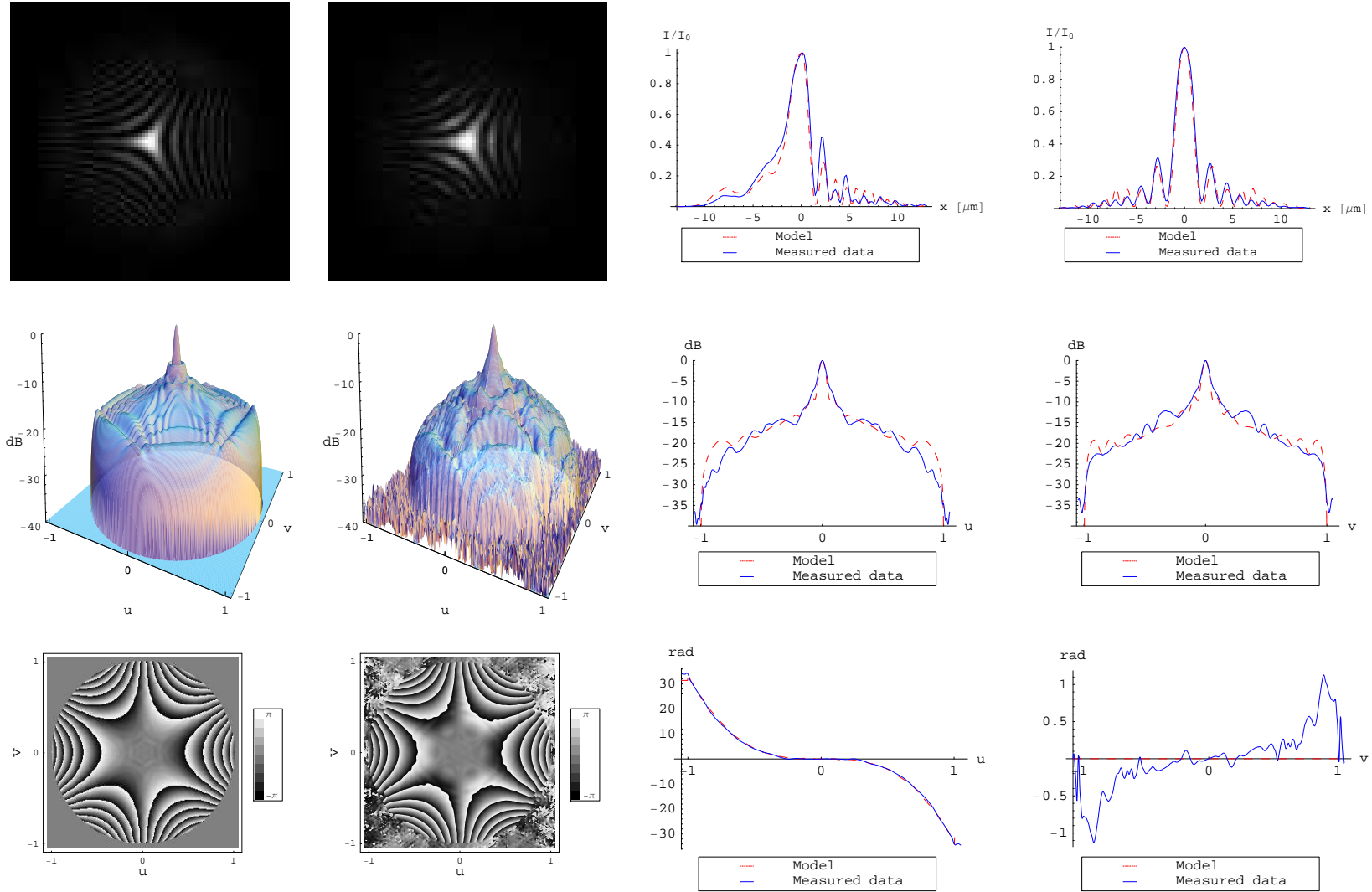
Figure 6.16: *From top to bottom: PSF, MTF and phase of the OTF of the microscope including a petal phase mask with parameters* $\alpha = 3.39$ *and* $\beta = -10.18$ *for* $W_{20} = 0\lambda$. *From left to right: modelled data, measured data, 1-dimensional horizontal and vertical plots. The pixel size of the PSF is $0.32\mu m$ in object space.*

Figure 6.17: *From top to bottom: measured PSF, MTF and phase of the OTF of the microscope with the petal phase mask ($\alpha = 3.39$ and $\beta = -10.18$). The pixel size of the PSF is $0.32\mu m$ in object space.*

6.6 Interim results with matched illumination
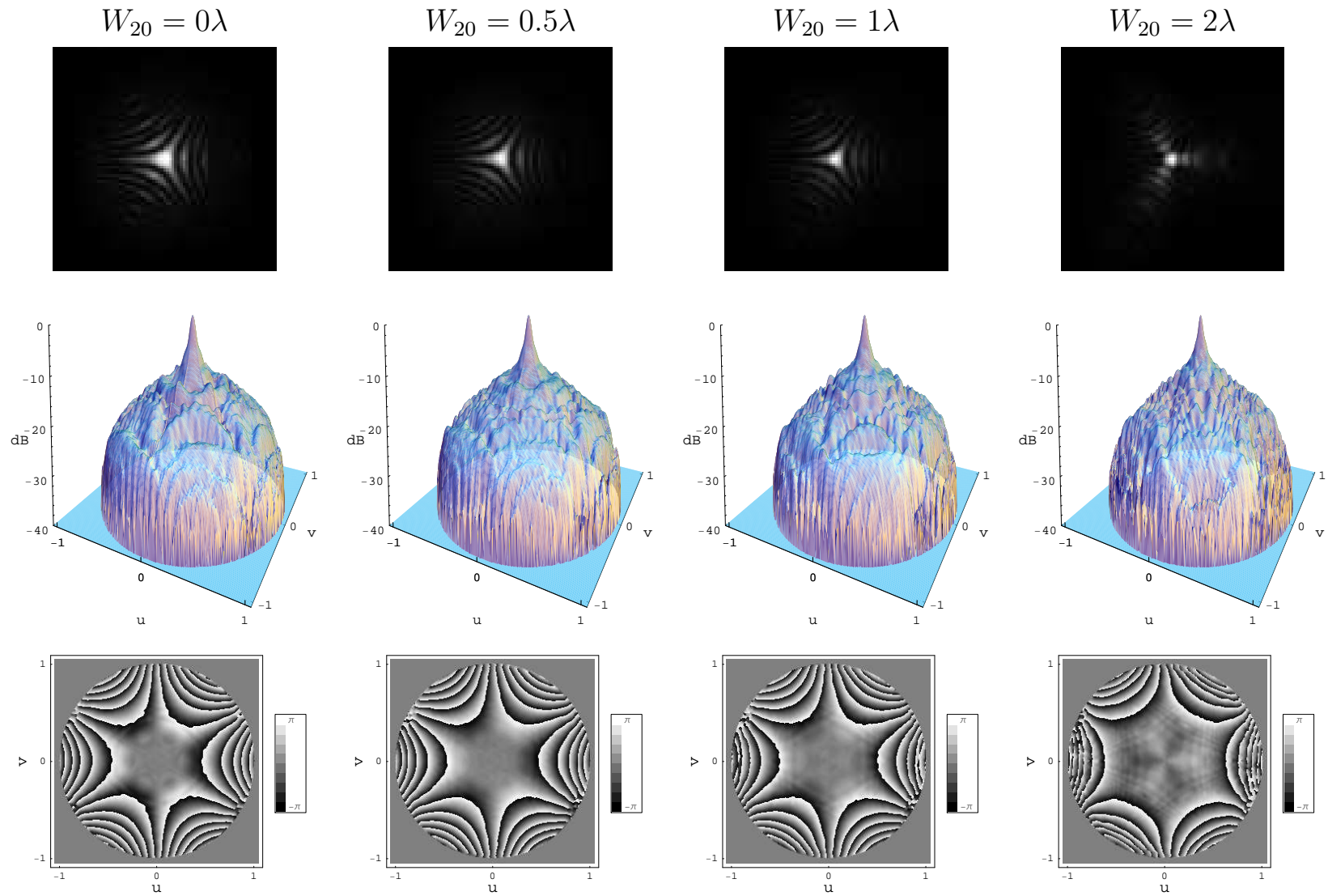
Matched illumination is achieved when $NA_c = NA_o$ and was originally thought to be critical to the implementation of WC in the transmission microscope. Indeed, since the light diffracted by an unresolved pinhole is guaranteed to fill the aperture of the MO, the measured OTF will include all spatial frequencies up to the cutoff frequency $\nu_0 = 2NA_o/\lambda$. If $NA_c < NA_o$ however, an image of a non-diffracting or weakly diffracting object will only be formed with the rays within the cone of light defined by NA_c. For such objects the highest spatial frequency transmitted by the microscope is $\nu_0 = (NA_c + NA_o)/\lambda$. There is therefore a mismatch between the image-forming cutoff frequency and the cutoff frequency of the measured OTF, used in the Wiener restoration filter, which prevents the restoration of WC images. For this reason, the active aperture of the MO was reduced to achieve matched illumination. This can be done by placing a diaphragm as close as possible to the AS of the MO and imaging a pinhole, of size approximately 2 orders of magnitude greater than λ. Such a pinhole is large enough to transmit non diffracted light with sufficient intensity but small enough to visualise the collimated beam between the MO and tube lens. Since the diffracted light is small compared to the transmitted light, the diameter of this beam is related to the effective NA of the condenser. By adjusting the aperture of the diaphragm to equal the beam width, one effectively reduces NA_o so that $NA_o = NA_c$.

6.6.1 PSF of the WC microscope with matched illumination

Because the NA of the MO was reduced to attain matched illumination, the active aperture of the petal phase mask was also reduced. The resulting severe reduction in phase encoding is shown on Figure 6.18. Following the procedure described in Section 6.5, the OTF of the system in matched illumination is modelled as well as measured. Figure 6.19 shows that the modelled and measured data are in good agreement. The change in MTF between $W_{20} = 0\lambda$ and $W_{20} = 1\lambda$ is presented in Figure 6.20.

By measuring the reduced cutoff frequency ν_{0c} of the OTF, NA_c can be estimated based on the following equality:

$$\frac{NA_c}{NA_o} = \frac{\nu_{0c}}{\nu_0},$$

(6.3)

where ν_0 is the cutoff frequency of the MO at full numerical aperture NA_o. From the measured MTF shown in Figure 6.19, one estimates that $\nu_{0c} \simeq 805 \text{cycles/mm}$ (in object space) at $\lambda = 640\text{nm}$. Using Eq. (6.3), the NA of the condenser is therefore estimated to be $NA_c \simeq 0.26$. Thus when the MO aperture is fully opened $NA_c/NA_o \simeq 0.43$, and when it is adjusted to avoid aliasing so that $NA_o \simeq 0.49$, $NA_c/NA_o \simeq 0.53$.
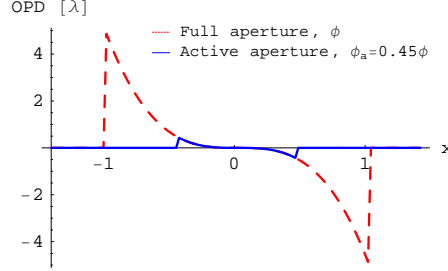
Figure 6.18: *OPD of the petal phase mask with a reduced active aperture due to matched illumination ($NA_c = NA_o \simeq 0.26$). The profile is taken along the direction of maximum peak-to-valley OPD difference (y=x).*

6.6.2 Interim experimental results

Interim experimental results are presented in this section with the chrome-on-glass USAF target (Edmund optics). This target has periodic bar patterns with calibrated spatial frequencies. The highest spatial frequency in the target is 645 cycles/mm and is located in the pattern group 9. Following the multiple-kernel image restoration described in Chapter 5, each WC image is restored with a set of filters based on PSF measured at different defocus parameters. Figure 6.21 presents the non-coded images, WC images and restored images for $W_{20} = 0\lambda$ and $W_{20} = 0.5\lambda$. The restored images are obtained after restoration with $\hat{W}_{20} = W_{20}$. The in-focus restored image is slightly degraded by bright replicas near dark bars. These image restoration artifacts strongly degrade the quality of the restored image shown in bottom right of Figure 6.21, despite the modest amount of defocus $W_{20} = \hat{W}_{20} = 0.5\lambda$. In the next section potential causes for these strong image artifacts will be discussed.
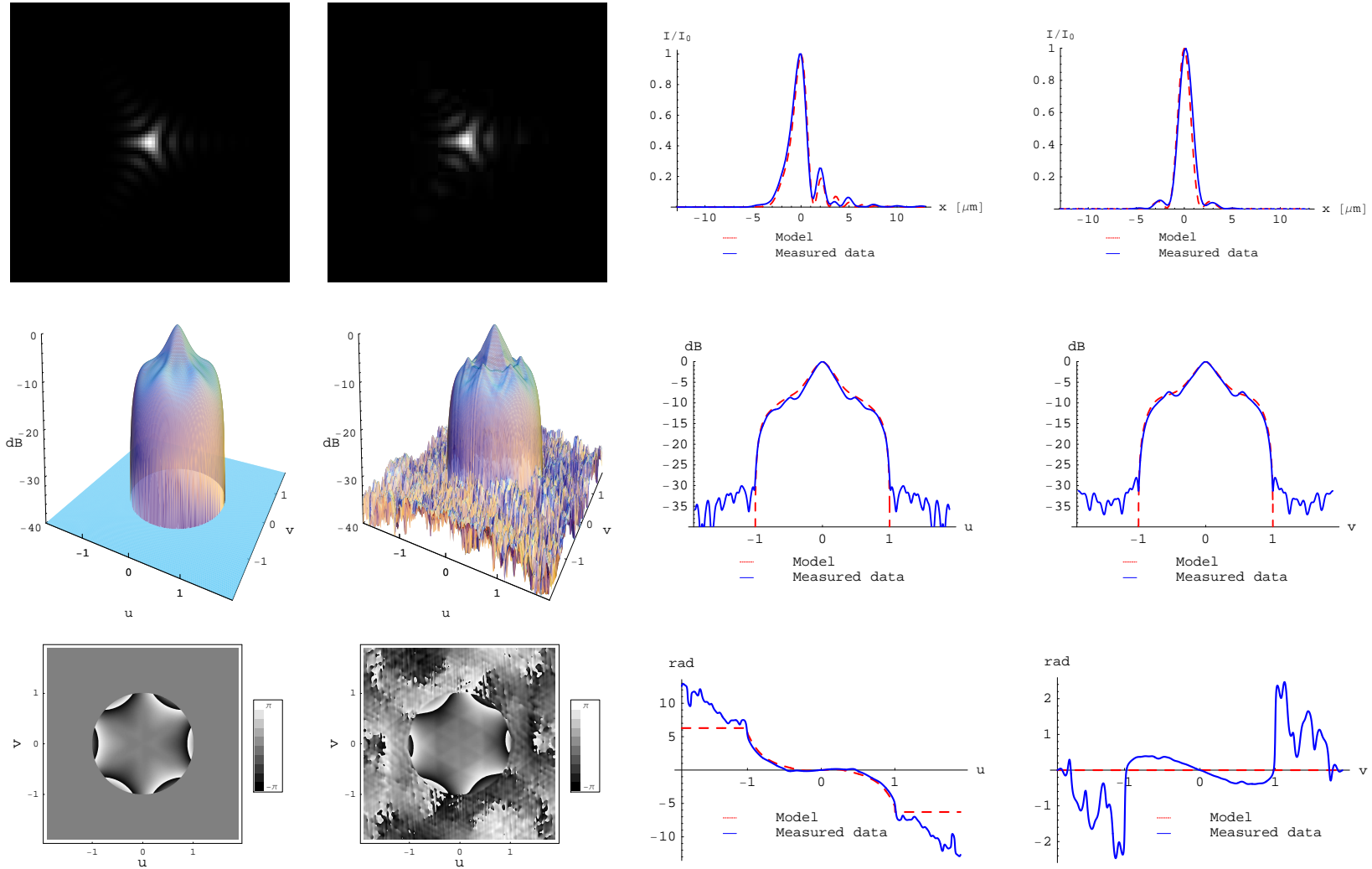
Figure 6.19: *From top to bottom: in-focus PSF, MTF and phase of the OTF of the microscope with the petal phase mask. Matched illumination with $NA_c = NA_o \simeq 0.26$. From left to right: modelled data, measured data, 1-dimensional horizontal and vertical plots. The pixel size of the PSF is $0.32\mu m$ in object space.*
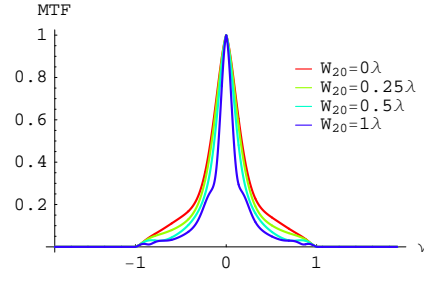
Figure 6.20: *MTF variation with defocus for the petal phase mask and matched illumination (see Figure 6.18).*

non-coded	WC	restored
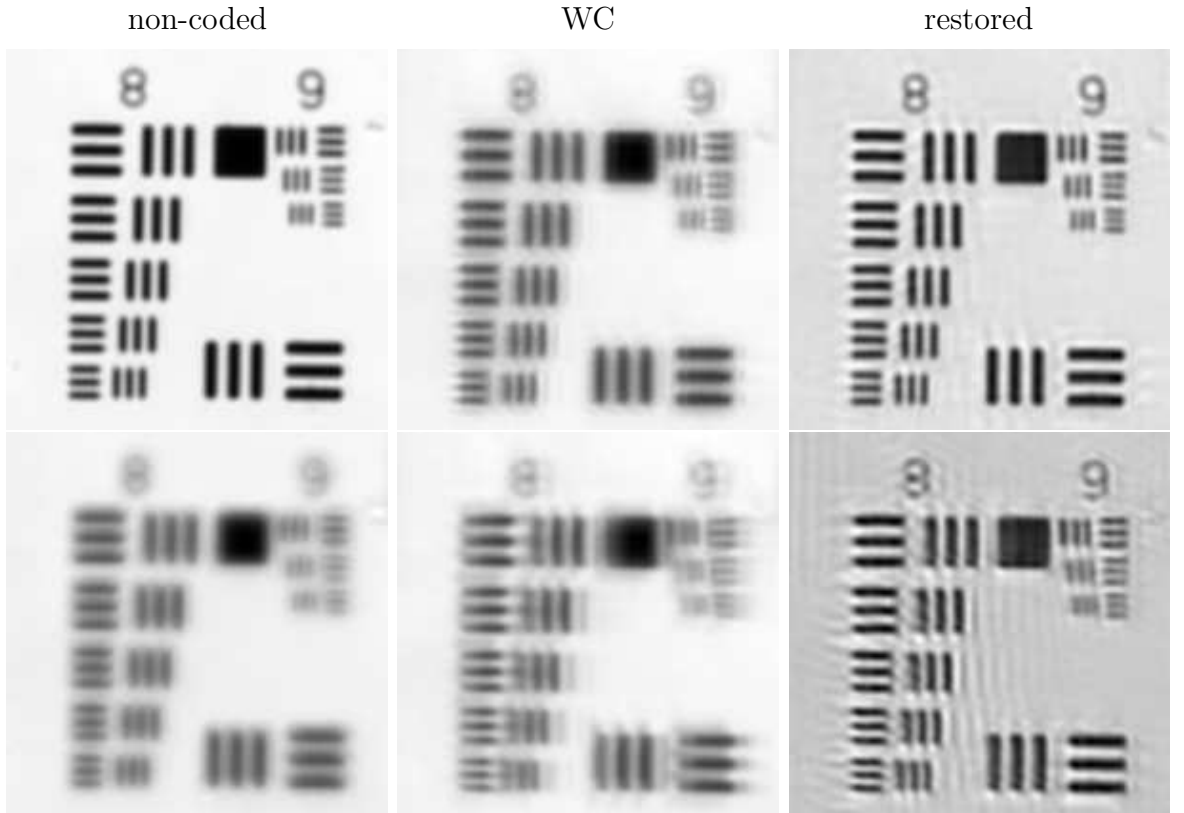
Figure 6.21: *Non-coded image (left), WC image (centre) and WC image restored with the defocus parameter $\hat{W}_{20} = W_{20}$. $W_{20} = 0\lambda$ (top row) and $W_{20} = 0.5\lambda$ (bottom row). Note the strong image artifacts that degrade the restored image at $W_{20} = 0.5\lambda$.*

6.6.3 Discussion

Possible reasons that may cause the strong image artifacts exhibited in Figure 6.21 are detailed here, together with the solutions applied to address them: 1) an incorrect PSF is used in the image recovery: the measured and modelled OTF displayed in Figure 6.19 are clearly in very good agreement, 2) mismatched illumination: the strong image artifacts were still present with matched illumination as was observed in Figure 6.21, 3) off-axis aberrations (spherical, astigmatism) not included in the modelled and measured PSF: this hypothesis was excluded because artifacts also appeared on-axis, 4) chromatic aberrations due to the phase mask: these were minimised by using a 10nm narrow band illumination, 5) aliasing: the active aperture of the MO was reduced to remove any aliasing, which was demonstrated in the OTF presented in Figures 6.15 and 6.19, 6) the image artifacts are inherent to the Wiener restoration algorithm itself: the restoration algorithm was validated with numerous simulated images.

Having addressed all these potential sources of errors it was suspected that the artifacts were related to the main characteristic that differentiates transmission microscopy from conventional photography, the illumination. It was found in the literature that the transmission microscope is in general not an incoherent system due to the transillumination. This would mean that the convolution product between the intensity distribution in the object plane and the PSF of the system no longer equals the detected intensity distribution in the image plane. Since this relation forms the basis of the image restoration we employ, this hypothesis could explain the distortion in the recovered images. These artifacts will in turn degrade the robustness of the defocus estimates and must be suppressed. In the next section the effect of the transillumination on the image formation in the microscope will be analysed.

6.7 Effect of transillumination on image formation

6.7.1 Image formation with partially coherent illumination

The transillumination can be shown to introduce some degree of spatial coherence in the optical system, even if a totally incoherent light source is employed. The reason

for this lies in the diffraction at the condenser lens, which creates an Airy disk in the object plane of the microscope objective (MO) for each secondary point source at the field stop. The light across each Airy disk is coherent, since it originates from a single point source. But the light of different Airy disks are incoherent, since they originate from different secondary point sources in the field stop. Consequently the sample in the object plane of the MO receives both coherent and incoherent contributions. Thus one needs to calculate the complex degree of coherence of light in the object plane. This quantity can be shown to depend on the spatial extension of the illuminated specimen, i.e. the FoV, and the numerical aperture NA_c of the condenser. A detailed analysis of the effect of specimen transillumination on the resolution in a microscope is given in [95]. We summarise here the key aspects of this discussion. Since the active region of the specimen is much larger than the effective size of the Airy disk due to the condenser, the illumination system described above is such that the condenser aperture is incoherently illuminated. The expression of the equal time complex degree of coherence $V(P_1, P_2)$ between to points $P_1(x_1, y_1)$ and $P_2(x_2, y_2)$ in the object plane of the MO is of the form:

$$V(P_1, P_2) = \frac{2J_1(u_{12})}{u_{12}} \quad , \quad u_{12} = \frac{2\pi}{\lambda_0} h_{12} n_c \sin \theta_c , \tag{6.4}$$

with $NA_c = n_c \sin \theta_c$ and $h_{12} = \sqrt{(x_1 - x_2)^2 + (y_1 - y_2)^2}$ the distance between the points P_1 and P_2. We define another point $P(x, y)$ in the object plane of the MO and denote by P' its conjugate in the image plane of the MO. We consider the contributions from the point sources at P_1 and P_2 to the intensity $I(P')$ detected at P':

$$I(P') = \left(\frac{2J_1(v_1)}{v_1} \right)^2 + \left(\frac{2J_1(v_2)}{v_2} \right)^2 + 2 \frac{2J_1(mv_{12})}{mv_{12}} \frac{2J_1(v_1)}{v_1} \frac{2J_1(v_2)}{v_2} , \tag{6.5}$$

where:

$$m = \frac{n_c \sin \theta_c}{n_o \sin \theta_o} , \tag{6.6a}$$

$$v_{12} = \frac{u_{12}}{m} , \tag{6.6b}$$

$$v_1 = \frac{2\pi}{\lambda_0} h_1 n_o \sin \theta_o , \tag{6.6c}$$

$$v_2 = \frac{2\pi}{\lambda_0} h_2 n_o \sin \theta_o , \tag{6.6d}$$

with $h_1 = \sqrt{(x - x_1)^2 + (y - y_1)^2}$, $h_2 = \sqrt{(x - x_2)^2 + (y - y_2)^2}$ and $NA_o = n_o \sin \theta_o$. The first two terms in Eq. (6.5) represent the incoherent contributions to $I(P')$ from

137

point sources at P_1 and P_2, whereas the third term is due to their partially coherent contributions. Note that when $m \to 0$, the intensity distribution $I(P')$ follows that of perfectly coherent illumination, whereas the illumination is totally incoherent when $m \to \infty$. Thus m is referred to as the incoherence parameter. Because of the term $2J_1(mv_{12})/mv_{12}$ in Eq. (6.5) the optical system is linear neither in amplitude, as in a perfectly coherent system, nor in intensity, as in a perfectly incoherent system. Instead the system is said to be bilinear because it depends on the object amplitude at two points [96, 97]. Eq. (6.5) can be used to determine the value of m that optimises the resolution. Born & Wolf [95] find that optimal resolution is achieved when $\mathrm{NA}_c = 1.5\mathrm{NA}_o$ and that it is slightly smaller than the $0.61\lambda_0/\mathrm{NA}_o$ achieved with totally incoherent illumination (providing that $\mathrm{NA}_c \geq \mathrm{NA}_o$).

It must be stated here that the partial coherence of the illumination in the microscope was only understood near the end of this project. As a consequence an interim solution that could be implemented rapidly was sought. A potential solution to obtain an incoherent system consists of illuminating the specimen by reflection. This solution suffers from low light collection and would result in higher noise levels in recorded images. We recall that noise amplification is the key tradeoff in WC systems. Interim results with this type of illumination suggested the high noise levels made WC impractical in this case. Another solution to remove coherence consists of placing a diffuser between the condenser and the specimen, very close to the specimen to minimise light losses. This solution offers the advantage of decoupling the illumination system from the microscope and ensures the resolution achieved is given by Eq. (6.2) regardless of NA_c. This is particularly useful in the present case since for practical reasons NA_c appeared to be smaller than NA_o, as was demonstrated in Section 6.6. Since image formation is now incoherent, the full aperture of the MO can be filled and is only slightly closed down to avoid aliasing effects. Hence the stronger phase encoding that comes with larger active apertures is performed and was shown in Figure 6.11. Similarly, the OTF presented in Section 6.5 can be used again in the restoration algorithm. The main drawback of this solution is to reduce the image contrast to that of an incoherent imaging system. It may also cause shadows and glare when the light reaching the specimen is uneven. It is worth noting that Köhler illumination was specifically designed to avoid

introducing such diffusers. However for the present work, implementation of WC in a wide-field microscope, the benefits of this solution in terms of imaging performances clearly outweighed its disadvantages.

6.7.2 Tradeoff between transverse resolution and contrast

Keeping in mind the Abbe's image formation theory, it is clear that if the degree of coherence of the light projected onto the grating is reduced, the diffracted rays will interfere less strongly in the BFP of the MO, resulting in a reduced contrast image. Since the degree of coherence in the object plane of the MO depends on NA_c according to Eq. (6.4), an increase in NA_c will reduce the overall degree of coherence of light illuminating the sample, thereby reducing the contrast of the image towards that of an incoherent system. Put differently, compared to conventional imaging where light at the object is incoherent, partial coherence in microscopy will increase image contrast. This also shows there is a tradeoff between contrast and transverse resolution in transilluminated microscopy. The necessary compromise between these two attributes can be obtained by adjusting the diaphragm in the aperture of the condenser. We illustrate the effect of the degree of coherence of light in the object plane by placing a diffuser between the condenser and the target. The diffuser greatly reduces the degree of coherence (increases m to infinity) resulting in a reduced image contrast but ensures that the full aperture of the MO is filled, thereby achieving maximum transverse resolution. This effect is illustrated in Figure 6.22.

6.7.3 OTF in partially coherent illumination

We recall that the OTF of a coherent imaging system is readily obtained from the pupil function. For incoherent imaging systems the OTF is given by the autocorrelation of the pupil function, thereby providing a two-fold increase in cut-off frequency, in agreement with Eq. (6.1) and (6.2), but with a near-linear attenuation of the high spatial frequencies. For partially coherent imaging systems, as is generally the case in transmission microscopy, the OTF becomes four-dimensional [79]. In addition to the degree of coherence of light in the object, the OTF is influenced by the mechanisms of image formation that vary with the type of object being imaged. For so-called
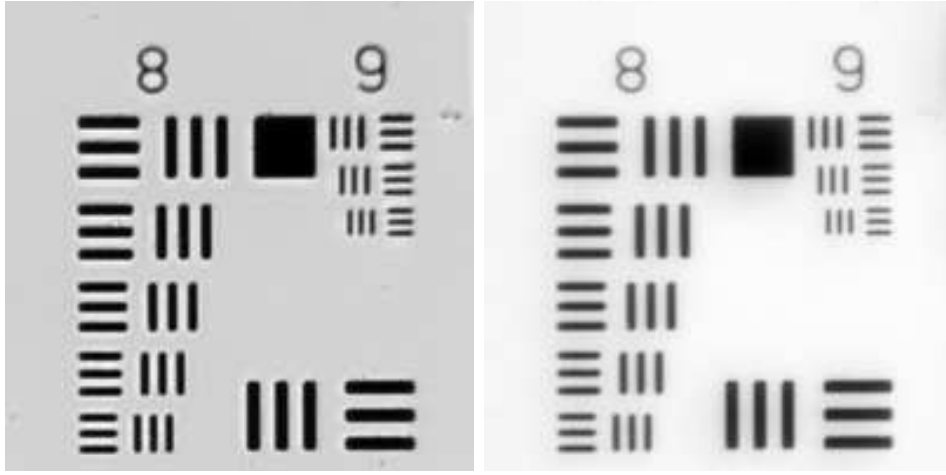
Figure 6.22: *Partial coherence effect on image contrast. Left: image recorded with partially coherent light. right: image recorded with a holographic diffuser placed between the condenser and the object (very close to the object), which decreases the light coherence. Note the reduced contrast of the image recorded in reduced light coherence (right image).*

strong objects, contrast is formed via diffraction and absorption. For such objects the partially coherent OTF is complex and four-dimensional. For weak objects, where the diffracted light is much less intense than the non-diffracted light the image is formed via phase and absorption. In this case, the OTF becomes two-dimensional and relates the object (complex) transmission function to the image intensity. The concept of three-dimensional aperture and three-dimensional transfer function for a partially coherent microscope is detailed by Streibl in [98] for such objects. Most importantly, Streibl shows that the transmission of the phase and absorption information of such objects is carried out via the real and imaginary parts of the OTF respectively. The two-dimensional defocused transfer function of a partially coherent microscope is expressed analytically in [96] for these objects. When the system is in-focus the cutoff frequency ν_0 of the OTF increases linearly with the coherence parameter m, in agreement with Eq. (6.1):

$$
\nu_0 = \begin{cases} \dfrac{\mathrm{NA}_o}{\lambda}(1+m) & \text{, for } 0 \leq m \leq 1\,, \\[2mm] \dfrac{2\mathrm{NA}_o}{\lambda} & \text{, for } m > 1\,. \end{cases} \tag{6.7}
$$

The contrast-resolution tradeoff in the transmission microscope is directly explained by the change in the OTF with the coherence parameter m.

6.8 Extended depth of field of the WC microscope

6.8.1 Restoration with modelled and experimental PSF

Following the discussion on the degree of coherence of the illumination, and detailed in the previous section, images of the sample are now recorded with a diffuser placed between the condenser and the sample. This diffuser has the effect to remove coherent contributions from the image formation. In this section the quality of the image restorations based on experimental and modelled PSF are compared. Images of the USAF target, oriented horizontally, are recorded for increasing amounts of defocus. At each value of defocus, the restored images presented have been selected from a set of images restored with filters having different estimated defocus parameter $\hat{W}_{20}$. The selection, performed here by a human operator, is based on the human perception of image quality (sharpness, contrast, artifacts/distorsion amplitude). Figure 6.23 presents non-coded images (left column) and WC images restored with experimental and modelled PSFs respectively (centre and right columns) for various amounts of defocus. Restored images in both cases clearly display increased resolution and contrast compared to the non-coded images. This demonstrates that extended DoF in the microscope is achieved. Small artifacts in restored images can be observed in the form of oscillations around strong edges and appear here as dark and bright spots. We recall that these artifacts were previously described in Section 5.4.2 with simulated images. It is important to note here that images restored with measured PSF (centre column) clearly exhibit lower levels of artifacts and have a higher contrast than those restored with the modelled PSF (right column). This result highlights the non-neglectable effect on restoration performance of the small differences between the measured and modelled OTF, whose origin were discussed in Section 6.5. Note that the defocus estimated from both restorations can differ by $\lambda/4$. Figure 6.23 also shows that image restoration performance decreases with large defocus values, typically $W_{20} = 2.5\lambda$.
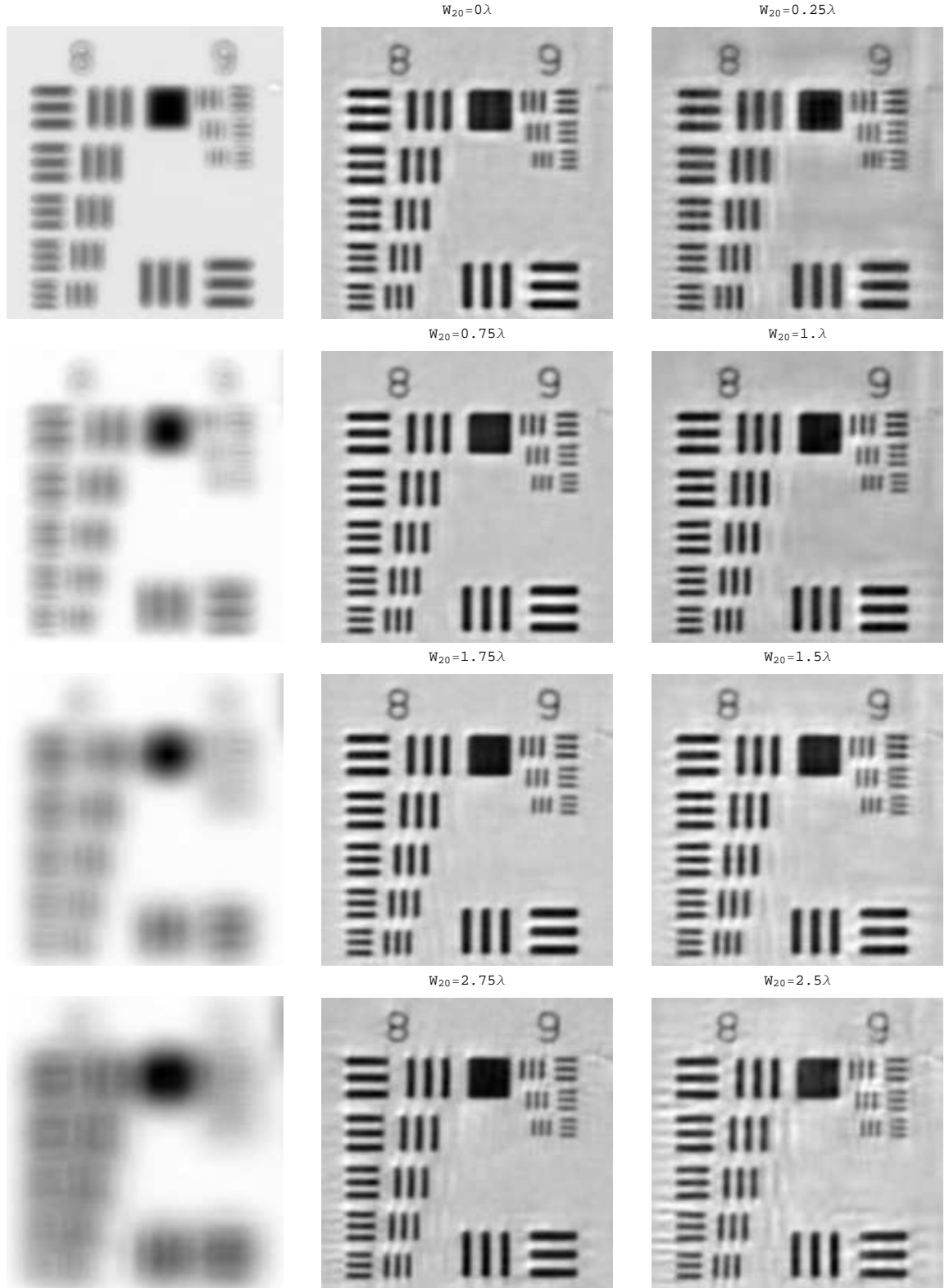
Figure 6.23: *Image restoration comparison. From left to right: non coded image, encoded image restored with measured and modelled PSF respectively. The estimated defocus parameter is shown above each image.*

6.8.2 Assessing the extended depth-of-field

In conventional WC systems the DoF is increased to the defocus region where only small variations in the PSF occur. In the previous section and in Chapter 5, the DoF is extended beyond this region by restoring the image with a set of PSFs corresponding to different defocus values. There is a lack in the literature of a simple optical based criterion to determine the boundary between these two regimes. Hopkin's DoF criterion, i.e. an 80% threshold in the ratio of the defocused MTF to the in-focus MTF, could be used but it does not account for the fundamental difference between DL and WC systems. Namely that the OTF of WC systems is complex. In addition, it is well known that the phase information in the spectrum of an image is dominant over its amplitude information [99]. It can therefore be argued that for WC systems, a DoF criterion must account for the difference between the phases of the defocused and in-focus OTFs. We propose a simple criterion based on the presence of phase inversions at any spatial frequency in the restored OTF of the system. The restored OTF is defined as the ratio of the defocused OTF to the in-focus OTF. Indeed, these phase inversions lead to strong image artifacts that are illustrated in Figure 6.24. The effects of phase inversions and zeros in the OTF is assessed by applying these distortions to a small region of the image spectrum. This region is chosen to match the high spectrum amplitude corresponding to a small part of the image (the three vertical bars located third from top left in the image). For both distortions we observe that this part of the image is more degraded than features with significantly different spectrum content. Note also that in both cases the whole image is degraded by spurious oscillations. However the image degradation due to phase inversions is clearly more severe than the one due to artificial spectrum nulls. For a diffraction limited system such phase inversions occur for values of W_{20} greater than $W_{20}^{\mathrm{inv}} = 2/\pi \simeq 0.64$. For the CPM and PPM previously described they occur when W_{20} is greater than 0.97 and 1.46 respectively. Figure 6.25 shows the phase inversions in the restored OTF of these three optical systems. Note that there is a difference between the phase inversions in DL and WC systems. Indeed for DL systems the phase inversion transitions in the OTF are accompanied by zeros in the MTF whereas this is generally not the case in the restored OTF of WC systems. Furthermore, for DL systems the phase of the restored OTF equals that of the defo-

cused OTF and is binary (equal to zero or π). For these reasons it may not be relevant to directly compare the values of W_{20}^{inv} in DL and WC systems. Nevertheless for WC systems, W_{20}^{inv} provides an upper limit to the defocus value that can be tolerated using a single filter restoration. Beyond this limit, phase inversions in the spectrum of the object cause strong spurious signals in the restored image. These can only be removed by mean of a deconvolution based on the PSF at W_{20}.

Figure 6.26 and 6.27 present simulation results of the image artifacts obtained with the PPM and the CPM respectively. These results show that the phase inversion criterion can be reasonably used to estimate the extended depth of field of these WC systems. Note however that for each phase mask the phase error, i.e. the phase of the restored OTF, varies differently with defocus. For instance, the phase error is strong in the first and third quarters of the OTF for the CPM, whereas it exhibits a degree of rotational symmetry of 3 for the PPM. This suggests that a criterion based on the total phase error might be more accurate in characterising the EDF of a phase mask using single kernel restoration.

6.9 Spatially variant restoration

In the previous section the extended DoF with multiple-kernel restoration in the WC microscope was assessed. This technique demonstrated a DoF extended up to 2.5λ in an horizontally oriented target. In the next section we seek to apply this technique to an object that exhibits features at different ranges. Image segmentation is therefore required and is performed here manually. A set of sub-images containing meaningful features, referred to as snippets in the image processing literature, are selected. For each snippet, the restored image that optimises the proposed metrics of defocus are selected. The defocus estimates are validated by a human operator, ensuring that the best perceived restored snippet was indeed selected by each metric. Since this procedure provides an estimate of the defocus parameter from which the range can be measured, a more accurate assessment consists in quantifying the uncertainty of the range estimates. This will be performed in the following section.
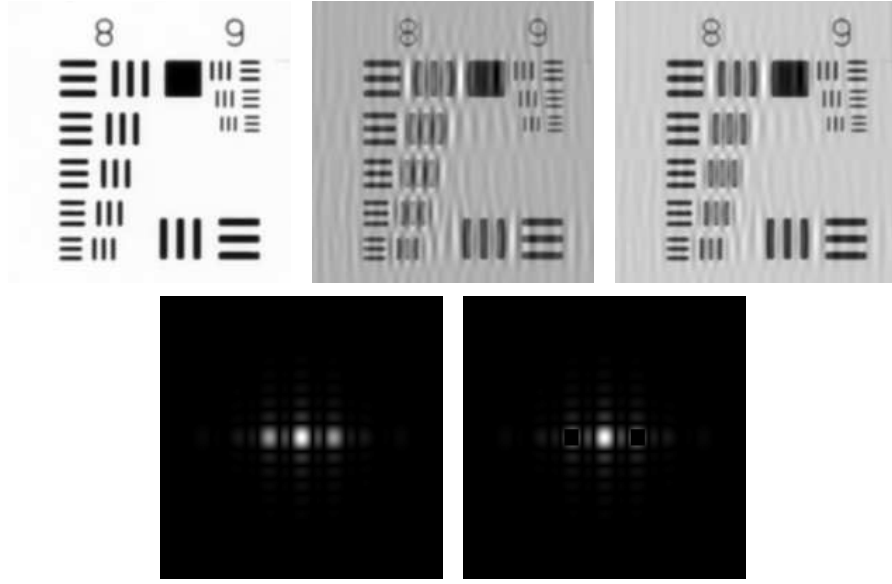
Figure 6.24: *Image artifacts due to phase inversions and zeros in the MTF. Top row: raw image (left), image resulting from phase inversions in its spectrum (centre) and image resulting from zeros in its spectrum (right). Bottom row: spectrum of the three vertical bars located third from top left in the raw image (left), same spectrum showing the regions where phase inversions and zeros are applied (right).*
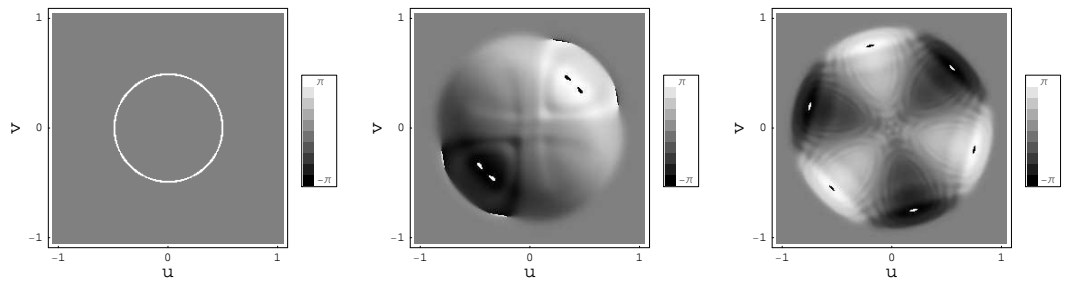
Figure 6.25: *Phase inversions in the restored OTF, $H(u; W_{20})/H(u; 0)$, of various systems. From left to right: DL system with $W_{20} = 0.64$, CPM with $W_{20} = 0.98$ and PPM with $W_{20} = 1.48$ respectively. Black and white regions indicate a phase inversion.*
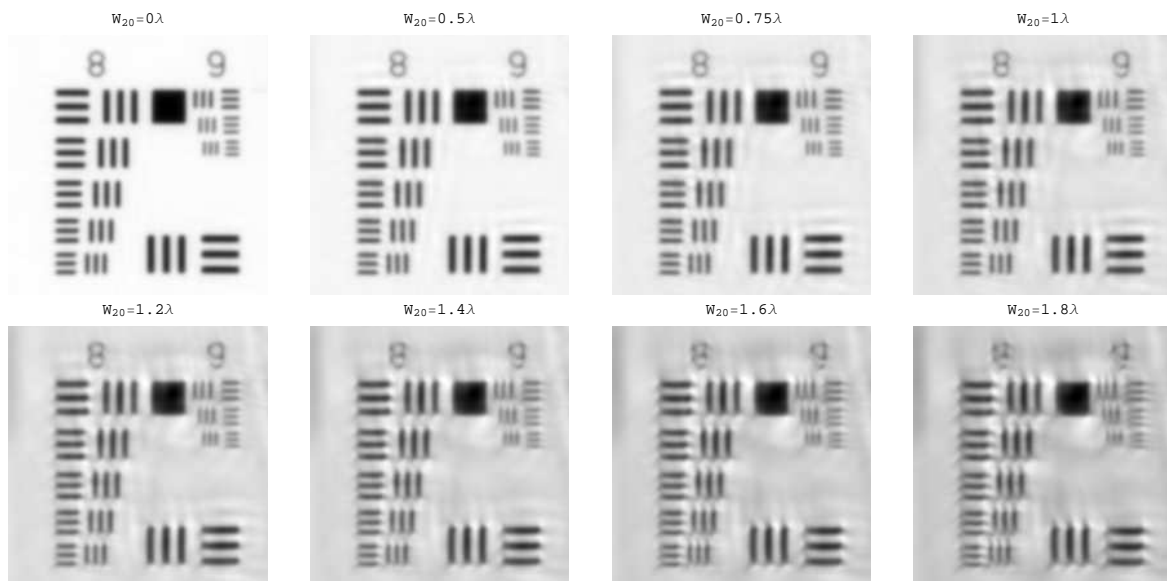
Figure 6.26: *Simulation of image artifacts with the PPM for various amounts of defocus.*
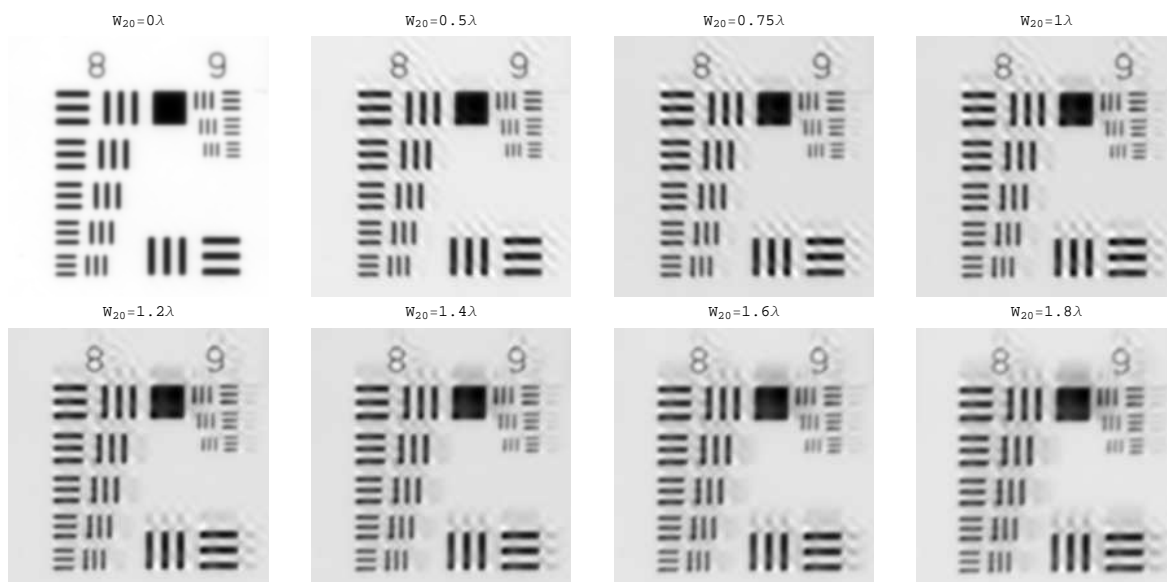
Figure 6.27: *Simulation of image artifacts with the CPM for various amounts of defocus.*

6.9.1 Metric validation

The chrome-on-glass USAF target is positioned at a slant angle so that its range varies linearly along the x axis and is constant along the y axis. Figure 6.28 shows the coded and non-coded images of this target. Figure 6.29 shows that both metrics provide reasonable estimates of W_{20} since the optimally restored snippets according to both metrics do not exhibit strong image artifacts. Figure 6.30 shows similar slightly improved performance is obtained when restorations are based on measured PSF. We observe that the MAD metric, described in Section 5.5.1, provides a more robust estimate of defocus than the variance metric. This is illustrated in the third column of Figures 6.29 and 6.30 where the variance estimator is biased by the distortion artefact typically associated with petal phase masks. In this case this estimator failed to select the best restoration available, which the MAD metric successfully achieved.

Practical experience showed that an accurate image segmentation is required to perform spatially variant restorations. Image segmentation is a field of research in itself and algorithms and levels of sophistication largely depend on the application. A complete implementation would require to test segmentation algorithms and assess their impact on the quality of the final image. In order to concentrate on the main issue here, the image was manually segmented. In an attempt to reduce the impact of this arbitrary block segmentation, the defocus metrics are computed for a set of windows that are translated relative to the centre pixel of the snippet. We then select the median value to reduce the weight of erroneous defocus estimates in the final defocus estimate. This assumes range continuity in a small neighbourhood, typically a few pixels.

6.9.2 Image fusion

Up to this point, the different features obtained from the image segmentation have been separately restored with the best kernel available based on different metrics. These features are now fused together to form a single image, which should exhibit a DoF that is extended beyond the limit achieved with single-kernel restoration methods in WC systems.
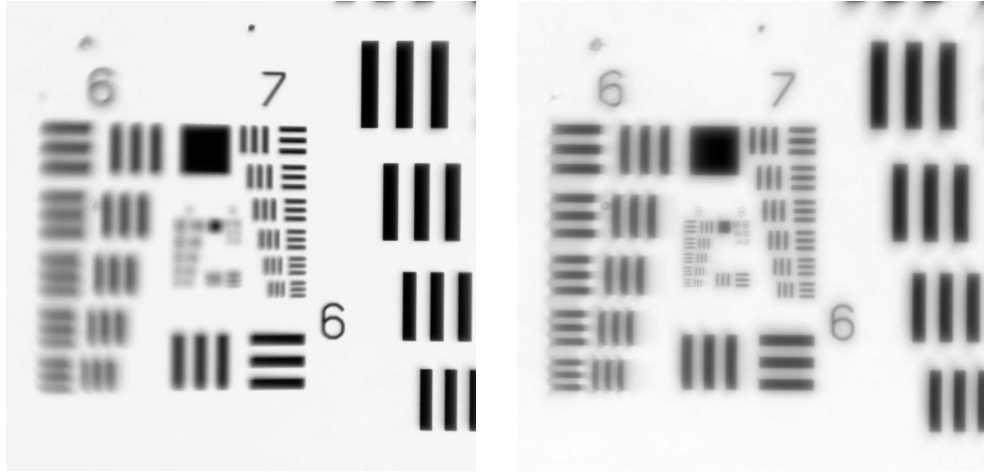
Figure 6.28: *Non-coded image (left) and coded image (right) of the USAF target positioned at slant angle. Defocus increases linearly from the right to the left sides of each image. The petal phase mask used is shown on Figure 6.11.*

First image fusion

Figure 6.31 presents the fused snippet image based on restorations with measured PSFs and estimations of W_{20} with the MAD metric. Note that some of the snippets fused here were presented in Figure 6.30. The initial image segmentation and the image fusion are made clear here with a white background. A uniform background can be justified under the assumption that no meaningful information is excluded from the selected region-of-interest (ROI). In order to reconstruct a more physically realistic image, the background can be adjusted to the highest gray level present in the original wavefront-coded image. The result of this operation is presented in Figure 6.32, where the fused images have been obtained with modelled PSFs. The non-coded image and the coded-image restored with a single kernel at $W_{20} = 1.5$ are also shown for comparison. The spatially variant multiple-kernel restoration (using either the variance or the MAD metrics of defocus) provides clear improvements in terms of image sharpness and artifacts amplitude over the single restoration WC image (top right). For instance, in the single-kernel restoration image, the horizontal bars on the right hand side suffer from strong artifacts and the number "6" on the left side of the image is distorted. These spurious signals are clearly removed with the spatially variant multiple-kernel restorations (bottom left and right images). This confirms that
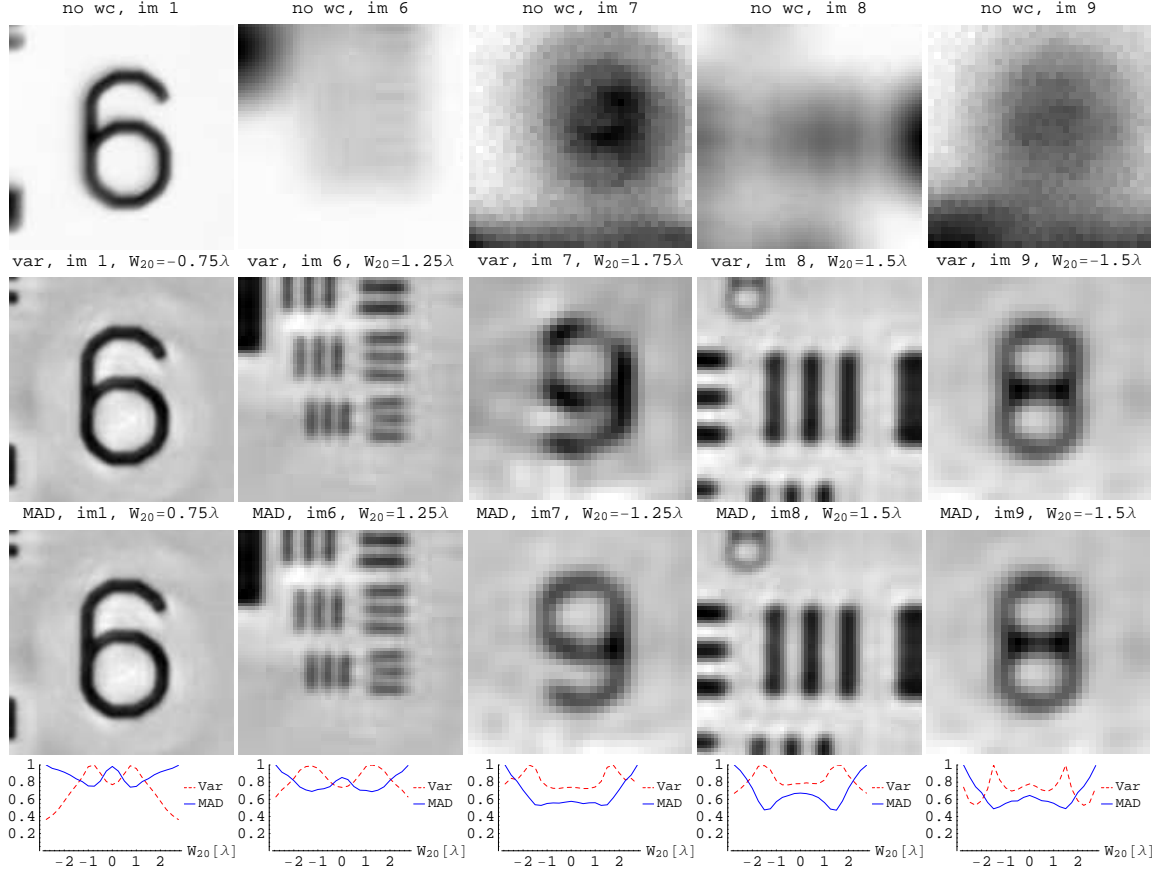
Figure 6.29: *Spatially variant restoration of the slanted USAF target based on the modelled OTF. Reference snippets in non-coded coded image (top row), corresponding snippets in WC images after restoration with best kernel, using the variance metric (second row) and the MAD metric (third row). Metrics as a function of W_{20} (bottom row).*
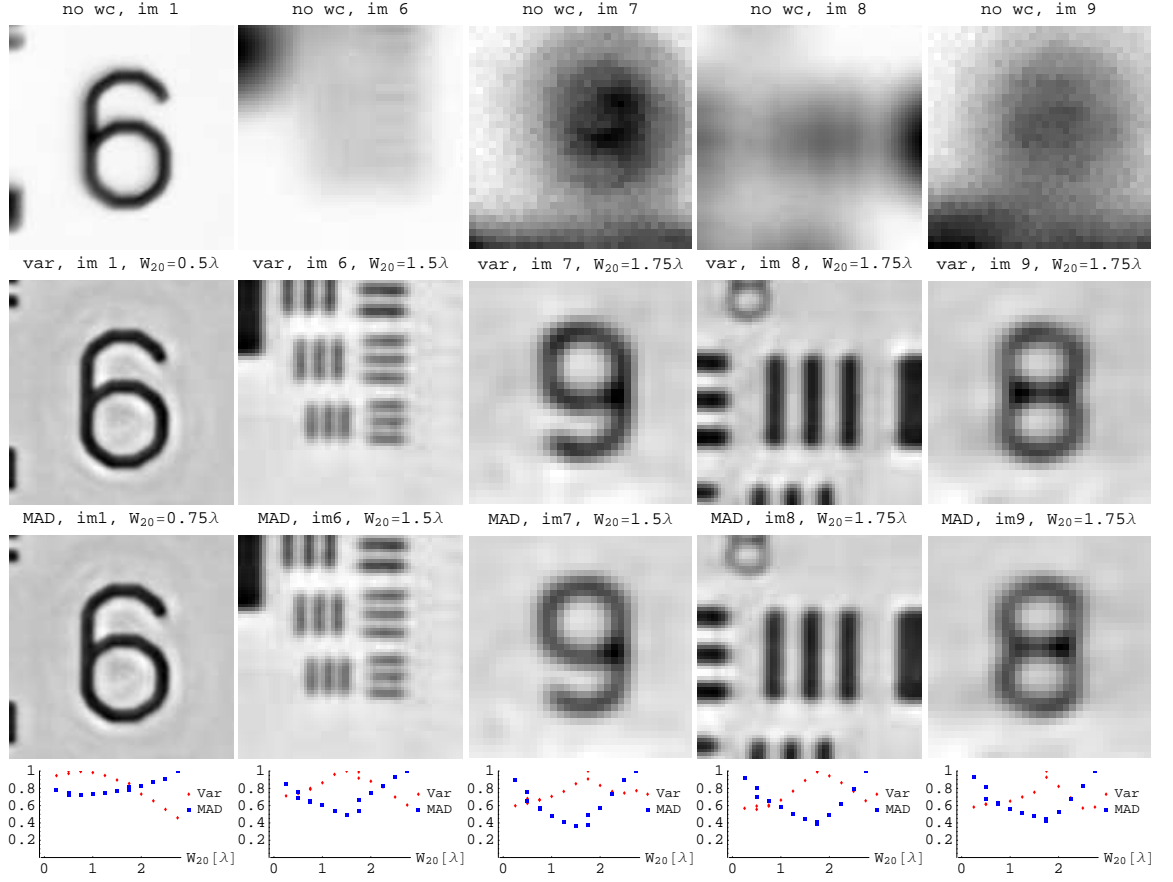
Figure 6.30: *Spatially variant restoration of the slanted USAF target based on the measured OTF. Results are presented in the same order as in Figure 6.29.*

the DoF is extended beyond that of a conventional WC system using single-kernel restorations. Moreover, these results are further improved when restorations are based on measured PSFs, see Figure 6.33. These results demonstrate a DoF extension by a factor of 11 with respect to a DL microscope, which corresponds to a tolerable defocus of $W_{20} = 2.75$, is achieved with the spatially variant multi-kernel restoration. Beyond this range of defocus values, the magnitude of the artifacts become too large and prevent the automatic kernel selection to be performed with acceptable accuracy.

The loss of contrast inherent to the Wiener restoration could be reduced with the use of more sophisticated restoration techniques such as iterative restoration methods (Lucy-Richardson,...). These methods usually clip negative values in the restored image since these values do not represent any physical reality but are merely due to restoration imperfections. For completeness we show the effect of this non-linear operation on our restored and fused images, see Figure 6.34.
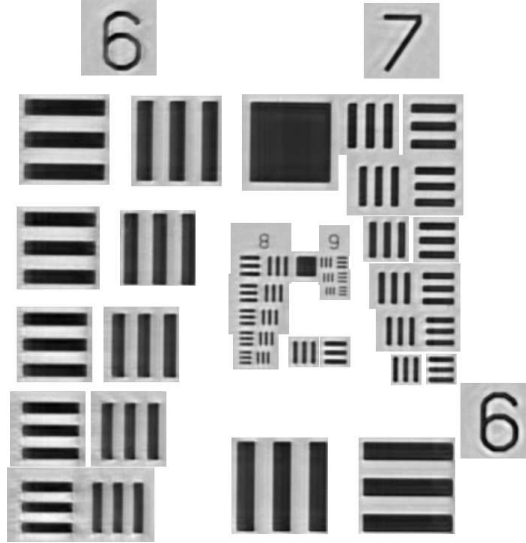
Figure 6.31: *Fused snippet image based on multiple-kernel restorations with measured PSFs. The initial image segmentation is made clear here with a white background. Defocus is estimated with the MAD metric.*

Image fusion with zeroth order interpolation

A physically more realistic solution than the uniform background previously discussed arguably consists of performing an interpolation of the defocus parameter outside the
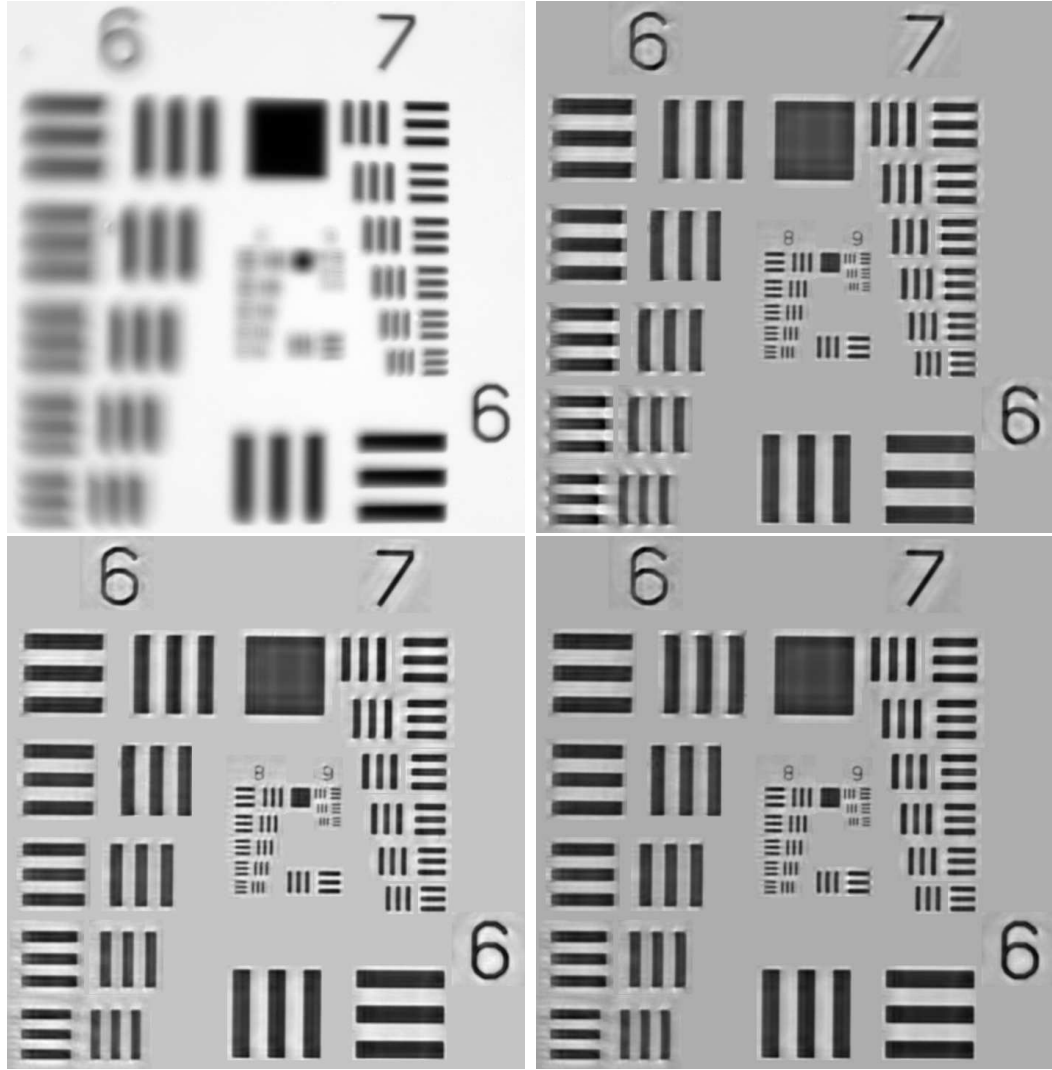
Figure 6.32: *Fused snippet images of the USAF target oriented at a slant angle. Non-coded image (top left), WC image restored with a single kernel at $W_{20} = 1.5$ (top right), corresponding to the defocus at the centre of the target. Images obtained after spatially-variant multiple-kernel restorations and estimation of the defocus with the variance (bottom left) and MAD (bottom right) metrics. Restorations are based on modelled PSFs.*
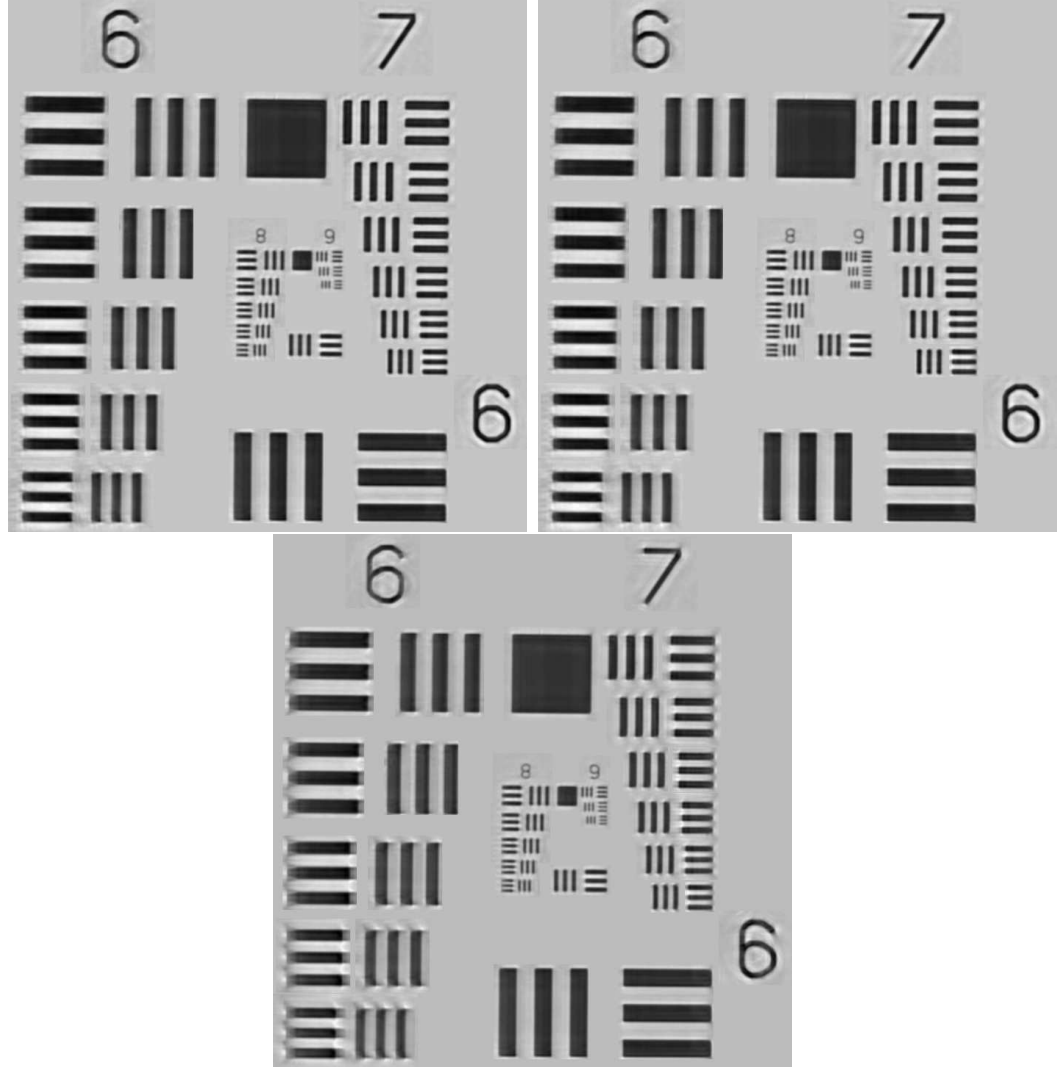
Figure 6.33: *Fused snippet images of the USAF target oriented at a slant angle. Images obtained after spatially-variant multiple-kernel restorations and estimation of the defocus with the variance (top left) and MAD (top right) metrics. WC image restored with a single kernel at $W_{20} = 1.5$ (bottom). Restorations are based on measured PSFs.*
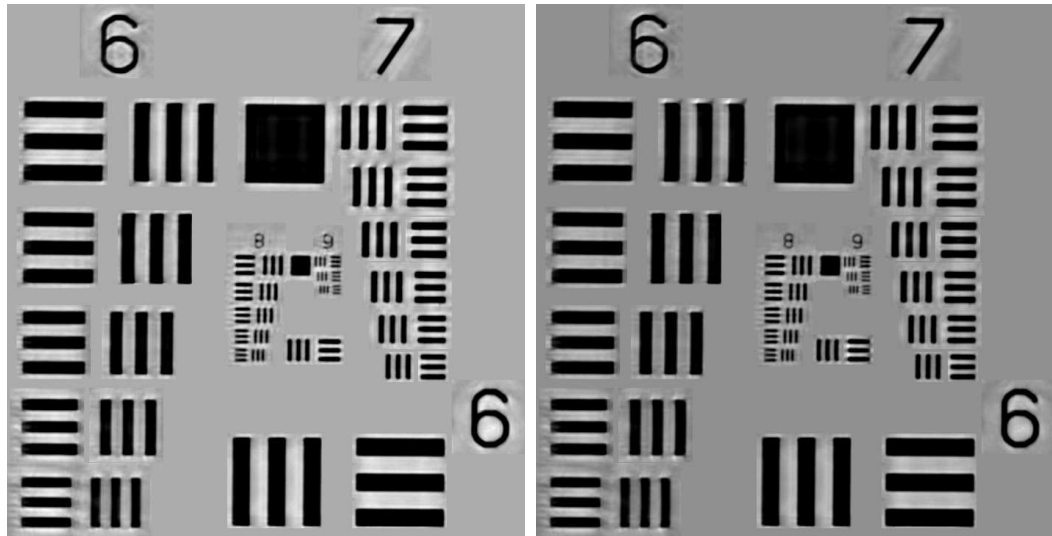
Figure 6.34: *Left to right: multiple kernel restoration with variance and MAD metrics respectively. Negative values in the restored blocks have been clipped.*

ROIs from its estimates inside the ROIs. This solution offers the advantage to be more robust to image segmentation errors because of the added continuity constraint. The interpolation is efficiently implemented here using the Voronoi diagram (used in nearest neighbour search) of the centroid of each snippet. Zeroth order interpolation of W_{20} is applied here and the results are displayed on Figure 6.35. Note that the continuity of the images is preserved here, as opposed to the images reconstructed with a uniform background and shown in Figure 6.33.

6.10   Range detection

The range information of features in extended DoF images can theoretically be extracted from the defocus estimates $\hat{W}_{20}$ with Eq. (4.2). In this section we seek to assess the accuracy of this range detection method. To that end the defocus estimates across the slanted USAF target presented in Section 6.9 are utilised.

In estimating range from the defocus parameter W_{20}, there is an ambiguity about the sign of the defocus parameter because the PSF is identical for $\pm W_{20}$. If features in the sample are located at both positive and negative values of W_{20}, this ambiguity has to be removed. In the results presented here this has been done using the *a priori*
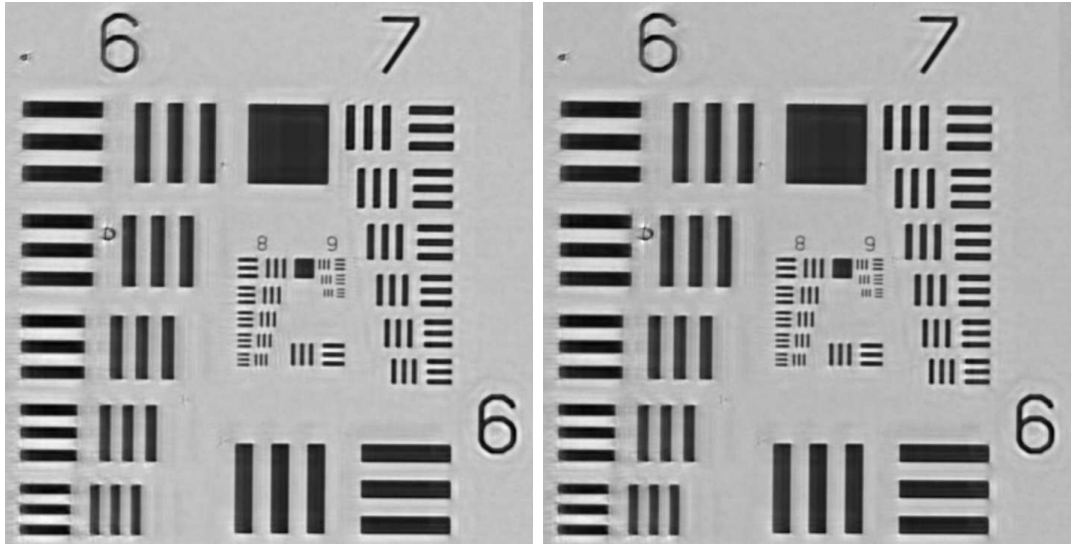
Figure 6.35: *Fused snippet images with zeroth order interpolation of W_{20} outside the ROIs. Multiple-kernel restorations are based on measured PSFs. Defocus is estimated with the variance (left) and MAD (right) metrics.*

information about the sample, i.e. using the knowledge that the target is positioned at a slant angle.

6.10.1 Calibration of the slant angle

In order to assess the accuracy of the range estimates of the proposed method, the slant angle of the USAF target has to be calibrated. This is achieved by focusing on an arbitrary image feature which will serve as a range reference (without phase mask). Bringing into focus other features across the target, the associated micro stage displacements are recorded. Although this method can in principle measure the absolute range of sample features, we only calibrate here their relative range positions. Thus the slant angle of the USAF target can be accurately calibrated. This is shown by correlation ratios higher than 0.99 on Figure 6.36 and 6.37. The error bars shown on these graphs are due to measurement errors that are approximated by the estimated DoF of the system, here $\simeq 1.1\mu$m.

6.10.2 Error of range estimates

Using the standard first order approximation of Eq. (4.2), the distance z between the defocused and the in-focus planes in object space can be rewritten as:

$$z = -8\lambda F_{/\#}^2 \overline{W}_{20}, \tag{6.8}$$

where the focused distance z_i equals the focal length f of the MO, $z = z_d - z_i$ and $\overline{W}_{20} = W_{20}/\lambda$. Consequently the error dz on the estimation of z is:

$$dz = -16\lambda \overline{W}_{20} F_{/\#} \, dF_{/\#} - 8\lambda F_{/\#}^2 \, d\overline{W}_{20}. \tag{6.9}$$

Using $F_{/\#} \simeq 0.94$, $dF_{/\#} = 10^{-2}$ and $d\overline{W}_{20} = 1/4$ we estimate dz as:

$$dz = -0.15\lambda \overline{W}_{20} - 1.77\lambda. \tag{6.10}$$

6.10.3 Results

Figure 6.36 shows the range estimates extracted from features across the USAF target placed at a slant angle and previously shown in Figure 6.32. Each point in these graphs corresponds to a different snippet. As expected, results are improved when restorations are performed with measured PSFs, see Figure 6.37. A few remarks about Figure 6.36 are necessary at this point. We use the plots shown on Figure 6.36 to assess the coefficient of correlation R^2 of the range estimations. Consequently we projected the 3D data points in the (X, Z) plane along the best fitted plane for each data set. This means identical range estimates with the variance and MAD metrics may appear at a different range location on these plots since these datasets have different linear regressions. In addition, we recall here that the calibrated data represents the relative, not absolute, range positions of sample features. Therefore the apparent vertical bias between the range estimates and the calibrated data is irrelevant. The validity of the proposed range finding method is based on the estimated slant angle error relative to its calibrated value, and on the correlation ratio of the range estimates. The variance and MAD metrics measure the slant angle $\hat{\theta}$ of the target at 3.8° and 4.7° respectively, compared with the 4.3° angle measured with the calibration method. This represents an absolute error $\Delta\theta$ of 12% and 8% respectively. This experiment was repeated and

similar accuracy was obtained. When restorations are performed with measured PSFs the accuracy of range estimates is improved as is shown by the 11% and 3% errors obtained in this case. These results, summarised in Table 6.2. The bias μ_z and the standard deviation σ_z of the range estimations are also reported in Table 6.2 with their corresponding values expressed in terms of W_{20}, $\mu_{W_{20}}$ and $\sigma_{W_{20}}$ respectively. These results show that the standard deviation of the defocus estimations is approximately 0.4λ for both the variance and MAD metrics. Both estimators suffer from a $\lambda/4$ bias, with the exception of the MAD estimator used with measured PSF where the bias is neglectable. These results indicate that further improvements in the accuracy of this range detection method are required to compete with fast refocusing systems, which can provide unbiased range estimations with a standard deviation of the order of $\lambda/4$.
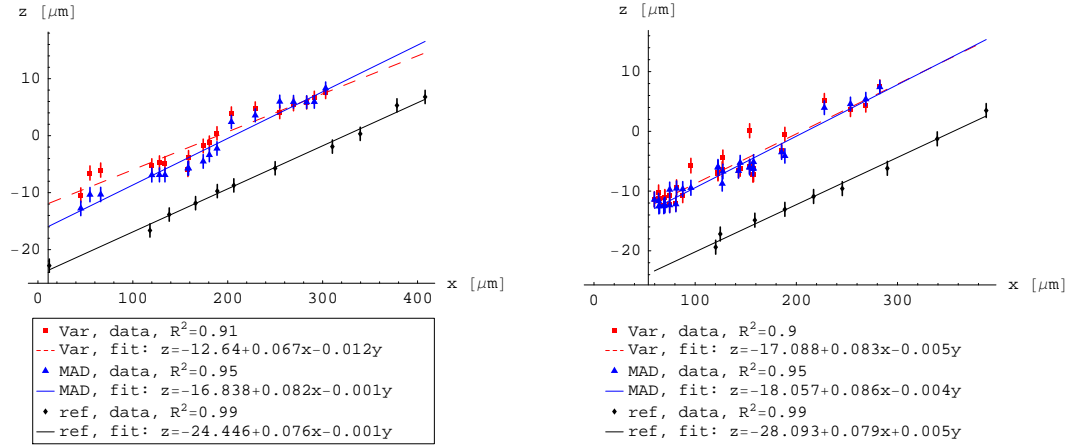
Figure 6.36: *Estimated range of features in the USAF target positioned at a slant angle along the x axis. The experiment was repeated twice and both results are shown here. Restorations are based on modelled PSFs.*
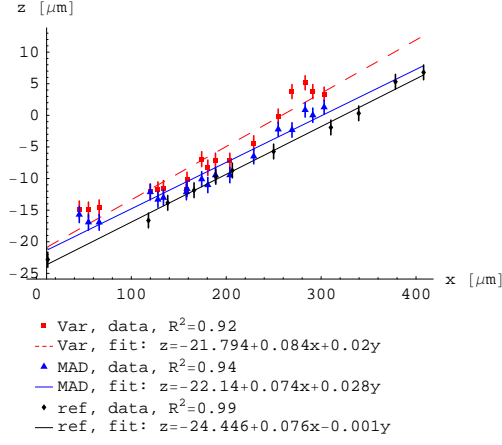
Figure 6.37: *Estimated range of features in the USAF target positioned at a slant angle along the x axis. Restorations are based on measured PSFs.*

Restoration	Method	$\hat{\theta}$	R^2	$\Delta\theta$	μ_z [μm]	$\mu_{W_{20}}$ [λ]	σ_z [μm]	$\sigma_{W_{20}}$ [λ]
	Calibration	4.32°	0.99					
modelled PSF	Variance	3.81°	0.91	12%	1.2	0.26	1.9	0.4
	MAD	4.68°	0.95	-8%	1.8	0.39	1.5	0.32
measured PSF	Variance	4.82°	0.92	-11%	0.8	0.17	2.3	0.5
	MAD	4.20°	0.94	3%	< 0.1	< 0.02	2.2	0.47
	Calibration	4.52°	0.99					
modelled PSF	Variance	4.76°	0.9	-5%	-0.8	-0.18	1.9	0.41
	MAD	4.93°	0.95	-9%	-1.2	-0.27	1.4	0.3

Table 6.2: *Range estimations and errors provided by the variance and MAD metrics with the USAF target.*

6.11   Restoration of weak objects

We conclude this chapter with a few remarks on the restoration of WC images for weak objects, i.e. objects where diffracted light is weak compared to non-diffracted so that interaction between diffracted rays can be neglected. As mentioned in Section 6.7.3, the weak OTF relates the transmission function of the object to the image intensity.

Thus, the restoration of WC images for such objects must be aimed at recovering their transmission function. For weak phase objects (no absorption) one therefore wishes to form an image which intensity is proportional to the phase of the object. Since conventional imaging systems are only sensitive to the intensity of light transmitted by the object, one can only record information about the amplitude changes and not the phase changes introduced by the object. Although non-interferometric techniques have been developed to image and extract the phase of the object, e.g. the phase contrast method proposed by Zernike [100], phase contrast in weak phase objects can also be obtained by introducing a small amount of defocus. Indeed, the imaginary part of the partially coherent weak OTF (without phase mask), which is responsible for transmitting phase information, is null when the system is in-focus but becomes non-zero in the presence of defocus. The variation in phase contrast with defocus can be observed in the human red blood cells (HRBC) shown on Figure 6.38 (left), where the slide has been oriented at a slant angle to introduce various amounts of defocus across the object. Taking advantage of this, quantitative phase retrieval can be performed from the recording of two images with small defocus W_{20} and $-W_{20}$ [96, 101].

Restoration of the WC image (centre) of the HRBC is presented on Figure 6.38 (right). HRBC typically are 6 to 8 μm wide and 2μm thick while the DoF in the non-coded image is 1.2μm. The (single-kernel) restoration clearly increases the quality of the WC image, but may be further improved with a more accurate knowledge of the image formation process. Further work will be required in particular to determine the model for the weak OTF (with and without WC) in the presence of the diffuser.

6.12 Conclusions

In this Chapter a transmission microscope was designed and implemented to accommodate pupil phase masks. The purpose of this experiment was to test the effectiveness of the image restoration method described in Chapter 5 to remove WC image artifacts, thereby further extending the DoF of WC systems. The compound microscope uses narrow-band Köhler illumination, an infinity-corrected 0.6 NA objective and a tube lens for a transverse magnification factor of 20. Phase encoding was realised with the

non-coded   WC   restored
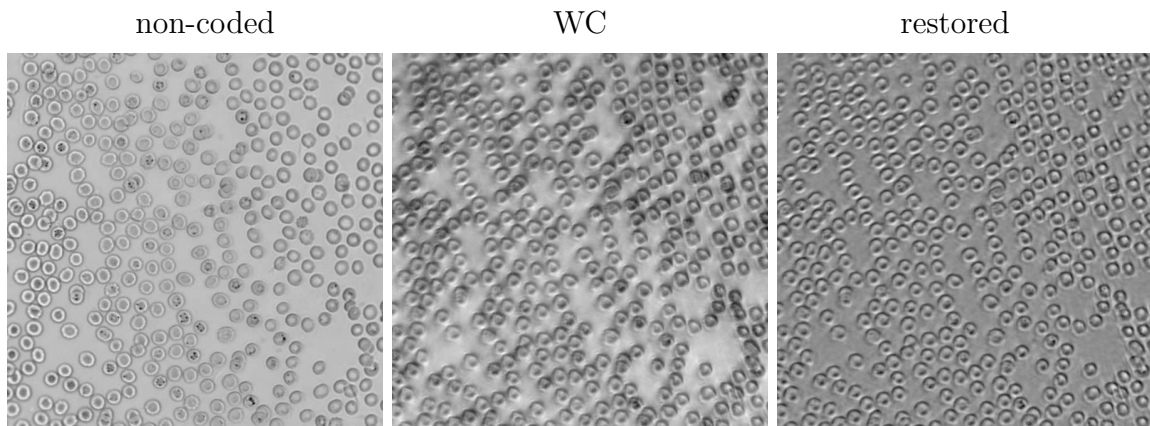
Figure 6.38: *Image of human red blood cells at different defocus (microscope slide is oriented at a slant angle in the left-right direction). Note the variation in phase contrast with defocus in the non-coded image (left). WC image (centre) and restored image (right) are shown.*

petal phase mask $(\alpha, \beta) = (3.39\lambda, -10.18\lambda)$ ($\lambda = 660$nm). The PSF of the microscope was measured and simulated in two situations: aliasing-free ($\mathrm{NA}_o = 0.49$, $\mathrm{NA}_c = 0.26$) and matched illumination ($\mathrm{NA}_c = \mathrm{NA}_o = 0.26$). In both cases the modelled and measured data are in good agreement. Restored images in matched illumination are shown to exhibit strong artifacts because of the degree of partial coherence in the object plane. Indeed, the image formation in the transmission microscope is well-known to be partially coherent due to the transillumination. There is therefore a mismatch between the image formation taking place in the microscope and the incoherent image formation assumed in the WC image restoration. Incoherent illumination was achieved with a diffuser positioned between the condenser lens and the sample. This modification enables the microscope to operate with WC in the aliasing-free configuration. Restored images of the USAF target demonstrate the extended DoF of the microscope, typically of the order of 1.25λ of defocus. For larger values of W_{20} the phase mismatch between the defocused and in-focus OTF creates strong artifacts in the restored image. For the petal phase mask used, phase inversions in the image occur when $W_{20} \geq 1.46\lambda$. Using the multiple-kernel restoration method described in Chapter 5, WC artifacts in the image of the USAF target oriented horizontally are shown to be greatly attenuated up to $W_{20} = 2.75\lambda$. This corresponds to a further extension of the DoF by a factor of

two. The method is tested in a 3D scene made of the USAF target oriented at a slant angle. Spatially variant restoration is effectively achieved in two steps: 1) segmented image features are separately restored using multiple-kernels and defocus estimation, 2) the restored features are fused together. The image smoothness is preserved outside the ROIs by performing a zeroth-order interpolation of W_{20} at each pixel. The reconstructed image displays the expected 2.75λ "super" extended DoF.

The accuracy of the defocus estimation employed as a range detection method is assessed in the final section. Results show that for both the variance and MAD metrics the standard deviation of the defocus estimations is approximately 0.4λ. Both estimators suffer from a $\lambda/4$ bias, with the exception of the MAD estimator used with measured PSF where the bias is neglectable. These results indicate that further improvements in the accuracy of this range detection method are required to compete with rapidly refocusing microscopes, which can provide unbiased range estimations with a standard deviation of the order of $\lambda/4$.

Further work will focus on improving the quality of WC restored images of weak objects, *e.g.* some biological tissues, red blood cells etc.. Quantitative phase extraction for weak phase objects is of particular interest in microscopy and requires the reconstruction of an image which intensity is directly proportional to the phase of the object. Whether WC may allow quantitative phase extraction or provide benefits for this application will have to be investigated. In addition it will be necessary to determine the model for the weak OTF (with and without WC) in the presence of the diffuser. Partially coherent systems can provide an optimum tradeoff between contrast and resolution and therefore offer increased imaging performances compared to fully coherent or incoherent systems. Further improvements in the image quality of WC microscopes could be aimed at including partial coherence effects in the image restoration. Finally, a promising application for extending the DoF with WC may be found in the widely employed fluorescence microscope because of the incoherence of fluorescent radiations.

Chapter 7

Conclusions and future work

In Chapter 2 we described the fundamentals of millimetre-wave synthetic aperture imaging. It was demonstrated that in synthetic aperture short-range mm-wave imaging, time-sequential recording of the visibility function offers a route to reduced array complexity. The tradeoff between array complexity, radiometric sensitivity and imaging frame rate that is associated with this technique were analysed. It was shown that if the visibility function is recorded with n_t time-sequential samples during which the array is moved relative to the target, point-spread-function and image quality can be maintained for a factor $\sqrt{n_t}$ reduction in the number of antennas and a factor n_t reduction in the number of correlators. This simplification is obtained at the cost of a deterioration in radiometric sensitivity, which can be recovered only by a factor n_t increase in the total integration time. This means that in principle, for certain applications where long integration times are feasible, acceptable sensitivity of 2K could be obtained for systems in which the number of antennas is an order of magnitude lower than for snapshot systems. Since the cost of these systems is largely driven by the number of antennas in the array, the proposed technique can significantly reduce the cost of mm-wave synthetic aperture personal scanners.

Near-field effects associated with short-range imaging were accounted for in the image reconstruction algorithm. We would like to mention here that the feasibility of adapting the backward-wave image reconstruction algorithm to synthetic aperture imagers was investigated. This algorithm is based on Fourier optics techniques [1] and takes advantage of the $O(N \log N)$ complexity of the FFT. It is computationally more effi-

cient than the correlation algorithm presented here, which has a $O(N^2)$ complexity. It was originally developed for acoustic holography [102] and was successfully applied to real-aperture millimetre-wave personnel scanning [10]. For synthetic aperture imaging, the algorithm is expected to consist of two two-dimensional (2D) Fourier Transforms, one 2D inverse Fourier Transform and multiplicative factors that account for near-field effects. Further details on this algorithm and its performances may be the object of a future paper as it is clear that short-range synthetic aperture imagers will benefit from such efficient algorithms. The frequency content of the interference pattern was analysed when a point source is in translation relative to the array. In general the signal recorded is a non-linear chirp (that is, the rate of variation of the frequency with time is not constant), but can be approximated to a linear chirp if the scanning of the source is restricted to a specific region. Interestingly, the Fourier-transform of this chirp has a form that matches the near-field (Fresnel region) diffraction pattern of plane waves by a 1D slit. Moreover such diffraction patterns are well known to be related to the fractional Fourier-transform [74] of such aperture functions. Thus it may prove useful to analyse interference patterns with the fractional Fourier-transform.

In Chapter 3 the array was designed to optimise the improved spatial frequency coverage achieved after linear or rotational scanning of the source. We show that a rotational scan more efficiently samples the spatial frequencies of the scene. We therefore design the array so that the uniformity of its sampling of the Fourier domain is maximised after rotational scanning, a technique we termed aperture rotation synthesis. To that end, a novel metric of the sampling uniformity was proposed and completes the array design presented in [17], where sampling uniformity was only assessed qualitatively. The proposed metric is based on a binless estimator of the entropy of the density of measurements across the Fourier plane. It is similar to the metric proposed by Cornwell [18] in that it also uses the logarithm of distances between samples, but it is computationally more efficient because of the restriction to the nearest neighbours only. Efficient implementation of this metric was achieved using Delaunay triangulation. In addition, the use of the differential entropy to derive this metric provides a rigourous justification and a new understanding of the design of antenna arrays. A 27 antenna array design obtained after optimisation of this metric with a

genetic algorithm is presented. The imaging performances of this array were assessed with simulated millimetre-wave scenes and compared with the more conventional Y-shaped array. We show that the optimised array exhibits greatly enhanced imaging performances. Furthermore, the genetic algorithm employed can readily be applied to different applications and include additional practical constraints on the antenna positions. The longer acquisition times of the proposed technique however increases sensitivity to instrument drift and temporal changes in average illumination, compared to a snapshot technique. This represents a serious calibration challenge and increases the necessity for a real-time calibration procedure.

In Chapter 4 the distinction between the digital refocusing ability and the DoF of interferometric synthetic aperture antenna arrays was presented. This is a new result as the DoF of synthetic aperture antenna arrays is not mentioned in the literature and was originally thought to be infinite. Digital refocusing is enabled by the separate recording of spatial frequencies at each baseline, which allows compensation for defocus related phase delays. We showed that ranging errors in the digital refocusing are mathematically equivalent to the defocus effect in a conventional optical system. This enabled us to analyse the DoF of antenna arrays with conventional optics tools such as the Strehl ratio. We derived an analytical expression of the Strehl ratio that includes the effect of defocus and established that this metric varies significantly with W_{20}. Thus it is demonstrated that antenna arrays have a finite DoF, even in the ideal case of point-like antennas, with the exception of circular arrays of point-like antennas. This general expression can be applied to any array configuration and is useful when designing short-range synthetic aperture arrays with a specific DoF. The parameters affecting the DoF of antenna arrays have been identified as the size of the antennas and their radial positions with respect to the aperture origin. Using Hopkin's criterion, the DoF of the Reuleux and Y-shaped arrays presented in Chapter 3 have been quantified as $\approx 0.37\lambda$ and 0.16λ respectively when focusing at a 2m distance, as compared with 0.215λ for real circular aperture systems with equal $F_{/\#}$. The expression of the Strehl ratio readily shows that circular arrays can achieve a very large DoF. A 27 antennas circular array with a fill factor of ≈ 0.004 was therefore designed with the optimisation

method described in Chapter 3. This array can record images with a 33λ DoF, which corresponds to a hyperfocal distance of 58cm. Thus requirements for axial refocusing is suppressed with this design.

In Chapter 5 the principles of wavefront coding were presented. In wavefront coded systems, reduced sensitivity to defocus is attained by placing specifically designed phase filters in the entrance pupil of the system. The reduced MTF causes the recorded image to be blurred, which is easily restored for a large range of defocus values with a single digital filter because the MTF does not contain any nulls. Two approaches, one analytical the other numerical, to designing pupil phase masks were detailed. Cubic-phase profiles in rectangular, linearly separable phase masks are derived analytically when the amplitude of the ambiguity function is constrained to be invariant with defocus. The numerical method, termed pupil phase engineering, optimises simultaneously the defocus sensitivity and the image restorability. This approach is attractive because it directly addresses the tradeoff between these two competing terms. It also enables the optimisation of phase masks with a circular aperture, which represents a significant advantage over the analytical approach. The defocus sensitivity metric was chosen as the L^2 norm of the second derivative of the OTF with respect to defocus, taken at $W_{20} = 0\lambda$, as proposed in [28]. This metric can be computed efficiently with only four two-dimensional FFT. We argue that choosing the Strehl ratio as the metric of image restorability, as in [27, 28], is suboptimal because it is biased by phase effects such as a transverse translation of the PSF. As a result, cubic phase masks are artificially penalised. When using the Strehl ratio metric our results are in agreement with those obtained in [27]. We propose instead to use the normalised L^2 norm of the PSF as the image restorability metric in order to be insensitive to phase information. In this case we show that the algorithm converges to a phase mask that is almost purely cubic, *i.e.* it has a small β/α ratio approximately equal to 0.06. This result confirms that cubic phase masks can be applied to circular aperture systems.

Restored images in wavefront coded systems were shown to be degraded by image artifacts in the form of oscillations and edge replicas. The origin of these artifacts is demonstrated to reside in the variations with defocus of the phase of the OTF. These artifacts are rarely mentioned in the literature but seriously limit the imaging perfor-

mance of wavefront coded systems. Removal of these artifacts is therefore critical. An iterative restoration method was therefore devised to remove these artifacts, which are first used as a signature of the defocus effect to estimate the defocus parameter W_{20}. The recorded image is then restored with the filter corresponding to this value of W_{20}. We assessed the robustness of several defocus metrics with simulated images and concluded that the MAD metric was the most robust for two-dimensional images. Future work will continue the development of more robust metrics of defocus. One promising approach briefly detailed in Chapter 5 is based on the correlation of edge profiles with calibrated data. Such correlation may be implemented with wavelet decomposition, which is known to be particularly robust for edge detection in noisy signals. It was also demonstrated that excellent suppression of these artifacts is still achieved with errors in the defocus estimates of the order of $\lambda/4$. The proposed image restoration method therefore extends the DoF beyond that of wavefront coded systems.

Recently, similar phase masks were designed by Tom Vettenburg of Heriot-Watt University using a different optimisation approach. Although further confirmation of the agreement of these results must be obtained, they may constitute a first evidence that the small β value plays the role of an apodisation term for the circular aperture. Further investigation of this hypothesis is required and could be validated if a value of 0 was obtained for β after applying the same optimisation to square aperture phase masks.

In Chapter 6 we describe the design and implementation of WC in an optical transmission microscope. This allows us to assess the effectiveness of the image restoration method described in Chapter 5 in removing WC image artifacts. The compound microscope uses a narrow-band Köhler illumination, an infinity-corrected 0.6 NA objective and a tube lens for a transverse magnification factor of 20. Phase encoding was realised with the petal phase mask $(\alpha, \beta) = (3.39\lambda, -10.18\lambda)$ (at $\lambda = 660$nm). The PSF of the microscope was measured and simulated in two situations: aliasing-free ($NA_o = 0.49$, $NA_c = 0.26$) and matched illumination ($NA_c = NA_o = 0.26$). In both cases the modelled and measured data are shown to be in good agreement. Nevertheless, restored images in matched illumination are shown to exhibit strong artifacts. We argue that these artifacts are caused by the degree of partial coherence in the object plane. Image

formation in transmission optical microscopes is partially coherent due to diffraction at the condenser lens. To our knowledge this issue has not been previously reported in the literature regarding WC adaptations to wide-field microscopy. Incoherent illumination of the sample was obtained with a diffuser positioned between the condenser lens and the sample. This modification enables the microscope to operate with WC in the aliasing-free configuration. Extended DoF of the order of 1.25λ of defocus is demonstrated in microscope images of the USAF target. For larger values of W_{20} the phase mismatch between the defocused and in-focus OTF creates strong artifacts in the restored image. For the petal phase mask employed here, phase inversions in the image occur when $W_{20} \geq 1.46\lambda$. Using the multiple-kernel restoration method, WC artifacts in the image of the USAF target oriented horizontally are shown to be greatly attenuated up to $W_{20} = 2.75\lambda$. This corresponds to a further extension of the DoF by a factor of two compared to conventional WC systems and validates the results presented in Chapter 5. The method is tested in a 3D scene made of the USAF target oriented at a slant angle. Spatially variant restoration is effectively achieved in two steps: 1) segmented image features are separately restored using multiple-kernels and defocus estimation, 2) the restored features are fused together. The image smoothness is preserved outside the ROIs by performing a zeroth-order interpolation of W_{20} at each pixel. The reconstructed image displays the expected 2.75λ "super" extended DoF.

The accuracy of the defocus estimation employed as a range detection method is assessed in the final section. Results show that for both the variance and MAD metrics the standard deviation of the defocus estimations is approximately 0.4λ. Both estimators suffer from a $\lambda/4$ bias, with the exception of the MAD estimator used with measured PSF where the bias is neglectable. These results indicate that further improvements in the accuracy of this range detection method are required to compete with rapidly refocusing microscopes, which can provide unbiased range estimations with a standard deviation of the order of $\lambda/4$.

Further work could focus on the determination of the model for the weak OTF (with and without phase mask) in the presence of the diffuser. The use of higher NA objectives is also desirable and will require the paraxial diffraction approximation assumed here to be replaced by a more accurate description of the diffraction such as Debyes

non-paraxial scalar formulation [103]. Partially coherent systems can provide an optimum tradeoff between contrast and resolution and therefore offer increased imaging performances compared to fully coherent or incoherent systems. Further improvements in the image quality of WC microscopes could therefore be aimed at including partial coherence effects in the image restoration. Alternatively it may be more straightforward to use WC in fluorescence microscopy because of the spatial incoherence of fluorescent radiations. Exploiting the full potential of the proposed restoration method to further extending the DoF in fluorescence microscopy may however be difficult because of the serious image segmentation challenge. Another line of research may be to improve the quality of WC images of weak objects, *e.g.* biological tissues, red blood cells etc.. Quantitative phase extraction for weak phase objects is of particular interest in microscopy and requires the reconstruction of an image which intensity is directly proportional to the phase of the object. Whether WC may allow quantitative phase extraction or provide benefits for this application will have to be investigated. In any case, the benefits of WC for microscopic thick tissue imaging are limited by the aberrations introduced by the biological tissue itself. It is therefore highly desirable to compensate for these perturbations in order to obtain high quality images. It has been pointed out that one dominant type of aberration degrading deep-tissue images is the spherical aberration caused by the refractive-index mismatch between the sample and the immersion (or air) medium [104]. This causes a small degradation in the transverse resolution compared to that in the axial resolution and a significant deterioration in the image contrast. The magnitude of these spherical aberrations vary with defocus and can not be corrected for in a single restoration as in conventional WC. Recently, Saavedra *et al.* [103] proposed to employ a radially symmetric version of the cubic phase mask to reduce the sensitivity of the system to spherical aberrations. Thus a single restoration may be employed again. Another promising approach to correcting specimen-induced aberrations is through the use of adaptive optics [104, 105], a technique originally developed in astronomy to compensate for aberrations introduced by atmospheric turbulence. Implementation of adaptive optics in a confocal microscope has been described [104] and is well suited to the correction of the low-order Zernike polynomials that characterise tissue-induced aberrations. This enhanced flexibility over

the WC approach is attained however at the cost of an increased hardware complexity and may be restricted in the future to high-end microscopes.

Appendix A

Publications and patents

The abstracts of the published papers related to this thesis are detailed below.

- [21] B. M. Lucotte, B. Grafulla-González, and A. R. Harvey. Array rotation aperture synthesis for short-range imaging at millimeter wavelengths. *Radio Sci.*, 44(RS1006), 2009.

  Millimeter-wave interferometric synthetic aperture imagers are currently being developed for short-range applications such as concealed weapons detection. In contrast to the traditional snapshot imaging approach, we investigate the potential of mechanical scanning between the scene and the array in order to reduce the number of antennas and correlators. We assess the trade-off between this hardware reduction, the radiometric sensitivity and the imaging frame rate of the system. We show that rotational scanning achieves a more uniform coverage of the (u, v) plane than the more conventional linear scanning. We use a genetic algorithm to optimize two-dimensional arrays for maximum uniform (u, v) coverage after a rotational mechanical scan and demonstrates improvements in the array point spread function. Imaging performance is assessed with simulated millimeter-wave scenes. Results show an increased image quality is achieved with the optimized array compared with a conventional power law Y-shaped array. Finally we discuss the increased demands on system stability and calibration that the increased acquisition time of the proposed technique places.

- [20] B. M. Lucotte and A. R. Harvey. Antenna rotation aperture synthesis for

short- range personnel scanning at mm wavelengths. In *PIERS Proc*, pages 400–410, 2007. Prague, Czech Republic.

Mm-wave interferometric synthetic aperture imagers are currently being developed for the detection of concealed weapons and usually operate in a snapshot. We investigate the potential of including a mechanical scanning between the scene and the array in order to reduce the number of antennas and to ease the calibration process. We show that rotational scanning achieves a more uniform coverage of the (u; v) plane than the linear scanning traditionally used in RAD-SAR systems. We optimize rotated evenly distributed Reuleux triangle arrays for maximum uniform (u; v) coverage with a genetic algorithm and present the improvements in the sidelobes of the Point Spread Function.

- [106]A.R. Harvey, T. Vettenburg, M. Demenikov, B. Lucotte, G. Muyo, A. Wood, N. Bustin, A. Singh, and E. Findlay. Digital image processing as an integral component of optical design. In *Novel optical systems design and optimization XI*, volume 7061 of *SPIE*, pages 6104–6104, 2008.

  The design of modem imaging systems is intricately concerned with the control of optical aberrations in systems that can be manufactured at acceptable cost and with acceptable manufacturing tolerances. Traditionally this involves a multi-parameter optimisation of the lens optics to achieve acceptable image quality at the detector. There is increasing interest in a more generalised approach whereby digital image processing is incorporated into the design process and the performance metric to be optimised is quality of the image at the output of the image processor. This introduces the possibility of manipulating the optical transfer function of the optics such that the overall sensitivity of the imaging system to optical aberrations is reduced. Although these hybrid optical/digital techniques, sometimes referred as wavefront coding, have on occasion been presented as a panacea, it is more realistic to consider them as an additional parameter in the optimisation process. We will discuss the trade-offs involved in the application of wavefront coding to low-cost imaging systems for use in the thermal infrared and visible imaging systems, showing how very useful performance enhancements can be achieved in practical systems.

The image reconstruction procedure described in Chapter 5 to remove artifacts from wavefront coded images has been registered as a patent [30]:

M. Demenikov, E. Findlay, A. Harvey, B. Lucotte, and G. Muyo. Artifact removal from phase encoded images. US patent number: 20100008597. Assignees: STMicroelectronics (Research & Development) Limited.

Appendix B

Optimised antenna array coordinates

X [mm]	Y [mm]		θ [°]
337	−194		3.6572
349	−128		19.8011
319	−27		34.3253
297	46		51.5663
275	122		43.9647
230	190		65.2286
179	262		81.3986
118	309		101.3825
83	347		98.7180
0	390		126.1992
−62	345		130.6662
−118	300		155.4044
(a) −172	257	(b)	160.7857
−231	177		166.6895
−276	98		-173.0896
−293	35		-171.2087
−341	−38		-149.7358
−342	−123		-135.6034
−339	−188		-122.9077
−278	−245		-112.7982
−216	−257		-97.1768
−109	−293		-80.1186
−43	−301		-70.8972
27	−295		-58.4105
112	−276		-41.8748
197	−260		-22.8052
285	−229		-7.7324

Table B.1: *Antenna coordinates of the optimised Reuleux array (a) and the optimised circular array (b).*

Appendix C

Derivation of the Strehl ratio for phase errors with various distributions

The power of the in-phase summation of N unit vector is N^2. When summing N unit vector G_i with a random phase, the expected power sum is:

$$
\begin{aligned}
\overline{P} &= \langle |\sum_i^N G_i|^2 \rangle \\
&= N^2 \langle \cos\phi \rangle + N(1 - \langle \cos\phi \rangle)
\end{aligned}
\tag{C.1}
$$

with ϕ the difference between the phases of two terms G_i and G_k. $\langle \cos\phi \rangle$ may be written as:

$$
\langle \cos\phi \rangle = \int_{-\infty}^{+\infty} \cos\phi \, f_\Phi(\phi) \, d\phi
\tag{C.2}
$$

with $f_\Phi(\phi)$ the probability density function of the random variable Φ.

C.1   Gaussian distributed phases

If the phase of G_i is a Gaussian distributed random variable with a standard deviation σ_G and $\mu = 0$, then ϕ is a Gaussian distributed random variable with standard deviation $\sqrt{2}\sigma_G$. We refer to this distribution with the notation Gaussian$(0, \sqrt{2}\sigma_G)$. One can show that $\langle \cos\phi \rangle$ is such that:

$$
\langle \cos\phi \rangle = e^{-\sigma_G^2}
\tag{C.3}
$$

and using Eq. (C.1) and (C.3) one obtains:

$$\overline{P} = N^2 e^{-\sigma_G^2} + N(1 - e^{-\sigma_G^2}) \tag{C.4}$$

This is Eq. (4) from [48]. Hence the Strehl ratio for unit vectors with random phases taken from a distribution Gaussian$(0, \sigma_G)$ is expressed as:

$$S = e^{-\sigma_G^2} \left(1 + \frac{e^{\sigma_G^2} - 1}{N} \right) \tag{C.5}$$

For $N >> e^{\sigma_G^2} - 1$, S is dominated by the term $e^{-\sigma_G^2}$.

C.2 Laplace distributed phases

It is argued in section 3.5 that for a linear instrument drift with time and Gaussian distributed random drift rates, the assumption of Laplace distributed random phases leads to a more accurate modelling of the Strehl ratio of the array compared to the assumption of Gaussian distributed phases. We therefore consider now the case when the phase of G_i is a Laplace distributed random variable with a scale parameter σ_G and a location parameter $\mu = 0$. We note this distribution Laplace$(0, \sigma_L)$. One needs to know the probability density function $f_\Phi(\phi)$ of the random variable $\Phi = \Phi_1 - \Phi_2$ where Φ_1 and Φ_2 both have a distribution Laplace$(0, \sigma_L)$. To that end we use the characteristic function $\varphi_X(t)$ of a random variable X and defined as:

$$\varphi_X(t) = \left\langle e^{jtX} \right\rangle \tag{C.6}$$
$$= \int_{-\infty}^{+\infty} e^{jtx} f_X(x)\, dx \tag{C.7}$$

The characteristic function $\varphi_\Phi(t)$ can written as:

$$\varphi_\Phi(t) = \left\langle e^{jt(\phi_1 - \phi_2)} \right\rangle = \left\langle e^{jt\phi_1} \right\rangle \left\langle e^{-jt\phi_2} \right\rangle = \varphi_{\Phi_1}(t)\, \varphi_{-\Phi_2}(t) \tag{C.8}$$

One can show that the characteristic functions $\varphi_{\Phi_1}(t)$ and $\varphi_{-\Phi_2}(t)$ are equal and expressed as:

$$\varphi_{\Phi_1}(t) = \varphi_{-\Phi_2}(t) = \frac{1}{1 + \sigma_L^2 t^2} \tag{C.9}$$

Using Eq. (C.8) and (C.9) one obtains:

$$\varphi_\Phi(t) = \frac{1}{(1 + \sigma_L^2 t^2)^2} \tag{C.10}$$

Looking at the definition of the characteristic function in Eq. (C.7) one observes that $\varphi_X(t)$ is equal to the inverse Fourier transform of the probability density function $f_X(x)$. Therefore $f_\Phi(\phi)$ may be expressed as the Fourier transform of $\varphi_\Phi(t)$:

$$
\begin{aligned}
f_\Phi(\phi) &= \text{FT}\left[\varphi_\Phi(t)\right] && \text{(C.11)} \\
&= \text{FT}\left[\varphi_{\Phi_1}^2(t)\right] && \text{(C.12)} \\
&= \text{FT}\left[\varphi_{\Phi_1}(t)\right] * \text{FT}\left[\varphi_{\Phi_1}(t)\right] && \text{(C.13)}
\end{aligned}
$$

where $*$ denotes the convolution product. The Fourier transform of $\varphi_{\Phi_1}(t)$ can be written as:

$$
\text{FT}\left[\frac{1}{1+\sigma_L^2 t^2}\right] = e^{-\frac{|\phi|}{\sigma_L}} \tag{C.14}
$$

Calculating the convolution product of Eq. (C.13), $f_\Phi(\phi)$ can be rewritten as:

$$
f_\Phi(\phi) = \frac{1}{4\sigma_L^2}(\sigma_L + |\phi|)e^{-\frac{|\phi|}{\sigma_L}} \tag{C.15}
$$

where a factor $1/4\sigma_L^2$ has been included to maintain the unity of the integral of $f_\Phi(\phi)$. Eq. (C.2) can now be calculated:

$$
\begin{aligned}
\langle \cos\phi \rangle &= \frac{1}{4\sigma_L^2}\int_{-\infty}^{+\infty} \cos\phi\,(\sigma_L + |\phi|)e^{-\frac{|\phi|}{\sigma_L}}\,d\phi \\
&= \frac{1}{2\sigma_L^2}\left(\sigma_L \int_0^{+\infty} \cos\phi\,e^{-\frac{\phi}{\sigma_L}}\,d\phi + \int_0^{+\infty} \phi\cos\phi\,e^{-\frac{\phi}{\sigma_L}}\,d\phi\right) \\
&= \frac{1}{(1+\sigma_L^2)^2} && \text{(C.16)}
\end{aligned}
$$

Using Eq. (C.1) and (C.16) the Strehl ratio obtained for unit vectors with random phases taken from a distribution $\text{Laplace}(0, \sigma_L)$ is finally expressed as:

$$
S = \frac{1}{(1+\sigma_L^2)^2}\left(1 + \frac{\sigma_L^2}{N}(2+\sigma_L^2)\right) \tag{C.17}
$$

When $N >> \sigma_L^2(2+\sigma_L^2)$, the Strehl ratio is dominated by the term $1/(1+\sigma_L^2)^2$.

C.3   List of useful integrals and Fourier transform

$$\int_0^{+\infty} e^{-ax^2} \cos bx \, dx = \frac{\sqrt{\pi}}{2a} e^{-b^2/4a^2}, \quad (a > 0)$$

$$\int_0^{+\infty} e^{-ax} \cos mx \, dx = \frac{a}{a^2+m^2}, \qquad (a > 0)$$

$$\int_0^{+\infty} xe^{-ax} \cos bx \, dx = \frac{a^2-b^2}{(a^2+b^2)^2}, \qquad (a > 0)$$

$$\text{FT}\left[e^{-a|t|}\right] = \sqrt{\frac{2}{\pi}} \frac{a}{a^2+\omega^2}$$

References

[1] J. W. Goodman. *Introduction to Fourier Optics*. Roberts & Company Publishers, 2004.

[2] A. R. Thompson, J. M. Moran, and G. W. Swenson. *Interferometry and Synthesis in Radio Astronomy*. Wiley, 2001.

[3] D. Huang, E. A. Swanson, C. P. Lin, J. S. Schuman, W. G. Stinson, W. Chang, M. R. Hee, T. Flotte, K. Gregory, and C. A. Puliafito. Optical coherence tomography. *Science*, 254:1178–81, 1991.

[4] A. F. Fercher, C. K. Hitzenberger, G. Kamp, and S. Y. El-Zaiat. Measurements of intraocular distances by backscattering spectral interferometry. *Opt. Comm.*, 117:43–48, 1995.

[5] T. S. Ralston, D. L. Marks, P. S. Carney, and S. A. Boppart. Interferometric synthetic aperture microscopy. *Nature Phys.*, 3:129 – 134, 2007.

[6] T. A. Klar, E. Engel, and S. W. Hell. Breaking abbe's diffraction resolution limit in fluorescence microscopy with stimulated emission depletion beams of various shapes. *Phys. Rev. E*, 64(6):066613, Nov 2001.

[7] M. G. L. Gustafsson. Surpassing the lateral resolution limit by a factor of two using structured illumination microscopy. *Journal of Microscopy*, 198(2):82–87, 2000.

[8] M. G. L. Gustafsson. Nonlinear structured-illumination microscopy: Wide-field fluorescence imaging with theoretically unlimited resolution. *Proc. Natl. Acad. Sci. USA*, 102(37):13081–13086, 2005.

[9] C. S. Ruf, C. T. Swift, A. B. Tanner, and D. M. Le Vine. Interferometric synthetic aperture microwave radiometry for the remote sensing of the earth. *IEEE Trans. Geosci. Remote Sens.*, 26(5):597–611, September 1988.

[10] D. M. Sheen, D. L. McMakin, and T. E. Hall. Three-Dimensional Millimeter-Wave Imaging for Concealed Weapon Detection. *IEEE transactions on Microwave theory and techniques*, 49(9), September 2001.

[11] R. Appleby. Whole body 35 GHz security scanner. In *Proceedings of SPIE*, Bellingham WA, August 2004.

[12] A. R. Harvey and R. Appleby. Passive mm-wave imaging from UAVs using aperture synthesis. *Aeronaut J*, 107(1068):87–97, 2003.

[13] O. Hupe and U. Ankerhold. X-ray security scanners for personnel and vehicle control: Dose quantities and dose values. *European Journal of Radiology*, 63:237–241, 2007.

[14] G. W. Swenson and N. C. Mathur. The Interferometer in Radio Astronomy. *Proc. Inst. Electr. Eng.*, 56(12):2114–2130, December 1968.

[15] M. Peichl, H. Suess, M. Suess, and S. Kern. Microwave imaging of the brightness temperature distribution of extended areas in the near and far field using two-dimensional aperture synthesis with high spatial resolution. *Radio Science*, 33(3):781–801, May-June 1998.

[16] C. Edelsohn, J. Gurley, H. McCord, R. Donnelly, P. Virga, W. Butler, and A. Jain. RADSAR (RADiometric SAR) experimental results. In *International Geoscience and Remote Sensing Symposium*, pages 372–374, Piscataway, NJ, 1998. IEEE.

[17] E. Keto. The Shapes of Cross-Correlation Interferometers. *Astrophys. J*, 475:843–852, Feb 1997.

[18] T. J. Cornwell. A Novel Principle for Optimization of the Instantaneous Fourier Plane Coverage of Correlation Arrays. *IEEE transactions on Antennas and Propagation*, 36(8):1165–1167, August 1988.

[19] R. L. Haupt. An Introduction to Genetic Algorithms for Electromagnetics. *IEEE Antennas Propag. Mag.*, 37(2):7–15, April 1995.

[20] B. M. Lucotte and A. R. Harvey. Antenna rotation aperture synthesis for short-range personnel scanning at mm wavelengths. In *PIERS Proc*, pages 400–410, 2007. Prague, Czech Republic.

[21] B. M. Lucotte, B. Grafulla-González, and A. R. Harvey. Array rotation aperture synthesis for short-range imaging at millimeter wavelengths. *Radio Sci.*, 44(RS1006), 2009.

[22] J. Ojeda-Castañeda, R. Ramos, and A. Noyola-Isgleas. High focal depth by apodization and digital restoration. *Appl. Opt.*, 27(12):2583–2586, 1988.

[23] J. Ojeda-Casta neda, L. R. Berriel-Valdos, and E. L. Montes. Line-spread function relatively insensitive to defocus. *Opt. Lett.*, 8(8):458–460, 1983.

[24] J. Nunez and J. Llacer. A general bayesian image reconstruction algorithm with entropy prior: preliminary application to hst data. *Astronomical society of the pacific*, 105(692):1192–1208, 1993.

[25] R. J. Hanisch. Image restoration for the hubble space telescope. In *Proc. SPIE*, volume 2198, 1994.

[26] E. Dowski and T. W. Cathey. Extended depth of field through wavefront coding. *Appl. Opt.*, 34:1859–1866, 1995.

[27] S. Prasad, T. Torgersen, V. P. Pauca, R. Plemmons, and J. van der Gracht. Engineering the pupil phase to improve image quality. In Z. Rahman, R. Schowengrdt, and S. Reichenbach, editors, *Proceedings of the SPIE on Visual Information Processing*, volume 5108 of *XII*, pages 1–12, 2003.

[28] D. S. Barwick. Efficient metric for pupil-phase engineering. *App. Optics*, 46(29):7258–7261, 2007.

[29] G. D. Muyo Nieto. *Principles and applications of wavefront coding*. PhD thesis, School of Engineering and Physical Sciences, Heriot Watt University, 2007.

[30] M. Demenikov, E. Findlay, A. Harvey, B. Lucotte, and G. Muyo. Artifact removal from phase encoded images. US patent number: 20100008597. Assignees: STMicroelectronics (Research & Development) Limited.

[31] John C. Curlander and Robert N. McDonough. *Synthetic Aperture Radar, Systems and Signal Processing.* Wiley series in remote sensing, 1991.

[32] D. Marcano and F. Duràn. Synthesis of antenna arrays using Genetic Algorithms. *IEEE Antennas Propag. Mag*, 42(3):12–20, June 2000.

[33] L. Kogan. Optimizing a Large Array Configuration to Minimize the Sidelobes. *IEEE transactions on Antenna and Propagation*, 48(7):1075–1078, July 2000.

[34] S. Hebib, N. Raveu, and H. Aubert. Cantor Spiral Array for the Design of Thinned Arrays. *IEEE Antennas and wireless propagation letters*, 5:104–106, 2006.

[35] C. S. Ruf. Numerical Annealing of Low-Redundancy Linear Arrays. *IEEE transactions on Antenna and Propagation*, 41(1):85–90, January 1993.

[36] L. E. Kopilovich. Non-redundant hexagonal array configurations for optical interferometric systems compactly covering central domains in the spatial-frequency plane. *Journal of Modern Optics*, 52(10):1415–1420, July 2005.

[37] C. S. Ruf. Antenna performance for a synthetic aperture microwave radiometer in geosynchronous earth orbit. In *International Geoscience and Remote Sensing Symposium*, volume II, pages 1589–1592, College Park, MD, May 1990.

[38] J. D. Victor. Binless strategies for estimation of information from neural data. *Physical review*, 66(051903):1–15, 2002.

[39] L. F. Kozachenko and N. N. Leonenko. On statistical estimation of entropy of random vector. *Problems Infor. Transmiss.*, 23(2):95–101, 1987. translated from Problemy Peredachi Informatsii, in Russian, vol. 23, No. 2, pp. 9-16, 1987.

[40] C. B. Barber, D.P. Dobkin, and H.T. Huhdanpaa. The quickhull algorithm for convex hulls. *ACM Transactions on Mathematical Software*, 22(4):469–483, December 1996.

[41] B. Grafulla-González, K. Lebart, and A. R. Harvey. Physical optics modelling of millimetre-wave personnel scanners. *Pattern Recognition Letters*, 27(15):1852–1862, 2006.

[42] Y. L. Chow. On designing a Supersynthesis Antenna Array. *IEEE transactions on Antennas and Propagation*, 20:30–35, 1972.

[43] F. Torres, A. Camps, J. Bará, and I. Corbella. Impact of receiver errors on the radiometric resolution of large 2D aperture synthesis radiometers. *Radio Sci.*, 32(2), March-April 1997.

[44] A. Camps, F. Torres, I. Corbella, J. Bará, and P. de Paco. Mutual coupling effects on antenna radiation pattern: An experimental study applied to interferometric radiometers. *Radio Sci.*, 33(6):15431552, 1998.

[45] F. Torres, A. Camps, I. Corbella, J. Bará, N. Duffo, and M. Vall-Lossera. Calibration methods in large interferometric radiometers devoted to earth observation. In P. Pampaloni and S. Paloscia, editors, *Microwave radiometry and remote sensing of the Earth's surface and atmosphere*, pages 459–464. VSP, 2000.

[46] C.S. Ruf and J. Li. A correlated noise calibration standard for interferometric, polarimetric, and autocorrelation microwave radiometers. *Geoscience and Remote Sensing, IEEE Transactions on*, 41(10):2187–2196, Oct. 2003.

[47] K. Maisinger, M. P. Hobson, R. D. E. Saunders, and K. J. B. Grainge. Maximum-likelihood astrometric geometry calibration of interferometric telescopes: application to the very small array. *Mon. Not. R. Astron. Soc*, 345(3):800–808, 2003.

[48] J. Ruze. Antenna tolerance theory - A review. volume 54, pages 633–640, April 1966.

[49] W. J. Smith. *Modern optical engineering*. New York, 2000.

[50] K. Strehl. Investigations in optics with special reference to the spectroscope. *Zeitfür Instrumkde*, 22:213, 1902.

[51] Lord Rayleigh. Investigations in optics with special reference to the spectroscope. *Philos. Mag.*, 8:261, 1879.

[52] H. H. Hopkins. The aberration permissable in optical systems. *Proc. Phys. Soc. B*, 70:449470, 1955.

[53] H. H. Hopkins. The use of diffraction-based criterion of image quality in automatic optical design. *Opt. Acta*, 13:343369, 1966.

[54] J. Ojeda-Castañeda, M. Martínez-Corral, P. Andrés, and A. Pons. Strehl ratio versus defocus for noncentrally obscured pupils. *Applied Optics*, 33(32):7611–7616, November 1994.

[55] G. Haüsler. A method to increase the depth of focus by two step image processing. *Opt. Commun.*, 6:38–42, 1972.

[56] W. T. Welford. Use of annular apertures to increase focal depth. *J. Opt. Soc. Am.*, 50(8):749–753, 1960.

[57] H. Bartelt, J. Ojeda-Castaneda, and E. E. Sicre. Misfocus tolerance seen by simple inspection of the ambiguity function. *Appl. Opt.*, 23:2693–2696, 1984.

[58] J. Ojeda-Castañeda, P. Andrs, and E. Montes. Phase-space representation of the strehl ratio: ambiguity function. *J. Opt. Soc. Am. A*, 4:313–317, 1987.

[59] Z.S. Hegedus and V. Sarafis. Superresolving filters in confocally scanned imaging systems. *J. Opt. Soc. Am. A*, 3(11):1892–1896, 1986.

[60] A. R. FitzGerrell, E. R. Dowski, and W. T. Cathey. Defocus transfer function for circularly symmetric pupils. *Appl. Opt.*, 36, 1997.

[61] S. S. Sherif, E. R. Dowski, and W. T. Cathey. Extended depth of field in hybrid imaging systems: circular aperture. *J. Mod. Optics*, pages 1–19, 2004.

[62] T.R.M. Sales and G.M. Morris. Axial superresolution with phase-only pupil filters. *Optics Communications*, 156:227–230, November 1998.

[63] J. Ojeda-Castañeda, L. E. A. Langrave, and H. M. Escamilla. Annular phaseonly mask for high focal depth. *Opt. Lett.*, 30:16471649, 2005.

[64] S. Mezouari, G. Muyo, and A. R. Harvey. Amplitude and phase filters for mitigation of defocus and third-order aberrations. In *Proc SPIE*, volume 4768, pages 21–31, 2003.

[65] D. S. Barwick. Defocus sensitivity optimization using the defocus taylor expansion of the optical transfer function. *App. Optics*, 47(31):5893–5902, 2008.

[66] R. Ng, M. Levoy, M Brédif, G. Duval, M. Horowitz, and P. Hanrahan. Light field photography with a hand-held plenoptic camera. Technical report, Stanford University, 2005.

[67] R. Ng. Fourier slice photography. Technical report, Stanford University, 2005.

[68] T. Adelson and J. Y. A. Wang. Single lens stereo with a plenoptic camera. *Pattern Analysis and Machine Intelligence, IEEE Transactions on*, 14:99–106, 1992.

[69] R. K. Tyson. *Principles of Adaptive Optics*. Academic Press, 2nd ed. edition, 1998.

[70] P. Favaro and S. Soatto. A geometric approach to shape from defocus. *Pattern Analysis and Machine Intelligence, IEEE Transactions on*, 27(3), 2005.

[71] K. Brenner, A. Lohmann, and J. Ojeda-Castañeda. The ambiguity function as a polar display of the otf. *Opt. Comm.*, 44:323–326, 1983.

[72] A. Papoulis. Ambiguity function in fourier optics. *J. Opt. Soc. Am.*, 64:779788, 1974.

[73] T. Alieva and M.J. Bastiaans. Wigner distribution and fractional fourier transform. In *Signal Processing and its Applications, Sixth International, Symposium on.*, volume 1, pages 168–169, 2001.

[74] L. B. Almeida. The fractional fourier-transform and time-frequency representations. *IEEE trans. on signal processing*, 42(11):3084–3091, Nov 1994.

[75] J. Ojeda-Castañeda. Bilinear optical systems - wigner distribution function and ambiguity function representations. *Opt. Acta*, 1:255–260, 1984.

[76] K. H. Brenner and J. Ojeda-Castañeda. Ambiguity function and wigner distribution function applied to partially coherent imagery. *Opt. Acta*, 31(2):213–223, 1984.

[77] S. Mallat. *A Wavelet Tour of Signal Processing*. Academic, 1998.

[78] M. Born and E. Wolf. *Principles of Optics: Electromagnetic Theory of Propagation, Interference and Diffraction of Light*, chapter 9, page 545. Cambridge University Press, Cambridge, England, seventh edition, 1999.

[79] C.J.R. Sheppard and A. Choudhury. Image formation in the scanning microscope. *Journal of Modern Optics*, 24(10):1051–1073, 1977.

[80] J. Ching, A.C. To, and S.D. Glaser. Microseismic source deconvolution: Wiener filter versus minimax, fourier versus wavelets, and linear versus nonlinear. *J. Acoust. Soc. Am.*, 115(6):3048–3058, June 2004.

[81] M. Born and E. Wolf. *Principles of Optics: Electromagnetic Theory of Propagation, Interference and Diffraction of Light*, chapter 4, pages 223–226. Cambridge University Press, Cambridge, England, seventh edition, 1999.

[82] G. Muyo and A. R. Harvey. Decomposition of the optical transfer function: wavefront coding imaging systems. *Opt. Letters*, pages 2715–2717, 2005.

[83] A. A. Michelson. *Studies In optics*. Chicago: University of Chicago Press, 1927.

[84] P. Sakellaropoulos, L. Costaridou, and G. Panayiotakis. A wavelet-based spatially adaptive method for mammographic contrast enhancement. *Phys. Med. Biol.*, 48:787–803, 2003.

[85] P. Lopez-Dekker, G. Farquharson, and S. Frasier. A comparison of contrast metrics for contrast-based phase calibration of digital beamforming remote sensing systems. In *IEEE IGARSS*, volume 1-8, pages 3036–3039, 2006.

[86] E. Peli. In search of a contrast metric: Matching the perceived contrast of gabor patches at different phases and bandwidths. *Vision Res.*, 37(23):3217–3224, 1997.

[87] K. Carlsson. Three-dimensional microscopy using a confocal laser scanning microscope. *Opt. Lett.*, 10(2):53–55, February 1985.

[88] C.J.R. Sheppard and T. Wilson. Depth of field in the scanning microscope. *Opt. Lett.*, 3(3):115, 1978.

[89] M.A.A. Neil, R. Juškaitis, T. Wilson, Z.J. Laczik, and V. Sarafis. Optimized pupil-plane filters for confocal microscope point-spread function engineering. *Optics express*, 15(4):245–247, February 2000.

[90] S. C. Tucker, W. T. Cathey, and E. R. Dowski Jr. Extended depth of field and aberration control for inexpensive digital microscope systems. *Optics express*, 4(11):467–474, May 1999.

[91] E.J. Botcherby, R. Juškaitis, M.J. Booth, and T. Wilson. An optical technique for remote focusing in microscopy. *Optics communications*, 281:880–887, 2008.

[92] E.J. Botcherby, M.J. Booth, R. Juškaitis, and T. Wilson. Real-time extended depth of field microscopy. *Optics express*, 16(26):21843–21848, December 2008.

[93] G. Muyo and A. R. Harvey. The effect of detector sampling in wavefront-coded imaging systems. *J. Opt. A: Pure Appl. Opt*, 11(054002), 2009.

[94] G. D. Boreman. *Modulation Transfer Function in Optical and Electro-Optical Systems*. SPIE Press Book, 2001.

[95] M. Born and E. Wolf. *Principles of Optics: Electromagnetic Theory of Propagation, Interference and Diffraction of Light*, chapter 10, pages 591–599. Cambridge University Press, Cambridge, England, seventh edition, 1999.

[96] C. J. R. Sheppard. Defocused transfer function for a partially coherent microscope and application to phase retrieval. *J. Opt. Soc. Am. A*, 21(5):828–831, May 2004.

[97] M. Born and E. Wolf. *Principles of Optics: Electromagnetic Theory of Propagation, Interference and Diffraction of Light*, chapter 10, page 603. Cambridge University Press, Cambridge, England, seventh edition, 1999.

[98] N. Streibl. Three-dimensional imaging by a microscope. *J. Opt. Soc. Am. A*, 2(2):121–127, 1985.

[99] M. J. Morgan, J. Ross, and A. Hayes. The relative importance of local phase and local amplitude in patchwise image reconstruction. *Biol. Cybern.*, 65(2):113–119, 1991.

[100] M. Born and E. Wolf. *Principles of Optics: Electromagnetic Theory of Propagation, Interference and Diffraction of Light*, chapter 8, pages 472–476. Cambridge University Press, Cambridge, England, seventh edition, 1999.

[101] A. Barty, K. A. Nugent, D. Paganin, and A. Roberts. Quantitative optical phase microscopy. *Opt. Lett.*, 23:817–819, 1998.

[102] A. L. Boyer. Reconstruction of ultrasonic images by backward propagation. *Acoustic Holography*, 3:333384, 1970.

[103] G. Saavedra, I. Escobar, R. Martínez-Cuenca, E. Sánchez-Ortiga, and M. Martínez-Corral. Reduction of spherical-aberration impact in microscopy by wavefront coding. *Opt. Express*, 17(16):13810–13818, 2009.

[104] M. J. Booth, M. A. A. Neil, R. Juškaitis, and T. Wilson. Adaptive aberration correction in a confocal microscope. *Proc. Natl. Acad. Sci. USA*, 99(9):57885792, 2002.

[105] M. J. Booth, M. Schwertner, T. Wilson, M. Nakano, Y. Kawata, M. Nakabayashi, and S. Miyata. Predictive aberration correction for multilayer optical data storage. *Appl. Phys. Lett.*, 88(3):031109, 2006.

[106] A.R. Harvey, T. Vettenburg, M. Demenikov, B. Lucotte, G. Muyo, A. Wood, N. Bustin, A. Singh, and E. Findlay. Digital image processing as an integral component of optical design. In *Novel optical systems design and optimization XI*, volume 7061 of *SPIE*, pages 6104–6104, 2008.